

Doctoral theses at NTNU, 2018:186

Leif Erik Andersson
**Short-term Iceberg Drift Estimation
and Prediction**

ISBN 978-82-326-3162-9 (printed version)
ISBN 978-82-326-3163-6 (electronic version)
ISSN 1503-8181

Doctoral theses at NTNU, 2018:186

NTNU
Norwegian University of
Science and Technology
Faculty of Information Technology
and Electrical Engineering
and Department of Engineering Cybernetics

Leif Erik Andersson

Short-term Iceberg Drift Estimation and Prediction

Thesis for the degree of Philosophiae Doctor

Trondheim, May 2018

Norwegian University of Science and Technology
Faculty of Information Technology
and Electrical Engineering
Department of Engineering Cybernetics



Norwegian University of
Science and Technology

NTNU

Norwegian University of Science and Technology

Thesis for the degree of Philosophiae Doctor

Faculty of Information Technology
and Electrical Engineering
Department of Engineering Cybernetics

© Leif Erik Andersson

ISBN 978-82-326-3162-9 (printed version)

ISBN 978-82-326-3163-6 (electronic version)

ISSN 1503-8181

ITK Report 2018-6-W

Doctoral theses at NTNU, 2018:186



Printed by Skipnes Kommunikasjon as

Summary

Short-term iceberg drift forecast is part of the Ice Management framework, which is a key component of the International Standard, ISO 19906 specifying requirements and guidance for the design, construction, transportation, installation and decommissioning of offshore platforms. Ice Management was developed and successfully applied to support operations in ice-infested waters, such as the oil and gas operations on the East Coast of Canada and the Barents Sea. If an iceberg approaches a platform, it must be deflected from its path. Physical iceberg management is an expensive and time-consuming operation. An accurate iceberg drift forecast reduces the amount of unnecessary towing actions. Consequently, it reduces the threat of iceberg interactions and risk of downtime and possible disconnection of oil and gas operations. Moreover, it simplifies the decision-making of platform operators.

A mechanistic dynamic iceberg model was previously developed in the 1980's. An operational iceberg drift model was developed at the National Research Council of Canada and implemented at the Canadian Ice Service and other agencies. However, significant uncertainties, especially in the ocean current forecast, along with the parametrisation of the model, prevent an accurate forecast. Furthermore, frequent iceberg position measurements, which may be available when the iceberg approaches an offshore facility, are not included in the conventional forecasts with the dynamic iceberg drift model. Consequently, important and available information is not considered in these drift forecasts.

A common method for platform operators to forecast an iceberg trajectory is to extrapolate the last two iceberg position measurements linearly. This thesis discusses different approaches to how frequent iceberg position measurements can be incorporated in the forecast process to improve the operational short-term iceberg drift forecast. The developed algorithms are tested on nine iceberg trajectories from two datasets collected during 2015 and 2016. Moreover, the thesis contains additional work analysing the ocean current based on the observed iceberg trajectory and deriving a Cramér-Rao bound for discrete-time systems with state con-

straints. Based on the latter, a Kalman filter for linear state equality constraints is developed.

Preface

The research presented in this thesis has been conducted at the Department of Engineering Cybernetics (ITK) at the Norwegian University of Science and Technology (NTNU) under supervision of Professor Lars Imsland, Dr. Francesco Scibilia, Professor Sveinung Løset and Professor Tor-Arne Johansen, in the period from March 2014 to May 2018. The work was supported by Statoil ASA, and in part by the Centre for Autonomous Marine Operations and Systems (Centre of Excellence AMOS, Research Council of Norway project number 223254). In part, the research presented in this thesis uses E.U. Copernicus Marine Service Information.

Acknowledgements

First, and foremost, I would like to extend my gratitude and thanks to Lars Imsland and Francesco Scibilia for their excellent supervision and scientific advice. I enjoyed our meetings, discussions and your valuable inputs. I am grateful that you provided me with so much freedom and were always positive towards my suggestions and ideas.

In addition, my sincere thanks to Lars for his trust and the opportunity to teach his course Modelling and Simulation during his sabbatical. I enjoyed this exciting *adventure*. In this context, I also like to thank my superb teaching assistants Mikkel Eske N. Sørensen and Eric Christopher Bradford.

I want to thank Associate Professor Luke Copland from the University of Ottawa, Canada, for providing me with a second iceberg drift dataset. While our first meeting in Ottawa was brief and actually more coincidental, it resulted in a very fruitful cooperation. In this context, I want to thank NSERC and ArticNet for funding and assistance with deployment of the iceberg trackers.

I want to thank my defence committee, Professor Biao Huang, Dr. Intissar Keghouche and Professor Morten Hovd for taking the time to revise my thesis and for providing insightful and constructive comments on improving the manuscript.

I want to thank Professor Brad deYoung and Associate Professor Entcho Demirov for their time and valuable inputs during my short visit at the Memorial University

in St. John's, Canada. I also want to thank Associate Professor Derek Mueller and his students Ron Saper, and Anna Crawford for their hospitality during my stay in Ottawa, Canada. Moreover, thanks be given to Adrienne Tivy and Hai Tran for inviting me to visit the Canadian Ice Service in Ottawa. This was a very interesting experience.

I want to thank Statoil, ArcticNet, the Canadian Coast Guard Ship *Amundsen* and its crew for contributing to a safe Offshore Newfoundland Research Expedition 2015. The iceberg drift dataset that we collected during the expedition was of great importance for this thesis.

Special thanks go to Muhammad Faisal Aftab who was my office colleague for almost the entire period of my research. You helped me in many occasions, had always time to listen and contribute in a constructive matter. I enjoyed our discussions, small talk and cooperation.

I also want to express my gratitude to the administrative staff at the ITK. The help and positive attitude of Tove Kristin Blomset Johnsen, Eva Amdahl, Unni Johansen, Bente Seem Lindquist, Janne Karin Hagen, Lill Hege Pedersen and Aud Marit Lervik is highly appreciated.

To my friends and colleagues at the department, thank you for making the last four years enjoyable. I will remember our coffee breaks, the cosy social gatherings and the times we spent travelling together. Special thanks to Stefano Brevik Bertelli and Glenn Angell, and the others from the cageball team. It has been a pleasure playing with you.

Last but not least, I want to thank my family. My grandparents, Inge, Günther, Harriet and Herbert, my sister Jarla, and my parents, Sven and Birgitta, who raised, encouraged and supported me throughout the years. Finally, I want to thank Konstanze for being there and taking this exciting chapter *Trondheim* together with me.

Contents

Summary	iii
Preface	v
Contents	xvi
1 Introduction	1
1.1 Ice Management	3
1.2 Notations	5
1.3 Contributions	5
1.4 Publications	6
1.4.1 Journal Publications	6
1.4.2 Conference Publications	6
1.5 Thesis Organization	7
2 Iceberg Shape Classification and Dynamic Iceberg Drift Model	9
2.1 Iceberg Geometry	9
2.2 Iceberg Shape	10
2.3 The Dynamic Iceberg Model	10

2.3.1	Sensitivity of parameters of the dynamic iceberg model . . .	13
2.4	Literature Review on Iceberg Drift Forecast	15
3	Theory and Methods	19
3.1	State Estimator	19
3.1.1	The Moving Horizon Estimator	20
3.1.2	Extended Kalman Filter	21
3.2	Empirical Mode Decomposition	21
3.2.1	Multivariate EMD	22
3.2.2	Mode Alignment Property	23
3.3	Model Identification and Granger's Causality	25
3.3.1	Model Order	26
I	Iceberg Dataset and Sensitivity Study	27
4	Iceberg Datasets	29
4.1	The Newfoundland Iceberg Dataset	29
4.1.1	Iceberg 1	30
4.1.2	Iceberg 2	30
4.1.3	Iceberg 4	31
4.2	The Baffin Bay Iceberg Dataset	32
4.2.1	Iceberg 1040	33
4.2.2	Iceberg 5450	34
4.2.3	Iceberg 3534	35
4.2.4	Iceberg 3651	35
5	Sensitivity Study of the Dynamic Iceberg Drift Model	37
5.1	Introduction	37

5.2	Data Collection	38
5.3	Iceberg Drift Simulation	40
5.3.1	Sensitivity of Iceberg Shape to Different Current Measurements	40
5.3.2	Sensitivity of Iceberg Model to Different Input Signals and Geometry Assumptions	41
5.4	Conclusion	44
 II Hybrid Iceberg Drift Forecast Algorithms		47
 6 The Ancillary Current Forecast Scheme		49
6.1	Introduction	49
6.2	The Dynamic Iceberg Drift Model	49
6.3	Choice of Estimated Parameters	50
6.3.1	Design Criteria	50
6.3.2	Design Criteria Applied to the Iceberg Model	50
6.3.3	The Ancillary Current	52
6.4	Data Acquisition	53
6.5	Simulation and Estimation Set-up	54
6.6	Simulation Study	56
6.6.1	Iceberg 1	56
6.6.2	Iceberg 2	57
6.6.3	Discussion	58
6.7	Estimation Study	59
6.7.1	Forecast Performance Indices	59
6.7.2	Iceberg 1	61
6.7.3	Iceberg 2	65

6.7.4	Comparison between chosen Design and Estimation of Air and Water Drag Coefficient	68
6.8	Discussion	71
6.9	Conclusion	72
7	The Inertial Current Forecast Scheme	75
7.1	Introduction	75
7.2	Problem Formulation	76
7.2.1	Motivation for Using the Moving Horizon Estimator	77
7.3	Case Study	77
7.3.1	Estimation Model	78
7.3.2	Observability	80
7.3.3	Estimation Setup	80
7.3.4	Estimation with the Simulated Model	81
7.3.5	Estimation with Real Data	84
7.4	Conclusion	88
8	Switching Scheme between Ancillary and Inertial Current Forecasts	91
8.1	Introduction	91
8.2	Statement of Theory and Definitions	92
8.2.1	Iceberg Drift Model	92
8.2.2	The Ancillary Current Forecast Scheme	92
8.2.3	The Inertial Current Forecast Scheme	94
8.2.4	Moving Horizon Estimator	94
8.3	Data Acquisition	94
8.4	Results	95
8.5	Conclusion	96

III Statistical Iceberg Drift Forecast Algorithms 99

9 An iceberg forecast approach based on a statistical ocean current model	101
9.1 Introduction	101
9.2 Motivation	102
9.3 Theory and Methods	104
9.4 Performance Indices	104
9.5 Dataset	106
9.5.1 Iceberg Data	106
9.5.2 Current Data	106
9.5.3 Wind Data	107
9.6 Pre-Analysis	108
9.6.1 Time Horizon of Kinematic Models	108
9.6.2 Cross-correlation of Variables	111
9.6.3 Model Order	112
9.7 Iceberg Forecast	112
9.7.1 Model Order	113
9.7.2 Moving Horizon Window Length	113
9.7.3 Forecast Horizon	114
9.7.4 First-order Model	116
9.7.5 Dynamic Iceberg Model	117
9.7.6 Relative Performance Index	121
9.8 Conclusion	122

IV Analysis and Forecast using the Multivariate Empirical Mode Decomposition 125**10 Analysis of Iceberg Drift Trajectories Using the Multivariate Empirical Mode Decomposition 127**

10.1 Introduction 127

10.2 The Datasets 128

10.2.1 Current Dataset 129

10.2.2 Wind Dataset 129

10.2.3 Tidal Current Dataset 129

10.3 Detection of Tidal and Inertial Current Oscillation in the Iceberg Drift Velocity 130

10.3.1 Iceberg 4 130

10.3.2 Iceberg 3651 132

10.4 Further Analysis of the Iceberg Velocity using Current and Wind Data. 134

10.4.1 Iceberg 3651 134

10.5 Conclusion 135

11 Multivariate Empirical Mode Decomposition Forecast Scheme 139

11.1 Introduction 139

11.2 Problem Description 140

11.3 The Forecast Algorithm 141

11.3.1 Basic Steps of Forecast Algorithm 141

11.3.2 Self-forecast 142

11.3.3 Input-forecast 143

11.3.4 Forecast Decision 144

11.3.5 Forecast of the Output Signal 144

11.4 Case Study 144

11.4.1	The Dataset	144
11.4.2	Forecast Results	144
11.5	Conclusion	147
V	Comparison of Forecast Algorithms	151
12	Comparison of Statistical Iceberg Forecast Models	153
12.1	Introduction	153
12.2	Theory and Methods	154
12.2.1	The Moving Horizon Estimator	154
12.2.2	The Extended Kalman Filter	154
12.2.3	Vector-Autoregression Model Fitting	154
12.2.4	The Multivariate Empirical Model Decomposition	154
12.3	Iceberg Drift Forecast Schemes	155
12.3.1	Dynamic Forecast scheme	155
12.3.2	Statistical Forecast Scheme	155
12.3.3	Kinematic Forecast Schemes	156
12.3.4	Hybrid Forecast Schemes	158
12.4	Dataset	160
12.4.1	Iceberg Data	161
12.4.2	Current data	162
12.4.3	Wind Data	162
12.5	Performance Indices	162
12.6	Comparison Iceberg Drift Forecast	163
12.6.1	Iceberg 2	164
12.6.2	Iceberg 1	165
12.6.3	Iceberg 4	165

12.6.4	Iceberg 4-3	166
12.6.5	Iceberg 1040-1	167
12.6.6	Iceberg 1040-2	168
12.6.7	Iceberg 5450	169
12.6.8	Iceberg 3534	169
12.6.9	Iceberg 3651	170
12.6.10	Summary Iceberg Forecast	171
12.7	New Statistical Forecast Schemes	172
12.8	Conclusion and Future Work	173
12.A	Extension to the Comparison of Iceberg Drift Forecasts	176
12.A.1	Iceberg 1	176
12.A.2	Iceberg 4	177
12.A.3	Iceberg 4-3	177
12.A.4	Iceberg 1040-1	177
12.A.5	Iceberg 1040-2	178
12.A.6	Iceberg 5450	179
12.A.7	Iceberg 3534	179
12.A.8	Iceberg 3651	180

VI Parameter and State Estimation under Constraints 191

13 Estimation of a Hydrodynamic Iceberg Geometry 193

13.1	Introduction	193
13.2	Data Collection	193
13.3	Estimation of the Iceberg Geometry	194
13.3.1	The Iceberg Geometry Model	194
13.3.2	Estimation Algorithm	196

13.3.3	Identifiability	197
13.3.4	Geometry Estimation	198
13.4	Conclusion	199
14	Constrained Posterior Cramér-Rao Bound for Discrete-Time Systems	201
14.1	Introduction	201
14.2	The CRB for the Nonlinear Filtering Problem	203
14.3	Constrained CRB	205
14.4	The Constrained CRB for the Nonlinear Filtering Problem	207
14.5	Reduction of the Constrained CRB	209
14.6	Computation of the Constrained CRB	209
14.6.1	The Linear Gaussian Case	209
14.7	Numerical Example	210
14.8	Conclusion	212
15	On Kalman Filtering with Linear State Equality Constraints	215
15.1	Introduction	215
15.2	Four Kalman Filter Variants	216
15.2.1	The Unconstrained Kalman Filter	217
15.2.2	The Estimate Projection Kalman Filter	217
15.2.3	The System Projection Kalman Filter	218
15.2.4	The Equality Constrained Kalman Filter	219
15.3	Comparison of Constrained Kalman Filters	221
15.4	Numerical Example	222
15.5	Conclusion	223
16	Concluding remarks	225

VII Appendices	231
A Linear Algebra	233
A.1 Matrix Inversion Lemma	233
A.2 Binomial inverse theorem	233
B PAPER E: The Moving Horizon Estimator Used in Iceberg Drift Estimation and Forecast.	235
References	243

Chapter 1

Introduction

The forecast for weather-driven systems is challenging. This statement is important for the interpretation of forecasting results, and it will be repeated throughout the thesis. The forecast of iceberg drift trajectories is an example of such a challenging system (Eik 2009).

Icebergs provide a threat to marine navigation and offshore installations. How dangerous icebergs can be to marine navigation was demonstrated by the collision of the RMS *Titanic* with an iceberg in the North-Atlantic on April 14, 1912. During this accident, the *Titanic* sank, and more than 1500 people died making it one of the deadliest commercial peacetime maritime disasters. Shortly after the accident, the *International Convention for the Safety of Life at Sea* was established. This included the foundation of the *International Ice Patrol*, which has since monitored icebergs in the North-Atlantic.

In addition to the increase of safety measures on the sea, the *Titanic* accident motivated the study of icebergs, including their physical properties and methods for their destruction (Barnes 1927). In later years, the idea to destroy icebergs with explosives was continued with limited success (Barash 1966, Goode and Teller 1971, Mellor and Kovacs 1972). A significant number of air bubbles in the glacier ice absorbed most of the explosion (C-CORE 2007). Today, the most common approach for physical iceberg management is iceberg towing (Rudkin et al. 2005).

Due to the advances in safety measures and sensor technologies, for instance, the marine radar system, icebergs can usually be detected in advance, and collision avoidance measures can be activated. While this is easy for ships and vessels, other marine operations, such as station keeping, subjected to drifting icebergs are less flexible, such as Floating Production-Storage and Offloading (FPSO), semi-submersibles and spar-platforms. An examples of such oil platforms are the Float-

ing Production-Storage and Offloading (FPSO) vessels *SeaRose* and *Terra Nova* of Canada's East Coast. The FPSO vessels may move off location. If an iceberg comes close to a platform and cannot be managed, then production must be suspended. Therefore, a good operational iceberg drift forecast is important to plan possible countermeasures for icebergs approaching the platform.

A simple mechanistic dynamic iceberg model was developed in the 1980's (Sodhi and El-Tahan 1980) and later further improved and tested (Mountain 1980, El-Tahan et al. 1983, Smith 1993, Bigg et al. 1996, Eik 2009, C-CORE 2013, Turnbull et al. 2015). An operational iceberg drift model was developed at the National Research Council of Canada and implemented at the Canadian Ice Service and other agencies (Kubat et al. 2005). The model uses environmental inputs (winds, waves, and currents) and a detailed description of the iceberg keel geometry to simulate iceberg drift. A similar operational model was developed to monitor ice conditions in the western Arctic zone by the Russian Federation (Kulakov and Demchev 2015).

Ocean currents are usually identified as the most important driving force for iceberg drift (Eik 2009, Turnbull et al. 2015, Kubat et al. 2005, Broström et al. 2009). However, ocean current direction and speed are also identified as the most uncertain iceberg drift model parameters. They introduce significant uncertainties into the iceberg drift forecast and make an accurate forecast very challenging (Allison et al. 2014). Even though the main drift direction of the operational iceberg model is claimed to be satisfactory (Mountain 1980, Kubat et al. 2005, Bigg et al. 1997), the modelled and observed iceberg trajectories may deviate from the beginning of the forecast and may even point in opposite directions (El-Tahan et al. 1983). The process noise (the difference between the modelled and real driving forces) plays an important role during the forecast and gives the forecaster a feeling that the iceberg drift follows a "chaotic" behaviour.

The mechanistic dynamic iceberg models are used in the Ice Services (e.g., CIS) to provide an occupancy grid map with information on how many icebergs occupy each grid cell. Once an iceberg is discovered by satellite imagery or a direct sighting by aeroplane or ship, it is included in the occupancy grid map. Together with the sea ice forecast, this provides shipping companies, fisherman, and insurance companies sufficient information about the risk entering the region.

At the Ice Services, each iceberg trajectory is forecasted with the help of current, wind and wave models. The iceberg deterioration is also modelled. The iceberg is removed from the grid map if the deterioration model suggests with some conservatism that the iceberg is melted completely.

Available information about icebergs to the Ice Services is often limited. They must work with infrequent or never updated information about the iceberg position as well as limited to no initial information about the iceberg shape or initial veloc-

ity. In such a situation, the only option to forecast the iceberg trajectory is to use the mechanistic dynamic iceberg model. On the other hand, as the iceberg approaches an offshore installation, more information about the iceberg becomes available. The iceberg may even be tracked continuously. In this situation, other approaches that include past information to forecast an iceberg trajectory are feasible, since an accurate short-term iceberg drift forecast is required to determine when icebergs should be managed to avoid potential impact with the platform. Moreover, if the physical management of the iceberg is not possible or unsuccessful, then the iceberg drift forecast determines when production or exploration activities should be shut-down, personnel evacuated, and platforms moved off-site. Accurate forecasts can influence management costs, downtime, and risk.

Today, the most common method is to use either the dynamic iceberg model approach or to linearly extrapolate the last two iceberg position measurements to predict the future position of an iceberg (Kubat et al. 2005, Rudkin et al. 2005).

The scope of the thesis is to investigate how the operational iceberg forecast (short-term up to 24 h) can be improved in situations when frequent measurements about the iceberg trajectories are available.

1.1 Ice Management

Ice Management is an important component in the Arctic offshore design and the oil and gas operations on the East Coast of Canada (Randell et al. 2009). Ice management refers to the sum of all activities where the objective is to reduce or avoid actions from ice features (Eik 2008). Consequently, it reduces the threat of iceberg interaction and risk of downtime and possible disconnection. Ice Management consists of several components, such as ice detection, monitoring, ice threat analysis, and physical ice management (Fig. 1.1). A key component off the threat evaluation and decision-making process is the iceberg drift forecast.

The area around a platform is typically divided into several zones (Fig. 1.2). The observations zone is for monitoring iceberg movements. Closer to the platform is the control zone, in which the iceberg is deflected to prevent it from reaching the alert zone, an even closer area around the platform. The alert zone radius is dynamic given by the "T"-time, which is the time required to suspend operations and move, if possible, off location (C-CORE 2007). The "T"-time must be greater at all times than the time the iceberg needs to reach the facility (Randell et al. 2009).

If an iceberg is identified as a threat to the platform, then the iceberg must be deflected. The two most important iceberg managing methods are towing and the use of water cannons. Water cannons are effective for smaller ice masses, while a single vessel is usually used to tow an iceberg. For larger icebergs, multi-vessel tows have also been carried out (Fuglem and Stuckey 2014).

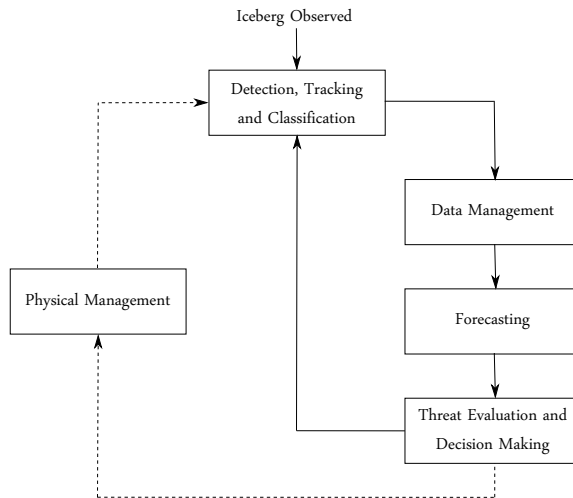


Figure 1.1: Ice management framework (Randell et al. 2009).

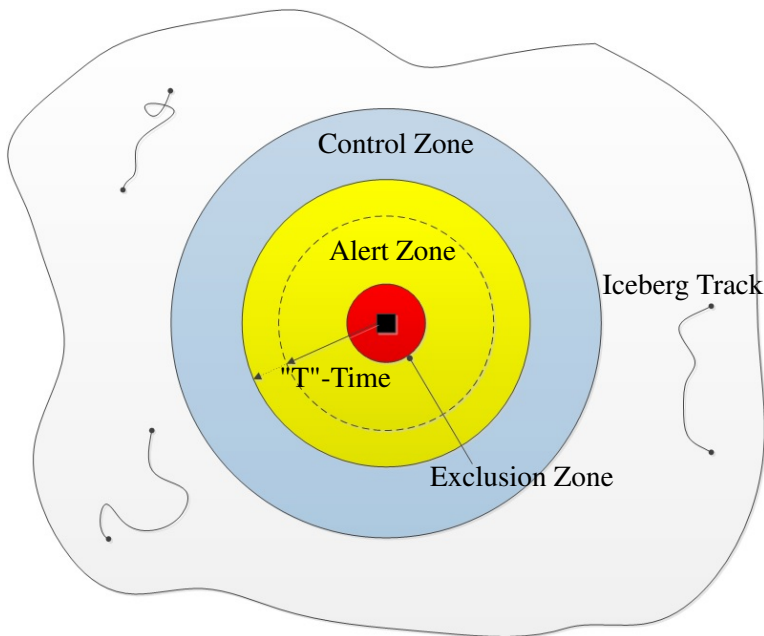


Figure 1.2: Ice Management zones around a facility (Randell et al. 2009).

An iceberg management operation is operationally successful if downtime was avoided. If one or multiple attempts achieve the desired change in the iceberg course, then the towing operation is seen as technically successful (C-CORE 2002).

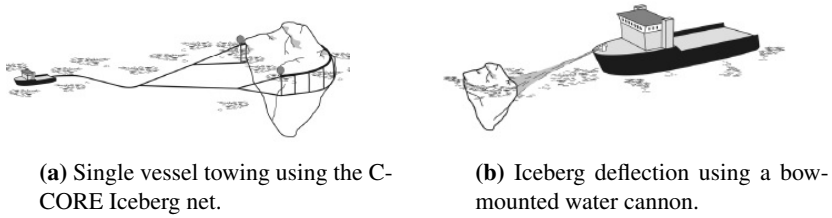


Figure 1.3: Two iceberg management methods (Randell et al. 2009).

A comprehensive overview of Iceberg management operations on the East Coast of Canada is given by Rudkin et al. (2005) with an analysis of about 1500 iceberg management operations. It concludes that about 99.3% of the iceberg management operations were operationally successful and 85.4% were technically successful. The median time to complete an operation was about 6 h. However, about 10% of the operations exceeded 24 h. The median distance an iceberg was deflected is about 5 nautical miles. For iceberg deflection, at least one vessel must be operational at all times. Consequently, physical iceberg management is an expensive and time-consuming operation. An accurate iceberg drift forecast reduces the cost and risk while easing the decision-making.

1.2 Notations

In this thesis, matrices are denoted by uppercase boldface (e.g., \mathbf{A}), linear spaces are denoted with calligraphic uppercase (e.g., \mathcal{N}), vectors are denoted by lowercase boldface (e.g., \mathbf{x}), and upper- or lowercase may denote scalars (e.g., C , k). For a matrix \mathbf{A} , \mathbf{A}^T , \mathbf{A}^{-1} , and $\mathcal{N}(\mathbf{A})$ denote its transpose, inverse, and the null space, respectively. For a symmetric matrix, $\mathbf{P} \geq \mathbf{0}$ denotes the fact the matrix is positive semi-definite.

1.3 Contributions

This thesis is aimed to improve short-term iceberg drift forecasting. It considers the situation when an iceberg approaches an offshore facility so that frequent updates about the iceberg position become available. The use of this information improves the iceberg forecast capabilities. This thesis will discuss how this information can be incorporated into short-term iceberg drift forecasts.

The main contribution of this thesis is the development of several forecast algorithms using dynamic, kinematic, and statistical iceberg drift models that incorporate position measurements of the iceberg trajectory. The developed algorithms combine iceberg models with system identification, estimation methods or signal processing methods, such as the moving horizon estimator or the empirical mode

decomposition. The algorithms are tested, compared, and validated on real iceberg drift trajectories, some of which were collected during the thesis.

Moreover, a constrained Cramér-Rao Bound for discrete-time systems with state equality constraints is developed. Based on this, an error covariance for Kalman filtering with linear state equality constraints is derived. The error covariance is compared to other equality constrained Kalman filters, and it is shown that it results in the smallest error covariance.

1.4 Publications

The following list of publications contributes towards the basis of this thesis, and are listed by type and sorted by date of publication.

1.4.1 Journal Publications

PAPER A: [Andersson et al. \(2016a\)](#) Leif Erik Andersson, Francesco Scibilia, and Lars Imsland. An estimation-forecast set-up for iceberg drift prediction. In: *Cold Regions Science and Technology*, 108:1–9 (2016). ISSN 0165-232X. doi: <https://doi.org/10.1016/j.coldregions.2016.08.001>

PAPER B: [Andersson et al. \(2018a\)](#) Leif Erik Andersson, Lars Imsland, Edmund Førland Brekke and Francesco Scibilia. On Kalman filtering with linear state equality constraints. In: *Automatica*, [submitted], (2018).

PAPER C: [Andersson et al. \(2018c\)](#) Leif Erik Andersson, Francesco Scibilia, Luke Copland, and Lars Imsland. Comparison of statistical iceberg forecast models. In: *Cold Regions Science and Technology*, [accepted], (2018).

PAPER D: [Andersson et al. \(2018d\)](#) Leif Erik Andersson, Francesco Scibilia, and Lars Imsland. An iceberg forecast approach based on a statistical ocean current model. In: *Cold Regions Science and Technology*, [submitted], (2018).

1.4.2 Conference Publications

PAPER E: [Andersson et al. \(2016d\)](#) Leif Erik Andersson, Francesco Scibilia, and Lars Imsland. The Moving Horizon Estimator Used in Iceberg Drift Estimation and Forecast. In: *2016 European Control Conference (ECC)*, Ålborg, Denmark, p. 1271–1277 (Jun. 2016). doi: <https://doi.org/10.1109/ECC.2016.7810464>

- PAPER F: [Andersson et al. \(2016b\)](#) Leif Erik Andersson, Francesco Scibilia, and Lars Imsland. Estimation of systems with oscillating input - applied to iceberg drift forecast. In: *2016 IEEE Conference on Control Applications (CCA)*, Buenos Aires, Argentina, pp. 1492–1498 (Sep. 2016). doi: <https://doi.org/10.1109/CCA.2016.7587934>
- PAPER G: [Andersson et al. \(2016c\)](#) Leif Erik Andersson, Francesco Scibilia, and Lars Imsland. An Iceberg Drift Prediction Study Offshore Newfoundland. In: *2016 Arctic Technology Conference (ATC)*, St. John's, Canada (Oct. 2016). doi: <https://doi.org/10.4043/27472-MS>
- PAPER H: [Andersson et al. \(2017c\)](#) Leif Erik Andersson, Francesco Scibilia, and Lars Imsland. A Study on an Iceberg Drift Trajectory. In: *ASME 2017 36th International Conference on Ocean, Offshore and Arctic Engineering (OMAE)*, Trondheim, Norway (Jun. 2017). doi: <http://dx.doi.org/10.1115/OMAE2017-62159>
- PAPER I: [Andersson et al. \(2017b\)](#) Leif Erik Andersson, Edmund Fjørland Brekke, Lars Imsland and Francesco Scibilia. Constrained Posterior Cramér-Rao Bound for Discrete-Time Systems. In: *IFAC-PapersOnLine*, 50(1): 3768–3773 (2017). ISSN 2405-8963. doi: <https://doi.org/10.1016/j.ifacol.2017.08.479>
- PAPER J: [Andersson et al. \(2017a\)](#) Leif Erik Andersson, Muhammad Faisal Aftab, Francesco Scibilia, and Lars Imsland. Forecasting using multivariate empirical mode decomposition – applied to iceberg drift forecast. In: *2017 IEEE Conference on Control Technology and Applications (CCTA)*, Kohala Coast, Hawaii, pp. 1097–1103 (Aug. 2017). doi: <https://doi.org/10.1109/CCTA.2017.8062605>
- PAPER K: [Andersson et al. \(2018b\)](#) Leif Erik Andersson, Francesco Scibilia, Luke Copland, Muhammad Faisal Aftab, and Lars Imsland. Analysis of iceberg drift trajectories using the multivariate empirical mode decomposition. In: *The Twenty-eighth (2018) International Ocean and Polar Engineering Conference (ISOPE)*, Sapporo, Japan, [accepted], (Jun. 2018)

1.5 Thesis Organization

To a large extent, each chapter corresponds to a publication, where introductory content common to several articles has been condensed in chapters 2 through 4 in the thesis. Chapters 5 through 15 are based on the publications list (Sec. 1.4),

which are the basis of the thesis.

In Part I, the iceberg datasets to compare the forecast algorithms are presented in Chapter 4. In Chapter 5, a sensitivity study using the dynamic iceberg model is discussed, and is based on [Andersson et al. \(2017c\)](#) (Sec. 1.4.2: PAPER H).

In Part II, the hybrid iceberg drift forecast algorithms are discussed. The forecast algorithms comprise the ancillary current forecast scheme in Chapter 6 and the inertial current forecast scheme in Chapter 7. The former is based on [Andersson et al. \(2016a\)](#) (Sec. 1.4.1: PAPER A) and the latter on [Andersson et al. \(2016b\)](#) (Sec. 1.4.2: PAPER F). Chapter 8 discusses how to combine both hybrid forecast schemes to improve the forecast results further, and is based on [Andersson et al. \(2016c\)](#) (Sec. 1.4.2: PAPER G).

Part III presents a statistical forecast algorithm in Chapter 9. A statistical current model is identified, which is used to forecast the iceberg velocity. The Chapter is based on [Andersson et al. \(2018d\)](#) (Sec. 1.4.1: PAPER D).

In Part IV, the iceberg velocity is analysed using the multivariate empirical mode decomposition (Chapter 10), and is based on [Andersson et al. \(2018b\)](#) (Sec. 1.4.2: PAPER K). Chapter 11 presents an idea of how the multivariate empirical mode decomposition can further be used to forecast the iceberg velocity, and is based on [Andersson et al. \(2017a\)](#): (Sec. 1.4.2: PAPER J).

Chapter 12 comprises all of Part V where all presented forecast algorithms are compared on the available iceberg drift datasets, and is based on [Andersson et al. \(2018c\)](#) (Sec. 1.4.1: PAPER C).

Part VI focuses on constrained parameter and state estimation. In Chapter 13, it is shown how a hydrodynamic iceberg geometry can be estimated based on measurements close to the iceberg. An iceberg geometry model is derived to reduce the estimation space and improve the estimation results. The Chapter is based on [Andersson et al. \(2017c\)](#) (Sec. 1.4.2: PAPER H). Consequently, this article was separated into Chapters 5 and 13. In Chapter 14, a constrained Cramér-Rao Bound for discrete-time system is derived and is based on [Andersson et al. \(2017b\)](#) (Sec. 1.4.2: PAPER I). It is also used in Chapter 15 to derive and compare an error covariance matrix for a constrained Kalman filter with other constrained Kalman filters. The chapter is based on [Andersson et al. \(2018a\)](#) (Sec. 1.4.1: PAPER B).

Chapter 16 concludes this thesis and states possible future work.

Chapter 2

Iceberg Shape Classification and Dynamic Iceberg Drift Model

In this chapter, the iceberg shape classification and the dynamic iceberg model is introduced. The iceberg shape classification introduces common terms related to the iceberg geometry, which are later used for the description of the iceberg datasets. The dynamic iceberg drift model plays an important role throughout the thesis. In all following chapters it will be used, often to compare and evaluate the performance of the developed iceberg forecast algorithms. At the end of this chapter, a brief literature review of the dynamic iceberg model and other iceberg forecast methods is provided.

2.1 Iceberg Geometry

In this section, the common terms related to the iceberg geometry are introduced (Fig. 2.1). An iceberg can be divided into a portion above the waterline, the sail or freeboard, and a submerged portion below the waterline, the keel or draft. Consequently, the sail height H_a is the highest point of an iceberg measured from the waterline. The keel depth H_w represents the same for the keel. The ice thickness H refers to the total height of the iceberg, which is given by the sum of sail height and keel depth. The iceberg length L refers to the longest and the iceberg width W to the smallest horizontal extension of the iceberg at the waterline. The sail and keel cross-section areas, A_a and A_c , are the vertical cross-section areas of the sail and keel, which may change depending on the perspective.

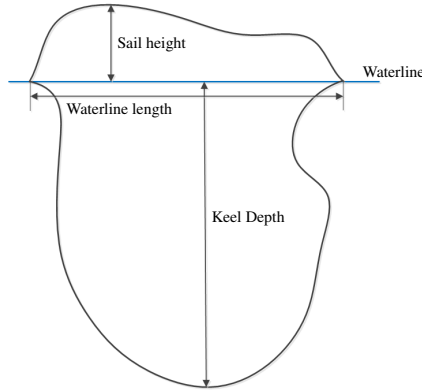


Figure 2.1: Schematic of iceberg geometry.

2.2 Iceberg Shape

In this thesis, the proposed forecast algorithms are tested on real iceberg trajectories. A common iceberg classification is based on their shape. Moreover, the shape is a common error source in the dynamic iceberg model. According to [WMO \(1970\)](#), an iceberg is a massive piece of ice of varying shape protruding more than five meters above the sea level. Different iceberg shapes are classified in [Table 2.1](#). [Broström et al. \(2009\)](#) also mentioned a weathered iceberg, which is an iceberg with an irregular shape due to an advanced stage of ablation.

2.3 The Dynamic Iceberg Model

In this section, the mechanistic dynamic iceberg drift model is introduced. Hereafter, the *North-East-Down* (NED) coordinate system is used throughout the thesis. Moreover, the ocean is always assumed to be a plane.

The iceberg model can be described by a set of ordinary differential equations (ODEs)

$$\dot{\mathbf{x}} = \mathbf{f}(\mathbf{x}, \mathbf{u}, \mathbf{p}), \quad \mathbf{x}_0 = \mathbf{x}(t_0), \quad (2.1a)$$

$$\mathbf{y} = \mathbf{h}(\mathbf{x}), \quad (2.1b)$$

where $\mathbf{x} \in \mathbb{R}^{n_x}$ is the vector of differential states, $\mathbf{u} \in \mathbb{R}^{n_u}$ the vector of inputs, $\mathbf{y} \in \mathbb{R}^{n_y}$ the vector of outputs, and $\mathbf{p} \in \mathbb{R}^{n_p}$ vector of parameters. For the iceberg model, the state \mathbf{x} contains the iceberg position and the velocity, the input \mathbf{u} contains the environmental driving forces, current, wind, and waves, and the output \mathbf{y} is the observed iceberg position.

More specifically, the mechanistic dynamic iceberg drift model is based on a


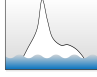

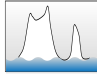


Tabular		A tabular iceberg (TAB) has a horizontal flat-top with length to height ratio is $\sim 5:1$ or more.
Pinnacle		A pinnacle iceberg (PNC) has a large central spire or pyramid with one or more spires dominating the overall shape.
Blocky		A blocky iceberg (BLK) has steep precipitous sides with a flat top. The length to height ratio is $\sim 2.5:1$.
Dry-Dock		A dry-dock iceberg (DDK) is eroded such that a large U-shape slot is formed with twin columns or pinnacles. The slot can extend under the waterline or close to it.
Tilted Tabular or Wedge		A tilted tabular (TT) or wedge (WDG) iceberg is a tabular iceberg, but the top is tilted. Around 25% of the tabular icebergs are tilted.
Dome or spherical		A dome (DOM) or spherical (SPH) iceberg has a large smooth rounded top.

Table 2.1: Iceberg shapes (McClintock et al. 2002).

momentum equation to calculate the acceleration of the iceberg mass

$$m\mathbf{a} = \sum_i \mathbf{f}_i, \quad (2.2)$$

where m is the iceberg mass, \mathbf{a} is the acceleration of the iceberg, and \mathbf{f}_i are forces acting on the iceberg. The main differences between the mechanistic dynamic iceberg drift models proposed in the literature lay in the choice of forces acting on the icebergs and their representation (Sodhi and El-Tahan 1980, Mountain 1980, Smith 1993, Bigg et al. 1996; 1997, Johannessen et al. 1999, Kubat et al. 2005, Eik 2009, Keggouche et al. 2009, Turnbull et al. 2015).

In this thesis, the following forces act on the iceberg (Fig. 2.2)

$$m\mathbf{a} = \mathbf{f}_{\text{cor}} + \mathbf{f}_a + \mathbf{f}_c + \mathbf{f}_r + \mathbf{f}_p, \quad (2.3)$$

where \mathbf{f}_{cor} , \mathbf{f}_a , \mathbf{f}_c , \mathbf{f}_r , and \mathbf{f}_p are the Coriolis force, the air drag force, the water drag force, the wave radiation force, and pressure gradient term, respectively. The total mass of the iceberg is m , which consists of the iceberg mass m_0 and added mass m_{add} ($m = m_0 + m_{\text{add}} = m_0(1 + C_m)$) due to the water field surrounding the

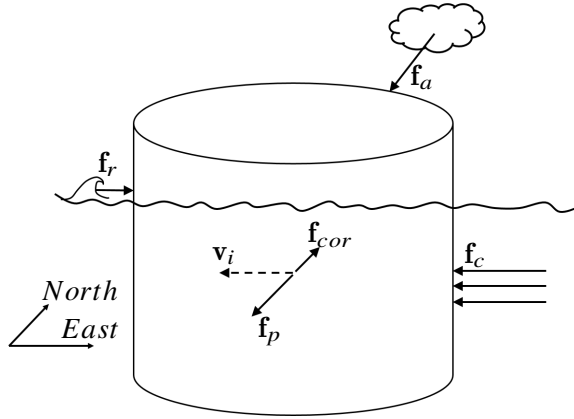


Figure 2.2: Forces acting on an iceberg.

iceberg (Sodhi and El-Tahan 1980).

The Coriolis force is expressed by

$$\mathbf{f}_{cor} = -m_0 f \mathbf{k} \times \mathbf{v}_i, \quad (2.4)$$

where $f = 2\omega \sin(\phi)$ is the Coriolis vector, \mathbf{k} is the unit vector directed upwards parallel to the z-axis, and \mathbf{v}_i is the velocity of the iceberg. The angular velocity of the earth and the latitude of the position of the iceberg is expressed as ω and ϕ . The rotation of the earth causes the Coriolis force. As a result, moving objects are deflected clockwise on the northern hemisphere.

The air drag force \mathbf{f}_a is caused by wind acting on the iceberg and is given by

$$\mathbf{f}_a = \frac{1}{2} \rho_a C_a A_a |\mathbf{v}_a - \mathbf{v}_i| (\mathbf{v}_a - \mathbf{v}_i), \quad (2.5)$$

where ρ_a is the air density, C_a the air drag coefficient, A_a the sail cross-section of the iceberg, and \mathbf{v}_a the wind velocity. The iceberg velocity \mathbf{v}_i can be typically neglected in (2.5).

The water drag force \mathbf{f}_c is caused by the current acting on the iceberg and is calculated by

$$\mathbf{f}_c = \frac{1}{2} \rho_c C_w \sum_k A_c(k) |\mathbf{v}_c(k) - \mathbf{v}_i| (\mathbf{v}_c(k) - \mathbf{v}_i), \quad (2.6)$$

where ρ_c is the water density, and C_w is the water drag coefficient. The keel cross-section of the iceberg and the current velocity in an underwater layer k is expressed as $A_c(k)$ and $\mathbf{v}_c(k)$. The water column is usually divided into vertical layers of 10-meters in height. In this thesis, we will use a mean current over the keel of the

iceberg such that the current is the same in every layer.

The wave radiation force is caused by the waves acting on the iceberg and is calculated as

$$\mathbf{f}_r = \frac{1}{4} C_r \rho_c g a^2 L \frac{\mathbf{v}_r}{\|\mathbf{v}_r\|}, \quad (2.7)$$

where C_r is the wave drift radiation coefficient, g the gravity, a the wave amplitude, L the characteristic length of the iceberg, and $\mathbf{v}_r/\|\mathbf{v}_r\|$ the wave direction. This equation can be used for wind waves and swell. In many situations throughout the thesis, the wave force is not included into the momentum balance (2.3) because often the wave force was not measured or information about the waves at the iceberg position was not available. However, as [Smith \(1993\)](#) points out, waves travelling in the same direction as the wind can be implicitly considered by a higher value of the air drag coefficient.

The pressure gradient in the water causes a force on the iceberg ([Kubat et al. 2005](#)), which is approximated by

$$\mathbf{f}_p = m_0 \left(\frac{d}{dt} \mathbf{v}_{mc} + f \mathbf{k} \times \mathbf{v}_{mc} \right), \quad (2.8)$$

where \mathbf{v}_{mc} is the mean current velocity and f is the Coriolis force parameter. The mass and cross-sectional areas are calculated with the characteristic length L_0 of the iceberg and its width W_0

$$m = L_0 W_0 C_f (H_w + H_a) \rho_{Ice}, \quad (2.9)$$

where H_w is the keel height, H_a is the sail height. The shape factor C_f for different iceberg shapes can be found in [McClintock et al. \(2002\)](#).

If not stated otherwise, the air drag C_a , water drag C_w and wave drift coefficient are selected to be 1.3, 0.9 and 0.6, respectively. Water, air, and ice densities are fixed to be 1027, 1.225 and 900 kg m⁻³, respectively. The added mass coefficient C_m is assumed to be 0.5 ([Eik 2009](#)).

2.3.1 Sensitivity of parameters of the dynamic iceberg model

In this section a brief discussion is given about the parameters of interest in the dynamic iceberg model. This discussion follows the sensitivity study presented in [Allison et al. \(2014\)](#). The sensitivity study in this article was performed for typical parameter values of the Grand Banks region. The authors tried to estimate from the base value a range of values large enough to encompass 95% of the uncertainty of the parameter. The estimation was based on verification data, but also on experience of the authors. During the study the authors varied one parameter and evaluated its influence on the iceberg drift in comparison to the base case. It has

Table 2.2: Summary of sensitivity analysis by Allison et al. (2014).

Parameter	Range	Base value	percentage of deviation
Iceberg Geometry			
Length	±50 %	37.5, 90, 160, 350 m	2.3 %
Added mass	0–1	0.5	0.5 %
Driving Forces			
Wind			
direction	±45°	225°	8.6 %
velocity	±30 %	10 m/s	2.9 %
drag coeff.	0.5–2.5	1.9	2.9 %
Current			
direction	±90°	135°	35.4 %
velocity	0–0.8 m/s	0.4 m/s	19.1 %
drag coeff.	0.5–2.5	1.3	5.1 %
Wave stress			
sig. wave height	±50 %	1.5 m	2.6 %
wave coeff.	0–0.3	0.15	4.0 %
direction	±45°	225°	2.6 %
period	±50 %	6 s	0.6 %
Swell stress			
sig. wave height	±50 %	1.5 m	4.3 %
swell coeff.	0–0.3	0.15	4.0 %
direction	±30°	315°	2.3 %
period	±25 %	8 s	0.6 %
Init. cond.			
position	±5 km	0 km	0.6 %
velocity	0–0.8 m/s	0.4 m/s	0.6 %
direction	±45°	0°	0.6 %

to be pointed out that the importance of a parameter based on this study is highly dependent on the base case that was chosen, e.g., the variation of the air drag coefficient has a higher significance if the wind velocity is high.

The results of the sensitivity study are shown in Table 2.2. The ocean current direction followed by its velocity and the wind direction are the most influential parameters. However, one has to keep in mind that the results are dependent on the base values. The current and wind velocity base values are relatively high. Still, a similar result, but probably not as distinct, is expected with smaller current and wind velocities.

Errors in the initial conditions are relatively unimportant for the dynamic iceberg model. This is expected in this experimental setup since all other parameters are not influenced by the initial conditions. On the other hand, the initial conditions are very influential on the statistical iceberg forecast methods presented below.

Dependencies between parameters, e.g. iceberg geometry influences drag coefficients, are usually not considered in the dynamic iceberg model and they are often assumed independent. In fact, in a sensitivity study varying only one parameter different parameters can have the same effect on the iceberg drift, e.g. variation of air drag coefficient, sail cross sectional area and absolute wind velocity or wave drift radiation coefficient, significant wave height and characteristic iceberg length. An important difference between these parameters is their variance and appearance in the driving force, e.g. air drag coefficient appears linear while

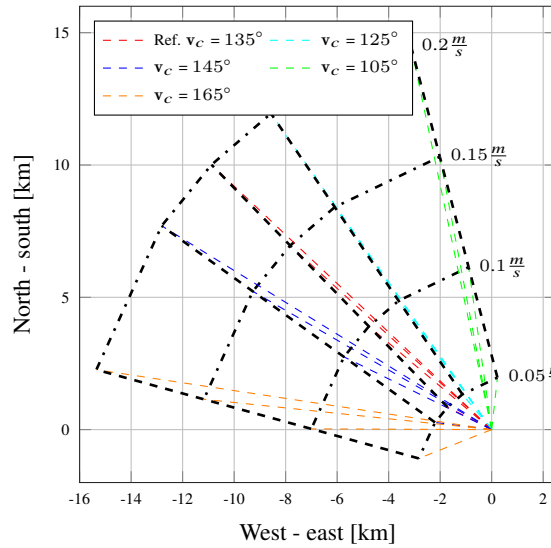


Figure 2.3: Example how the ocean current velocity and direction influences the iceberg drift trajectory in a 24 h period. The direction varies $\pm 30^\circ$ and the velocity in the range 0.05 m/s to 0.2 m/s. Each iceberg trajectory is a straight line since the simulation is initialised in steady state. Each rectangle shows the extreme end positions of the iceberg trajectory using the parameter values given in the legend.

the absolute velocity quadratic in (2.5).

An example how the ocean current velocity and direction influence the iceberg drift trajectory is shown in Fig. 2.3. An error in the ocean current velocity or direction will cause a significant deviation in the end position of the simulated iceberg trajectory. The *region of uncertainty* increases if more uncertain parameters are included into the simulation. On the other hand, the region can be reduced if the uncertainty of the parameter can be reduced with, for example, parameter estimation techniques.

2.4 Literature Review on Iceberg Drift Forecast

The literature about iceberg drift forecasting, or hindcast, is dominated by the mechanistic dynamic iceberg model. Many authors developed, tested, and evaluated this type of models, including EI-Tahan et al. (1983), Smith and Banke (1981), Bigg et al. (1996), Lichey and Hellmer (2001), Kubat et al. (2005), Eik (2009), Kegnouche (2010), and Turnbull et al. (2015). However, their conclusion may differ depending on the number of iceberg tracks evaluated, the region, and period the iceberg tracks were observed. For example, Bigg et al. (1996), Kegnouche et al. (2009), and Eik (2009) investigated long-term iceberg drift fore-

casts over several months, while [Sodhi and El-Tahan \(1980\)](#), [Smith \(1993\)](#), and [Turnbull et al. \(2015\)](#) investigated short-term to mid-term iceberg drift forecasts of 11 h to 73 h. On the other hand, the articles have strong similarities as they each investigated the driving forces and parametrisation of a dynamic iceberg model.

The ocean current is usually identified as the most important variable ([Kubat et al. 2005](#), [Broström et al. 2009](#), [Allison et al. 2014](#)). [Bigg et al. \(1996\)](#) found that nonlinear advection in the ocean current due to the pressure gradient term becomes important for long-term drift forecasts. Others, investigating short-term iceberg drift forecasts, found that the term can be neglected ([Sodhi and El-Tahan 1980](#), [Smith 1993](#)). [Eik \(2009\)](#) and [Broström et al. \(2009\)](#) investigated the oceanographic data used to forecast the iceberg. They found that in open water and with some distance to the ice edge the wave force becomes as essential as the current force. They pointed out that the wave force may be adjusted depending on the size of the iceberg since small icebergs (20 m to 50 m waterline length) move with the waves while large icebergs reflect waves.

For similar (long-term) forecast periods, [Keghouche et al. \(2009\)](#) found that the current, wind, and Coriolis force are most important. They also investigated the parametrisation of the dynamic iceberg model and found, independent of the chosen geometry, a common ratio between the drag coefficients. [Keghouche et al. \(2009\)](#) found that the drag coefficients become more important for longer periods of one to two months. They suggested adjusting the drag coefficients according to the observed iceberg trajectory. A similar idea to optimise the drag coefficients for short-term iceberg drift forecasts was proposed by [Smith \(1993\)](#). However, [Smith \(1993\)](#) achieved only small improvements in the forecast by tuning the drag coefficients. Similar results were achieved by [Gaskill and Rochester \(1984\)](#) and [Kubat et al. \(2005\)](#).

[Smith \(1993\)](#) neglected the wave force and pointed out that a higher air drag coefficient C_a implicitly accounts for waves travelling in wind direction.

An operational iceberg drift model was developed at the Canadian Ice Service ([Kubat et al. 2005](#)). The model uses environmental inputs such as winds, waves, and currents along with a detailed description of the iceberg keel geometry to simulate the iceberg drift. A similar operational model was developed by the Russian Federation to monitor ice conditions in the western Arctic zone ([Kulakov and Demchev 2015](#)). An empirical iceberg geometry model for pinnacle iceberg shapes based on the waterline length was developed by [Barker et al. \(2004\)](#). [Kubat et al. \(2005\)](#) and [Turnbull et al. \(2015\)](#) found that the iceberg geometry and the iceberg keel geometry are important parameters to model the iceberg drift. At the same time, they found that a mean current averaged over the keel of the iceberg yields only a small error compared to a detailed vertical profile of the ocean current.

On the other hand, [Smith \(1993\)](#), [Gaskill and Rochester \(1984\)](#) and [EI-Tahan et al. \(1983\)](#) stated that the modelled iceberg trajectories are relatively insensitive to variations in the estimated mass and cross-sectional areas of the iceberg. A possible explanation of these different observations is that the icebergs, as investigated by [Smith \(1993\)](#), are driven by near-surface ocean currents and that [EI-Tahan et al. \(1983\)](#) and [Gaskill and Rochester \(1984\)](#) did not consider a layered ocean current.

A new research effort lead by C-CORE developed and improved iceberg profiling, which may result in new insights about the iceberg keel geometry. It is now possible to profile the iceberg in a relatively short time ([McGuire et al. 2016](#)) and use these profiles in Iceberg Management systems to prepare towing operations ([Bruce et al. 2016](#)), model iceberg impacts ([Stuckey et al. 2016](#)) or evaluate the risk to sub-sea installations ([King et al. 2016](#), [Fuglem et al. 2016](#)). These iceberg profiles are collected by approaching the iceberg with a ship while others work on profiling the iceberg sail and keel with underwater vehicles, such as [Wang et al. \(2015\)](#) and [Zhou et al. \(2016\)](#). However, it is not straightforward to include a detailed 3D iceberg profile into the dynamic iceberg model.

On the one hand, the main drift direction of dynamic iceberg models is claimed to be satisfactory ([Mountain 1980](#), [Bigg et al. 1997](#), [Kubat et al. 2005](#)). On the other hand, it was observed that the modelled and observed trajectories could deviate from the beginning and point in different directions ([EI-Tahan et al. 1983](#), [C-CORE 2007](#)). [Eik \(2009\)](#) found that the dynamic iceberg model provides better results in situations with strong winds, since the wind may dominate the iceberg drift as the wind model is less uncertain.

[Mountain \(1980\)](#) found that the error in the iceberg drift modelling is mostly random. For this reason, [Marko et al. \(1988\)](#) claimed that statistical models have superior performance for short-term forecasts compared to the dynamic ones. [Garrett \(1985\)](#), [De Margerie et al. \(1986\)](#), and [Moore \(1987\)](#) presented simple statistical methods that use historical and recently observed data about the iceberg drift to predict iceberg motion, while [Gaskill and Rochester \(1984\)](#) used the dynamic iceberg model and past iceberg motions to calculate currents required for the past motions. In a second step, they applied those currents to other icebergs passing through the same area at a later time.

Even though statistical methods have been proven to be superior for short-term iceberg drift forecasts ([Marko et al. 1988](#)), they were critiqued by authors using the dynamic iceberg model ([Smith 1993](#)). They state that the uncertainty of in the position is large compared to the net displacement of the most probable iceberg position ([Moore 1987](#)) and if the velocity changes auto-correlation models may forecast the iceberg trajectory with a wrong velocity causing a large error ([Smith 1993](#)). Therefore, statistical models are rarely used.

Some more specific models were not included into the discussion, such as mod-

els that describe the iceberg drift in sea ice ([Yulmetov et al. 2016](#)) or wind-driven iceberg drift models ([Crepon et al. 1988](#), [Wesche and Dierking 2016](#)).

Even though most often the mechanistic dynamic iceberg model is used, the conclusions and observations are different. Different datasets, regions of interest, and forecast horizons cause this issue. A benchmark of iceberg trajectories to test forecast algorithms does not exist.

Chapter 3

Theory and Methods

This chapter introduces theory and methods common to many of the articles, which are also the basis of the thesis.

3.1 State Estimator

The mechanistic dynamic system from Section 2.3 can be described by the set of ordinary differential equations (ODEs)

$$\dot{\mathbf{x}}(t) = \tilde{\mathbf{f}}(\mathbf{x}(t), \mathbf{u}(t)), \quad \mathbf{x}_0 = \mathbf{x}(t_0), \quad (3.1a)$$

$$\mathbf{y}(t) = \mathbf{h}(\mathbf{x}(t)), \quad (3.1b)$$

where $\mathbf{x} \in \mathbb{R}^{n_x}$ is the vector of differential states, $\mathbf{u} \in \mathbb{R}^{n_u}$ the vector of inputs, and $\mathbf{y} \in \mathbb{R}^{n_y}$ the vector of outputs. For example, in the iceberg model, the state vector \mathbf{x} may contain the iceberg position and velocity (and possibly the ancillary/inertial current), the input vector \mathbf{u} may contain the ocean current and wind forecast and the output vector \mathbf{y} may contain the iceberg position. Discretizing the continuous time model yields

$$\mathbf{x}_{k+1} = \mathbf{f}(\mathbf{x}_k, \mathbf{u}_k) + \mathbf{w}_k, \quad \mathbf{x}_0 = \mathbf{x}(t_0), \quad (3.2a)$$

$$\mathbf{y}_k = \mathbf{h}(\mathbf{x}_k) + \mathbf{v}_k, \quad (3.2b)$$

in which the subscript k denotes the samples taken at discrete time t_k . The vector $\mathbf{w}_k \in \mathbb{R}^{n_x}$ is an additive process noise, which accounts for unknown disturbances on the system states. The measurement noise $\mathbf{v}_k \in \mathbb{R}^{n_y}$ is added to the measured outputs.

3.1.1 The Moving Horizon Estimator

The Moving Horizon Estimator (MHE) for the above model is the optimisation problem (Robertson et al. 1996):

$$\min_{\{\mathbf{x}_i, \mathbf{w}_i, \mathbf{v}_i\}} \|\hat{\mathbf{x}}_M - \mathbf{x}_M\|_{\mathbf{P}}^2 + \sum_{i=M}^N \|\mathbf{v}_i\|_{\mathbf{R}}^2 + \sum_{i=M}^{N-1} \|\mathbf{w}_i\|_{\mathbf{Q}}^2 \quad (3.3a)$$

$$\begin{aligned} \text{s.t. } \quad & \mathbf{x}_{i+1} = \mathbf{f}(\mathbf{x}_i, \mathbf{u}_i) + \mathbf{w}_i \quad \forall i = M, \dots, N-1 \\ & \mathbf{y}_i = \mathbf{h}(\mathbf{x}_i) + \mathbf{v}_i \quad \forall i = M, \dots, N \\ & \mathbf{x}_i \in \mathbb{X}, \mathbf{w}_i \in \mathbb{W}, \mathbf{v}_i \in \mathbb{V}, \end{aligned} \quad (3.3b)$$

where $\mathbf{P} \in \mathbb{R}^{n_x \times n_x}$ is the estimated error covariance matrix, $\mathbf{R} \in \mathbb{R}^{n_y \times n_y}$ the measurement noise covariance matrix and $\mathbf{Q} \in \mathbb{R}^{n_x \times n_x}$ the process noise covariance matrix. The vector $\hat{\mathbf{x}}$ represents the estimated vector. The matrices \mathbf{Q} and \mathbf{R} can be used as tuning parameters. In addition to their statistical interpretation, the matrix \mathbf{Q} can be seen as a measure of confidence in the model equations and the matrix \mathbf{R} as a measure of confidence in the process data (Scibilia and Hovd 2009). The horizon contains $(N - M + 1)$ measurements, taken at times $t_{k=M} < \dots < t_{k=N}$. The sets \mathbb{X} , \mathbb{W} , and \mathbb{V} are closed and convex, and, usually, they are finite dimensional polyhedral sets

$$\begin{aligned} \mathbb{X} &= \{\mathbf{x}_i \in \mathbb{R}^{n_x} \mid \mathbf{D}_x \mathbf{x}_i \leq \mathbf{d}_x\}, \\ \mathbb{W} &= \{\mathbf{w}_i \in \mathbb{R}^{n_x} \mid \mathbf{D}_w \mathbf{w}_i \leq \mathbf{d}_w\}, \\ \mathbb{V} &= \{\mathbf{v}_i \in \mathbb{R}^{n_y} \mid \mathbf{D}_v \mathbf{v}_i \leq \mathbf{d}_v\}, \end{aligned} \quad (3.4)$$

where $\mathbf{D}_x \in \mathbb{R}^{n_x \times n_x}$, $\mathbf{D}_w \in \mathbb{R}^{n_x \times n_x}$ and $\mathbf{D}_v \in \mathbb{R}^{n_y \times n_y}$ are matrices. The MHE formulation is a constrained least-squares problem. The optimisation variables are \mathbf{x}_i , \mathbf{w}_i , and \mathbf{v}_i , which represent the state, the process noise, and the measurement noise vector, respectively, in the optimisation horizon. Substitution can reduce the variable space of the optimisation problem to the initial state \mathbf{x}_M and the process noise $\{\mathbf{w}_i\}_{i=M}^{N-1}$ over the optimisation horizon. The arrival cost term is represented by $\|\hat{\mathbf{x}} - \mathbf{x}_M\|_{\mathbf{P}}^2$, which summarises past data ($t < t_{k=M}$) that is not explicitly part of the present objective function. The arrival cost is key to the stability of the MHE, and is derived from dynamic programming arguments, such as Kalman filter based updates (Kühl et al. 2011). \mathbf{x}_M denotes the optimal estimate of $\hat{\mathbf{x}}_M$. The arrival cost is updated with the update scheme developed by Tenny and Rawlings (2002). The MHE is chosen in this work since it provides an improved state estimation and greater robustness to both poor guesses of the initial state and tuning parameters compared to the extended Kalman filter (EKF) (Haseltine and Rawlings 2005).

3.1.2 Extended Kalman Filter

The performance of the MHE is compared below with that of a standard extended Kalman Filter (EKF). To obtain the state estimates, the EKF linearises the non-linear system around the last filter estimate and then applies the Kalman filter (Rawlings and Bakshi 2006). With the following linearisation

$$\mathbf{F}_k = \left. \frac{\partial \mathbf{f}_k}{\partial \mathbf{x}} \right|_{\hat{\mathbf{x}}_k^+}, \quad \mathbf{H}_k = \left. \frac{\partial \mathbf{h}_k}{\partial \mathbf{x}} \right|_{\hat{\mathbf{x}}_k^-}, \quad (3.5)$$

the method can be summarised in a recursion with time update

$$\hat{\mathbf{x}}_{k+1}^- = \mathbf{f}(\hat{\mathbf{x}}_k^+, \mathbf{u}_k), \quad (3.6a)$$

$$\mathbf{P}_{k+1}^- = \mathbf{F}_k \mathbf{P}_k^+ \mathbf{F}_k^T + \mathbf{Q}, \quad (3.6b)$$

where the minus sign represents the a priori time update and the plus sign the a posteriori measurement update. In a second step, the measurement update is performed, and the mean and covariance are given by

$$\mathbf{K}_k = \mathbf{P}_k^- \mathbf{H}_k^T (\mathbf{H}_k \mathbf{P}_k^- \mathbf{H}_k^T + \mathbf{R})^{-1}, \quad (3.7a)$$

$$\hat{\mathbf{x}}_k^+ = \hat{\mathbf{x}}_k^- + \mathbf{K}_k [\mathbf{y}_k - \mathbf{h}(\hat{\mathbf{x}}_k^-)] \quad (3.7b)$$

$$\mathbf{P}_k^+ = (\mathbf{I} - \mathbf{K}_k \mathbf{H}_k) \mathbf{P}_k^-, \quad (3.7c)$$

where \mathbf{Q} and \mathbf{R} are the process and measurement noise covariances.

3.2 Empirical Mode Decomposition

The empirical mode decomposition (EMD) is a fully data-driven adaptive signal processing method that finds its ways into areas like image and data fusion (Hariharan et al. 2006, Mandic et al. 2008), medical applications (Blanco-Velasco et al. 2008) and remote sensing (Chen et al. 2008). The EMD decomposes an input signal $x(t)$, which is the input to the EMD and not the state x_k of (3.2), into amplitude- or frequency-modulated components called intrinsic mode functions (IMFs) $c_i(t)$ and a bias term $r(t)$, such that

$$x(t) = \sum_{i=1}^N c_i(t) + r(t). \quad (3.8)$$

The IMF has symmetric upper and lower envelopes where the number of zero crossings and extrema differ at most by one (Huang et al. 1998). An iterative process that extracts high-frequency modes from slower ones extracts the IMFs (Aftab et al. 2016). This sifting process is initiated by identifying extrema, calculating the

local mean $m(t)$ from the envelope constructed by spline fitting of the extrema and subtracting the local mean from the signal to calculate the detail $d(t)$. The iteration is continued until the detail is considered as zero-mean IMF according to some stopping criterion. Afterward, the IMF is subtracted from the input signal $x(t)$ and the sifting process restarted. When it is no longer possible to extract an IMF, the iteration process is stopped, and the remaining signal is defined as residual $r(t)$ (Rilling et al. 2003).

3.2.1 Multivariate EMD

The standard EMD performs a decomposition on a univariate signal. Extensions to bivariate, trivariate, and multivariate signals have been proposed by Rilling et al. (2007), Ur Rehman and Mandic (2010a), and Ur Rehman and Mandic (2010b). The main challenges in decomposing multivariate signals are the identification of the local extrema, generation of envelopes, and calculation of a local mean in higher dimensions. The problem is overcome by projecting the signal in multiple directions and averaging over the previously created envelopes (Ur Rehman and Mandic 2010b).

The Multivariate EMD (MEMD) method can be summarised in the following algorithm (Aftab et al. 2016):

1. Set up K direction vectors \mathbf{u}^k with $k = 1, \dots, K$ by choosing uniformly distributed points on the n -dimensional sphere.
2. Find the projections $\mathbf{p}^k(t)$ of the input signal $\mathbf{x}(t)$ along the direction vectors \mathbf{u}^k .
3. Find the time instants t^k corresponding to the maxima of the projections $\mathbf{p}^k(t)$.
4. Generate the multivariate envelope $\mathbf{e}^k(t)$ via spline fitting of points $[t^k, \mathbf{x}(t^k)]$.
5. Calculate the mean of the envelope curve

$$\mathbf{m}(t) = \frac{1}{K} \sum_{k=1}^K \mathbf{e}^k(t). \quad (3.9)$$

6. Extract the detail $\mathbf{d}(t) = \mathbf{x}(t) - \mathbf{m}(t)$ as in the EMD.
7. Repeat steps 1-6 until $\mathbf{d}(t)$ fulfils the stoppage criterion for a multivariate IMF.
8. Calculate the residue $\mathbf{r}(t) = \mathbf{x}(t) - \mathbf{d}(t)$, and iterate the same procedure until all IMFs are extracted from the signal.

3.2.2 Mode Alignment Property

An appealing consequence of the MEMD is its mode alignment property that makes it possible to align 'common scales' present in the multivariate data in the same indexed IMFs (Ur Rehman and Mandic 2010b). An illustrative example of a tetra-variate signal with individual components containing four oscillatory modes (f_1, f_2, f_3, f_4) is considered. The signals have common modes among them, but not all modes are present in each signal. Moreover, a phase lag is added to the oscillations of some components. The signal composition is given in Table 3.1. The signals and the resulting IMFs from the MEMD are given in Figure 3.1.

By viewing the IMFs, it is easily detectable that the common oscillation of signal B and D with frequency f_4 is present in IMF#1. IMF#2 captures frequency f_3 that is present only in component C . Frequency f_2 extracted in IMF#3 is common to the components B and C , while the last frequency f_1 is present in the residue of components A , B , and D . The MEMD behaves essentially as a sequence of band-pass filters, which decompose the input signals into different components (IMFs) with varying frequency bands. The bands are aligned in the IMF's, and the MEMD aligns common oscillatory modes. However, the MEMD may also generate spurious IMFs due to spline fitting issues and leakage effects where one IMF may leak into another (Aftab et al. 2016, Peng et al. 2005). On the other hand, these IMFs are nearly orthogonal and poorly correlated with the original signal. Therefore, the rank correlation between the original signal $x(t)$ and its IMF c_i can be used to detect the significance of each IMF.

Normalised Correlation Coefficient Matrix

The correlation coefficient ρ_{ij} is calculated by

$$\rho_{ij} = \text{corr}(\mathbf{c}_{ij}^{t_0:t_k}, \mathbf{x}_j^{t_0:t_k}), \quad j = 1, \dots, M, \quad i = 1, \dots, N, \quad (3.10)$$

where corr is the rank correlation of the j^{th} input signal $\mathbf{x}_j(t)$ with its i^{th} IMF $\mathbf{c}_{ij}(t)$. The total number of input signals and IMFs is given by M and N , respectively.

To achieve a common threshold for each signal component j the correlation

Table 3.1 Signal composition of mode alignment example.

	f_1	f_2	f_3	f_4	Phase lag
A	×	-	-	-	
B	×	×	-	×	$\angle f_1 = -\pi/2$
C	-	×	×	-	$\angle f_2 = -\pi/4$
D	×	-	-	×	$\angle f_1 = \pi/3, \angle f_4 = -\pi/4$

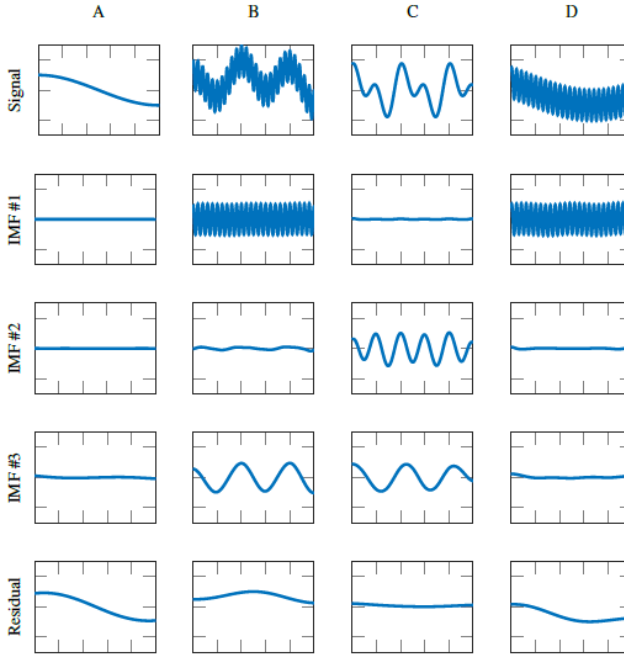


Figure 3.1: Mode alignment example.

coefficient is normalised

$$\lambda_{ij} = \frac{\rho_{ij}}{\max_i(\rho_{ij})}, \quad j = 1, \dots, M, \quad i = 1, \dots, N. \quad (3.11)$$

An $N \times M$ matrix $\mathbf{\Lambda}$ is constructed in such a way that each row contains the normalised correlation coefficients of similarly indexed IMFs, just as in the order in Figure 3.1.

Grouping Algorithm

The grouping technique sets the correlation coefficients in every row of the correlation matrix $\mathbf{\Lambda}$ exceeding a certain threshold η to one while all others to zero:

$$\delta_{ij}(\lambda_{ij} \geq \eta) = 1, \quad (3.12a)$$

$$\text{else } \delta_{ij} = 0. \quad (3.12b)$$

In this way, components in a row representing the same oscillatory modes are grouped and significant IMFs of each signal are identified.

The steps of the grouping algorithm are given below (Aftab et al. 2016):

1. Calculate the matrix $\mathbf{\Lambda}$ with the normalised correlation coefficients.
2. Find δ_{ij} with condition (3.12).
3. The row i for which $\delta_{ij} = 1$ represents signals with a similar oscillatory mode.

A threshold of $\eta = 0.5$ is used in this work.

To better capture the local behaviour of the signal, one may not use the global but only a local (moving horizon) signal to construct the correlation matrix

$$\rho_{ij}^{\{t_l:t_k\}} = \text{corr}(\mathbf{c}_{ij}^{\{t_l:t_k\}} \mathbf{x}_j^{\{t_l:t_k\}}), \quad i = 1, \dots, N, \quad j = 1, \dots, M, \quad (3.13)$$

where $k-l$ represents the horizon with $0 < l < k$. Considering the local signal may result in a negative correlation between the input signal and its IMFs. Therefore, the threshold should be tested against the absolute values $|\lambda_{ij}| \geq \eta$ also to find the signals shifted by about 180° .

3.3 Model Identification and Granger's Causality

An important model identification step is to identify causality between input and output variables of the model. Different methods, like transfer entropy (Yang and Xiao 2012) or partial directed coherence (Landman et al. 2014), were proposed. Granger's causality (G-causality) is used, since it is frequently used, simple to implement, and offers sufficient performance for the scope of this thesis.

A variable \mathbf{u}_1 is said to G-cause a variable \mathbf{u}_2 if the past of \mathbf{u}_1 contains information that helps to predict the future of \mathbf{u}_2 over and above information already in the past of \mathbf{u}_2 (Granger 1969).

If we combine this with an estimated Vector-Autoregression model (VAR-model), which is identified in Chapter 9, then the simplest unconditional G-causality can be motivated as follows (Barnett and Seth 2014):

Suppose \mathbf{u}_k can be split into two jointly distributed multivariate processes

$$\mathbf{u}_k = \begin{pmatrix} \mathbf{u}_{1,k} \\ \mathbf{u}_{2,k} \end{pmatrix}. \quad (3.14)$$

As a VAR formulation, the model of this vector can be denoted as

$$\begin{pmatrix} \mathbf{u}_{1,k} \\ \mathbf{u}_{2,k} \end{pmatrix} = \sum_{i=1}^p \begin{pmatrix} \mathbf{A}_{11,i} & \mathbf{A}_{12,i} \\ \mathbf{A}_{21,i} & \mathbf{A}_{22,i} \end{pmatrix} \begin{pmatrix} \mathbf{u}_{1,k-i} \\ \mathbf{u}_{2,k-i} \end{pmatrix} + \begin{pmatrix} \boldsymbol{\varepsilon}_{1,k} \\ \boldsymbol{\varepsilon}_{2,k} \end{pmatrix} \quad (3.15)$$

moreover, the residual covariance matrix as

$$\boldsymbol{\Sigma}_{\mathbf{u}_1 \mathbf{u}_1} = \text{cov} \begin{pmatrix} \boldsymbol{\varepsilon}_{1,k} \\ \boldsymbol{\varepsilon}_{2,k} \end{pmatrix} = \begin{pmatrix} \boldsymbol{\Sigma}_{11} & \boldsymbol{\Sigma}_{12} \\ \boldsymbol{\Sigma}_{21} & \boldsymbol{\Sigma}_{22} \end{pmatrix}. \quad (3.16)$$

The parameters of the VAR-model are fitted by solving an optimisation problem. The \mathbf{u}_1 -component of the regression (3.15) is

$$\mathbf{u}_{1,k} = \sum_{i=1}^p (\mathbf{A}_{11,i} \mathbf{u}_{1,k-i} + \mathbf{A}_{12,i} \mathbf{u}_{2,k-i}) + \boldsymbol{\varepsilon}_{1,k} \quad (3.17)$$

from which we see that the dependency of \mathbf{u}_1 on the past of \mathbf{u}_2 , given its past, is encapsulated in the coefficients $\mathbf{A}_{12,i}$. If these coefficients are zero, there is no conditional dependency on the past of \mathbf{u}_2 . These lead to the reduced regression, which omits the past of \mathbf{u}_2

$$\mathbf{u}_{1,k} = \sum_{i=1}^p \mathbf{A}_{11,i} \mathbf{u}_{1,k-i} + \hat{\boldsymbol{\varepsilon}}_{1,k}, \quad (3.18)$$

so that $\mathbf{u}_{1,k}$ is predicted by its past only.

G-causality can be calculated with the two residuals in (3.17) and (3.18) and their covariance matrices $\hat{\Sigma}_{11} \equiv \text{cov}(\hat{\boldsymbol{\varepsilon}}_{1,k})$. The G-causality from \mathbf{u}_2 to \mathbf{u}_1 is defined to be the log-likelihood ratio

$$\mathcal{F}_{\mathbf{u}_2 \rightarrow \mathbf{u}_1} \equiv \ln \frac{|\hat{\Sigma}_{11}|}{|\Sigma_{11}|}. \quad (3.19)$$

Thus, G-causality quantifies the reduction in the prediction error when the past of the process \mathbf{u}_2 is included in the explanatory variables of the VAR model of \mathbf{u}_1 .

3.3.1 Model Order

The determination of the necessary model order for the VAR current model is done with the Bayesian Information Criterion (BIC). This is a model selection method that penalises the maximum likelihood criteria. It has a single component that quantifies the goodness-of-fit, for example, through maximum likelihood, and one component that discounts the goodness-of-fit by the degree to which it was accomplished using a complex model:

$$BIC = -2 \ln f(\mathbf{U}|\hat{\theta}) + d \ln(n), \quad (3.20)$$

where d refers to the number of free parameters, n refers to sample size, and $\hat{\theta}$ refers to the maximum likelihood estimate. The model with the lowest criteria is the best.

Part I

Iceberg Dataset and Sensitivity Study

Chapter 4

Iceberg Datasets

In this chapter, two iceberg datasets containing eight iceberg tracks used to compare and verify the forecast algorithms are introduced.

4.1 The Newfoundland Iceberg Dataset

During the Offshore Newfoundland Research expedition in Spring 2015 conducted by Statoil and ArcticNet ([ArcticNet 2004-2018](#)), three icebergs were tracked (Fig. 4.2). The Canadian Coast Guard research vessel *Amundsen* was used during the expedition (Fig. 4.1), and the author of this thesis participated in this expedition.

The GPS beacons deployed on the iceberg provided at least an hourly position update. The icebergs names are related to the order of their discovery. Iceberg 3 was excluded from the dataset and not presented here since the sea ice concentration around the iceberg was dense. Consequently, its drift may be strongly influenced by sea ice. A summary of the Newfoundland iceberg data set is given in Tab. 4.1.

Table 4.1: Newfoundland iceberg data set. The iceberg geometries are from the day of the GPS beacon deployment.

	Iceberg shape	Horizontal dimensions [m]	Freeboard [m]	Keel depth [m]	Measurement frequency [h]	Drift data [days]	GPS tracker
Iceberg 1	dry-dock	210 × 150	30	45 – 60	1	8	Canatec
Iceberg 2	rounded	100 × 100	16	75	1	4	Canatec
Iceberg 4	wedged	290 × 100	30	90 – 100	1	37	2 Canatec & 2 (1) Solara
Iceberg 4-3	–	–	–	–	1	52	Solara



Figure 4.1: The Canadian Coast Guard Ship *Amundsen* is a Pierre Radisson-class icebreaker and Arctic research vessel.

4.1.1 Iceberg 1

Iceberg 1 had a dry-dock iceberg shape (Sec. 2.2). The sea ice concentration, indicated as the ratio of sea area covered by sea ice to the total area (WMO 1970) was less than $\frac{3}{10}$ at the start of the tracking on April 22, 2015. Throughout the thesis, it is assumed that the sea ice concentration has a minor influence on the iceberg drift. Therefore, the sea ice force is neglected in all simulations.

The iceberg was discovered close to St. John's (Fig. 4.3), and a Canatec GPS tracker was deployed by helicopter onto the iceberg, which has an accuracy of about 1.8 m. A position measurement was received with a five-minute frequency. The sail height H_a of about 30 m was estimated from the ship by triangulation. The length L and width W was estimated to be 210 m and 150 m, respectively. A ship-mounted SX90 sonar measured the iceberg keel depth to be within 45 m to 60 m.

Iceberg 1 was tracked for about eight days, and it is likely that the iceberg grounded and rolled close to Ireland's Eye.

4.1.2 Iceberg 2

Iceberg 2 had a spherical or dome-shaped iceberg shape (Fig. 4.2). The sea ice concentration was similar to the situation at the initial position of Iceberg 1. In fact, the Iceberg 2 was initially tracked only 8 km apart from Iceberg 1 on April 22, 2015 (Fig 4.3). A Canatec GPS tracker was deployed by helicopter on the iceberg, which provided position measurements with a five-minute frequency.

The sail height H_a of Iceberg 2 was estimated from the ship by triangulation to be about 16.5 m. The length L and width W of the iceberg were estimated to be about 100 m, and the keel height H_w was estimated by a ship-mounted SX90



(a) Iceberg 1 on April 22, 2015.
Shape: Dry dock.



(b) Iceberg 2 on April 22, 2015.
Shape: Dome-shape.



(c) Iceberg 4 on April 24, 2015. Shape: Wedged.

Figure 4.2: (a) Iceberg 1 located close to Bonavista on Newfoundland with horizontal dimensions of about 210×150 m. (b) Iceberg 2 located close to Bonavista on Newfoundland with horizontal dimensions of about 100×100 m. (c) Iceberg 4 with the horizontal dimensions of about 290×100 m.

sonar to be about 75 m. The total water depth at the initial iceberg position was about 200 m.

The iceberg was tracked for nearly four days until the signal was lost close to Catalina on Newfoundland, where the iceberg probably grounded or rolled.

4.1.3 Iceberg 4

Iceberg 4 has a wedged iceberg shape (Fig. 4.2). On the iceberg, four GPS beacons, two Canatec GPS trackers and two Solara GPS trackers, were deployed by helicopter. It was possible to land on the iceberg and drill the beacons into the iceberg. At first, the Canatec and Solara GPS trackers provided five and one-minute position updates, respectively. After 24 h to 48 h, the position update frequency was reduced to 15 min and 1 h, respectively.

The iceberg length L was estimated to be 290 m, width W of 100 m, sail height H_a of 30 m, which was estimated by triangulation from the ship. The keel depth was measured by a ship-mounted SX90 sonar to be about 90 m to 100 m. The smallest extension of the iceberg was in the middle, which gave it a form of a dumbbell. The iceberg was tracked for about 37 days. However, after about 5.5 days, the iceberg broke into two pieces and likely broke in the middle, where it had the smallest sail height. Interestingly, three GPS trackers remained on the iceberg, while one GPS tracker tracked the smaller piece, which is referred as Ice-

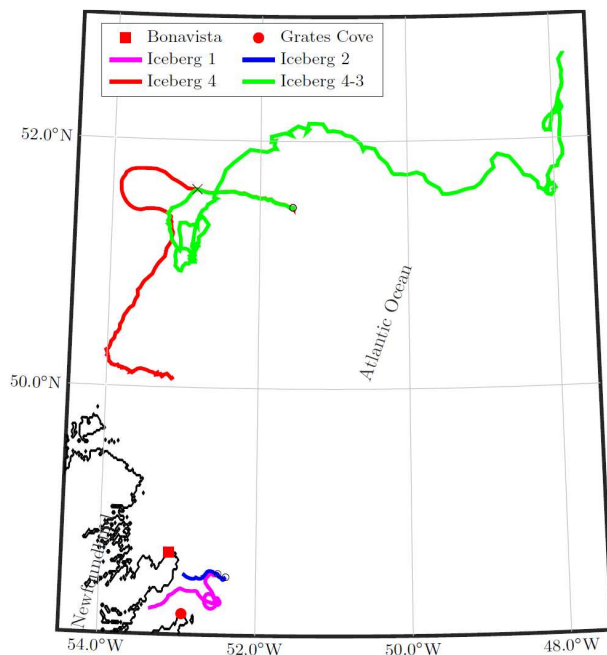


Figure 4.3: Map of iceberg drift trajectories. Icebergs 1 and 2 are close to the shoreline of Newfoundland while Icebergs 4 and 4-3 drift on the open ocean. The initial positions of the icebergs are marked with a circle and the location where the Iceberg 4 broke with a cross. For better orientation the weather station in Bonavista is marked on the map.

berg 4-3.

Iceberg 4-3 was tracked for 52 days. After evaluating the pictures of Iceberg 4, it is assumed that breakage happens at about $2/3$ of the waterline length. Mass, width, draft, and sail are adjusted accordingly of both icebergs in the simulations. The two remaining icebergs (Iceberg 4 and Iceberg 4-3) are likely more dome-shaped than wedged.

4.2 The Baffin Bay Iceberg Dataset

The Baffin Bay Iceberg dataset was provided by Luke Copland from the University of Ottawa. The icebergs were tracked in the northern Baffin Bay from August to October 2016 (Fig. 4.5) either with a RockSTARTM GPS receiver or a MetOcean CALIB GPS beacon deployed from a helicopter.

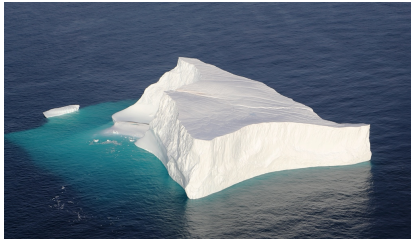
Also, for this expedition, the CCGS *Amundsen* was used as a research vessel. The icebergs are named after the GPS tracker serial number. The iceberg dataset contains four icebergs, of which only Iceberg 1040 was not grounded during the observation period. A summary of the Baffin Bay data set is given in Tab. 4.2.



(a) Iceberg 1040 on August 9, 2016.
Shape: Tabular.



(b) Iceberg 5450 on August 9, 2016.
Shape: Tabular.



(c) Iceberg 3534 on August 6, 2016.
Shape: Tabular.



(d) Iceberg 3651 on August 6, 2016.
Shape: Tabular.

Figure 4.4: (a) Iceberg 1040 located in the northern Baffin Bay with horizontal dimensions of about 1000×1000 m and ice thickness of 92 m. (b) Iceberg 5450 located in the northern Baffin Bay with horizontal dimensions of about 600×400 m and ice thickness of 67 m. (c) Iceberg 3534 located in the northern Baffin Bay with horizontal dimensions of about 250×200 m and a sail height of about 45 m. (d) Iceberg 3651 located in the northern Baffin Bay with horizontal dimensions of about 300×300 m and a sail height of about 40 m.

4.2.1 Iceberg 1040

Iceberg 1040 was located in the northern Baffin Bay and tracked with a MetOcean CALIB GPS beacon that was deployed on August 9, 2016. The dataset in the thesis begins on August 17, 2016. The iceberg was a large tabular ice island with horizontal dimensions of about 1×1 km (Fig. 4.4(a)). The ice thickness was measured at about 92 m near the centre of the ice island using a 10 MHz ground-penetrating radar system.

The measurement frequency was 1 h. However, due to a transmission error, the same position measurement was received every three consecutive hours, reducing the effective sampling frequency for this iceberg to 3 h. Moreover, the position measurements between September 22 and October 4, 2016 were removed due to another transmission error causing the iceberg not to move or "jump." The iceberg trajectory is, therefore, divided into two parts: Iceberg 1040-1 and Iceberg 1040-2.

Iceberg 1040-1 contains 36 days (August 17 - September 22) of drift data and Iceberg 1040-2 about 15 days (October 04 - 19) (Fig. 4.5).

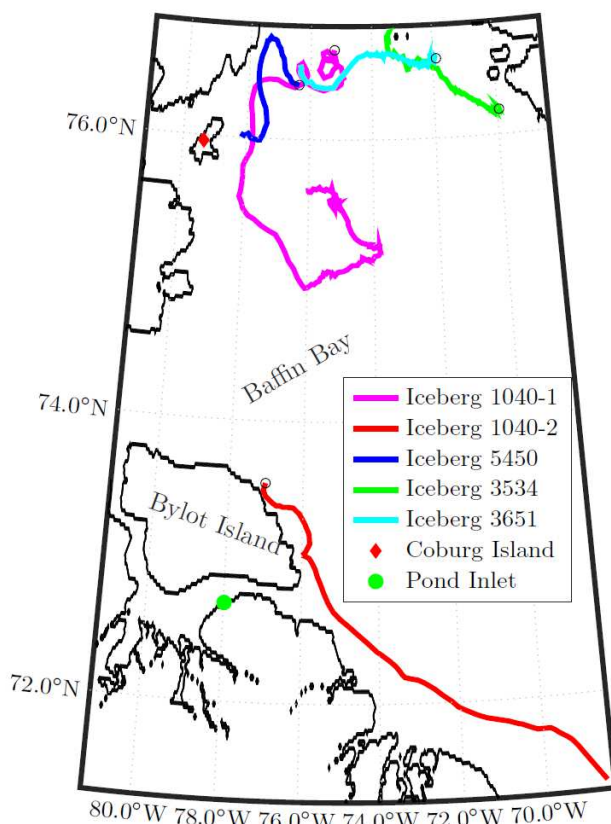


Figure 4.5: Map of iceberg drift trajectories. Iceberg 1040-1, 5450, 3534, and 3651 drift in the northern part of Baffin Bay. Iceberg 1040-2 drifts southwards towards the Davis Strait. The initial positions of the icebergs are marked with a circle. Bylot Island and two other land marks are shown on the map for reference.

4.2.2 Iceberg 5450

Iceberg 5450 was located in the northern Baffin Bay and was also tracked with a MetOcean CALIB GPS beacon deployed on August 9, 2016. In this thesis the dataset begins on August 12, 2016, with a measurement frequency of 1 h. Transmission problems were not observed. The iceberg is a large tabular ice island with horizontal dimensions of about 600×400 m (Fig. 4.4(b)). The ice thickness was measured at about 67 m with a 10 MHz ground-penetrating radar system.

The iceberg grounded on August 21, 2016, so about 8 days of drift data is available for this iceberg (Fig. 4.5). On the other hand, it is possible based on the sea depth to get an estimate about the keel depth of the iceberg. The GEBCO 2014 global bathymetry grid at 30 arc-second intervals suggests a sea depth of about

Table 4.2: Baffin Bay iceberg data set. The iceberg geometries are from the day of the GPS beacon deployment.

	Iceberg shape	Horizontal dimensions [m]	Freeboard [m]	Keel depth [m]	Measurement frequency [h]	Drift data [days]	GPS tracker
Iceberg 1040-1	tabular	1000 × 1000	92	–	1	36	MetOcean CALIB
Iceberg 1040-2	–	–	–	–	1	15	MetOcean CALIB
Iceberg 5450	tabular	600 × 400	67	–	1	8	MetOcean CALIB
Iceberg 3534	tabular	250 × 200	–	45	1	15	RockSTAR TM
Iceberg 3651	tabular	300 × 300	–	40	1	11	RockSTAR TM

100 m to 110 m at the grounding location ([GEBCO -](#)).

4.2.3 Iceberg 3534

Iceberg 3534 was tracked with a RockSTARTM GPS receiver deployed on August 6, 2016, and the dataset in this thesis begins on August 8, 2016. The iceberg is tabular with horizontal dimensions of about 250×200 m (Fig. 4.4(c)). The sail height was estimated to be about 45 m. The iceberg grounded on August 19, 2016 giving us about 15 days of drift data (Fig. 4.5). The measurement frequency was 1 h, and transmission problems were not observed. The iceberg moved again for a few days after the first *grounding event*. However, this period was excluded from the drift dataset, since it was short and may be influenced by other forces such as sea ice or interactions with the seabed. The GEBCO 2014 global bathymetry grid at 30 arc-second intervals suggests a sea depth of about 190 m at the grounding location ([GEBCO -](#)). The final location has a sea depth of about 105 m, which is more likely in the range of the keel depth of the iceberg. It may be that the first *grounding event* is actually done to sea or fast ice, but it may also be just due to a coarse bathymetry map that the sea depth is overestimated at the location.

4.2.4 Iceberg 3651

Similar to the other icebergs from the Baffin Bay dataset, Iceberg 3651 was located in the northern Baffin Bay and tracked with a RockSTARTM GPS receiver deployed on August 6, 2016. The dataset in this thesis begins on August 8, 2016. The iceberg was large tabular with horizontal dimensions of about 300×300 m and a sail height of about 40 m (Fig. 4.4(d)).

The iceberg grounded on August 19, 2016 giving us about 11 days of drift data. At the grounding location, the GEBCO 2014 global bathymetry grid at 30 arc-second intervals suggests a sea depth of about 100 m. Also, this iceberg starts moving again for a few days. However, these periods were excluded from the dataset.

Chapter 5

Sensitivity Study of the Dynamic Iceberg Drift Model

This chapter is based on PAPER H ([Andersson et al. 2017c](#)), which is separated into two parts to better fit within the thesis organisation. The first part of the paper is presented in this chapter with the second included in Chapter 13.

The chapter illustrates how extracting iceberg trajectories from the data collected during this PhD study remains challenging to forecast or even hindcast using dynamic iceberg models, even if the uncertainties in currents, winds, and waves are reduced by measuring the forces close to the iceberg due to the sensitivity of the model to its parameters and inputs.

5.1 Introduction

One of the most comprehensive iceberg drift datasets was collected by [Smith and Donaldson \(1987\)](#), which included current profiles and wind data from twelve track segments of seven different icebergs. In addition, the mass and cross-sectional areas were estimated based on sonar profiles and photographs. The dynamic model reasonably represented the majority of the observed tracks reasonably. However, drag coefficients were optimised and the wind was corrected for their analysis. Furthermore, some observed tracks showed considerable deviation from the modelled track.

A new research effort lead by C-CORE developed and improved iceberg profiling. It is now possible to profile the iceberg in a relatively short time ([McGuire et al. 2016](#)) and use these profiles in Iceberg Management systems to prepare towing ([Bruce et al. 2016](#)), model iceberg impacts ([Stuckey et al. 2016](#)) or evaluate the risk to sub-sea installations ([King et al. 2016](#), [Fuglem et al. 2016](#)). These iceberg

profiles are collected by approaching the iceberg with a ship. Profiling the iceberg sail and keel with underwater vehicles was undertaken by other groups (Wang et al. 2015, Zhou et al. 2016). However, it is not straightforward to include a detailed 3D iceberg profile into the dynamic iceberg model.

In Spring 2015, ArticNet (ArcticNet 2004-2018) and Statoil conducted an Off-shore Newfoundland Researcher Expedition. During this expedition a dataset of one iceberg track similar to the one collected by Smith and Donaldson (1987) was collected. This chapter discusses the sensitivity of the dynamic iceberg model to different input signals and model parameters.

5.2 Data Collection

The iceberg discussed here was discovered during the Offshore Newfoundland Research Expedition on April 24, 2015, and is labelled Iceberg 4 (Section 4.1.3).

Without a more precise overview of the iceberg, the side-pictures would suggest that it had a width of about 100 m to 190 m. The keel depth was estimated with the ship-mounted SX90 sonar to be 90 m to 100 m. There are several empirical formulas available to estimate the iceberg draft. Barker et al. (2004) proposed the two equations

$$H_w = 2.91L^{0.71}, \quad (5.1a)$$

$$H_w = 0.7L, \quad (5.1b)$$

while two alternate equations were proposed by C-CORE (2007),

$$H_w = 3.27L^{0.68}, \text{ and} \quad (5.2a)$$

$$H_w = 3.31L^{0.56}H_a^{0.17}. \quad (5.2b)$$

These formulas result in an overestimation of the draft of the iceberg with 160m, 197m, 151m, and 140 m, respectively. The dumbbell shape of the iceberg most likely causes this deviation (Fig. 5.1). It is probable that only one "bell" is responsible for the keel depth while the other has a smaller keel depth. The larger "bell" of the iceberg has a length of about 145 m, which results in an iceberg draft of about 96 m to 101 m using (5.1 - 5.2). This is very close to the actual measured keel depth. It is also likely that the later observed breakage of the iceberg happens between the two bells.

Four GPS beacons were deployed on the iceberg at around 15:15 UTC on August 24, 2015. The iceberg velocity and rotation is shown in Fig. 5.2. The velocity in the north-south and east-west directions changes only slightly during the observation. The long axis of the iceberg rotates between $\pm 15^\circ$ from the north direction, and the period of this oscillation is about 3 h.

Between 14:20 and 21:50 UTC, a wave glider operated close to the iceberg,

and collected wave, current, and wind data. At the same time, current data was collected from the icebreaker CCGS *Amundsen*, which stayed close to the iceberg (Fig. 5.3).

Wind information was available from the CCGS *Amundsen*, the wave glider (5 min frequency), manual observations (1 h frequency) on the CCGS *Amundsen*, and from the weather forecast (6 h frequency). The automatic wind measurements on the CCGS *Amundsen* were excluded from the analysis since they did not correlate with the other wind information sources. Therefore, it was assumed that they were error-prone and not trustworthy (Fig. 5.4).

The current information was received by the Shipboard Acoustic Doppler Current Profiles (SADCP) and measured with a 5 min frequency. The current profiles important for the iceberg are shown in Fig. 5.5 with the layer size at 8 m and the centre of the first 8 m height bin at 23.2 m. It is assumed that the surface current is similar to the current measured in the first bin. Because of the position of the sonar underneath the ship, it was not possible to measure currents closer to the surface. The currents are similar in the current layers. Nevertheless, sometimes a direction change can be detected between the near surface and deeper currents. Between hours 3 to 4, the current measurements show strong peaks, which are probably several outliers (due to significant errors in the current measurement). The overall current velocity is small.

The wave glider measured significant wave height and wave peak direction with a measurement frequency of 30 min. The waves propagate from southeast-east to northwest-west. Consequently, waves have a stronger westerly component and a weaker northerly component (Fig. 5.6). In comparison, the wind blows from northeast-east to southwest-west. The average difference between wave and wind directions is 26° with the average wave height of 1.56 m and average wind velocity 8.7 m/s.



(a) Iceberg view from one side.



(b) Iceberg view from opposite side.

Figure 5.1: View of Iceberg 4 from additional perspectives compared to Fig. 4.2(c).

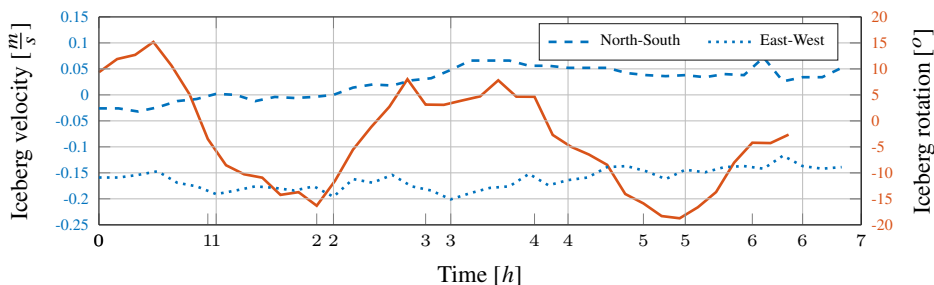


Figure 5.2: Iceberg velocity in north-south (dashed) and east-west (dotted) directions and the rotation of the iceberg (solid).

5.3 Iceberg Drift Simulation

In this section, the iceberg is simulated based on the measured forces on the iceberg. While a simulation period of 6.5 hours is short, some conclusions may still be considered. The iceberg model used in these simulations is described in Section 2.3.

5.3.1 Sensitivity of Iceberg Shape to Different Current Measurements

Three different iceberg keel shapes are considered: rectangular, semi-elliptic, and triangular (Fig. 5.7). The mass is assumed constant for each keel shapes.

In the first simulation study, the wave force is neglected. The initial iceberg velocity is calculated with the first two iceberg position measurements. If the measured SADC data is used the three iceberg keel shapes behave considerably differently (Fig. 5.8). The error between simulated and observed iceberg trajectory increases over the observation horizon for all three iceberg keel shapes. The triangularly shaped iceberg keel shows the smallest and the rectangularly shaped iceberg keel the largest error. The triangularly shaped iceberg keel is more strongly influenced by the surface and near-surface currents than the other iceberg shapes. Therefore, the surface current layer is likely not weighted strong enough during the simulations with the rectangular and elliptical iceberg keel shape.

If only the surface current layer is used as current for the entire iceberg keel, then the error between the observed and simulated iceberg trajectories reduces significantly compared to the results as shown in Fig. 5.8. For this new configuration, the elliptic iceberg keel produces the smallest error. The triangular iceberg keel overestimates the east velocity of the iceberg compared to the other iceberg keel shapes caused by the strong eastward wind velocity observed by the wave glider at the end of the observation horizon (Fig. 5.4).

The manual wind observations, on the other hand, show a decrease in wind

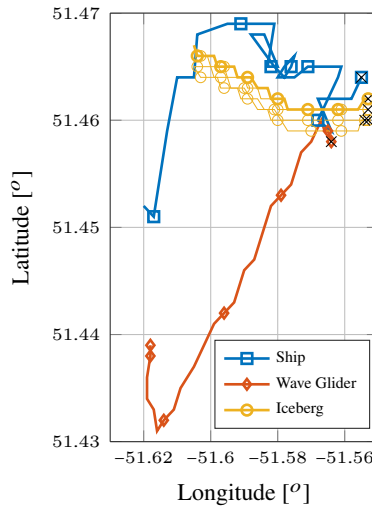


Figure 5.3: Ship, glider, and iceberg positions. Every hour is a mark set into the trajectory. The position of four GPS beacons on the iceberg is shown. The initial positions of the trajectories are marked with a cross.

velocity. If the iceberg is simulated using the first current layer and the manually observed wind velocities, then the rectangularly shaped iceberg keel has the smallest final position error. This error is even smaller than the final error of the elliptically shaped iceberg using the wind velocities measured by the wave glider.

So, all three geometries may behave best depending on the combination of input signals used in the simulations.

5.3.2 Sensitivity of Iceberg Model to Different Input Signals and Geometry Assumptions

To further investigate the influence of different input signals and the iceberg shape assumptions, every possible combination of the following variables were simulated:

1. Iceberg keel shape: rectangular, triangular, semi-elliptic
2. Current input: mean current, surface current, layered current
3. Wind input: manually observed wind, wave glider wind, wind forecast
4. Wave input: included or excluded
5. Pressure gradient force: yes or no
6. Coriolis force: yes or no

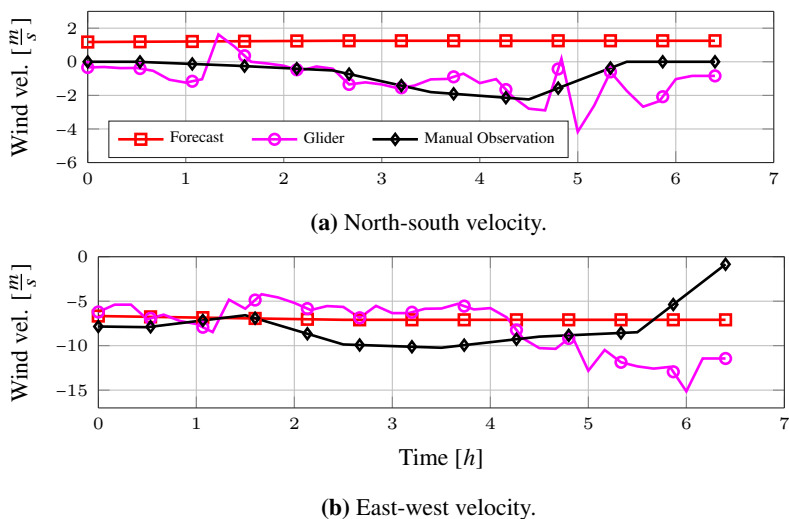


Figure 5.4: Wind velocity in north-south and east-west directions. Wind direction is positive if it blows in the north and east directions. The forecast and manual observations are interpolated to fit the measurement frequency of the wave glider. The marks are only added for simpler differentiation of the lines in the plot.

Other parameters, such as the drag coefficients, were not changed during the 216 iceberg drift simulations. The root mean square error, final, and a maximum error of the drift hindcast were analysed, first for each simulation option and afterwards for different combinations of options.

The smallest root mean square error of 102 m is achieved with the combination: rectangular iceberg keel shape, surface current, manually observed wind, no waves, no pressure gradient force, and with the Coriolis force. The second best hindcast was achieved by switching on the pressure gradient force, which resulted in a root mean square error of 178 m.

The largest root mean square error was 1741 m from the combination: triangular iceberg shape, surface current, manually observed wind, waves, no pressure gradient force, and with the Coriolis force. A similar error was achieved with the pressure gradient force. The difference for the best one is due to the iceberg shape and the wave force.

In a second step, the results were visualised by fitting the performance indices into a kernel distribution and plotting the resulting *probability density function* (pdf) (interpreting the mean square error from the different experiments as a random variable) (Fig. 5.9). It can be seen that the triangularly shaped iceberg has a larger variance in the root mean square error as well as larger mean compared to the other iceberg shapes.

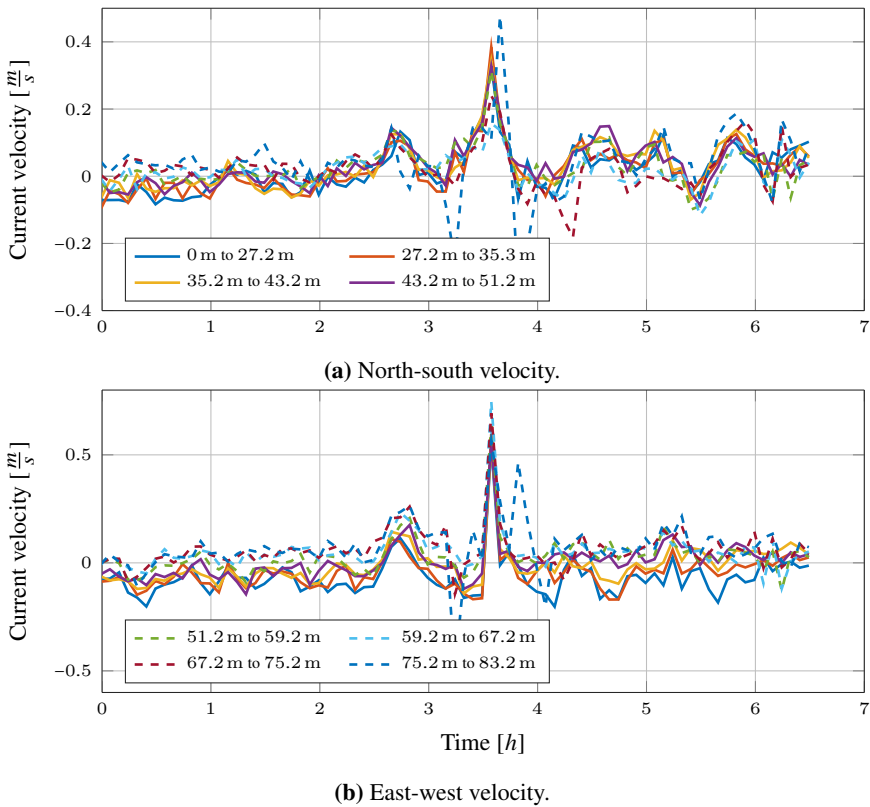


Figure 5.5: Current velocities in different layers. The layer diameter is given in $[m]$. The first four layers have solid lines and the second four layers are dashed.

More substantial errors are produced by the triangular iceberg using surface currents since both pdf's show a similar right tail. Using the triangular iceberg shape results, on the one hand, in smaller errors than with the other iceberg shapes, but on the other hand, it also produces the largest errors.

As seen in Figures 5.9c and 5.9d that it is beneficial to exclude the wave and Coriolis forces. The problem with the wave force is that the simulated iceberg overshoots into the north and east directions. If the wave force is excluded the northerly component is hindcasted well (Fig. 5.8) while the simulated iceberg does not drift far enough in the east direction.

If the triangularly shaped iceberg keel is excluded from the analysis and only the rectangular and elliptic shapes are considered, then the right tail of the pdf is similar for all considered current inputs, while the surface current produces a smaller mean error.

The pressure gradient force has only a small influence on the root mean square

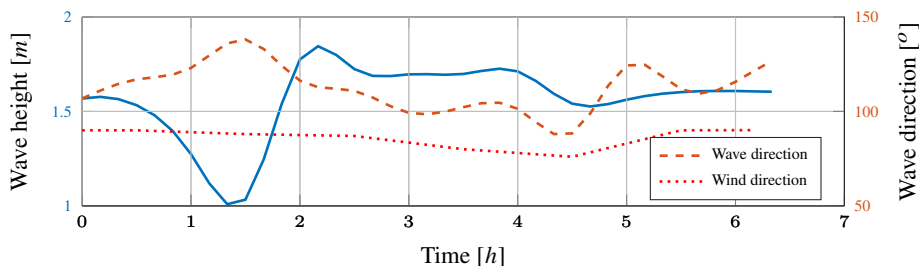


Figure 5.6: Significant wave height (blue, solid) and average direction (orange, dashed).

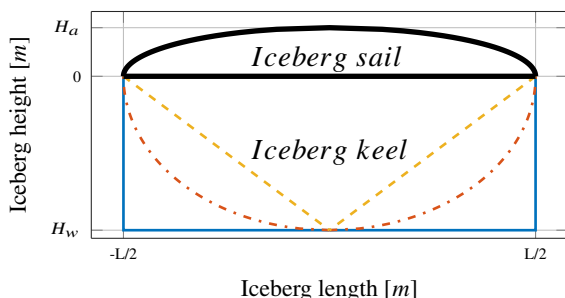


Figure 5.7: Schematic of different iceberg keel geometries. The solid line shows a rectangular shape, the dashed-dotted line a semi-elliptical shape and the dashed line a triangular shape.

error, and the pdf's are nearly on top of each other. If the wave, Coriolis, and pressure gradient forces are excluded, then the resulting pdf of the mean square error has the smallest mean error and a relatively small variance.

5.4 Conclusion

The chapter showed data taken from one iceberg trajectory. Current, winds, and waves were measured close to the iceberg. Even though only one iceberg trajectory was studied, this section illustrated how sensitive the dynamic iceberg model is to changes in the inputs and assumptions about the iceberg keel shape. The root mean square error varies from 178 m to 1741 m with a mean error of 791 m. The final distance between simulated and observed iceberg trajectories varies between 180 m to 3376 m, with a mean final error of 1447 m. This variation was achieved without adjusting the mass or the drag coefficients of the iceberg.

By not using presumably relevant information, such as the wave, Coriolis or pressure gradient forces, the mean root mean square error and the mean final error can be reduced to 641 m and 1080 m. Even though the current, wind, and waves were measured directly at the iceberg position, it is difficult to hindcast the iceberg trajectory with the measured forces. Furthermore, it is not necessarily advanta-

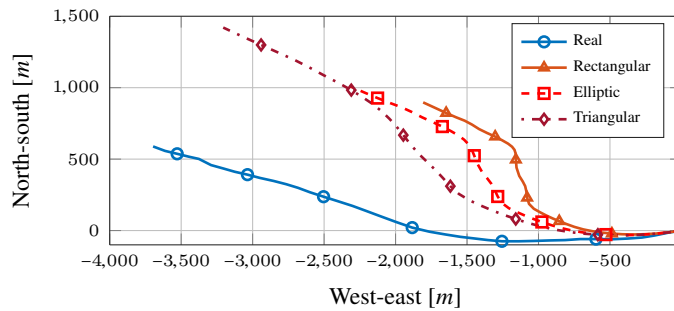


Figure 5.8: Iceberg trajectories for different iceberg keel assumptions with SADC data and wind measured by the wave glider.

geous to include more forces to the dynamic model, since they do not consistently improve the hindcast result. Moreover, a simple kinematic model, which considers only the mean current velocity and a 2% deflection by the wind, produces a similar result as the best dynamic model (Fig. 5.10). The root mean square error of the kinematic model is 140 m and the final error 187 m.

While this may be an exception in this particular case, it shows that variance in the drift trajectories of the dynamic model is significant, because of the many uncertain parameters in the model. In addition, it is not straightforward to include detailed information, for example, about the iceberg shape in the quite simplified dynamic iceberg model. In contrast, a more detailed and complicated dynamic model increases the number of parameters and, most likely as a consequence, the variance of the model.

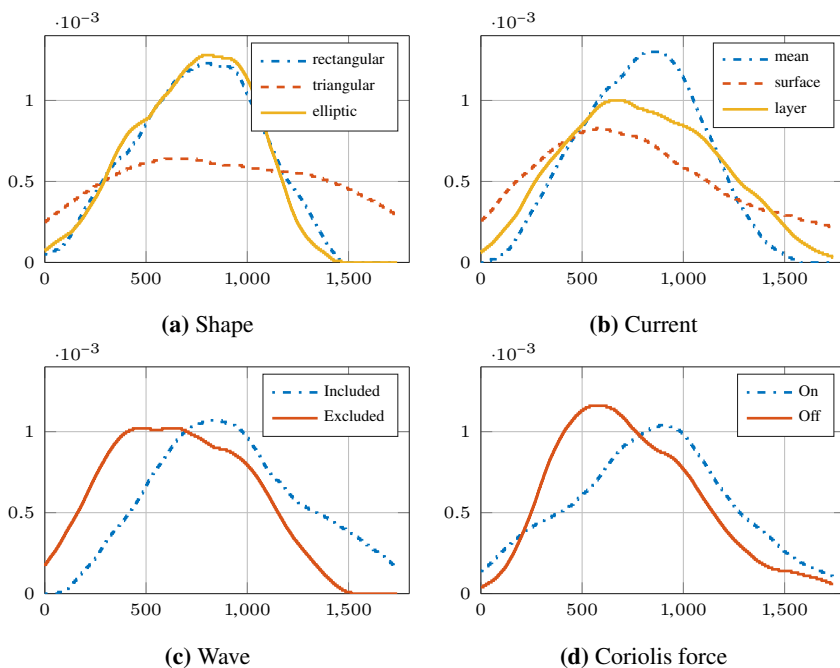


Figure 5.9: Probability density functions of the root mean square error in $[m]$ for different variables. The y-axis shows the root mean square error and the x-axis the probability of this error in all simulations with the specific parameter value (e.g., in (a), the root mean square error of all simulations performed with a rectangular iceberg keel shape are represented by the blue dash-dotted line). Besides the one mentioned in the label of the figure all other variables are varied in their discrete states. As given in the list at the beginning of the section (5.3.2), the variables are: iceberg keel shape, current, wind and wave input, pressure gradient and Coriolis force.

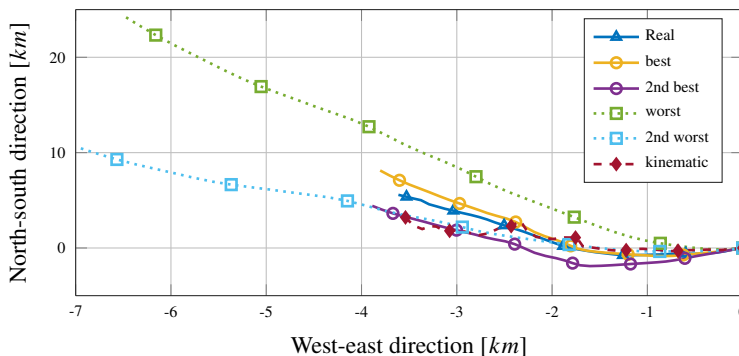


Figure 5.10: Iceberg trajectories for the dynamic model (two best and two worst) and the trajectory of the kinematic model.

Part II

Hybrid Iceberg Drift Forecast Algorithms

Chapter 6

The Ancillary Current Forecast Scheme

This chapter is based on PAPER A ([Andersson et al. 2016a](#)) and introduces the ancillary current forecast scheme. A property of this forecast scheme is that it uses the dynamic iceberg model while adapting some of its parameters based on past observations with a moving horizon estimator. Since it combines the dynamic iceberg model with statistical methods, it is referred to as a *Hybrid Iceberg Drift Forecast Algorithm*.

6.1 Introduction

This chapter focuses on improving short-term iceberg drift predictions with the help of parameter estimation techniques. Criteria are introduced on how to choose which parameters to update in processes with large uncertainties. With the help of those criteria, different options based on the dynamic iceberg model are discussed. Thereafter, a moving horizon estimator (MHE) is implemented, which estimates the chosen parameters. A case study on real iceberg trajectories measured offshore Newfoundland in spring 2015 illustrates how the proposed estimation scheme can improve short-term iceberg drift predictions.

6.2 The Dynamic Iceberg Drift Model

The dynamic iceberg drift model was presented in Section 2.3. A small adaptation of the mass and cross-sectional area was done in the original article ([Andersson et al. 2016a](#)). The Cross sectional areas are calculated with the help of L_0 and

W_0 , the mass is given by

$$m = L_0 W_0 (C_{H_w} H_w + C_{H_a} H_a) \rho_{Ice}. \quad (6.1)$$

The difference between (2.9) and (6.1) is that both sail and keel become independent shape factors C_{H_w} and C_{H_a} . The iceberg is a cuboid if the shape coefficients are 1.0, whereas the shape coefficients are 0.5 for a triangular shape. Consequently, the iceberg shape can be adapted with the shape coefficients to represent the observed iceberg more accurately. Nevertheless, accurate iceberg shapes and masses are not very critical for the later proposed estimation-forecast scheme.

6.3 Choice of Estimated Parameters

6.3.1 Design Criteria

An important task in parameter estimation is to analyse the model structure such to find physically reasonable parameters which describe the measured output adequately. The main tool for this is sensitivity analysis (Brun et al. 2001).

The parameters to estimate in the iceberg model should fulfil three important criteria:

1. The model output should be sensitive to changes in the parameters.
2. The estimated parameters should be independent from each other.
3. The parameters should be a physically reasonable representation of the process noise (process noise in this context means non-deterministic inputs, such as modeling errors and external disturbances (Walter and Pronzato 1997)).

The first criterion ensures that errors in the output can easily be adjusted by changes in the parameters. The second criterion guarantees that the problem is not ill-conditioned, such that changes in one parameter cannot be compensated by appropriate changes in other parameters. The third criterion ensures that the chosen parameters have a reasonable physical interpretation, e.g., that the mechanistic model is not degraded to a black-box model, which just describes the input-output behaviour of the process.

6.3.2 Design Criteria Applied to the Iceberg Model

The sensitivity of the model to changes in the environmental forces and to changes in iceberg parameters was investigated earlier by among others Smith and Banke (1983), Kubat et al. (2005), Allison et al. (2014). The results depend on the environmental conditions. However, the current was usually identified as the most

influential force on the iceberg. The investigated parameters were air drag coefficient C_a , the water drag coefficient C_w , the wave drift radiation coefficient C_r , the geometric parameters m , L , A_a and A_c as well as the input variables, current, wind and waves.

Smith (1993) and Turnbull et al. (2015) used the air drag and water drag coefficients to tune the iceberg model. Both coefficients were selected in a way that the error between observed and hindcasted iceberg trajectories was minimized. Turnbull et al. (2015) interpreted the results further and categorized based on the optimal drag coefficients whether the icebergs were primarily current or wind-driven. With limited success, Smith (1993) calculated the drag coefficients for one part of the iceberg trajectory and applied those to the second part in order to improve the forecast. The given explanation for the limited success was that the iceberg velocity closely follows the mean water current. For this reason, the water drag force is usually small and therefore the water drag coefficient has limited influence on the iceberg drift. Regarding the air drag coefficient, the explanation was that the wind force is typically of less importance which reflects on the air drag coefficient.

Keghouche (2010) updated both drag coefficients in an ensemble Kalman filter to identify periods when the forcing field was inaccurate. However, the previously introduced criteria are violated if those parameters are chosen to tune the iceberg model. This can be revealed in a simple example.

The air drag force in (2.5) can be written as

$$\mathbf{f}_a = \frac{1}{2} \rho_a C_a A_a |\mathbf{v}_a| \begin{pmatrix} v_a^n \\ v_a^e \\ 0 \end{pmatrix}, \quad (6.2)$$

where V_a^n and V_a^e are the wind velocities in north-south and east-west direction. The iceberg velocity is neglected. The (6.2) can be rewritten as

$$\mathbf{F}_a = \frac{1}{2} \rho_a C_a A_a |\mathbf{v}_a|^2 \begin{pmatrix} \cos(\phi_a) \\ \sin(\phi_a) \\ 0 \end{pmatrix}, \quad (6.3)$$

where ϕ_a is the wind direction. This simple conversion shows that the air drag coefficient C_a influences only the first part of (6.3) (until brackets) while the second part (vector in brackets) cannot be influenced. Consequently, the air drag coefficient C_a accounts for errors in the absolute wind velocity, sail cross section and air density, but not for errors within the wind direction. Moreover, it should be noted that errors in the absolute velocity are accounted quadratically while errors in the cross section area are accounted linearly. Similar observations can be made for the current, where only the relative velocity between current and iceberg can be corrected, but not directional errors. The change of a single parameter cannot

influence the directions. Therefore, both have to be changed to account for directional error. Consequently, the parameters depend on each other. Moreover, a physical interpretation of the estimated parameters is not possible and should be avoided, since wind and drag coefficients have to be adjusted in the same time to correct, for example, directional errors in the current force.

6.3.3 The Ancillary Current

The design discussed above can be improved by decomposing the drag coefficient. Considering the current, which has been identified to be the most important driving force, the water drag force can be rewritten as

$$\mathbf{f}_c = \frac{1}{2} \rho_c A_c |\mathbf{v}_{mc} - \mathbf{v}_i| \begin{pmatrix} C_w^n (v_{mc}^n - v_i^n) \\ C_w^e (v_{mc}^e - v_i^e) \\ 0 \end{pmatrix}, \quad (6.4)$$

where C_w^n and C_w^e are the decomposed water drag coefficients and \mathbf{V}_{mc} is the mean current in the water column over the iceberg keel. A second option is to correct the current directly with two current coefficients C_w^{e*} and C_w^{n*}

$$\mathbf{f}_c = \frac{1}{2} \rho_c A_c |\mathbf{v}_{mc} - \mathbf{v}_i| \begin{pmatrix} (C_w^{n*} v_{mc}^n - v_i^n) \\ (C_w^{e*} v_{mc}^e - v_i^e) \\ 0 \end{pmatrix}. \quad (6.5)$$

However, both designs violate the first design criterion. In the first case, the model becomes insensitive to changes of the water drag coefficients if the iceberg velocity is close to the current velocity. In the second case, the model becomes insensitive and even singularities occur if the current velocity in one of the directions becomes zero. An example of such an estimation process is shown in Fig. 6.1. Large values and short time excitations of the current coefficients in situations of low current velocities in one or both directions make this design not suitable for use in short-term forecasts.

In order to avoid singularities and to be able to account for large uncertainties, this work proposes to estimate instead an artificial current that we denote *ancillary current*. This ancillary current is added to the measured or predicted current in the model to correct for the observed iceberg drift trajectory. The water drag force is rewritten as

$$\mathbf{f}_c = \frac{1}{2} \rho_c A_c C_w |(\mathbf{v}_{mc} + \mathbf{v}) - \mathbf{v}_i| \begin{pmatrix} (v_{mc}^n + v^n) - v_i^n \\ (v_{mc}^e + v^e) - v_i^e \\ 0 \end{pmatrix}, \quad (6.6)$$

where \mathbf{v} is the ancillary current. The ancillary current can correct directional and absolute velocity errors in the current force. The process noise, like uncertainties

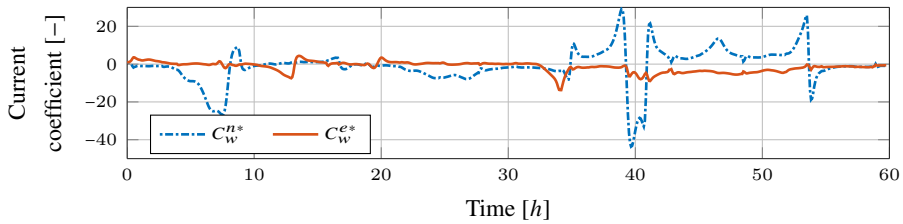


Figure 6.1: Estimation of current coefficients.



(a) SVP.



(b) SLDMB.

Figure 6.2: The MetOcean SVP and SLDMB buoys.

in environmental driving forces and geometrical uncertainties, are collected and corrected with the ancillary current. Since the current has the largest uncertainty, it is beneficial to correct the current with the estimated variable. Thus, this new design fulfils all three criteria.

6.4 Data Acquisition

The iceberg trajectories used in this case study were measured during the Offshore Newfoundland Research Expedition conducted by ArcticNet ([ArcticNet 2004-2018](#)) and Statoil in spring 2015. The two icebergs discussed in this chapter are Iceberg 1 and Iceberg 2 (Sec. 4). Only the first 60 h of the drift trajectory is studied in this Chapter. The limiting factor here is the available current data from the current drifter deployed close to the icebergs.

Two current drifters deployed close to each icebergs that collected current information, one MetOcean Iridium surface velocity program buoy (SVP) with a 15 m drogue and one MetOcean Iridium self-locating data marking buoy (SLDMB), which measured the surface current (Fig. 6.2). Position updates from the SVP were received with an hourly frequency, while SLDMB position updates were received with a ten minutes frequency. Both measurements were interpolated in simulations to fit the time stamp of the position data of the iceberg.

Both current drifters measured similar current velocities at Iceberg 1. At Ice-

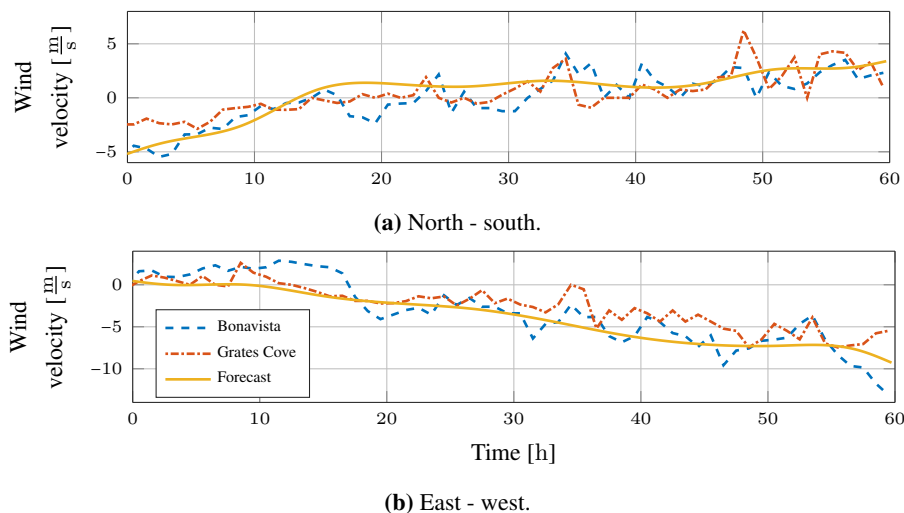


Figure 6.3: Predicted and measured wind velocity in both directions. The location of Bonavista is shown in Fig. 4.3.

berg 2, the data of the SVP drifter was not received and consequently only the surface current data of the SLDMB drifter is available for simulations. Thus, during simulations and estimations for Iceberg 1, the 15 m current information from the SVP drifter is used, and for Iceberg 2 the surface current information from the SLDMB drifter is used. Since deeper currents were not measured, the overall current force on the iceberg keel is uncertain. Wind and wave information was obtained by a weather forecast provided twice a day by Amec Foster Wheeler. The forecast time step was 6 h. In order to have values in between the time steps the wind and wave information was interpolated to fit the data points of the iceberg position. The weather forecast location and initial iceberg positions are around 110–125 km apart. Additional wind information was received by two weather stations located in Bonavista and Grates Cove on Newfoundland. They are about 30–60 km apart from the iceberg positions. Predicted wind at the forecast location and measured wind at the two weather stations are similar with respect to velocity and direction (Fig. 6.3).

6.5 Simulation and Estimation Set-up

The shape coefficients C_{H_w} and C_{H_a} are chosen to be 0.6 and 0.15 for Iceberg 1 and 0.8 and 0.8 for Iceberg 2. The dry-dock sail shape factor is taken from Rudkin et al. (2005), whereas the others are guessed based on the geometry of the iceberg and the assumed ratio between keel and sail cross-section. Other parameter values

can be found in Section 2.3.

During the observation of the icebergs, the significant wave height did not exceed 1.5 m and was most of the time less than 0.5 m. Such small waves can be neglected, since they have only a minor influence on the iceberg drift. Consequently, the wave radiation force (2.7) is removed from the dynamic iceberg drift model (2.3).

The states \mathbf{x} of the dynamic system are the iceberg position and iceberg velocity. In addition, the state vector is augmented with the ancillary current. Thus, the estimation model has six states and four inputs \mathbf{u} , which are the current and wind velocity. The measured output \mathbf{y} is the iceberg position.

The initial iceberg velocity is not known and assumed zero. Consequently, the initial state for the MHE is

$$\mathbf{x}_0 = [0, 0, 0, 0, 0, 0]^T, \quad (6.7)$$

where the first two states represent the iceberg position, the next two the iceberg velocity and the last two the ancillary current. The iceberg position is given in m, whereas the iceberg velocity and ancillary current is given in m s^{-1} . The iceberg certainly moved when the GPS was deployed. However, the error introduced by the assumption of zero initial iceberg velocity is small for simulations longer than 1–2 h. In addition, the error is corrected by the estimator. The initial error covariance is chosen to be

$$\mathbf{P}_0 = \text{diag}(1, 1, 1, 1)^2, \quad (6.8)$$

the measurement noise covariance is

$$\mathbf{R} = \text{diag}(20, 20)^2, \quad (6.9)$$

and the process noise covariance is

$$\mathbf{Q} = \text{diag}(3 \cdot 10^{-6}, 3 \cdot 10^{-6}, 6 \cdot 10^{-6}, 6 \cdot 10^{-6}, 6 \cdot 10^{-5}, 6 \cdot 10^{-5})^2. \quad (6.10)$$

The covariances are chosen in a way such that model uncertainties are largely corrected with changes in the ancillary current. The states of the process are estimated for the first 60 h after the surface drifters were deployed. If not stated otherwise, the horizon length of the MHE is chosen to be 24 h. The MHE performance in the iceberg drift case shows little sensitivity to changes in the horizon size. Nevertheless, slight improvements can be detected with increasing horizon size. The MHE problem is implemented in the Python programming language and solved by using the open-source software tool CASADI (Andersson et al. 2012). The software package IPOPT is used as solver for the nonlinear program (Wächter and Biegler 2006). The computational burden is not a limitation, as the optimization can be solved on a personal computer in less than a second for the proposed horizon length.

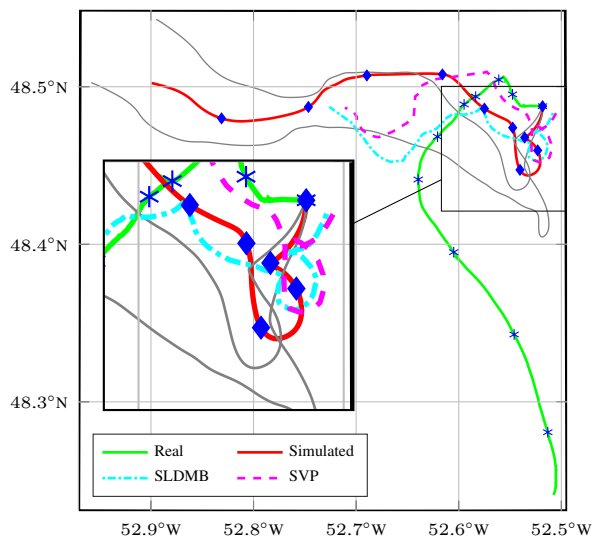


Figure 6.4: GPS measured (green) and simulated (red) Iceberg 1 trajectories as well as SLDMB and SVP drifter trajectories. Every 6 h a mark is set in the measured and simulated trajectories. The grey lines show the simulated iceberg trajectories when wind measured by the weather stations is used.

6.6 Simulation Study

The iceberg trajectories are simulated in the simulation study by using the iceberg drift model with constant parameters. The icebergs initial position is the first measured GPS position and the wind input is taken from the weather forecast.

6.6.1 Iceberg 1

The simulated Iceberg 1 diverges immediately from the measured iceberg trajectory (Fig. 6.4). The real iceberg drifts first towards the west, it follows for a period of 25 h approximately the underwater contour lines, before it changes drift direction and drifts towards south-east. The simulated iceberg drifts first south-westwards, makes a half circle to the east, and drifts afterward the westwards, towards the coastline. The coastline does not represent an active constraint in the simulation model; therefore, it is possible that simulated iceberg trajectories drift on land regions. This can be avoided by grounding the iceberg and stopping the simulation when the iceberg enters shallow water regions close to the coastline. Both measured current and predicted winds are directed approximately to the west. Consequently, those forces cannot explain the real iceberg trajectory. The influence of the wind force within the observation horizon is weak because the wind velocity is relatively small. The simulated iceberg trajectories change only

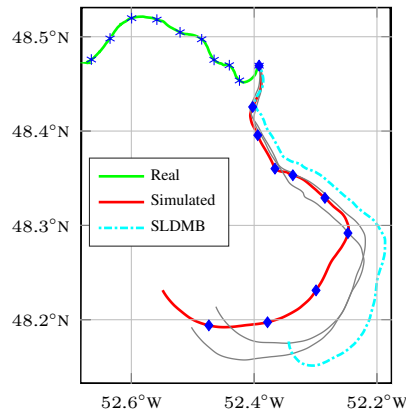


Figure 6.5: GPS measured (green) and with *SLDMB* current simulated (red) Iceberg 2 trajectories and *SLDMB* drifter trajectories. Every 6 h a mark is set in the measured and simulated trajectories. The grey lines show the simulated iceberg trajectories when wind measured by the weather stations is used.

slightly if wind measured at the weather stations is used (Fig. 6.4: grey lines).

6.6.2 Iceberg 2

The simulated iceberg trajectories of Iceberg 2 also diverge immediately from the measured iceberg trajectory (Fig. 6.5). The divergence is even stronger than for Iceberg 1. The real iceberg drifts westward, while the simulated iceberg trajectory drifts southwards the first 6 h and south-eastwards the next 24 h. Thereafter, it makes a turn and drifts westwards. The mean velocity of the simulated iceberg is twice as high as of the observed iceberg. Consequently, the overall trajectory of the simulated iceberg is twice as long as the one of the real iceberg. The use of measured winds from the weather stations changes only insignificantly the simulated iceberg trajectory compared to the iceberg trajectory where forecasted wind is used (Fig. 6.5: grey lines).

The simulated trajectory of Iceberg 2 can be improved by the current measurements of the SVP current drifter deployed at Iceberg 1 (Fig. 6.6). The same observation can be obtained if the data of the *SLDMB* current drifter deployed at Iceberg 1 is used. Iceberg 1 and 2 are about 9 km apart from each other at the beginning of the observations. It is, therefore, reasonable to assume that currents (15 m or surface current) provide a better proxy for current in the water column at Iceberg 2 than the surface current measured at Iceberg 2. In addition, the distance between SVP drifter and Iceberg 2 shortly after initialization is smaller than the distance between *SLDMB* drifter deployed at Iceberg 2 and Iceberg 2. In general, it can be expected that the current drifter closest to the iceberg provides the best

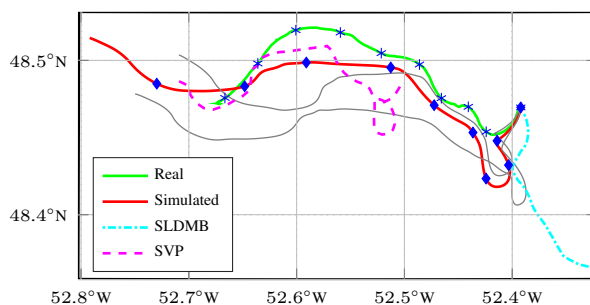


Figure 6.6: GPS measured (green) and with *SVP* current simulated (red) Iceberg 2 trajectories as well as *SLDMB* and *SVP* drifter trajectories. Every 6 h a mark is set in the measured and simulated trajectories. Grey lines show simulated iceberg trajectories if wind measured by the weather stations is used.

estimate of the current at the iceberg position. The overall direction of the iceberg trajectory is simulated correctly. However, there exists some discrepancy in time and place between observed and simulated iceberg trajectory. The simulated iceberg trajectory describes a half circle at the beginning of the simulation. Such a behavior cannot be observed for the real trajectory. As a consequence, the simulated iceberg trajectory has a delay of about 6 h to the observed trajectory. At the end of the observation horizon, a higher simulated iceberg velocity due to upcoming wind balances the delay. For this reason, the simulated and observed iceberg trajectories are only 860 m apart from each other after 54 h.

6.6.3 Discussion

The simulation study shows that the overall influence of wind measurements is small. This is a consequence of strong similarities between wind measurements and forecast, but surely also due to relatively weak winds during the observations. In contrast, the influence of the measured current is strong in the simulations. The measured surface or near-surface currents at the two icebergs differ significantly, even though the initial positions are close to each other. The simulations of the two icebergs with current measured at both icebergs do not correlate well with the observed iceberg trajectories. However, the measured currents are surface or near-surface currents, which are mainly wind driven and do not represent the whole current in the water column of the iceberg keel. Hence, it can be concluded that for iceberg drift simulations only surface current information is not enough and may even lead to erroneous forecasts. An improvement in the simulated trajectories of Iceberg 2 can be observed if the currents measured at Iceberg 1 are used in simulations. Consequently, it can be assumed that the current measured at Iceberg 1 is a better overall representation of the current at Iceberg 2 than the surface current measured at Iceberg 2. In order to further improve simulation and predic-

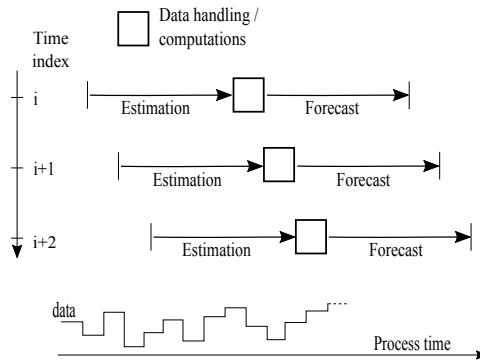


Figure 6.7: Estimation and forecast procedure with MHE.

tion with the given information it is necessary to update/adjust parameters in the iceberg model.

6.7 Estimation Study

If the measured and predicted forcing does not agree with the actual iceberg trajectory, it is important to use the available information to correct the forcing within the operational iceberg model to improve the simulation and forecast results. One may say that the ideal drifter to estimate the forcing on the iceberg is the iceberg itself. The estimation-forecast procedure is envisioned as follows (Fig. 6.7): In an MHE smoothing scheme, the measurements are used to estimate the state vector of the iceberg model. The state vector contains iceberg position, velocity and ancillary current. This state vector x_0 is given as initial condition to the forecast, which performs a forward simulation of the iceberg model. During the forecast the position and velocity of the iceberg changes with time, while the ancillary current is constant. This procedure is repeated as new measurements are received.

In the analysis it is assumed that the surface current measurements are available during the forecast. Current measurements are typically unavailable for operational iceberg drift forecasts, therefore current forecasts are used more often instead. If the time-varying ancillary current were known a priori, it would be possible to predict almost perfectly the iceberg drift trajectory. However, the ancillary current is not known a priori, but it is estimated as new measurements are received.

6.7.1 Forecast Performance Indices

In order to quantify the performance of the forecast at a specific time, the square root of mean squared distance between predicted $\bar{\mathbf{X}}$ and measured $\bar{\mathbf{X}}$ iceberg tra-

jectory is calculated

$$\zeta_N(t) = \sqrt{\frac{1}{N} \sum_{i=1}^N \|\tilde{\mathbf{X}}(t+i) - \bar{\mathbf{X}}(t+i)\|_2^2}, \quad (6.11)$$

where N is the length of the forecast period and t is the initial time of the forecast. The performance index (PI) for the whole observation horizon is the root mean square of ζ_N (6.11) with the same forecast horizon N

$$PI(N) = \sqrt{\frac{1}{M} \sum_{i=1}^M \zeta_N(t_i)^2}, \quad (6.12)$$

where M is the number of forecasts performed and t_i is the initial time of the forecast.

A discrepancy measurement between modelled and observed iceberg trajectories is the absolute velocity of the ancillary current. An overall discrepancy index (DI) is the root mean square of all calculated absolute velocities of ancillary currents

$$DI(N) = \sqrt{\frac{1}{M} \sum_{i=1}^M \|\mathbf{v}(t_i)\|_2^2}. \quad (6.13)$$

The most recently estimated ancillary current is used as ancillary current vector over the whole forecast horizon. The assumption is, therefore, that the ancillary current does not change during the prediction. As new measurements of the iceberg trajectory are received, the estimated ancillary current is updated and a new forecast is initialized. The overall forecast error is caused by discrepancy in the forecasted wind and current inputs as well as other model errors. However, the ancillary current gives a numerical value to the discrepancy in the iceberg model. Therefore, the difference between a new estimated (actual) ancillary current $\hat{\mathbf{v}}$ and the previously assumed (forecasted) ancillary current $\bar{\mathbf{v}}$ indicates the magnitude of the prediction error. This observation leads directly to the ancillary current performance index (API), which is strongly correlated with the average distance ζ_N (6.11)

$$API(t) = \sqrt{\frac{1}{N} \sum_{i=1}^N \|\bar{\mathbf{v}}(t+i) - \hat{\mathbf{v}}(t+i)\|_2^2}. \quad (6.14)$$

While the average distance ζ_N gives the outcome of the forecast, the API provides more an explanation for the error of the prediction. The advantage of evaluating

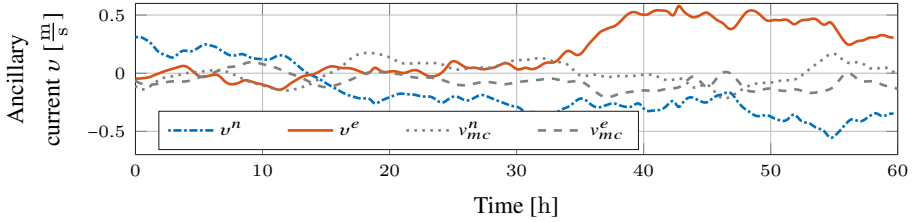


Figure 6.8: The ancillary current calculated with an MHE smoothing scheme (coloured) and the measured SVP current (grey) for Iceberg 1.

the forecast performance with the API , is that the average distance ζ_N can be directly influenced by the assumed ancillary current vector \bar{v} . The assumed ancillary current \bar{v} is an input to the forecast model and it is assumed constant during the forecast in this paper. However, other options like linearly decreasing or clockwise rotating ancillary currents could be used for forecasting iceberg trajectories. The API represents a direct measure to evaluate those options.

The root mean square of all API s is the *ancillary current performance prediction index* (APPI)

$$APPI(N) = \sqrt{\frac{1}{M} \sum_{i=1}^M API(t_m)^2}. \quad (6.15)$$

The $APPI$ is similar to the PI and gives an overall reason for the discrepancy in the forecasts.

6.7.2 Iceberg 1

Estimation of Ancillary Current

The ancillary current for Iceberg 1 is shown in Fig. 6.8. Small, consistently changing oscillations can be observed within the estimated ancillary current. Significant direction changes are detected around hour 15 and 38. An almost constant ancillary current is observed from the hours 20 to 35. If the ancillary current evolution was known a priori and used in simulation, the iceberg trajectory of Iceberg 1 could be almost perfectly simulated (Fig. 6.9). The difference between observed and simulated iceberg trajectory can be further reduced by tuning (selecting other process and measurement noise parameters). However, doing this may influence numerical conditioning of the MHE.

Forecast of Iceberg Trajectory with the Help of the Estimated Ancillary Current

In Fig. 6.10, several 12 h iceberg drift predictions with and without the use of the ancillary current are illustrated. The iceberg trajectories predicted with calcu-

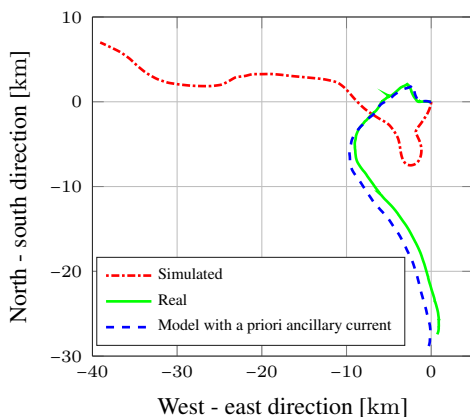


Figure 6.9: GPS measured (green) and simulated iceberg trajectory without ancillary current (red) as well as with ancillary current known a priori (blue) of Iceberg 1.

lated ancillary current (indicated as closed-loop) are compared with the trajectories forecasted without using the ancillary current (indicated as open-loop, since no feedback from estimates is used). The terminology *open-loop* and *closed-loop* is frequently used in process system engineering for control loops with feedback (closed-loop) and control loops without feedback (open-loop).

In open-loop, the iceberg drift model is reinitialized at the last measured iceberg position. The results indicate higher prediction performance by using the ancillary current. The improvement is especially substantial in the first few hours (short time horizons). For forecasts over longer horizons, the assumption of constant ancillary current over the forecast horizon is less correct and prediction performance decreases. However, significant improvements are noted if the ancillary current is almost constant over the forecast horizon (hour 20–35).

It should be emphasized that the use of ancillary current allows the prediction of wind induced direction changes, as it can be seen at the end of the observation horizon. Strong winds cause a clockwise loop, which is approximately predicted by the ancillary current set-up (last forecasted trajectory of closed-loop in Fig. 6.10).

The square root of mean squared distance between predicted and measured iceberg trajectory calculated with (6.11) decreases significantly in the closed-loop case (Fig. 6.11). Closed-loop predictions show considerably better performance compared to open-loop prediction in the short time forecasts (~ 1 h). The prediction error in closed-loop is reduced by 95%. A reason for the significant improvement is the almost constant ancillary current within a short time period. Consequently, the correction, performed by the ancillary current, remains almost constant and an almost correct current force is applied during the forecast. If the an-

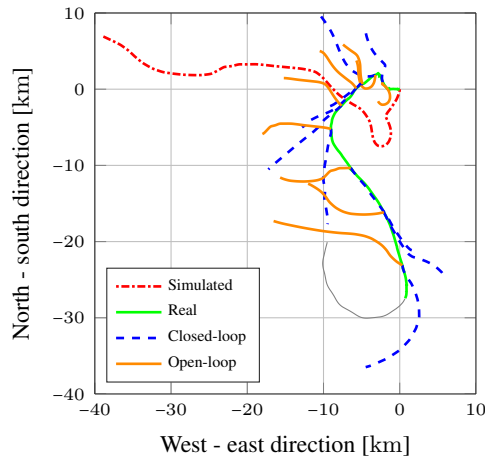


Figure 6.10: Closed-loop (blue) and open-loop (orange) 12 h predictions in 6 h intervals of Iceberg 1. The reference trajectories are the simulated iceberg trajectory (dotted) and the measured iceberg trajectory (solid). The grey line shows the measured iceberg drift for the first 12 h after the 60 h observation horizon.

cillary current is used for longer time predictions, the square root of mean squared distance (6.11) can be larger in the closed-loop case than in the open-loop case (\sim hour 12 in Fig. 6.11(b)). Those periods correspond to periods of strong changes in estimated ancillary current. Hence, the offset between predicted input forces and real forces, which is adapted with the help of ancillary current, changes. Nevertheless, the overall averaged prediction performance improves significantly in closed-loop. In addition, the predicted direction of the iceberg drift is correct at the beginning of each forecast.

In order to obtain the performance of the forecast for a specific horizon, the PI s (6.12) are calculated for different prediction horizons. In closed-loop, the PI reduces about 80 % in a six-hour forecast and about 70 % in a twelve-hour forecast. Even in a 24 h-forecast, the PI is reduced about 50 % (Table 6.1).

If improved information about the input forces is used, as for example the measured wind at the weather stations, the forecast will in general benefit from it. This applies especially for longer forecasts. For instance, in closed-loop the PI is for a 12 h forecast with forecasted wind 3315 m. This can be improved to 3060 m

Table 6.1: The PI (6.12) of Iceberg 1 for different prediction horizons N .

Horizon N [h]	1	3	6	12	24
Open-loop [m]	809	2399	4819	9799	20020
Closed-loop [m]	40	308	1026	3315	9723

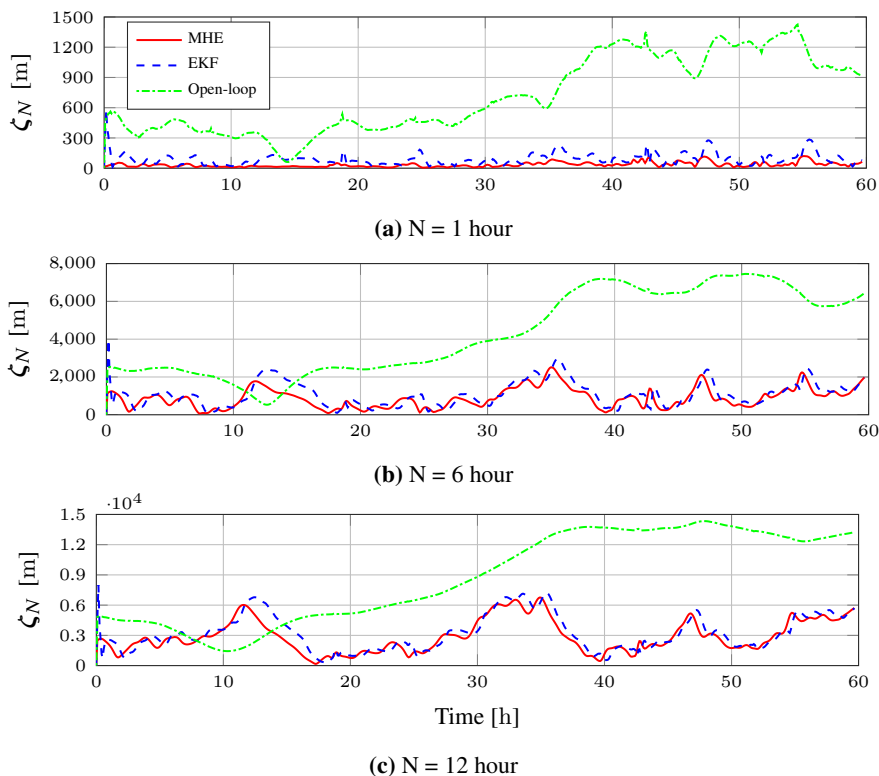


Figure 6.11: The square root of mean squared distance ζ_N (6.11) of closed-loop and open-loop case of Iceberg 1 are compared for different forecast horizons N . The ancillary current was calculated with a MHE and an EKF.

by using only measured wind data (during estimation and forecast). However, the measured wind is not available during forecasts. If, instead, forecasted wind is used during forecast and measured wind during estimation, the PI decreases to 3643 m. The differences in this example are relative small since the predicted and measured winds are similar. A change of input information between estimation and forecast step is not recommended, since it is detrimental to the forecast quality when estimating the ancillary current. The ancillary current is calculated for a specific combination of input forces to the model and it corrects for this input set-up. A change of the input set-up in the forecast will change the process noise, which is approximately represented by the ancillary current.

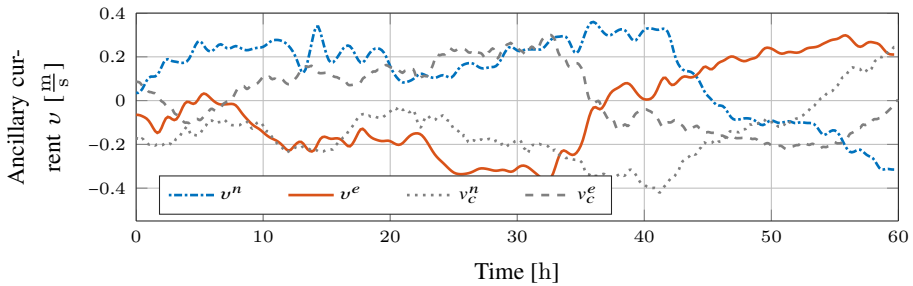


Figure 6.12: The ancillary current calculated with an MHE smoothing scheme and the measured SLDMB current for Iceberg 2.

6.7.3 Iceberg 2

Estimation of Ancillary Current

Fig. 6.12 shows the ancillary current for Iceberg 2 when the SLDMB surface current measurements at Iceberg 2 are used. The northern component experiences a significant change around hour 42. The eastern component experiences two small changes around hour 10 and 25 and a large change, similar to Iceberg 1, around hour 35. As already stated for Iceberg 1, it is expected that the forecast will especially improve in areas outside of large changes of ancillary current.

Forecast of Iceberg Trajectory with the Help of Estimated Ancillary Current

Fig. 6.13 displays a 12 h prediction in closed-loop and open-loop every 6 h. The closed-loop set-up prevents the predicted iceberg trajectories from having wrong directions at the beginning of the prediction, as it happens in the open-loop case. However, it is not guaranteed to be correct over a longer forecast horizon. It can happen that after already a relative short period the applied ancillary current is not correct any more and the predicted trajectory diverges from the observed one. For longer forecast horizons, this can cause a lower forecast accuracy with ancillary current than without (Fig. 6.14(c): Hour 42). However, those situations are not common. Hence, the PI (6.12) of the forecast with ancillary current is superior to the one without (Tab. 6.2).

The forecast of Iceberg 2 can be significantly improved if the measured SVP current at Iceberg 1 are used instead of the measured SLDMB surface current at Iceberg 2, as discussed in Section 6.6.2, cf. Fig. 6.5 and 6.6. The ancillary current indicates well which input combination is most suitable, since it represents a factor of discrepancy between modelled and observed iceberg trajectories. Fig. 6.15(a) shows the ancillary current estimated for Iceberg 2 when the SVP current measurements of Iceberg 1 are used. In addition, the absolute ancillary current of the SVP

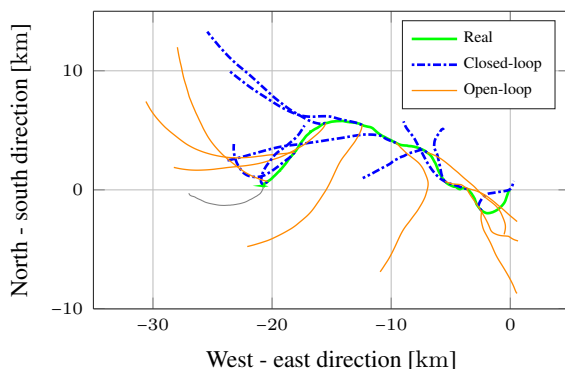


Figure 6.13: Closed-loop (blue) and open-loop (orange) 12 h prediction in 6 h intervals of Iceberg 2. The reference trajectory is the measured iceberg trajectory (solid). The grey line shows the measured iceberg drift for the first 12 h after the 60 h observation horizon.

case (dashed red line) and SLDMB case (solid black line) is shown in Fig. 6.15(b). The absolute ancillary current with SVP current is most of the time lower than the ancillary current with SLDMB current. The DI (6.13) for the case with SLDMB current is 0.2936 m s^{-1} and with SVP current 0.1521 m s^{-1} . This indicates that the SVP current is superior to the SLDMB current for open-loop simulations of Iceberg 2. However, the improvement in closed-loop is by far smaller than for the open-loop case (Tab. 6.3 in comparison to Tab. 6.2). While in open-loop the PI approximately halves for all prediction horizons, the improvements in closed-loop for short-term forecasts are small and increase only for longer forecasts (longer than 6 h).

Again, this observation is connected to the parameter estimation scheme presented here. It is expected that the estimated ancillary current is able to compensate for poor quality input for short enough forecasts. Therefore, the prediction of the iceberg trajectory with the help of the ancillary current will be in a certain range from the real drift, which is defined by the maximum possible change of ancillary current within the prediction horizon. This motivated the introduction of the API (6.14). Fig. 6.16 shows the API for two forecast horizons for both considered input combinations of Iceberg 2. The square root mean squared distance ζ_N (6.11)

Table 6.2: The PI (6.12) of Iceberg 2 for different prediction horizons N , when $SLDMB$ current is used in the forecasts.

Horizon N [h]	1	3	6	12	24
Open-loop [m]	606	1801	3589	7104	13801
Closed-loop [m]	36	295	1053	3678	11831

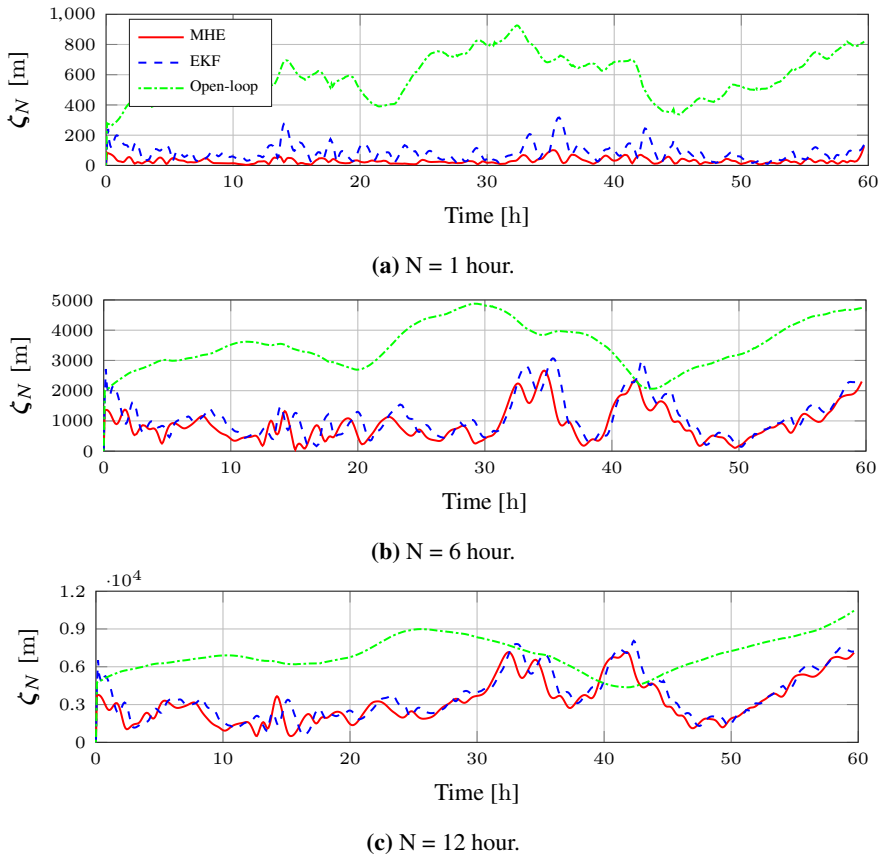
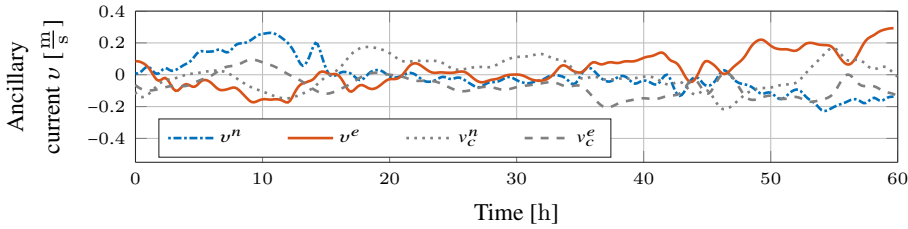


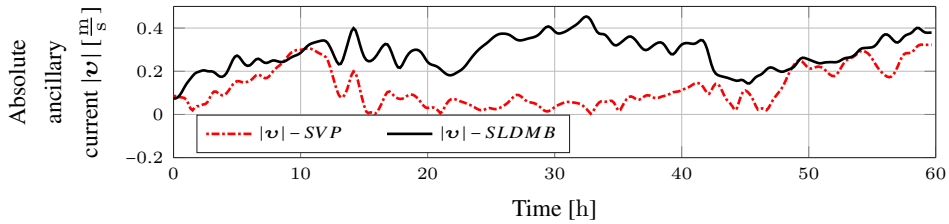
Figure 6.14: The square root of mean squared distance ζ_N (6.11) between closed-loop and open-loop case of Iceberg 2 are compared for different forecast horizons N . The ancillary current was calculated with a MHE and an EKF, and as current input the SLDMB current was used.

in Fig. 6.14(c) and the API_{SLDMB} in Fig. 6.16(b) have a similar evolution, since both values are strongly connected to each other. The API for a 1 h forecast (Fig. 6.16(a)) shows strong oscillations and sudden changes. Both API s are comparable in magnitude. The $APPI$ for the one hour forecast is 0.0469 m/s with SLDMB current and 0.0462 m/s with SVP current. Both values are similar as expected, since the PI is also very similar (Tab. 6.2 and 6.3). However, for longer predictions the $APPI$ is significant lower for the SVP case (12 h: SVP = 0.1298 m s^{-1} , SLDMB = 0.2144 m s^{-1}), which indicates in average a better performance of the SVP case.

However, there are periods where the SLDMB case is superior to the SVP case. Those periods correlate to periods where the API of the SLDMB case is smaller than the one of the SVP case.



(a) The ancillary current when SVP current at Iceberg 1 is used. The grey lines show the measured current.



(b) Absolute ancillary current of SVP case (dashed red) and SLDMB case (solid black).

Figure 6.15: Ancillary current calculated with a MHE smoothing scheme for Iceberg 2 with SVP current.

6.7.4 Comparison between chosen Design and Estimation of Air and Water Drag Coefficient

In order to validate the discussion in Section 6.3, air and water drag coefficients are estimated with the MHE and EKF instead of the ancillary current. The coefficients are constrained between [0.01, 2.5], which are physically reasonable values for the coefficients (Turnbull et al. 2015).

Iceberg 1

The value of the estimated drag coefficients are both at the lower boundary of 0.01 for most of the time (Fig. 6.17). The performance of the forecast decreases significantly, even though some improvement compared to the open-loop case can be observed (Tab. 6.4 and Fig. 6.18). The performance decrease is explained by a low sensitivity of the model output to changes of the water and air drag coefficients

Table 6.3: The PI (6.12) of Iceberg 2 for different prediction horizons N, when SVP current is used in the forecasts.

Horizon N [h]	1	3	6	12	24
Open-loop [m]	314	955	2042	4818	10521
Closed-loop [m]	40	302	949	2897	7001

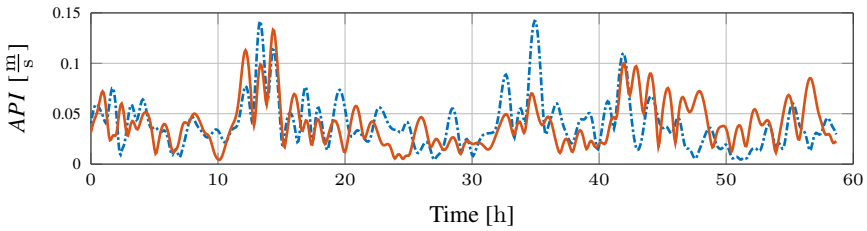
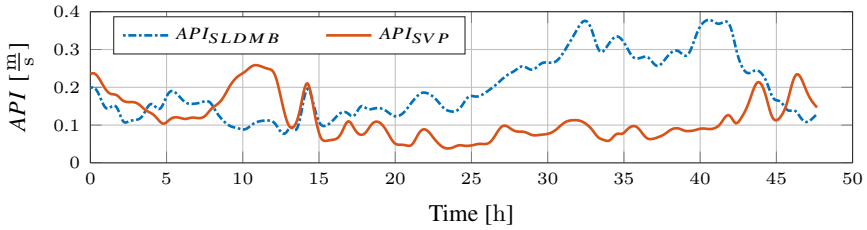
(a) $N = 1$ hour.(b) $N = 12$ hour.

Figure 6.16: The API (6.14) for prediction of trajectory of Iceberg 2 with SLDMB current and SVP current for different prediction horizons.

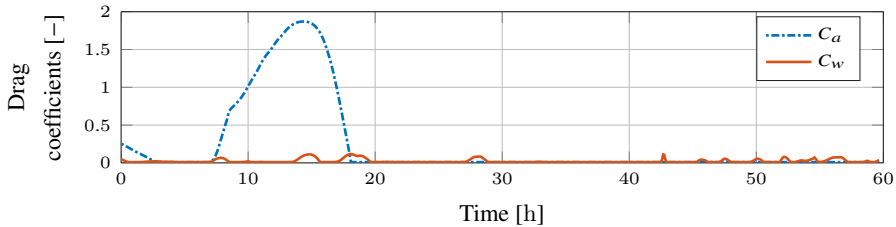


Figure 6.17: Estimated drag coefficients for Iceberg 1.

(Sec. 6.3.2). Without constraints on the drag coefficients, a similar performance as with the ancillary current can be achieved in a 1 h forecast. However, the performance decreases significantly for longer prediction horizons. In addition, negative values for the drag coefficients can be obtained, which is non-physical.

Iceberg 2

Fig. 6.19 shows the MHE and EKF results for the drag coefficients of Iceberg 2 when the SVP current of Iceberg 1 is used as current input. Constraints can be easier and more directly included in the MHE than in the EKF calculations. Furthermore, when estimating drag coefficients the estimation model is more non-linear. Nonlinearities can be better handled by the MHE than by the EKF. For these reasons, the two estimators have larger differences when drag coefficients

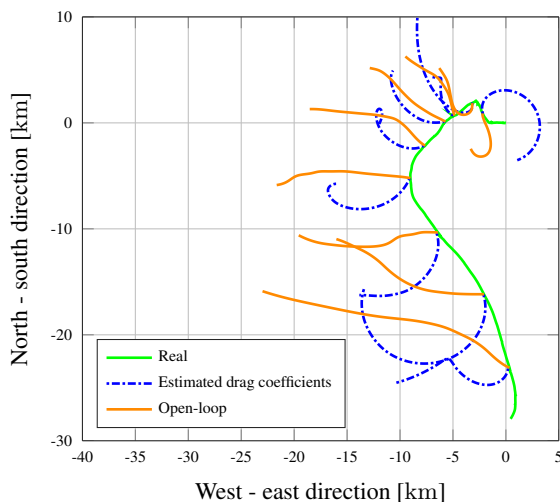


Figure 6.18: Twelve hour forecasts with estimated drag coefficients (blue) and open-loop (orange). Reference trajectory is the measured iceberg trajectory (solid).

are estimated than in the case when ancillary currents are estimated.

During the 60 h observation, the average values of the MHE calculated air and water drag coefficients are $C_a = 0.41$ and $C_w = 0.20$, while the EKF calculates average values of $C_a = 0.48$ and $C_w = 0.51$. The larger difference between both estimators in water drag is also caused by larger nonlinearities of the water drag force compared to the air drag force.

Fig. 6.20 shows the drag coefficients for Iceberg 2 where the SLDMB current of Iceberg 2 is used. The average air drag is $C_a = 1.19$ and the average water drag is $C_w = 0.05$. The difference between the calculated drag coefficients with SVP current (Fig. 6.19) and with SLDMB current (Fig. 6.20) is large. However, the interpretation of the estimated drag coefficients is difficult. They do not reflect a specific characteristic of the iceberg itself but of the used input forces. The air drag coefficient is on the upper boundary from hour 16 to hour 38, while the water drag coefficient is small. This may indicate that during this period the wind force is

Table 6.4: The PI (6.12) in 1, 6 and 12 h forecast with estimated drag coefficients.

Horizon [h]	1	6	12
PI [m]	305	3013	7040
Reference (Tab. 6.1)			
PI - Open-loop [m]	809	4819	9799
PI - Closed-loop [m]	40	1026	3315

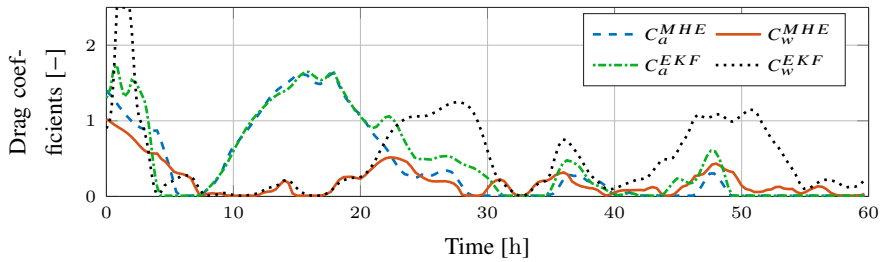


Figure 6.19: Estimated drag coefficients using MHE and EKF for Iceberg 2 with SVP current.

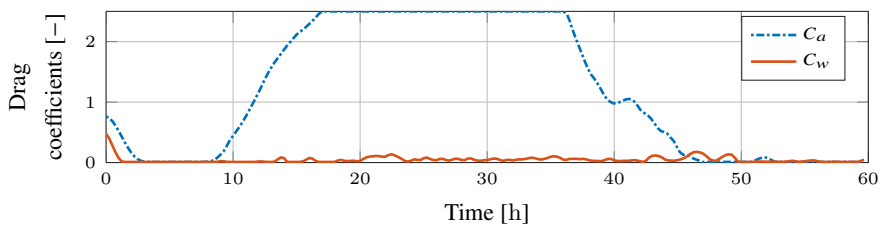


Figure 6.20: Estimated drag coefficients for Iceberg 2 with SLDMB current.

more strongly prioritised by the prediction scheme to explain the iceberg motion. Nonetheless, it cannot be concluded that the iceberg is mainly wind-driven, since the overall wind force on the iceberg is still small. Instead, it can be deduced that the iceberg is current-driven, but the current input is wrong. As a consequence, it is beneficial for the optimizer to reduce this wrong force and amplify another to reduce the error.

6.8 Discussion

In the estimation study, the ancillary current is estimated for two icebergs. The square root of mean squared distance ζ_N , represented by the PI , can be reduced by using the ancillary current for both icebergs compared to the open-loop case. The ancillary current allows increasing significantly the accuracy of the prediction of the iceberg trajectory in short forecasts. Moreover, improvements for longer forecasts can also be observed. However, it should be emphasised that the open-loop case using only the near surface currents is a low standard against which to evaluate the closed-loop model. Measured current profiles or current forecasts from ocean models, the latter is often available during offshore operations, would probably improve the quality of the used input information, and may reduce the improvements offered by the closed-loop model.

It is illustrated that improved input information will ultimately lead to an improved forecast. However, one should use consistent (the same type of) inputs in the estimation and forecast process, since the estimated ancillary current corrects errors in the inputs that are used in the estimation process. Furthermore, it is illustrated how the ancillary current can be used to evaluate different input sources. For example, if two different wind forecasts are available the one with the smallest absolute ancillary current represents best the real wind situation at the iceberg and will most probably also generate the best open-loop forecast. However, this cannot be guaranteed over the whole forecast horizon.

The ancillary current can be a good tool to compare different current inputs. Furthermore, the ancillary current may be a good starting point for investigating whether available current information is useful for the iceberg forecast. A large ancillary current can indicate that the current information is error-prone and that it should be excluded from the forecast.

The forecast quality by use of ancillary current, on the other hand, is strongly correlated with the *API* and the *APPI*. These indices express on the one hand the change of discrepancy between simulated and observed iceberg trajectory and on the other hand they can be used to evaluate directly different options of predicted ancillary current trajectories used in the forecast.

An important observation for the forecast with ancillary current is that the ancillary current can correct the overall discrepancy between real iceberg and observed iceberg caused, for example, by erroneous inputs. Such biased inputs are not only observed when surface drifters are used but also, for example, in current forecasts from ocean models (Eik 2009). As long as the discrepancy stays the same, the assumption of constant ancillary current is correct and the forecast scheme produces good quality forecasts.

The approach of estimating an ancillary current is compared to estimation of drag coefficients, which has been suggested in previous works. The adjustment of drag coefficients improved the forecast marginally and significantly less than using ancillary current. Moreover, the physical meaning of the estimated drag coefficients is lost and interpretations should be done with care.

6.9 Conclusion

This chapter proposed the concept of an estimated ancillary current to correct for discrepancy between observed and simulated iceberg trajectories. It was discussed why an added current force is superior to other possible corrections, like correction of the drag coefficients. A case study was performed and the proposed correction scheme was tested on two real iceberg trajectories. In both cases, the forcing on the iceberg and the iceberg geometry were uncertain and produced large discrepancies between predicted and actual iceberg trajectories in simulations. Suitable

performance indices were introduced to give numerical values for the uncertainties in the forcing on the iceberg, as well as for the forecast performance.

The ancillary current is a suitable variable to express the process noise and can correct for discrepancy between simulated and observed iceberg trajectories. The calculation of the ancillary current was performed by an optimization-based MHE. It was shown that a similar performance can be achieved with less complicated estimators, like the EKF. However, that is a trade-off between performance and complexity.

It was shown that the iceberg forecast can be improved with the help of the ancillary current. The improvement was especially large in short-term forecast or in cases when the discrepancy was almost constant. However, the improvement usually decreased for longer predictions horizons. The relative improvement by using the ancillary current was large in the two case studies, since the input forces were to a high degree uncertain and erroneous. It is believed that the improved forecast performance with the proposed set-up will carry over to other cases, for example, where measured current profiles or currents from ocean models are used.

Chapter 7

The Inertial Current Forecast Scheme

This chapter is based on PAPER F ([Andersson et al. 2016b](#)).

An input estimation problem to distinguish between an oscillating and a non-oscillating input is considered. This problem can be encountered in the estimation of iceberg motions, and a moving horizon estimator is proposed as a solution. In several simulation examples, it is shown that the moving horizon estimator can solve the considered estimation problem and is superior to an extended Kalman filter. In a second part of the chapter, the proposed estimation scheme is successfully tested on a real iceberg trajectory with the purpose to capture the forces on the iceberg correctly and use this to forecast the iceberg drift trajectory. The forecast results with the proposed scheme are promising since it produces small forecast errors and avoids including highly uncertain current information, which may be a disadvantage of the ancillary current forecast scheme (Chapter 6).

The inertial current forecast scheme is also categorised as a *hybrid* Iceberg Drift Forecast Algorithm, since it combines the dynamic iceberg drift model with statistical methods.

7.1 Introduction

This chapter deals with the problem of nonlinear input estimation to distinguish a non-oscillating from an oscillating part of an indirectly measurable input signal. The oscillation itself can have non-constant means and changing amplitudes. Oscillations are present in many processes, from chemical engineering to medical applications and maritime processes ([Miao and Seborg 1999](#), [Taylor et al. 1998](#), [De Young and Tang 1990](#)). In the signal processing literature the topic

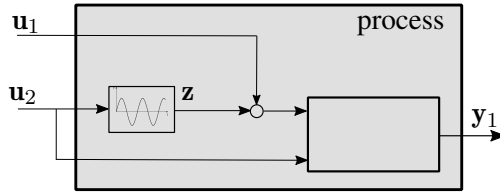


Figure 7.1: Representation of the considered problem. The process is the grey box.

has received considerable attention with frequency tracking of stationary and non-stationary signals (Bittanti and Savaresi 2000, Hajimolahoseini et al. 2012, Streit and Barrett 1990) and oscillation characterisation (Srinivasan et al. 2007). The correct identification of the oscillation can be vital to processes and increase the performance of the considered applications (Huang et al. 1998). However, in many cases, it is assumed that the oscillating signal can be directly measured. When that is not feasible, the input of the process has to be estimated (Coreless and Tu 1998). In a control loop, a central role is to reject periodic disturbances (Serrani 2006). However, knowledge of oscillations can also be used to enable system prediction (Stone et al. 1996) and, while not detected, oscillations will decrease prediction performance.

7.2 Problem Formulation

The problem considered in this chapter is a nonlinear input estimation problem (Fig. 7.1). The problem consists of two inputs and measured output. The input u_1 is non-oscillating and unknown. A signal is characterised as unknown if no information about the magnitude of the signal is available. Nonetheless, information of rate-of-change of the signal may be available, such that the rate-of-change can be constrained. The input u_2 is non-oscillating and uncertain. Uncertain in this context means that low-frequency information about the input u_2 is available, such that the magnitude of the signal is known within some range. However, the low-frequency information is not sufficient to successfully calculate the oscillation z of the process, which is caused by input u_2 .

The internal state z has a non-zero mean as long as the forcing u_2 is present. However, as the oscillation develops without additional excitation, a zero mean is approached. The output y_1 is frequently measured with relative small measurement noise. The goal of the input estimation process is to estimate u_1 , u_2 , and the internal variable z , while especially important is the distinction between the non-oscillating part u_1 and oscillating part z .

The problem can be formulated as

$$\dot{\mathbf{x}} = \mathbf{f}(\mathbf{x}, \mathbf{u}) \quad (7.1a)$$

$$\mathbf{y} = \mathbf{h}(\mathbf{x}, \mathbf{u}), \quad (7.1b)$$

where \mathbf{x} are the differential states and \mathbf{u} is the input. The internal state \mathbf{z} can be represented by

$$\dot{\mathbf{z}} = \mathbf{S}\mathbf{z} + \mathbf{B}(\mathbf{u}), \quad (7.2)$$

where the system is stable and has complex eigenvalues. The frequency of the oscillation is known and given by f . These kind of problems can frequently be encountered in maritime applications. Ocean drifters are directly influenced by wind and indirectly via wind-induced inertial current. An example of such a process is iceberg drift.

7.2.1 Motivation for Using the Moving Horizon Estimator

The estimation problem is difficult. Not only is input \mathbf{u}_1 not known and input \mathbf{u}_2 uncertain, but the model for the internal state \mathbf{z} (7.2) and the overall process model (7.1) are also uncertain. Key to a successful estimation of the considered problem is to include as much prior knowledge as possible. The process, measurement, and state constraints can be easily included into a moving horizon estimator (MHE) (Kühl et al. 2011). Moreover, it provides improved state estimation and greater robustness to both poor guesses of the initial state and tuning parameters compared to the extended Kalman filter (EKF) (Sec. 3.1.2) (Haseltine and Rawlings 2005). The MHE uses a time series of past data, such that the full influence of the excited oscillation can be considered. This is believed to be an advantage to distinguish between the oscillating and non-oscillating parts of the input. Consequently, the MHE was chosen to approach the estimation problem (Sec. 3.1.1).

7.3 Case Study

Iceberg drift estimation is an example of the problem described in Section 7.2. An iceberg is influenced by wind, mean current, and wind-induced inertial current (Fig. 2.2).

Mechanistic dynamic iceberg models are based on a momentum equation to describe the change of velocity of the iceberg mass

$$m\mathbf{a} = \mathbf{f}_{\text{cor}}(\mathbf{x}) + \mathbf{f}_a(\mathbf{u}) + \mathbf{f}_c(\mathbf{x}, \mathbf{u}) + \mathbf{f}_p(\mathbf{x}, \mathbf{u}), \quad (7.3)$$

where m is the iceberg mass, \mathbf{a} is the acceleration of the iceberg and \mathbf{f}_{cor} , \mathbf{f}_a , \mathbf{f}_c , and \mathbf{f}_p are the Coriolis force, the air drag force, the water drag force and pressure gradient term, respectively (Sec. 2.3).

Inertial current represents one part of the current force that drives the iceberg and is usually initiated by the wind. Afterward, it can be seen as a freely oscillating

system. The most common source is an abrupt wind change, typically associated with a passage of a weather front (De Young and Tang 1990).

The inertial current oscillation of the ocean can be approximated by using a simple model of forces by the wind stress (Pollard and Jr. 1970) as

$$\dot{\mathbf{z}} = \mathbf{B}(\mathbf{u}) + f\mathbf{k} \times \mathbf{z} - c\mathbf{z}, \quad (7.4)$$

where \mathbf{z} is the inertial oscillation velocity, $\mathbf{B}(\mathbf{u})$ is the wind excitation and c is a decay factor. For typically observed oscillations in the ocean, the dissipation time scale is roughly 4-6 days. The wind excitation can be expressed as

$$\mathbf{B}(\mathbf{u}) = C_d p_3 |\mathbf{u}_2|^2 \begin{pmatrix} \cos \phi_a \\ \sin \phi_a \end{pmatrix}, \quad (7.5)$$

where C_d is a dimensionless drag coefficient, p_3 a parameter, ϕ_a the wind direction, and \mathbf{u}_2 the wind velocity. The drag coefficient is given by Large and Pond (1981) as

$$C_d = 1.2 \cdot 10^{-3}, \quad 4\text{m/s} \leq |\mathbf{u}_2| < 11\text{m/s} \quad (7.6a)$$

$$C_d = (0.49 + 0.065|\mathbf{u}_2|) \cdot 10^{-3}, \quad 11\text{m/s} \leq |\mathbf{u}_2| \leq 25\text{m/s}, \quad (7.6b)$$

where the wind speed is given at the height of 10 m.

7.3.1 Estimation Model

The model (7.4) has to be slightly adapted before using it for estimation. The discontinuous drag coefficient (7.6) is approximated by

$$C_d = (1.2 + 0.065(|\mathbf{u}_2| - 11)) \frac{1}{1 + e^{-2(|\mathbf{u}_2| - 11)}} 10^{-3}, \quad (7.7)$$

which provides a sufficiently accurate approximation for our objectives. In addition, it is assumed that the lower boundary for the constant drag coefficient (7.6) is a wind velocity of 0 m/s. Even though Yelland and Taylor (1996) showed an increase of the drag coefficient at lower wind velocities, the overall error produced with the assumption is negligible.

The model is augmented with the mean current \mathbf{u}_1 and wind velocity \mathbf{u}_2 to be able to estimate the inputs. Furthermore, it is assumed that the augmented states are constant. This assumption is not strictly true, since both mean current and wind velocity change. However, the measurement frequency is high enough such that the error introduced by this assumption is small.

The iceberg position (\mathbf{y}_1) is measured in the process. Furthermore, the approximate magnitude of the wind velocity (\mathbf{u}_2) is given by the wind forecast, which is given to the estimator as an additional measurement. Estimated are the iceberg

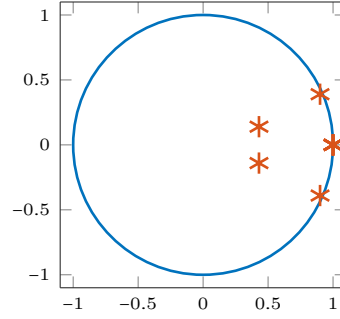


Figure 7.2: Eigenvalues of the linearised system matrix (7.9).

position and velocity as well as the mean current (\mathbf{u}_1), the oscillating inertial current (\mathbf{z}), and the wind velocity (\mathbf{u}_2) (Fig. 7.1). The resulting estimation model has 10 states, which include iceberg position (x_1, x_2), iceberg velocity (x_3, x_4), mean current (x_5, x_6), inertial current (x_7, x_8), and wind velocity (x_9, x_{10}),

$$\dot{x}_1 = x_3, \quad (7.8a)$$

$$\dot{x}_2 = x_4, \quad (7.8b)$$

$$\dot{x}_3 = f(x_6 + x_8 - x_4) + \frac{1}{m} \left[p_1 \sqrt{(x_9 - x_3)^2 + (x_{10} - x_4)^2} (x_9 - x_3) + p_2 \sqrt{(x_5 + x_7 - x_3)^2 + (x_6 + x_8 - x_4)^2} (x_5 + x_7 - x_3) \right], \quad (7.8c)$$

$$\dot{x}_4 = -f(x_5 + x_7 - x_3) + \frac{1}{m} \left[p_1 \sqrt{(x_9 - x_3)^2 + (x_{10} - x_4)^2} (x_{10} - x_4) + p_2 \sqrt{(x_5 + x_7 - x_3)^2 + (x_6 + x_8 - x_4)^2} (x_6 + x_8 - x_4) \right], \quad (7.8d)$$

$$\dot{x}_5 = 0, \quad (7.8e)$$

$$\dot{x}_6 = 0, \quad (7.8f)$$

$$\dot{x}_7 = \left[1.2 + 0.065(\sqrt{x_9^2 + x_{10}^2} - 11) \frac{1}{1 + e^{-2(\sqrt{x_9^2 + x_{10}^2} - 11)}} \right] 10^{-3} (x_{10}^2 + x_9^2) \cos(\text{atan2}(x_{10}, x_9)) p_3 - f x_8 - c x_7, \quad (7.8g)$$

$$\dot{x}_8 = \left[1.2 + 0.065(\sqrt{x_9^2 + x_{10}^2} - 11) \frac{1}{1 + e^{-2(\sqrt{x_9^2 + x_{10}^2} - 11)}} \right] 10^{-3} (x_{10}^2 + x_9^2) \sin(\text{atan2}(x_{10}, x_9)) p_3 + f x_7 - c x_8, \quad (7.8h)$$

$$\dot{x}_9 = 0, \quad (7.8i)$$

$$\dot{x}_{10} = 0, \quad (7.8j)$$

where p_1, p_2, p_3, m, c , and f are model parameters.

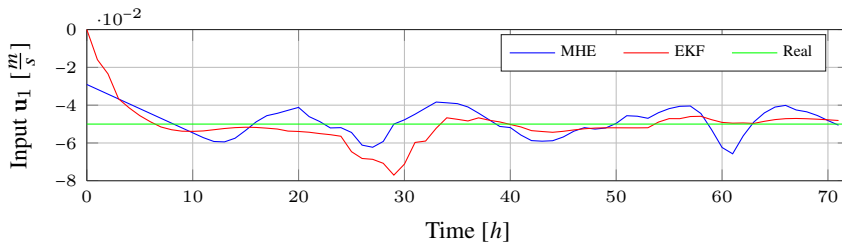


Figure 7.3: Estimation result of u_1 if input u_2 is known and u_1 constant.

The MHE and EKF problems are implemented in the Python programming language and solved using the open-source software tool CASADI (Andersson et al. 2012). The software package IPOPT is used as a solver for the nonlinear program (Wächter and Biegler 2006). The computational burden is not a limitation, as the optimisation problem can be solved on a personal computer in less than a second.

7.3.4 Estimation with the Simulated Model

The first results are given based on simulated iceberg trajectories with known forces, to see the ability of the estimation schemes to estimate the force terms. Both dimensions are simulated and estimated, but for ease of illustration, only the results of one dimension are presented here.

Input u_1 is not known and constant while u_2 is known

The estimator does not know the input u_1 and initial conditions of the other states, as well as the input u_2 , are known. The goal is to estimate the input u_1 correctly.

Both EKF and MHE estimate u_1 correctly (Fig. 7.3). However, the error produced by the MHE is smaller and is also true for the other states of the system. Moreover, the EKF changes the value of the known input u_2 considerably. Nevertheless, both estimators approximate the system states correctly. Furthermore, uncertainty in the initial condition of the internal state z does not decrease the performance of the estimators.

Input u_1 is not known and time-varying while u_2 is known

The overall design stays the same. However, the input u_1 is no longer constant, but describes a ramp function.

The MHE tracks the time-varying signal, while the EKF detects the change delayed (Fig. 7.4). The error in variable u_1 is smaller compared to example 1 (Sec. 7.3.4), and the overall performance of the MHE is superior to the one of the EKF. For the EKF, it was only possible to find tunings, which either filters the dynamics of the system strongly, such that the internal state z is not oscillating as all

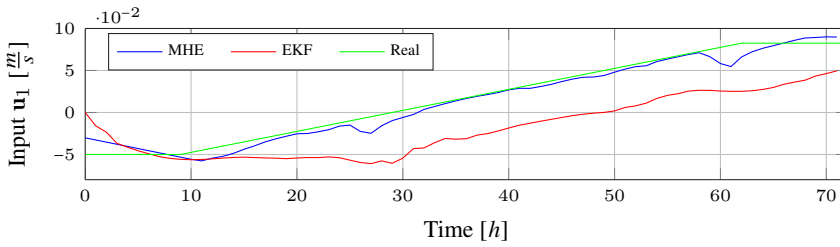


Figure 7.4: Estimation result of \mathbf{u}_1 if input \mathbf{u}_2 are known and \mathbf{u}_1 is time varying.

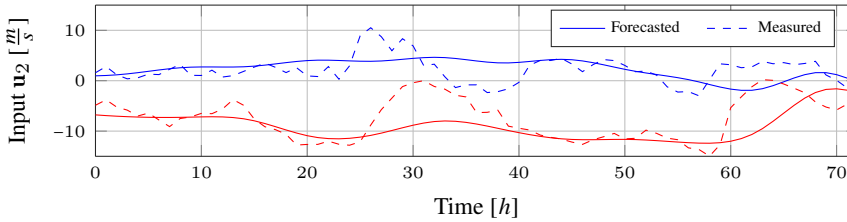


Figure 7.5: Both dimensions of real input \mathbf{u}_2 (dashed) and input \mathbf{u}_2 used during estimation (solid).

estimates have a delay, or captures the dynamics of the system while introducing stronger oscillations into the internal state \mathbf{z} . The former type of tuning is used in the presented results in this example.

Input \mathbf{u}_1 is not known and constant, and \mathbf{u}_2 is uncertain

Only the approximate magnitude of input \mathbf{u}_2 is unknown. To produce a realistic example, measured wind and forecasted wind for the same location are used (Fig. 7.5). The wind is well forecasted. However, significant errors between forecasted and measured wind in one or both dimensions can be observed from 25 h to 40 h and 60 h to 70 h. The measured wind is used to simulate the system, while the forecasted wind is used during the estimation.

Both estimators show relatively poor performance in estimating \mathbf{u}_1 and \mathbf{u}_2 (Fig. 7.6). The estimators cannot distinguish well between the non-oscillating inputs \mathbf{u}_1 and \mathbf{u}_2 . On the other hand, the oscillation of the state \mathbf{z} is well captured.

Input \mathbf{u}_1 is not known and time-varying and \mathbf{u}_2 is uncertain

The same design as in the previous section (Sec. 7.3.4) is used. However, the input \mathbf{u}_1 describes a ramp function as in Section 7.3.4.

The change in input \mathbf{u}_1 is detected by both estimators (Fig. 7.7). However, the MHE detects the change faster, while the EKF shows a delayed reaction. Large errors and substantial changes of the input variable \mathbf{u}_2 (Fig. 7.5) not captured

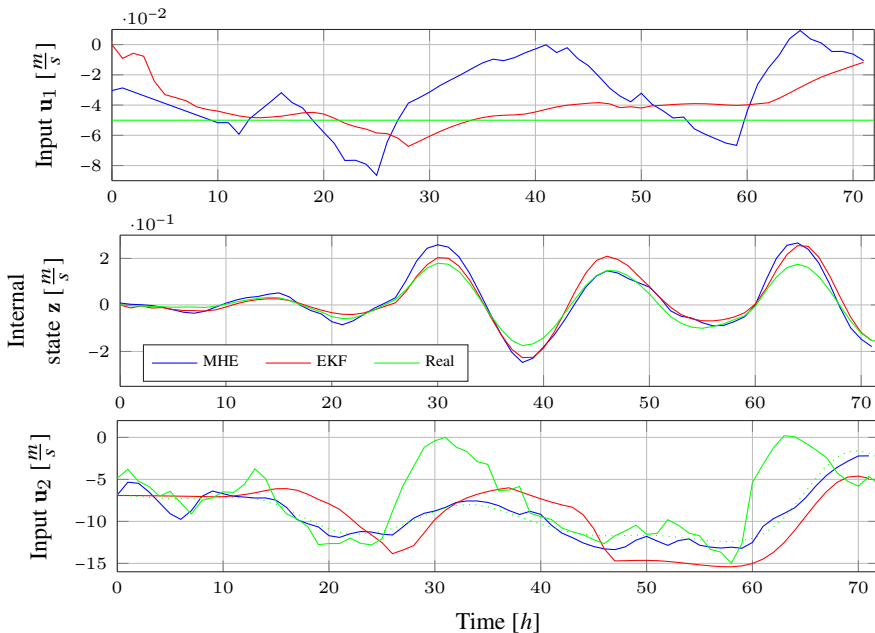


Figure 7.6: Estimation results for input u_1 and u_2 as well as internal state z , if u_2 is uncertain and u_1 constant.

by the forecast causes an error in the MHE estimate of u_1 . Nevertheless, the error induced by the strong dynamics in u_2 are recovered by the MHE. On the one hand, the EKF is less influenced by these strong dynamics. On the other hand, the EKF smooths the dynamics of u_1 strongly. Consequently, changes in the system are detected with delay. Furthermore, the EKF smooths the derivative of the measured output more strongly than the MHE (Fig. 7.7), which is a disadvantage for the forecast.

Discussion

The dynamics of the system are better captured by the MHE as tuning is central to this problem. The advantage of the MHE, besides handling a time series of data, is the simple incorporation of constraints on states and process noise. For this reason, the MHE avoids oscillations in input u_1 and at the same time, captures the dynamics of the process well. The EKF cannot avoid oscillations in the input u_1 without filtering the dynamics of the process strongly. As a result, changes in the dynamics in u_1 are detected with delays.

The estimator cannot completely correct large errors between expected and real inputs u_2 . Both distribute detected motion change across all estimated states. Nevertheless, the MHE detects the dynamics of the process well and can distinguish

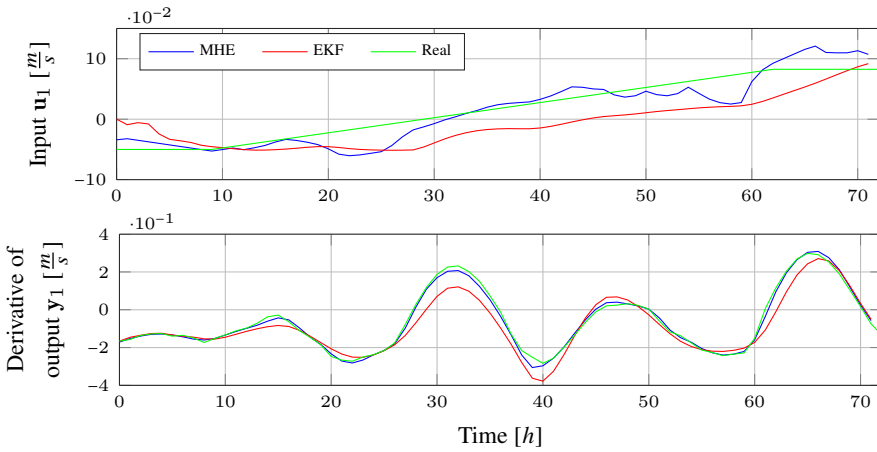


Figure 7.7: Estimation results for input u_1 and the derivative of the output y_1 , if u_2 is uncertain and u_1 time varying.

between oscillating and non-oscillating input signals. Moreover, less uncertain input data u_2 improves the estimate of all states.

7.3.5 Estimation with Real Data

The proposed estimation scheme, with the same setup as described in the previous section, was applied to real iceberg drift data, and the results are presented in this section.

Considerable uncertainty in model parameters, such as the iceberg geometry and decay factor of the inertial current, make the problem complicated. Furthermore, the iceberg and inertial models are only approximations of the real process.

The iceberg studied in this section is Iceberg 4 (Sec. 4.1.3) specifically covering the first 72 h of the iceberg drift data after the GPS beacon deployment.

Wind information was obtained by a local weather forecast service (Amec Foster Wheeler), and the weather forecast location and initial iceberg position were approximately 80 km apart.

The measurement frequency of the iceberg position was 1 h. To receive the necessary samples for the wind forecast, which was supplied with a 6 h frequency, the forecast points were interpolated. The initial state for both estimators was taken to be $x_0 = [0, 0, x_{3_0}, x_{4_0}, 0, 0, 0, 0, u_{1_0}^n, u_{1_0}^e]^T$, where the iceberg velocity $[x_{3_0}, x_{4_0}]^T$ was calculated from the first two position measurements.

Estimation

The estimated and measured iceberg velocities are shown in Fig. 7.8. Both estimators well compensate existing measurement noise. As already seen in the previous

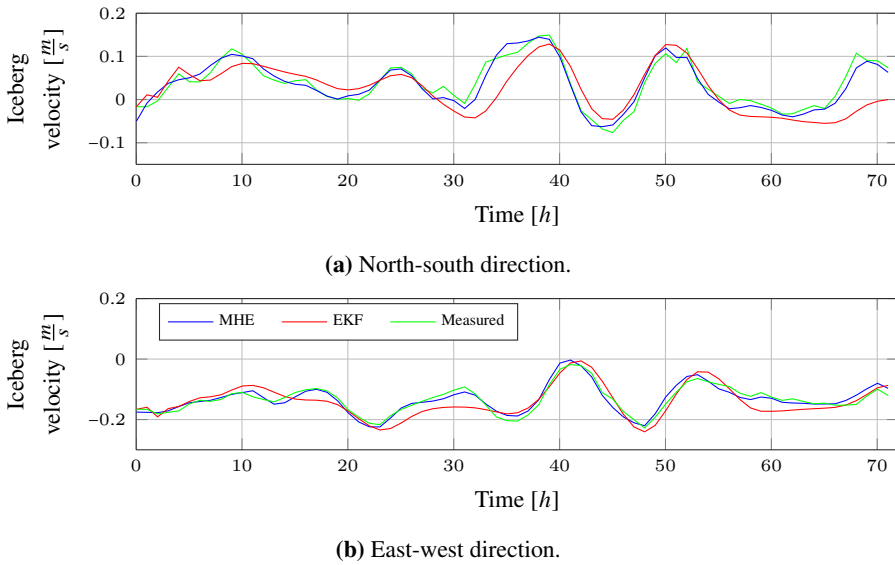


Figure 7.8: Iceberg velocity results with MHE (blue) and EKF (red). As reference the unfiltered measured iceberg velocity (green) is included.

section, the reaction of the EKF with the chosen tuning is delayed. Differences between MHE and EKF can also be observed in the estimated variables of mean current, wind velocity, and inertial current (Fig. 7.9). The first 12 h of the MHE estimates are smoothed meaning that it shows the MHE estimate at 12 h after initialisation. As a result, only the EKF shows initial oscillation. However, without smoothing, both estimators would show similar initial phases. This is a consequence of the poor initial guess as well as the poor observability of the problem. Consequently, time is required to converge.

The EKF smooths the mean current more strongly. However, the reaction of the EKF compared to the MHE is delayed (Fig. 7.9(a) and Fig. 7.9(b)). Both estimators can estimate the oscillation of the inertial current. However, the EKF captures the dynamics of the problem with a delay, which causes a delay in the iceberg velocity (Fig. 7.8) and inertial current estimation (Fig. 7.9(e)).

MHE follows the wind forecast, while the EKF estimate shows an offset in addition to a delay (Fig. 7.9(c) and Fig. 7.9(d)). The overall influence of the wind estimation error is small. Nevertheless, the MHE follows the wind forecast only in the last point of the horizon, which is the most recent wind estimate. While moving forward, earlier points on the horizon, which are older wind estimates, are adapted and depart from the wind forecast to excite the inertial current. As a result, oscillation in the wind velocity within the whole estimation horizon is introduced. This

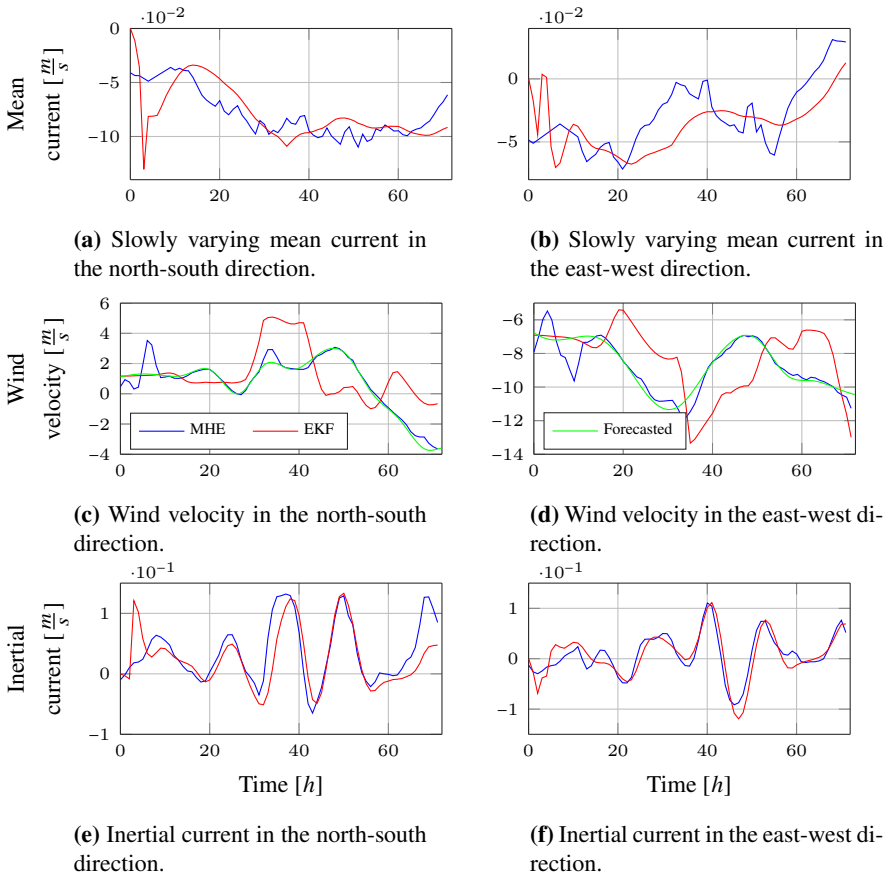


Figure 7.9: Estimation results of MHE (blue) with a 24 h horizon size and EKF (red) for different states. The forecasted wind is also shown (green).

is apparently visible in the first 12 h of the wind estimate of the MHE. The most recent wind estimate has only a minor influence on the inertial current. Hence, it can closely follow the measured value. However, to guarantee inertial currents, abrupt changes in the wind velocity are necessary, which is not provided by the interpolated forecasted wind inputs. Hence, the MHE introduces those necessary changes of the wind velocity within the estimation horizon. Furthermore, deviation from the expected oscillation is also balanced with changes of wind estimates in the horizon, which propagate through the inertial current to the most current estimate. The EKF cannot calculate the propagation of the wind velocity into the inertial current over a time horizon.

Forecast

The overall purpose of the estimation of the iceberg and ocean states is to forecast the iceberg trajectory. During the forecast, the mean current is assumed constant, and the inertial current is forecasted with the inertial current model. The initial state used in the forecast is the main difference between MHE and EKF.

To quantify the performance of forecasts at a specific time, the average distance between the predicted $\tilde{\mathbf{X}}$ and measured $\bar{\mathbf{X}}$ iceberg trajectory is calculated as

$$\zeta_N(t) = \frac{1}{N} \sum_{i=1}^N \|\tilde{\mathbf{X}}(t+i) - \bar{\mathbf{X}}(t+i)\|, \quad (7.12)$$

where N is the length of the forecast horizon and t is the initial time of the forecast. The performance index (PI) for the whole observation horizon is the mean of all average distances ζ_N (7.12) with the same forecast horizon N

$$PI(N) = \frac{1}{M} \sum_{i=1}^M \zeta_N(t_i), \quad (7.13)$$

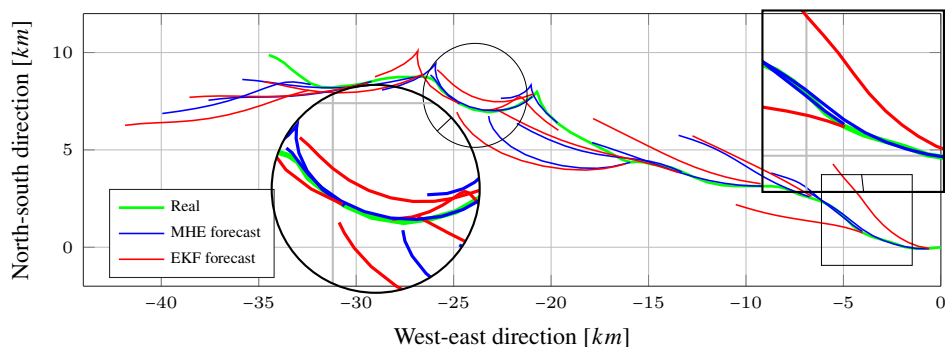
where M is the number of forecasts performed, and t_i is the initial time of the forecast. The performance index PI (7.13) and distance ζ_N are defined differently in this section compared to in Sec. 6.7.1.

In Table 7.1, the forecast results for MHE and EKF are shown. Especially for longer forecast horizons, it is important to estimate the inertial current more accurately, while for shorter forecast horizons (1 h to 3 h), the distinction between mean current and inertial current is less important, since the overall current change is small. For short forecasts, quick detection of changing dynamics are more important. Therefore, the EKF underperforms for shorter forecasts, while it performs better for longer forecasts. If the EKF were tuned such that the dynamics are detected faster, and a stronger oscillation is introduced to the mean current estimate, the the short-term forecast performance would increase, while the longer forecast performance (24 h) would decrease.

The proposed MHE method for iceberg drift prediction is highly successful for example iceberg drift data. The maximum error of all forecasts in the observed 72 h is only 10.0 km for a 24 h MHE forecast, and 4.0 km for a 12 h MHE forecast. For the EKF, the maximum forecast error is 12.1 km for 24 h and 6.0 km for 12h forecasts. In Figure 7.10, several 12 h forecasts in a 6 h hour frequency of both MHE and EKF are shown. In many instances, the MHE forecast is superior to the EKF forecast. Moreover, the MHE forecast predicts in some cases the measured iceberg trajectory very precisely. Two especially successful forecasts are emphasized in Fig. 7.10 (circle and rectangle scope).

Table 7.1 PI (7.13) for different forecast horizons N of MHE with horizon size of 24 h and EKF.

Horizon [h]	1	3	6	12	24
EKF [m]	253	450	830	1525	2654
MHE [m]	64	196	493	1096	2195

**Figure 7.10:** MHE (blue) and EKF (red) 12-hour forecast in 6-hour intervals. The measured iceberg trajectory is the reference line (green).

7.4 Conclusion

A moving horizon estimator and extended Kalman filter were implemented to distinguish between an oscillating and non-oscillating input signal to use this information for forecasting an iceberg trajectory. Significant uncertainties in the current usually prohibit successful iceberg drift forecasts. The proposed forecast scheme avoids using current information directly. Instead, this information is estimated based on the observed iceberg movement and available wind information.

It is shown via simulation that the MHE with a sufficiently long horizon and well-chosen process noise constraints can estimate the dynamics of the system correctly as well as distinguish between non-oscillating and oscillating inputs.

The EKF produced more substantial errors within the estimation process. It was possible to tune the EKF such that it could distinguish the oscillating and non-oscillating part of the input, but this came at the cost of delays in the detection of the dynamics of the process. Tuning this allowed for the reduction of these delays, but reduced the capability of the EKF to distinguish oscillating and non-oscillating input.

It was shown that a time-varying mean current could be an advantage to distinguish between the direct influence of the wind and the mean current. Input information about the wind is necessary to estimate the states and inputs of the

system successfully. Otherwise, the system is not observable. The estimation result can be improved with more frequent and less uncertain wind information.

The performance of the MHE compared with the EKF was further evaluated on real iceberg drift data. The MHE outperformed the EKF, since the dynamics of the process were better captured. The overall performance of the proposed estimation-forecast scheme for the particular iceberg data considered was excellent. Furthermore, the proposed scheme does not require frequent iceberg position measurements or current information, which can be significantly advantageous when working with iceberg surveillance solutions based on satellite or aerial platforms. Future work may investigate how parameter uncertainties in the iceberg and inertial model affect the estimates. A further interesting question to look into is if there exist several oscillations, such as tidal and inertial oscillations, then how can these be simultaneously detected and distinguished.

Chapter 8

Switching Scheme between Ancillary and Inertial Current Forecasts

This chapter is based on PAPER G (Andersson et al. 2016c). The two forecast schemes, the ancillary current (Sec. 6) and the inertial current estimation-forecast scheme (Sec. 7), are briefly presented. A switching scheme and a simple criterion when to switch are also proposed. The scheme switches between the two iceberg drift forecasts and is implemented and tested on an iceberg drift trajectory measured during a research expedition offshore Newfoundland conducted by ArcticNet and Statoil. It is shown that the use of two forecast schemes and a timely decision on which scheme to use improves the iceberg drift forecast compared to using only one scheme.

8.1 Introduction

Chapter 6 included a proposal to correct the uncertain current input received from current measurements or ocean models with an ancillary current. The ancillary current is an artificial parameter introduced to the iceberg model, which is calculated with the help of the observed iceberg trajectory. We will refer to this scheme as the *ancillary current estimation-forecast scheme* (ACE).

In Chapter 7, we proposed a scheme to estimate currents based on wind information and the observed iceberg trajectory. These currents are then used in a second step to forecast the iceberg drift trajectory. We will refer to this scheme as the *inertial current estimation-forecast scheme* (ICE).

In this chapter we discuss how we can improve the short-term iceberg drift pre-

dictions with the help of parameter estimation techniques. We will generalise the theory behind the ancillary current and use both schemes to forecast the iceberg drift trajectory.

8.2 Statement of Theory and Definitions

8.2.1 Iceberg Drift Model

The mechanistic dynamic iceberg model, which describes the change of velocity of the iceberg mass, is used

$$m \frac{d\mathbf{v}_i}{dt} = \mathbf{f}_{\text{cor}} + \mathbf{f}_a + \mathbf{f}_c + \mathbf{f}_r + \mathbf{f}_p, \quad (8.1)$$

where m , \mathbf{v}_i , \mathbf{v}_{cor} , \mathbf{v}_a , \mathbf{v}_c , \mathbf{v}_r , and \mathbf{v}_p are the iceberg mass, velocity, Coriolis force, air drag force, water drag force, wave radiation force, and pressure gradient term, respectively (Sec. 2.3).

8.2.2 The Ancillary Current Forecast Scheme

The ancillary current is an artificial correction term introduced into the iceberg model (Sec. 6.3.3). The purpose of the ancillary current is to adjust the current information from current measurements or ocean models such that it corresponds to the observed iceberg movement.

Fig. 8.1 shows the block diagram of the proposed ancillary current setup. The first block describes the ancillary current function, while the second block is the iceberg model. The measured or predicted current input \mathbf{u} is transformed by a function \mathbf{g} . After the transformation, the current \mathbf{u}^* enters the iceberg model. The output of the model is the iceberg position \mathbf{y} . With the iceberg model, the measured iceberg position, and the environmental driving forces of winds and waves, it is possible to estimate the actual current input \mathbf{u}^* as well as the function \mathbf{g} .

The generalized ancillary current function can have the form

$$\mathbf{u}^* = \mathbf{g}'(\mathbf{u}) + \mathbf{v}, \quad (8.2)$$

where \mathbf{v} is a parameter and \mathbf{g}' is a function, which depends on the input \mathbf{u} . The function \mathbf{g}' can have a positive or negative time delay.

The proposed ancillary current in Sec. 6.3.3 is a special subclass of the ancillary current function (8.2) and has the form

$$\mathbf{u}^* = \mathbf{I}\mathbf{u} + \mathbf{v}, \quad (8.3)$$

where \mathbf{g}' is chosen to be \mathbf{I} , and the parameter \mathbf{v} is called the *ancillary current*. The parameter is updated every time a new iceberg position measurement is available.

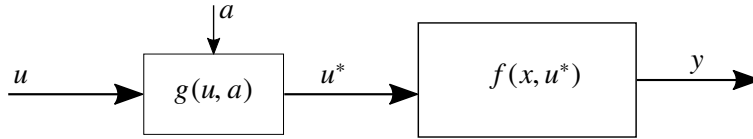


Figure 8.1: Representation of the ancillary current.

Afterward, the parameter is used to forecast the iceberg drift trajectory.

It is not within the scope of this chapter to discuss how to find an optimal ancillary current function. However, we introduce two criteria, which the function should fulfil:

- The parameters in the ancillary function (8.2) should be constant (or slightly changing over time).
- The ancillary function should be as simple as possible.

Both criteria can be tested with a model selection method, such as the penalised maximum likelihood criteria. The first criteria corresponds to the goodness-of-fit for the model, which guarantees a reasonable iceberg drift forecast. The second criteria penalise the goodness-of-fit by the degree to which it was accomplished using a complex model.

If a simple and constant ancillary current function can be found, the input information \mathbf{u} is valuable. If the parameter of the ancillary current function significantly changes over time, then the input information \mathbf{u} is faulty. An input signal identified as faulty should not be used for iceberg drift forecasting. After an input signal \mathbf{u} was identified as faulty, it is possible that *after some time* the input signal recovers and the input information is classified as valuable (not faulty) again.

In the situation that the input signal is identified as faulty, several alternatives exist to forecast the iceberg without current information. For example,

- use as the ancillary current function

$$\mathbf{u}^* = \mathbf{0}\mathbf{u} + \mathbf{v}, \quad (8.4)$$

and assume a constant \mathbf{v} during the forecast, or

- use the inertial current estimation-forecast scheme, which is presented in the next section.

In this chapter we will only focus on the second alternative. A suitable criterion to decide when the iceberg forecast should switch between the ACE and the ICE is

the ancillary current performance index (*API*) (6.14). The *API* penalizes changes of the ancillary current parameter.

The ACE is used as long the *API* is within some threshold. When the *API* exceeds the threshold then the ICE is used.

8.2.3 The Inertial Current Forecast Scheme

The ICE was presented in Chapter 7. The principle behind the forecast scheme is that the total current consists of different components of tidal currents, the inertial current, and mean current.

The tidal current is taken from tidal models, which is assumed to be reasonable accurate. The mean and inertial currents are estimated with a moving horizon estimator based on wind information, such as wind measurements or wind forecasts, and the iceberg drift trajectory. The inertial current oscillation of the ocean is approximated using a model of forces from wind stress (Pollard and Jr. 1970, De Young and Tang 1990)

$$\dot{\mathbf{z}} = \mathbf{B}(\mathbf{u}) + f\mathbf{k} \times \mathbf{z} - c\mathbf{z}, \quad (8.5)$$

where \mathbf{z} is the inertial oscillation, $\mathbf{B}(\mathbf{u})$ is the wind excitation, f the Coriolis vector, and c is a decay factor.

8.2.4 Moving Horizon Estimator

The moving horizon estimator (MHE) is used to estimate the ancillary current parameter in the ACE and the currents and winds in the ICE. The MHE was introduced in Sec. 3.1.1.

8.3 Data Acquisition

The iceberg trajectory used in this case study is the first 72 h of drift observations for Iceberg 2 (Sec. 4.1.2).

Wind and wave information was obtained by a local weather forecast service (Amec Foster Wheeler), which was supplied with a 6 h frequency. To receive the same samples for the wind forecast as for the iceberg position samples, the wind forecast points were interpolated. The weather forecast location and the initial iceberg position were approximately 80 km apart.

A MetOcean Iridium surface velocity program buoy (SVP) (Fig. 6.2) was deployed close to the iceberg to collect current information. The position updates of the buoy were received with an hourly frequency. The measurements were interpolated to fit the time stamp of the position data of the iceberg.

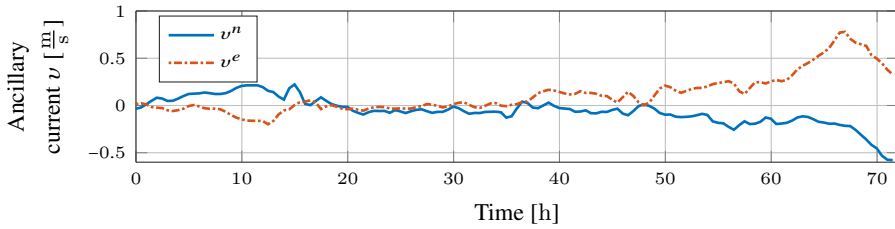


Figure 8.2: The ancillary current calculated with an MHE.

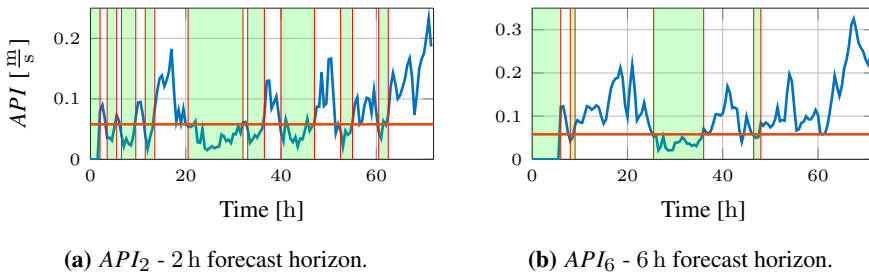


Figure 8.3: The API of the iceberg for different forecast horizons. The horizontal line gives the threshold. The ancillary estimation-forecast scheme is used in the marked intervals. Green areas indicate when the ACE is used, and the white areas for ICE.

8.4 Results

For both forecast schemes, ACE and ICE, the estimation is performed in a 30 min frequency. The estimated ancillary current of the iceberg calculated with the MHE is shown in Figure 8.2. Substantial changes of the ancillary current are detected around 10 h to 20 h and 60 h to 72 h. In these periods, the switch between both forecast models should be performed.

The API is calculated for a 2 h and 6 h forecast horizon, which is denoted by API_2 and API_6 (Fig. 8.3). The threshold is set to 0.06 m/s. Every time the threshold is violated for two consecutive API s the forecast scheme is switched between ACE and ICE. The API checks the change of the ancillary current in the previous forecast horizons. Therefore, the value of the API at the beginning of the observation is zero. The API_2 receives the first API value after 2 h. This is an advantage over the API_6 , which has a larger delay. On the other hand, the API_6 evaluates more ancillary current values. Consequently, the API_6 graph is smoother and the system has less forecast model switches.

The forecast performance of the models is evaluated with the root mean square error ζ_N between predicted $\tilde{\mathbf{X}}$ and measured $\bar{\mathbf{X}}$ iceberg trajectory (6.11).

Figure 8.4 shows the performance of the switching scheme, the ACE, the ICE

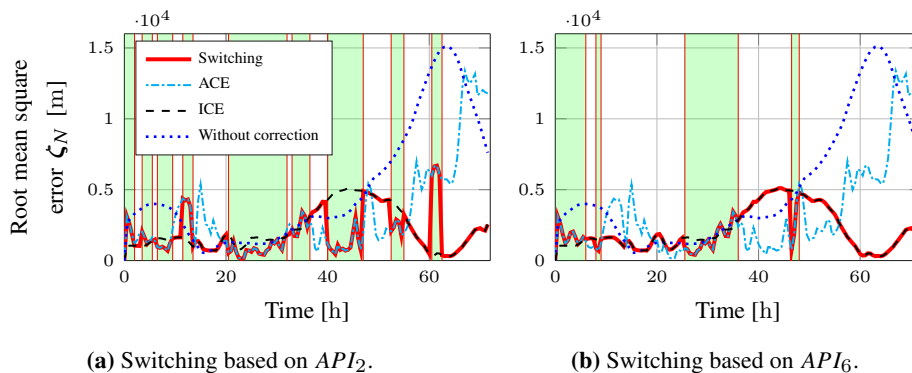


Figure 8.4: The root mean square error ζ_N (6.11) for a 12 h forecast horizon. The switching between forecasts is chosen with API_2 and API_6 . Green areas indicate that the ACE is used, and white areas for the ICE.

and the drift prediction without any correction for a 12 h forecast. In addition, the two different switching intervals are included in the figures. The switches between forecast schemes are performed based on the API calculations. In both cases, API_2 and API_6 , the switches between forecast schemes usually result in a superior forecast. However, it is apparently visible that in not all cases the switch is beneficial. For the API_2 case, it is not beneficial to switch to the ICE between 36.5 h to 40 h as well as it is not beneficial to switch to the ACE between 60.5 h to 62.5 h. For the API_6 case, it is not beneficial to forecast the iceberg drift with the ICE between 36 h to 46.5 h.

The occurrence of non-beneficial switches was expected since the decisions of which forecast scheme should be used are based on short-term forecast results with the assumption having the same tendency for longer forecasts. However, this cannot be guaranteed for all forecasts. Furthermore, it is not guaranteed that the ICE performs better than the ACE in cases of large API s. Nevertheless, the overall forecast performance increases with the switching scheme. This is evaluated with the performance index (PI) (6.12).

Table 8.1 shows the PI for the different forecast schemes where a small PI indicates high performance. The significantly larger PI of the ACE compared to the ICE is caused by the large forecast errors of the ACE at the end of the observation horizon.

8.5 Conclusion

The chapter shows the potential of using several iceberg forecast schemes to forecast iceberg drift trajectories. A switching algorithm between two forecast schemes, the ACE and ICE, is proposed. Switching between these two forecast schemes can

Tab. 8.1: The PI (6.12) of the Iceberg for a forecast horizon N of 12 h.

Ancillary current [m]	4562
Inertial current [m]	2601
Without correction [m]	6667
Switching with API_2 [m]	2401
Switching with API_6 [m]	2555

improve the iceberg drift forecast compared to using only a single forecast scheme. The API is used as an indicator for when to switch between both schemes. It is shown that short-term forecast information (2 h and 6 h) can be used to compare forecast schemes and decide which to use for longer forecasts. Even though the presented switching scheme produces a superior forecast to a single forecast scheme, future work is required to address some issues.

The proposed switching scheme has to be tested on several iceberg trajectories to evaluate how it behaves for different iceberg geometries and environmental conditions.

At the moment only the ACE is checked with the help of the API , while it is assumed that the ICE performs well in cases when the ACE does not. This can not be guaranteed. A general criterion has to be introduced, such that it can be decided efficiently which forecast scheme to use for iceberg drift predictions.

A further interesting question to investigate is how optimal ancillary functions for iceberg drift forecast can be found.

Part III

Statistical Iceberg Drift Forecast Algorithms

Chapter 9

An iceberg forecast approach based on a statistical ocean current model

This chapter is based on PAPER D ([Andersson et al. 2018d](#)). The difference between the statistical iceberg model forecast scheme and the hybrid forecast schemes (Part II) is that the statistical forecast schemes do not use the dynamic iceberg model and rely on a statistical model, which is identified by a training set.

This chapter proposes a statistical model for short-term iceberg drift forecasts by transforming the problem of forecasting the iceberg velocity into a problem to forecast the ocean current velocity. A Vector-autoregression model is identified using historical ocean current data as a training set. On four real iceberg drift tracks the proposed forecast scheme is tested and analysed. Based on these recommendations about the forecast horizon, the filter horizon and model order are given. Moreover, it is shown that the statistical forecast approach presented in this chapter offers superior performance to the conventional dynamic iceberg forecast model for short-term drift forecasts.

9.1 Introduction

The available information about icebergs to the Ice Services (e.g., CIS) is often limited. They must work with infrequent or no updated information about iceberg positions and limited to no initial information about iceberg shape or initial velocities. In such situations the only option to forecast the iceberg trajectory is to use the mechanistic dynamic iceberg drift model. On the other hand, as an iceberg approaches an offshore installation, more information about the iceberg becomes

available, and the iceberg may even be tracked continuously.

In this situation, other approaches that include past information to forecast an iceberg trajectory are feasible. A statistical model using historical data and recently observed data about the iceberg drift was proposed (De Margerie et al. 1986). They assumed that predictors of iceberg velocity and position could be written as a sum of tidal-, inertial-, wind-driven, and single-term auto-correlation components (Marko et al. 1988). Another statistical iceberg prediction model based on past iceberg trajectory observations was developed by Moore (1987), who used a mixed auto-regression integrated moving average approach.

Gaskill and Rochester (1984) used the dynamic iceberg model and past iceberg motions to estimate currents required for the past motions. In a second step, they applied the currents to other icebergs passing through the same area at a later time. In Section 6, it is suggested to correct the uncertain current input received from current measurements or ocean models with an ancillary current, an artificial parameter introduced to the iceberg model, which is calculated with the help of the observed iceberg trajectory (Andersson et al. 2016a). In Section 7, a scheme is designed to estimate currents based on wind information and the observed iceberg trajectory (Andersson et al. 2016b). These currents are used in a second step to forecast the iceberg drift trajectory.

In this chapter another approach is proposed, which is motivated in the following section.

9.2 Motivation

It was observed that for the short-term forecasts (1 h to 24 h) of iceberg trajectories, the models that incorporate past observations exhibit superior performance relative to the mechanistic dynamic models (Andersson et al. 2016a, Marko et al. 1988). This is not surprising since the models work with more information. The discrete-time nonlinear system can describe the iceberg drift model

$$\mathbf{x}_{k+1} = \mathbf{f}_k(\mathbf{x}_k, \boldsymbol{\omega}_k), \quad (9.1a)$$

$$\mathbf{z}_k = \mathbf{h}_k(\mathbf{x}_k, \boldsymbol{\nu}_k), \quad (9.1b)$$

where the subscript k is the time index, and $\mathbf{x}_k \in \mathbb{R}^n$ and $\mathbf{z}_k \in \mathbb{R}^y$ represent the state and measurement vectors, respectively. The vectors $\boldsymbol{\omega}_k \in \mathbb{R}^n$ and $\boldsymbol{\nu}_k \in \mathbb{R}^y$ are mutually independent white noise processes and \mathbf{f}_k and \mathbf{h}_k are nonlinear functions, which may depend on the time k . The white noise processes are described by known probability density functions (pdf) $p(\boldsymbol{\omega}_k)$ and $p(\boldsymbol{\nu}_k)$. Furthermore, it is assumed that the initial state \mathbf{x}_0 has a pdf $p(\mathbf{x}_0)$.

Let the complete state and measurement histories up to the time instant k be denoted as $\mathbf{X}_k = [\mathbf{x}_0^T, \mathbf{x}_1^T, \dots, \mathbf{x}_k^T]^T$ and $\mathbf{Z}_k = [\mathbf{z}_0^T, \mathbf{z}_1^T, \dots, \mathbf{z}_k^T]^T$, respectively. The

joint pdf of state and measurement histories $p(\mathbf{X}_k, \mathbf{Z}_k)$ may be written as

$$p(\mathbf{X}_k, \mathbf{Z}_k) = p(\mathbf{x}_0) \prod_{i=0}^k p(\mathbf{z}_i | \mathbf{x}_i) \prod_{i=1}^k p(\mathbf{x}_i | \mathbf{x}_{i-1}) \quad (9.2)$$

respecting that the stochastic system (9.1) is a Markov process. In (9.2), the first term on the right-hand side is the prior information, the second represents the measurement model (9.1b), and the third is the process model (9.1a).

Many mechanistic dynamic model approaches to iceberg forecasting use only the prior and process model to forecast the iceberg trajectory, and they do not correct their model with measurements due to lack of this information.

Moreover, only limited knowledge exists on how well the simplified mechanistic dynamic iceberg model represents the actual iceberg drift situation. Recently, a new research effort lead by C-CORE developed an improved iceberg profiling, which may lead to a better understanding of the iceberg drift (McGuire et al. 2016, Bruce et al. 2016, Stuckey et al. 2016, King et al. 2016, Fuglem et al. 2016).

An attempt to capture the uncertainty in the dynamic model by describing the uncertainties of the parameters with several distributions was done by Allison et al. (2014). Statistical methods often have an error term that may describe the uncertainty (9.2) in the iceberg forecast (Garrett 1985, Moore 1987).

A major issue for the iceberg drift forecast problem is the limited and expensive datasets. Only for a handful of icebergs are the keel shape, drift trajectory, and current close to the iceberg measured and analysed. Even in such idealistic conditions, it was not always possible to forecast or even hindcast the iceberg trajectory with the given dataset (Smith and Donaldson 1987, Andersson et al. 2017c).

The actual process model (9.1a) and, especially, the process noise distribution was not analysed because of the limited dataset. Moreover, we believe that the process noise distribution will depend on the iceberg location and how well the currents and winds are represented by the environmental models at a specific location. Furthermore, the iceberg trajectories represent a Lagrangian particle flow where the observer moves with the particle. Consequently, a significant number of iceberg trajectories passing through the same region has to be available to find location-specific noise distributions. As of today, this data is not available and not feasible to receive. New satellite programs from the European, American or other space agencies may improve the situation in the future.

This chapter chooses another way to overcome the lack of iceberg drift data. The idea is to use the well-known kinematic relationship between iceberg, ocean current, and wind velocities

$$\mathbf{v}^i = \mathbf{v}^w + \alpha \mathbf{v}^a, \quad (9.3)$$

where \mathbf{v}^i , \mathbf{v}^w , and \mathbf{v}^a are the iceberg, ocean current and wind velocity, respectively. The parameter α is about 0.017 to 0.02 (Smith 1993, Bigg et al. 1997, Garrett et al. 1985). This empirical relationship was also recently derived analytically (Wagner et al. 2017).

Basic Premise 9.2.1. *An iceberg simulation model given by $p^i(\mathbf{v}_k^i|\mathbf{v}_{k-1}^i)$, where \mathbf{v}_k^i are the states of the iceberg model (9.1) and p^i is its pdf, can be approximated by a current simulation model given by $p^w(\mathbf{v}_k^w|\mathbf{v}_{k-1}^w)$, where \mathbf{v}_k^w are the states of the current model and p^w is its pdf.*

Reasoning. Assuming that we want to predict the iceberg model behaviour and we have given (9.3), we can express the logarithm of the probability density function of the iceberg model (9.2) by $\ln p^i(\mathbf{v}_k^i|\mathbf{v}_{k-1}^i) = \ln p^w(\mathbf{v}_k^w|\mathbf{v}_{k-1}^w) + \ln p^a(\mathbf{v}_k^a|\mathbf{v}_{k-1}^a)$, where \mathbf{v}_k^a is the state of the wind model and p^a is its pdf. Assuming the contribution of the wind to the model uncertainty is small, we get that the uncertainty of the iceberg model can be approximated by

$$p^i(\mathbf{v}_k^i|\mathbf{v}_{k-1}^i) \approx p^c(\mathbf{v}_k^c|\mathbf{v}_{k-1}^c) \quad (9.4)$$

■

This approximation has several consequences. It transfers the problem of predicting the iceberg velocity to a problem of predicting the current velocity at a specific location. Moreover, the confidence regions and uncertainty bounds can be approximated by a current prediction model. The advantage of this transmission is that sufficient current velocity data is available to identify a current model for short-term predictions. This model can then be used for further analysis.

9.3 Theory and Methods

The theory and methods used in this chapter can be found in Sections 3.2 and 3.3.

9.4 Performance Indices

The performance of the iceberg forecast is measured directly with the mean $\hat{\zeta}$ and median $\tilde{\zeta}$ so that the end position error $\zeta = |\hat{\mathcal{X}}_{end} - \mathcal{X}_{end}|$ of all forecasts performed

$$\hat{\zeta} = 1/N \sum_i^N \zeta_i, \quad (9.5a)$$

$$\tilde{\zeta} = \zeta_{N/2}, \quad (9.5b)$$

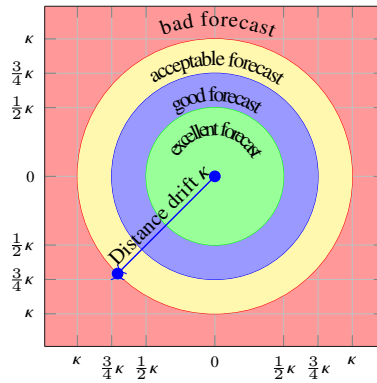


Figure 9.1: Relative performance index. If the end position of the iceberg forecast is encapsulated in the inner circle is defined as excellent, followed by two rings where the forecast is defined good and acceptable. If the forecast is not encapsulated by the outer circle is defined as bad.

where $\hat{\chi}_{end}$ and χ_{end} are the end positions of the forecasted and measured iceberg drift trajectories.

Moreover, a relative performance index is introduced to compare the different forecast models on different icebergs. It may be that the icebergs drift considerably differently (for instance, with different drift velocities). These may result in a larger mean and median error compared to slow icebergs. The relative forecast error is defined as

$$|\chi_{end} - \hat{\chi}_{end}| < \kappa |\chi_{end} - \chi_{init}|, \quad (9.6)$$

where χ_{init} is the initial position of the measured iceberg trajectory. The value κ is a performance index. For this chapter, the following forecast categories are chosen (Fig. 9.1):

- Bad forecast: $\kappa > 1$,
- Acceptable forecast: $1 \geq \kappa > 0.75$,
- Good forecast: $0.75 \geq \kappa > 0.5$,
- Excellent forecast: $\kappa < 0.5$.

The relative performance index penalises a wrong drift direction more strongly than a wrong drift velocity. To achieve an excellent forecast performance, the drift direction must be correct within $\pm 30^\circ$, and for a good forecast performance,

it must be within $\pm 48.6^\circ$. While for the former, the velocity must be 75 %, and for the latter 44 %, of the correct drift velocity. If the drift direction is forecasted correctly the velocity can be within 50 % to 150 % for the former and 25 % to 175 % for the latter. The relative performance index has a pole if the actual iceberg trajectory describes a closed loop. In this case, every forecast will be classified as bad.

9.5 Dataset

9.5.1 Iceberg Data

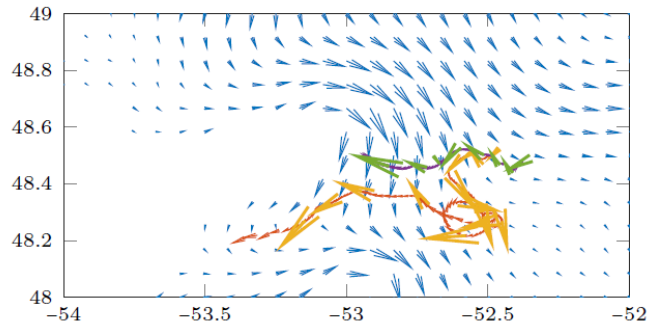
In this chapter, the iceberg trajectories of Iceberg 1 (Sec. 4.1.1), Iceberg 2 (Sec. 4.1.2) and Iceberg 4 (Sec. 4.1.3) are analysed.

9.5.2 Current Data

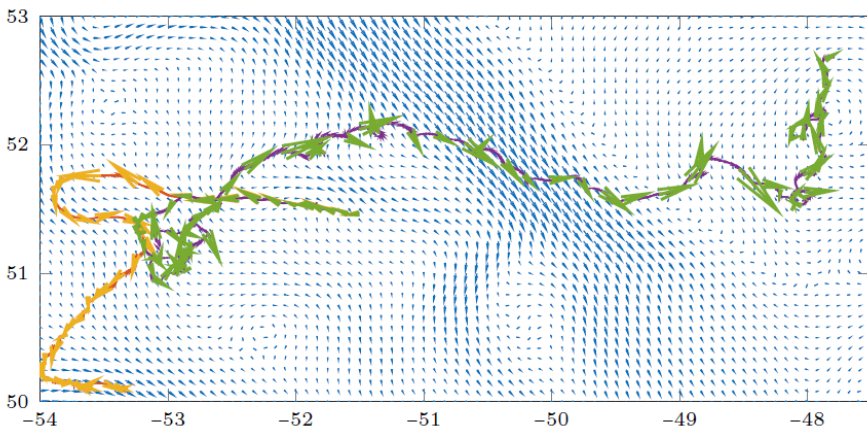
The current dataset was received from the E.U. Copernicus Marine Service, and the Global Ocean 1/12° Physics Analysis and Forecast model was used. The Operational Mercator global ocean analysis and forecast system at 1/12° provides ten days of 3D global ocean forecasts that are updated daily. More specifically, in this chapter the one-hour surface current and daily mean current information are used. For two different areas, the current was extracted from the global model. One region is constrained within 49.5° to 53° latitude and -54.5° to -47.5° longitude, and the other is within 48.0° to 49° latitude and -54° to -52° longitude. The first results are within an approximate 400×500 km large grid with 85×43 (Lon×Lat) grid cells and the second within an approximate 110×150 km large grid with 25×13 grid cells. These are the two regions of interest where the icebergs discussed in this research were tracked. In both cases, the last year of current data before the iceberg discovery is used to identify the ocean current model equivalent to 8760 time points.

Figure 9.2, the iceberg drift directions can be compared with the yearly mean surface current directions. It is not expected that the iceberg drifts with the mean current direction, but the mean current can give valuable insights about the local current regime.

Both the drift direction of Iceberg 1 and Iceberg 2 do not correlate well with the mean current direction. The drift direction of Iceberg 4, on the other hand, correlates relatively well with the mean current direction. Again, the drift direction of Iceberg 4-3 does not correlate well with the mean current. It can, however, be observed that the iceberg drift directions change more often in areas with diverse current regimes (i.e., it seems more "random" in these regions) (Fig. 9.2).



(a) Iceberg 1 and Iceberg 2.



(b) Iceberg 4 and Iceberg 4-3.

Figure 9.2: Maps showing the yearly mean surface current. The arrows indicate the direction of the surface current in each grid cell. In addition, the iceberg drift trajectories and iceberg drift directions are plotted.

9.5.3 Wind Data

The wind data was also received from the E.U. Copernicus Marine Service. The blended global ocean mean wind fields are used and are estimated from scatterometer retrievals. They have a horizontal resolution of $0.25^\circ \times 0.25^\circ$ and are updated every 6 h. The wind information is used at the same time and local frame as the current data. Consequently, the region covered by the grid cell is the same as for the current grid cell. Since the grid cells are larger, fewer cells are necessary to cover the region, which results in a $29 \times 15 \times 1460$ and $9 \times 5 \times 1460$ (Lon \times Lat \times time) large grid. Possible empty data points were removed from the dataset. In addition, the wind data points are linearly interpolated onto the current grid cells.

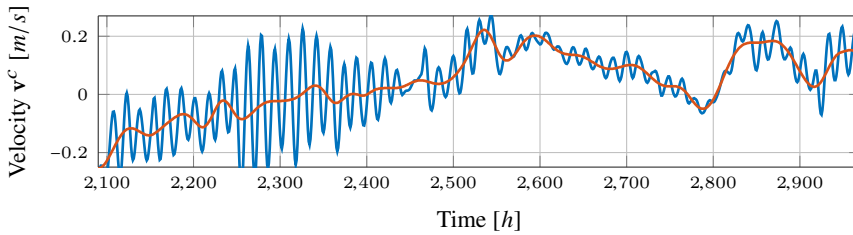


Figure 9.3: Example iceberg velocity with a smoothed velocity profile.

9.6 Pre-Analysis

9.6.1 Time Horizon of Kinematic Models

Current Data

An important parameter for the operational iceberg forecast is the time horizon for which kinematic models are reliable. For this, the auto-correlation of the current-velocity, current-acceleration, and higher derivatives (also called moments) are compared to their future values. As the current-data comes from a model (which contains smoothed data), it can only give an upper bound on how long the derivative of the position may be correlated.

The joint probability density functions $p(\mathbf{x}_i|\mathbf{x}_{i-t})$ are plotted. As long as these probability density functions contain some structure, a model could exploit the structure and improve the forecast. In contrast, when no structure can be detected, the initial information about the moment is completely degraded to Gaussian noise. If this state is reached, then a kinematic model assuming, for example, constant velocity or constant acceleration is no longer beneficial. In fact, the most likely value for the considered moment would be zero.

To analyse the correct frequency range, fast frequencies within the aimed forecast horizon t_h must be removed from the dataset. These frequencies can corrupt the analysis performed here considerably by adding additional change to the current velocity and its derivatives. Therefore, these frequencies (tidal and inertial frequencies) are removed with the help of the MEMD. The IMFs containing oscillations with a period of less than 30 h were removed (the intention was eliminate oscillations with a period smaller than 24 h, and we added buffer of 6 h). The remaining IMFs and the bias were added up to represent the smoothed dataset (Fig. 9.3).

The example shown here represents one grid cell, but similar observations were also obtained for the other grid cells. It can be seen that over time the correlation between initial and actual velocity decreases (Fig. 9.4(a)–9.4(d)). On the

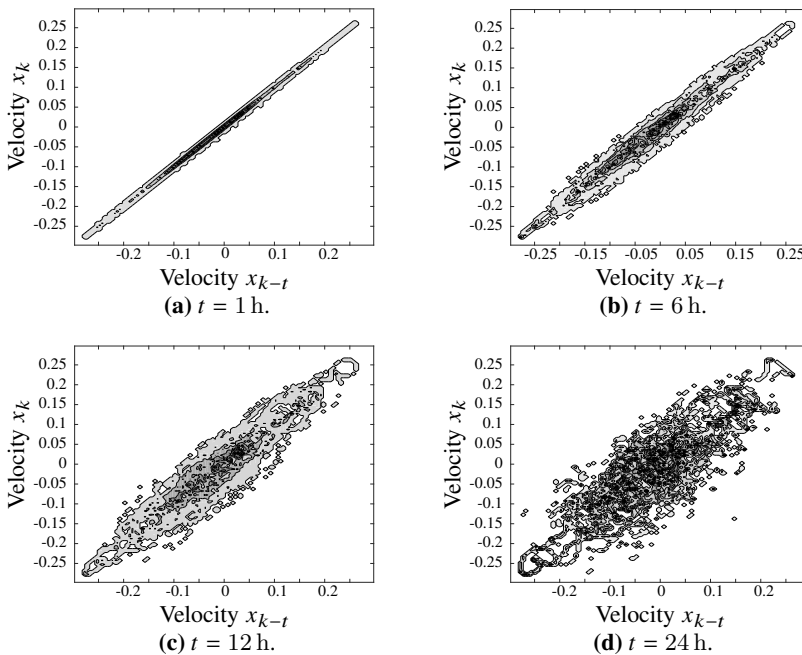


Figure 9.4: The Joint probability of one current velocity profile ($p=1$) for different intervals. The grey shading shows the likelihood.

other hand, it can also be observed that a model assuming constant velocity will be approximately correct in the first hours (Fig. 9.4(a)). Even though a correlation after 24 h can still be detected, the variance is significant, introducing a considerable uncertainty into the model that only assumes constant velocity.

The auto-correlation of the acceleration is shown in Figure 9.5, which shows the variance of the joint probability distribution of a 1 h interval is relatively small. Thus, the uncertainty of a model assuming constant acceleration is also small. On the other hand, after 6 h the joint probability distribution approaches a Gaussian distribution, and after 12 h the joint probability distribution is Gaussian. The structure which we would like to exploit during the forecast is vanished. Moreover, after 24 h we can even detect a linear structure opposite to the one observed for the smaller intervals. Hence, for extreme acceleration values, it is more likely to change sign than stay constant.

To conclude, it can be seen that the diffusion due to process noise of the acceleration is nearly complete after 12 h, and only minimal information remains from the initial acceleration.

For the higher derivatives, the correlation between initial and future values decreases further. It is, therefore, unlikely that kinematic models based on higher-

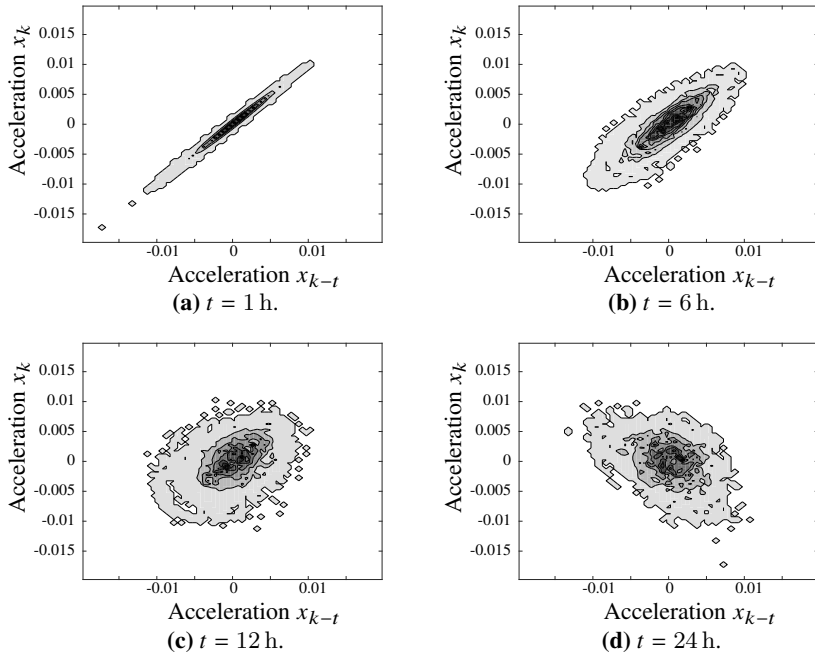


Figure 9.5: The Joint probability of one current acceleration ($p=2$) for different intervals.

order derivatives are beneficial, since considering that filtered and unsmoothed data are used in a real forecast scenario. If a filter horizon t_f of 12 h is used, then the acceleration ($p = 2$) is Gaussian after about 7 h and the jerk ($p = 3$) after 5 h.

Iceberg Data

We analysed in the previous subsection the ocean current velocity and its derivatives, and we saw how the process noise quickly degrades the auto-correlation to Gaussian noise, especially for higher derivatives. To verify our assumption that a statistical ocean current model can be used to help with the iceberg forecast, we compare the forecast results of kinematic iceberg models assuming constant velocity or higher derivatives and integrating them to the iceberg position

$$\begin{pmatrix} \dot{\mathbf{x}}_1 \\ \vdots \\ \dot{\mathbf{x}}_{p+1} \end{pmatrix} = \begin{pmatrix} \mathbf{x}_2 \\ \vdots \\ 0 \end{pmatrix} \quad (9.7)$$

where \mathbf{x}_1 represents the velocity and \mathbf{x}_2 the acceleration. The kinematic model is assumed to be noise free. Considering the observation made in the previous section, the model should be limited to $p = 3$, if not even $p = 2$.

The forecast for different horizons using the simple kinematic model assuming either constant velocity, acceleration or jerk is shown in Figure 9.6. For every iceberg, the same pattern can be detected. In the first hours, higher-order models are beneficial. However, the simple constant velocity model has a similar performance. After about 9 h, the model assuming constant jerk performance worse than the lower-order models. The model assuming constant acceleration performs worse for Iceberg 1 and Iceberg 4-3 after about 10 h and for Iceberg 2 and Iceberg 4 after about 16 h. The reason for this behaviour was discussed in the previous subsection.

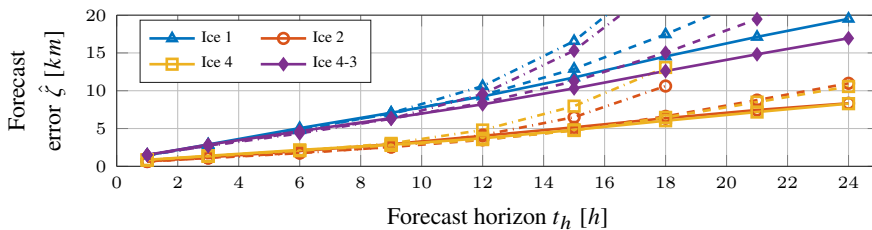


Figure 9.6: Mean forecast error $\hat{\zeta}$ of the iceberg drift forecast for different horizons t_h using different kinematic models. The solid lines assume constant velocity, dashed lines constant acceleration and dash-dotted lines constant acceleration change.

9.6.2 Cross-correlation of Variables

In the previous subsection, it was shown that up to a certain order the current velocity derivatives are strongly auto-correlated. A simple auto-correlation model was proposed and tested on the iceberg dataset. Nevertheless, a statistical current model may be improved by also considering cross-correlations of the ocean current to other variables, such as wind velocities and the orthogonal current-velocity.

A Vector-Autoregression (VAR) model is identified using the MVGC Multivariate Granger Causality Toolbox (Barnett and Seth 2014). An important prerequisite for model identification is the analysis of input and output correlations of the system. For this, Granger's causality is used. The analysis is performed on the original data, since pre-filtering may severely degrade Granger-causal inference and also increase the VAR model order (Barnett and Seth 2014). Causality can be detected between orthogonal current velocities and the ocean current and wind velocities in the same direction. Hence, it is beneficial to forecast the current velocity with past information about its velocity, the wind velocity in the same direction, and the orthogonal ocean current velocity.

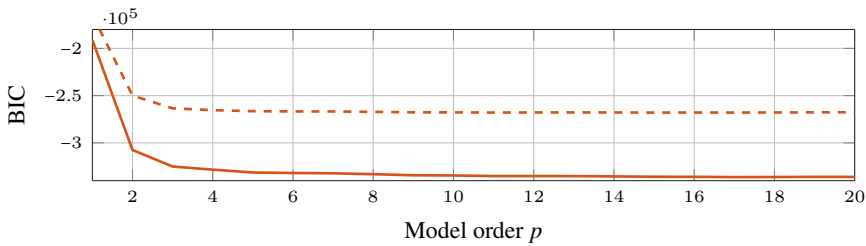


Figure 9.7: Value of Bayesian Information Criteria for model order up to $p = 20$. Solid line VAR model for Iceberg 4 and Iceberg 4-3 and dashed for Iceberg 1 and Iceberg 2.

9.6.3 Model Order

As part of the G-causality analysis, a VAR model was fitted into the current data. Before this, the optimal model order was estimated by the BIC with a maximum model order restricted to $p = 20$. In theory, we can identify a VAR model for each grid cell of the current grid, which improves the local characteristic of the iceberg drift. However, in this presentation, it was chosen to only identify two VAR models at the initial position of Iceberg 1 and Iceberg 4. The result of BIC for the two models is seen in Figure 9.7. The minimum for the BIC for Iceberg 4 is at a model order of $p = 17$, and $p = 15$ for Icebergs 1 and 2. However, the largest relative improvements are achieved within the first few model orders. In fact, the improvement from a first to a second order model is about 80% of the total improvement. An additional increase to a third-order model gives 90% of the overall improvement. Even though, the BIC suggests a higher-order model it is likely that already a low-order model can achieve adequate prediction results.

9.7 Iceberg Forecast

In this section, the forecast of the iceberg trajectories using the identified VAR ocean current model are discussed. The forecast procedure, assuming that a VAR model was already identified, is given in Algorithm 1.

The forecast performance of different order VAR models, the influence of the filter, and the forecast horizon will be closely examined. Moreover, it is tested if the cross-correlation between north and east velocity directions is beneficial for the iceberg forecast and if the wind information will improve the forecast. Both causalities were detected in the analysis and included into the model. However, the current model is fitted with modelled current and wind data. In the iceberg forecast case, however, the wind is uncertain. Moreover, the iceberg velocity and, therefore, the current velocity are corrupted by measurement noise. In addition, the modelled current is smoothed, so high-frequency changes are excluded from

Algorithm 1 Iceberg drift forecast

```

Set  $\hat{\chi}_0 = \chi$  and  $k = 0$ ;
while Simulation horizon ( $t_s$ )  $\leq$  Forecast horizon ( $t_h$ ) do
  Get iceberg position  $\hat{\chi}_k$ ;
  Estimate iceberg velocity  $\mathbf{v}_k^i$  (filter may be necessary);
  Estimate current velocity with  $\mathbf{v}_k^c$  (9.3);
  Take VAR model identified for grid cell closest to iceberg position;
  Calculate new current velocity  $\hat{\mathbf{v}}_{k+1}^c$  with VAR model;
  Calculate new iceberg velocity  $\hat{\mathbf{v}}_{k+1}^i$  with (9.3);
  if Fast frequency components considered important then Add fast frequency
  components that were removed using f.e. MEMD;
  end if
  Integrate to iceberg position  $\hat{\chi}_{k+1}$ ;
  Set  $k = k+1$ ;
end while

```

the modelled data, which is not the case for the iceberg velocity data. Therefore, the iceberg velocity data is filtered before every forecast step. A moving average filter is used, which presents a relatively small phase lag in comparison to other filters tested. Nevertheless, a time lag is present, which degrades the performance of the forecast. The robustness of the forecast to different window sizes will be tested.

9.7.1 Model Order

The BIC suggests an optimal model order of $p = 15$ to $p = 17$.

The four icebergs were tested on VAR models of different orders. The iceberg velocity is filtered with a 13 h moving average filter. The mean and median end position errors, $\hat{\zeta}$ and $\tilde{\zeta}$, of the iceberg drift forecast is shown in Figure 9.8. A minimum can be detected at a model order $p = 3$. Larger model orders do not or only slightly improve the forecast (Iceberg 2). Overall, the VAR model order is not as sensitive to higher model orders as the simple kinematic model (Fig. 9.6).

The wind influence is small. The most considerable improvement, if including the wind, is observed for Iceberg 4-3. On the other hand, the forecast of Iceberg 4 improves if wind is excluded.

9.7.2 Moving Horizon Window Length

The moving average filter (or any other filter chosen) plays an important role in the forecast scheme. How robust the VAR model against different filter lengths t_f is important, which indicates how robust the model is to measurement noise. The

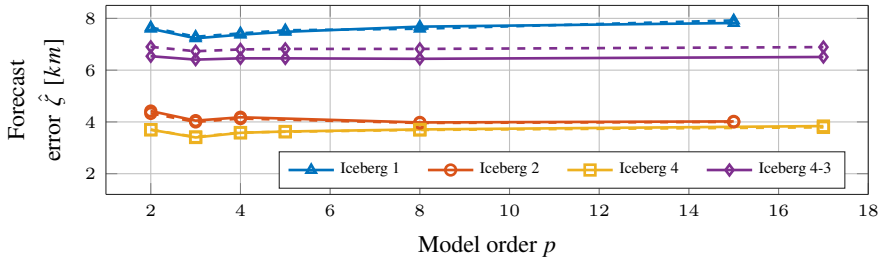


Figure 9.8: Results of different model orders p with and without wind input. Solid and dashed lines represent the mean error ζ with wind and without wind.

third-order VAR model is used since it performed well when the different model orders were compared.

Figure 9.9 shows the mean and median 12 h forecast errors, $\hat{\zeta}$ and $\tilde{\zeta}$, for the different icebergs including or excluding cross-correlation between orthogonal velocities.

The forecast performance of the VAR model differs between icebergs. While for Iceberg 2 and Iceberg 4, a minimum mean forecast error of about 3.2 km to 3.5 km can be reached, Iceberg 1 and Iceberg 4-3 have a minimum mean error at about 6 km to 7 km. If the cross-correlation is included in the model, then the optimal filter horizon t_f^{opt} is about 7 h to 10 h. If the cross-correlation is excluded, then longer filter horizons are necessary. The optimum t_f^{opt} is about 13 h to 15 h. Moreover, if cross-correlation is excluded from the forecast, then it is more sensitive to small filter horizons, while with cross-correlation the performance does not degrade as much as if the filter horizon is too short.

The drift trajectory of Iceberg 1 and Iceberg 4-3 have several loops. For these icebergs, it is beneficial to include cross-correlation between the orthogonal ocean current velocities. While the loops may not be forecasted precisely, every trajectory using this cross-correlation has a clock-wise bend, which reduces the forecast error ζ if the iceberg trajectory loops clock-wise (which it usually does).

Overall, the mean and median end position errors, $\hat{\zeta}$ and $\tilde{\zeta}$, change only slightly around the optimal filter horizon t_f^{opt} indicating the models are robust. A conservative approach would be to use a longer filter horizon t_f .

9.7.3 Forecast Horizon

The forecast horizon t_h from which recently measured information can be exploited to improve the forecast is limited. Figure 9.10 shows the mean and median end position error, $\hat{\zeta}$ and $\tilde{\zeta}$, of the iceberg drift forecast using different forecast horizons t_h . Iceberg 2 was excluded from the figure because of the short dataset.

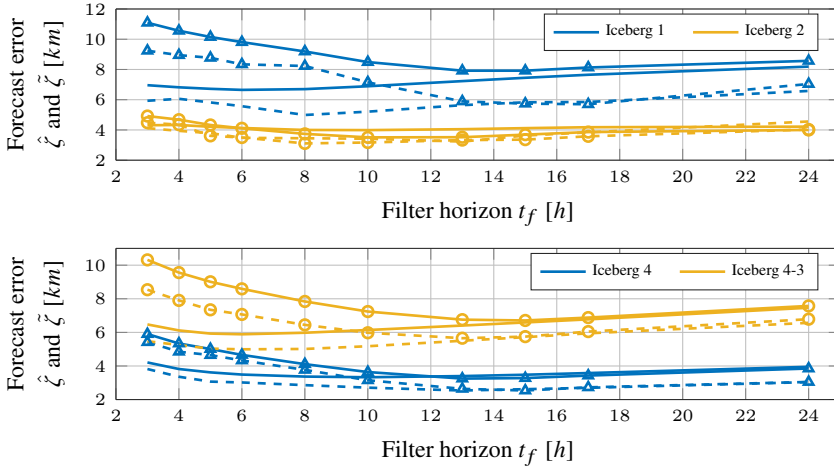


Figure 9.9: Forecast results for different filter horizons t_f . Solid line: mean error $\hat{\zeta}$. Dashed line: median error $\tilde{\zeta}$. Marked lines: without cross-correlation between orthogonal velocities.

The error change with respect to the forecast horizon is defined as

$$\hat{\Gamma} = \frac{\hat{\zeta}^{T_2} - \hat{\zeta}^{T_1}}{T_2 - T_1}, \quad (9.8)$$

where T_1 and T_2 describe the different length of the forecast horizons with $T_2 > T_1$. The same equation can be used for the median error change by replacing $\hat{\zeta}$ with $\tilde{\zeta}$.

The error change Γ has a minimum at $T = 12$ h. The iceberg drift is influenced by tidal currents, which have an oscillation period T of about 12 h and 24 h. Consequently, these oscillations introduce the smallest error at multiples of $1/2T$. Therefore, the change of the forecast error is oscillating with the same frequency (Fig. 9.10). However, it can be detected that the error change Γ increases slightly over time.

It can be concluded that including measured information is beneficial for forecasts up to at least 12 h. Longer forecast may be possible, but will exhibit larger error growths Γ .

In the case of short forecast horizons t_h of about 1 h to 6 h, the filter horizon t_f should be in the range of about 1 h to 3 h. Afterward, the filter horizon t_f should be increased to the ranges discussed in the previous section.

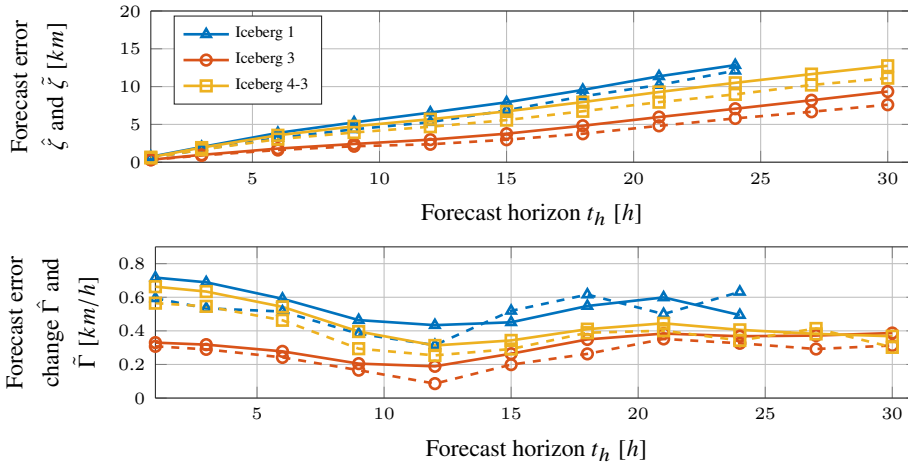


Figure 9.10: Mean $\hat{\zeta}$ and median $\tilde{\zeta}$ of the forecast error for different forecast horizons t_h and change of the forecast error Γ for the first and third order VAR model.

9.7.4 First-order Model

A first-order model can always be created from the VAR-model with

$$\mathbf{A} = \sum_{i=1}^p \mathbf{A}_i, \quad (9.9)$$

where \mathbf{A}_i contains the regression coefficients. The VAR model reduces to

$$\mathbf{u}_k = \mathbf{A}\mathbf{u}_{k-1}. \quad (9.10)$$

In this case the wind is negligible, indicating that it mainly influences the ocean current acceleration. The first-order model is stable with two complex conjugated eigenvalues close to the unit cycle. The real parts are about 0.997 to 0.9993 while the complex part is about 0.0005 to 0.005 depending which identified model is used. As it can be seen from the magnitude of the complex parts, the cross-correlation becomes small.

The higher-order VAR models produce a slightly better 12 h forecast than the first-order VAR model (varying from 2 % for Iceberg 4 to 25 % for Iceberg 1).

In comparison to the simple first-order kinematic model, the first-order VAR model provides a 3 % to 13 % better 12 h forecast. The improvement of the forecast with the first-order VAR model is due to the inclusion of the forecasted wind effects.

9.7.5 Dynamic Iceberg Model

For comparison and to indicate the performance of the VAR ocean model, the icebergs are modelled with the dynamic iceberg drift model (Sec. 2.3). The iceberg length, width, sail height, and keel depth were measured onsite and used in the model. Since a longer period is examined, a simple deterioration model is implemented assuming a daily 2% deterioration of the iceberg length, width, draft, and sail height. This seemed reasonable as it allowed that Iceberg 4 and Iceberg 4-3 to be observed for such an extended period.

The iceberg mass is approximated using the shape coefficients for spherical, wedged, and dry-dock icebergs according to the International Ice Patrol (C-CORE 2007). Iceberg 4 breaks apart after about 5.5 days. After evaluating the pictures of the iceberg, it is assumed that breakage happens at about 2/3 of the waterline length. Mass, width, draft, and sail are adjusted accordingly in the simulations. The two remaining icebergs are likely more dome-shaped than wedged. The shape factor is, therefore, adjusted after the breakage.

The iceberg is simulated using either the hourly surface current or the layered daily mean current provided by Copernicus Marine. Tidal current from the *Tidal Model Driver* (Egbert and Erofeeva 2002) is added to the daily mean current to approximate the lower frequency components.

Two, one, and four surface drifters were deployed close to Iceberg 1, 2, and 4, respectively. The measured surface current velocity is compared to the modelled surface current received from the Copernicus Marine webpage. The model captures the overall current velocity. However, the mean error in the north and east directions is about 5 cm s^{-1} and 1 cm s^{-1} , respectively. The standard deviation in both directions is about 14 cm s^{-1} . The absolute velocity is under-predicted by about 6 cm/s . In addition, the measured current direction is more directionally distributed than the modelled one (Fig 9.4). The Copernicus Marine dataset considers grid cells of about $10 \times 10 \text{ km}$, which smooths the current signal and reduces the amplitudes of the fast frequency components.

Using a scatter diagram to investigate the modelled and measured current velocities, we find that a possible correction is

$$\tilde{v}^{c,n} = 1.5v^{c,n}, \quad (9.11a)$$

$$\tilde{v}^{c,e} = v^{c,e} - 0.05, \quad (9.11b)$$

where the subscripts stand for the north and east directions. This reduces the mean errors in both directions to zero and improves the directional distribution (Fig 9.11). However, the error in absolute velocity remains similar. We will continue using the original ocean current data.

The iceberg keel shape is approximated using either a triangular, semi-elliptic

Table 9.1: Forecast error change $\hat{\Gamma}$ and $\tilde{\Gamma}$ [km/h] of the dynamic, VAR, and stationary models. Boldface is used to indicate the model with the smallest error growth.

	Change of mean error [km/h]												Change of median error [km/h]											
	1 h	3 h	6 h	9 h	12 h	15 h	18 h	21 h	24 h	1 h	3 h	6 h	9 h	12 h	15 h	18 h	21 h	24 h						
Ice 1	Dym. Mod.	0.70	0.87	0.86	0.77	0.72	0.71	0.71	0.67	0.63	0.61	0.80	0.83	0.90	0.99	0.71	0.69	0.62	0.58					
	VAR Mod.	0.72	0.69	0.59	0.46	0.43	0.45	0.55	0.60	0.49	0.59	0.53	0.51	0.38	0.32	0.52	0.62	0.50	0.63					
	Stat. Mod.	0.87	0.85	0.77	0.65	0.54	0.50	0.51	0.49	0.47	0.76	0.73	0.68	0.58	0.85	0.55	0.09	0.07	0.38					
Ice 2	Dym. Mod.	0.52	0.76	0.79	0.77	0.75	0.64	0.66	0.62	0.58	0.54	0.76	0.76	0.69	0.61	0.36	0.59	0.56	0.48					
	VAR Mod.	0.29	0.29	0.29	0.31	0.36	0.31	0.35	0.37	0.40	0.27	0.31	0.27	0.37	0.07	0.32	0.43	0.59	0.49					
	Stat. Mod.	0.46	0.45	0.45	0.47	0.50	0.29	0.44	0.46	0.49	0.48	0.50	0.48	0.43	0.53	0.31	0.42	0.39	0.49					
Ice 3	Dym. Mod.	0.38	0.57	0.63	0.63	0.63	0.65	0.63	0.62	0.61	0.33	0.49	0.53	0.54	0.56	0.61	0.54	0.57	0.54					
	VAR Mod.	0.33	0.32	0.28	0.20	0.19	0.26	0.35	0.38	0.37	0.31	0.29	0.24	0.17	0.09	0.20	0.26	0.35	0.33					
	Stat. Mod.	0.69	0.67	0.65	0.62	0.61	0.66	0.63	0.62	0.61	0.61	0.58	0.56	0.51	0.53	0.56	0.54	0.55	0.58					
Ice 3-2	Dym. Mod.	0.65	0.65	0.59	0.50	0.46	0.49	0.50	0.49	0.47	0.55	0.57	0.52	0.42	0.37	0.40	0.43	0.45	0.38					
	VAR Mod.	0.66	0.63	0.54	0.40	0.31	0.34	0.41	0.45	0.41	0.57	0.55	0.46	0.29	0.25	0.29	0.39	0.40	0.34					
	Stat. Mod.	0.99	0.96	0.89	0.80	0.75	0.74	0.74	0.72	0.68	0.91	0.88	0.83	0.78	0.73	0.80	0.78	0.67	0.63					

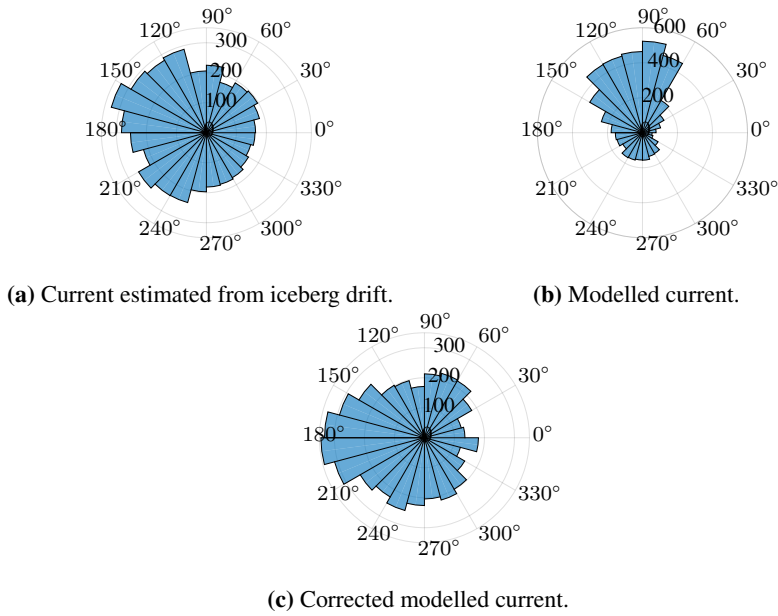


Figure 9.11: Directional distribution of the current from the iceberg drift (a) versus directional distributions from the Copernicus Marine ocean current model (b) and corrected modelled current (c).

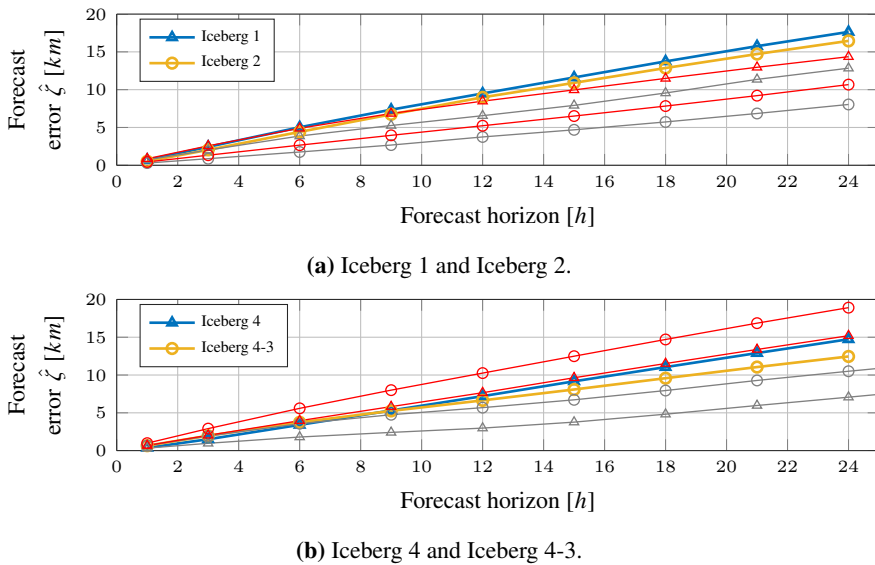


Figure 9.12: Forecast error $\hat{\zeta}$ (solid) for different forecast horizons for the dynamic (blue and yellow), stationary (red) and VAR model (grey).

or rectangular iceberg shape (Andersson et al. 2017c). The triangular iceberg shape produces the smallest error ζ for Iceberg 2, 4, and 4-3. For Iceberg 1, the elliptic iceberg keel shape works best. Overall, the performance is similar using the layered mean plus tidal current or the surface current. Only the error for Iceberg 4-3 reduced considerably using the surface current, which indicates the iceberg is most likely small and driven by surface currents.

The best mean and median error, $\hat{\zeta}$ and $\tilde{\zeta}$, of all simulations for each iceberg are shown in Figure 9.12. The stationary model assumes that the iceberg does not move. The error growth Γ of the dynamic, VAR and stationary models are shown in Table 9.1.

For Iceberg 1 and Iceberg 2 (Fig. 9.12(a)), the dynamic iceberg model produces worse results than assuming the icebergs are stationary. For the VAR model, the border is reached after 15 h (Iceberg 1), which is the only iceberg where the border is reached within a 24 h forecast. For Iceberg 4 (Fig. 9.12(b)), the dynamic iceberg model has a similar error change Γ as the stationary model (Tab. 9.1).

For the short-term drift forecasts, the VAR model produces better forecast results. However, the tendency of the error change Γ for longer forecast horizons decreases for the dynamic iceberg model while increases for the VAR model indicating that there may be a crossing point in time after which the dynamic iceberg model performs better.

If the corrected current (9.4) is used, then the forecast of Iceberg 2 and Iceberg 4 improves, worsens for Iceberg 4-3, and remains the same for Iceberg 1. The overall forecast performance improves slightly, but the VAR model forecast remains superior.

Even though the VAR model is on in average superior, only the dynamic model can forecast rapid and sudden direction changes. This can be seen in Figure 9.13(a) where the iceberg makes a sudden "unexpected" (by the VAR model) change of direction. The VAR model was well-adjusted before the change, but was not able to predict the change. Even though the forecast is not very good, the dynamic iceberg model predicts a direction change. After the change of direction, the VAR model adjusts itself again, and its forecast improves.

On the other hand, it can happen that with the dynamic drift model, a direction change is predicted but not observed in the actual iceberg trajectory (Fig. 9.13(b)). In this example, the forecast direction is predicted up to 180° incorrect by the dynamic iceberg model.

The VAR forecast model can approximate curves and sometimes direction changes (Fig. 9.13(c)) and loops (Fig. 9.13(d)) if the observed dataset indicates these changes. For this, the cross-correlation term should be included in the model.

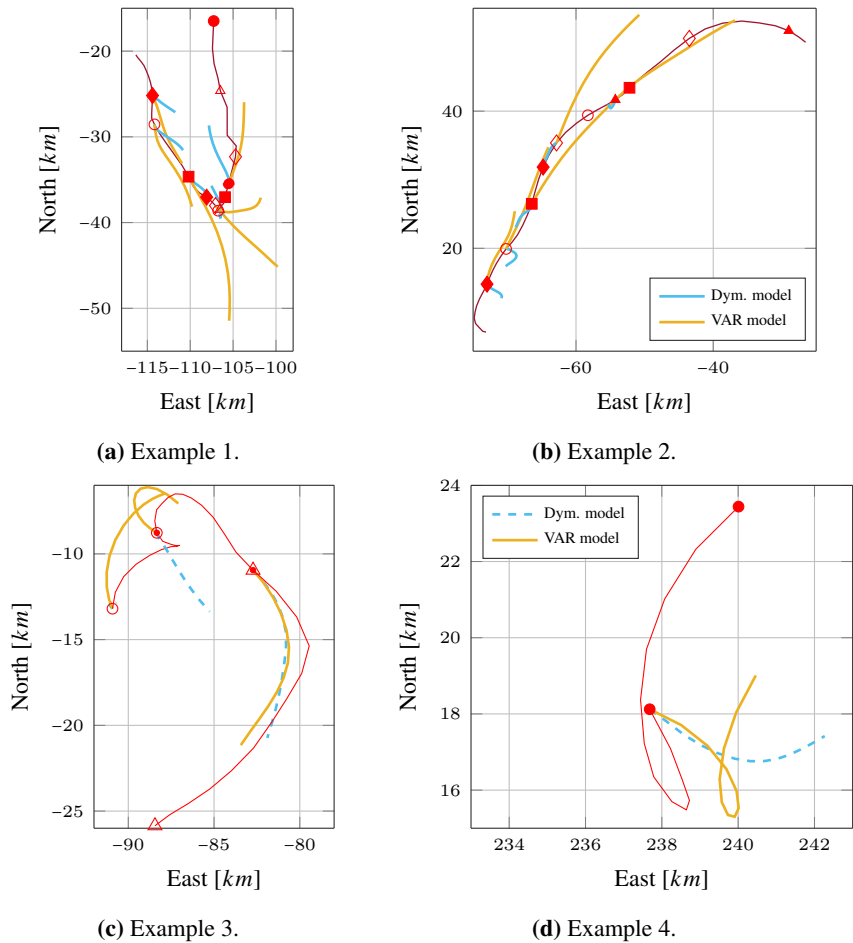


Figure 9.13: Several forecast examples for the VAR and dynamic iceberg models. The initial and end point of each forecast are denoted with the same markers on the observed iceberg trajectory.

9.7.6 Relative Performance Index

The relative performance index κ improves a comparison of different icebergs compared to an absolute performance index, such as the mean or median end position error, $\hat{\zeta}$ and $\tilde{\zeta}$. The stationary model was already included in the previous section.

Iceberg 4 shows the best relative performance κ for the VAR model (Fig. 9.14(c)). This correlates with the mean position error $\hat{\zeta}$. However, the VAR model has a similar relative performance κ for Iceberg 2 (Fig. 9.14(b)) and Iceberg 4-3 (Fig. 9.14(d)), which was not revealed by the mean forecast error $\hat{\zeta}$.

The dynamic iceberg model forecasts Iceberg 4-3 best but still considerably

worse than the VAR model. Moreover, the dynamic forecast model has the worse relative forecast performance κ for Iceberg 2 followed by Iceberg 1. This was also not clear considering the absolute error ζ , which had an opposed order.

Another good example where the relative forecast performance κ is more informative is when the yearly mean current is used to forecast the icebergs. If the forecast error $\hat{\zeta}$ is considered the order, starting with the best, is Iceberg 2, Iceberg 4, Iceberg 4-3, and Iceberg 1. However, the order of the relative forecast performance κ is Iceberg 4-3, Iceberg 4, Iceberg 2, and Iceberg 1. The differences are mainly because for Iceberg 2, the slow velocities are forecasted, but the directions are wrong. This caused a smaller absolute error ζ .

Overall, the change between forecast performance categories over a changing forecast horizon is relatively small after the initial phase of a few hours. This may be a useful property to estimate the performance for longer forecast horizons based in on a short iceberg drift forecast.

9.8 Conclusion

This chapter proposes a statistical approach to short-term iceberg forecasting. The basic premise is that the dynamics and uncertainties of the iceberg velocity can be approximated by the dynamics and uncertainties of the ocean current velocity. The advantage of this transformation is that sufficient ocean current velocity data (modelled or measured) is available to identify a statistical ocean current model. Two interesting effects arise from this transformation are. First, it is possible to identify a VAR model for each grid cell including local specifics of the iceberg model. Second, during the identification of the ocean current model, an error term is identified which may help to compute confidence regions (pdfs (9.2)) of the iceberg drift forecast. However, it is recommended to use measured ocean current data that has fast frequency components like the measured iceberg velocity.

After the identification of a VAR current model, its applicability to iceberg forecasting was analysed and tested on four real iceberg drift tracks. It was shown that a model order of $p = 3$ is sufficient to forecast the iceberg drift. Since the VAR model is identified with modelled current data, and the iceberg forecast uses measured iceberg position data, a filter is necessary. If the cross-correlation between orthogonal current velocities was included in the model, then a shorter filter horizon of about 7 10h was sufficient. If the cross-correlation was excluded, then a filter horizon of about 13 15h was necessary. The statistical approach can be used for a forecast up to at least 12 h where a minimum error change Γ was observed. Longer forecast horizons t_h are possible, but usually larger error growth than before were observed. In comparison with the dynamic iceberg model, this statistical approach had superior performance for all tested iceberg drift tracks up to a forecast horizon of 24 h. Longer forecast horizons were not compared.

A relative performance index was introduced that compares the forecast error to the drift distance within the forecast horizon. It was shown that this performance index improves the comparison between the forecast performances of different iceberg drift tracks.

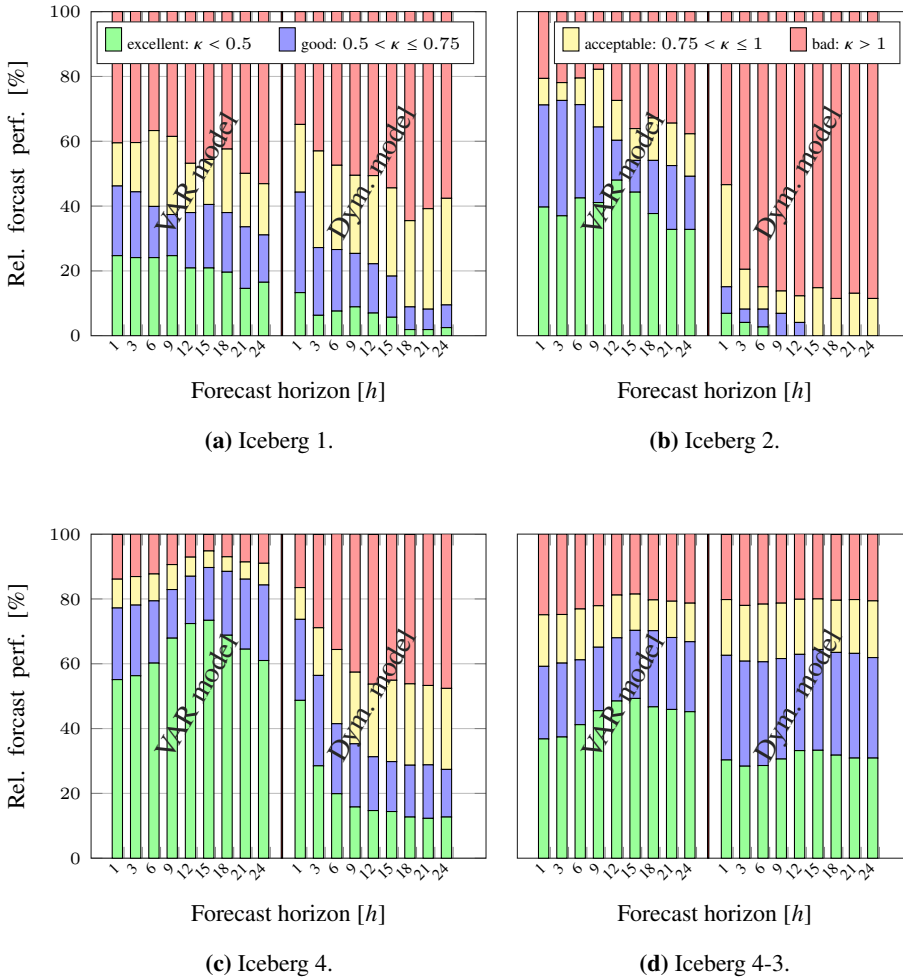


Figure 9.14: Relative forecast performance of Iceberg 1, 2, 4, and 4-3. The relative forecast performance is grouped in four categories (Sec. 9.3): bad (red), acceptable (yellow), good (blue), excellent (green). Each iceberg forecast performed is grouped in one of the categories. Each vertical bar shows the percentage of each category for a certain method and forecast horizon. The performance of the VAR model is on the left-hand side and the right-hand side of a dynamic model.

Part IV

Analysis and Forecast using the Multivariate Empirical Mode Decomposition

Chapter 10

Analysis of Iceberg Drift Trajectories Using the Multivariate Empirical Mode Decomposition

This chapter is based on PAPER K ([Andersson et al. 2018b](#)). We show how to detect and extract the tidal and inertial oscillation from iceberg velocity data by using the multivariate empirical model decomposition. Due to the similar frequencies of both oscillations in regions subject to drifting icebergs, this is an extremely challenging filtering problem. The method is tested on two iceberg drift trajectories from the east coast of Canada, one at about 51°N and one at about 76.5°N . The two icebergs differ in latitudinal location, such that the inertial and tidal oscillations in the first dataset have a slightly different frequency and in the other they are approximately the same. For the latter case a second filtering stage has to be included that uses tidal current information from a tidal current model. Finally we show how the multivariate empirical model decomposition can be used to analyse connections between current, wind and iceberg velocities. This information may help to improve either the ocean current and meteorological models or the iceberg drift model.

10.1 Introduction

The current direction and current speed are usually identified as most important for iceberg drift, but also as most uncertain ([Kubat et al. 2005](#), [Eik 2009](#), [Broström](#)

et al. 2009, Allison et al. 2014, Turnbull et al. 2015). The iceberg drift and current profile are closely correlated and a simple kinematic relationship between ocean currents, wind and iceberg velocity was experimentally discovered by Smith (1993), Garrett et al. (1985), Bigg et al. (1996) and even derived from the operational iceberg drift model by Wagner et al. (2017). Consequently, the study of iceberg drift trajectories may reveal information about the local current regime and may help to improve ocean current models.

In this chapter the empirical mode decomposition (EMD) and its extension to multivariate signals, the multivariate empirical mode decomposition (MEMD), is used to analyse iceberg velocity (Sec. 3.2). In addition, the current and wind velocities are included in the analysis. The EMD decomposes a signal into frequency-modulated components. This helps to identify, for example, tidal and inertial current oscillations in the iceberg velocity. Moreover, it is believed that this method may improve the understanding of iceberg drift and therefore improve capabilities to model the iceberg drift.

The gravity field of the moon and sun acting on the elastic earth causes the tidal current. The tidal current consist of several tidal constituents, sometimes also called partial tides (Stewart 2005). The most important constituents at the location under consideration are the principal lunar (M2) and principle solar (S2) constituents, which have a period of about 12 h. A similar period but a smaller amplitude at the location of the icebergs have the larger lunar elliptic (N2) and luni-solar semidiurnal (K2) constituents.

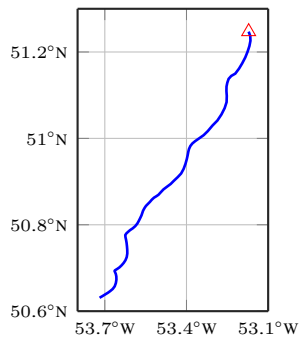
If the water moves only under the influence of the Coriolis force after an impulse that sets the water in motion, the resulting current is called inertial current. Due to earth's rotation the inertial current is rotating clockwise in the northern hemisphere. This motion can be described in its simplest form by a harmonic oscillator. Inertial currents can be caused by rapid changes of the wind at the sea surface and they typically decay in a few days (Stewart 2005).

10.2 The Datasets

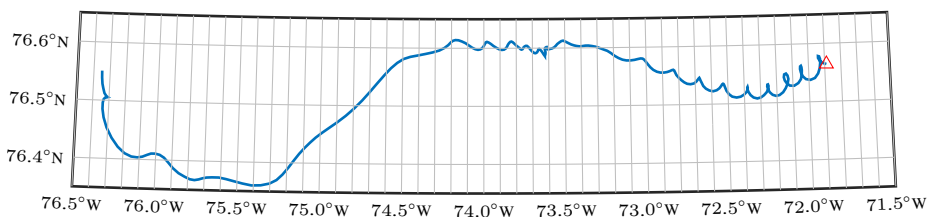
This section presents the iceberg drift trajectory datasets used in the analysis. The supporting datasets, such as local wind and current velocity, are interpolated linearly in time and positioned onto the iceberg trajectory.

Iceberg Dataset

In this chapter the trajectory of Iceberg 4 (Sec. 4.1.3) and Iceberg 3651 (Sec. 4.2.4) is analysed. Both iceberg drift trajectories show loops and wave patterns in parts of their tracks, which suggests that they are influenced by oscillations (Fig. 10.1).



(a) Iceberg 4 track close to Newfoundland from May 8, 2015 3:30am to May 11, 2015 7:30pm.



(b) Iceberg 3651 track in Baffin Bay from August 8, 2016 2am to August 19, 2016 3pm.

Figure 10.1: Map of iceberg drift trajectories.

10.2.1 Current Dataset

In this analysis, current data from the E.U. Copernicus Marine Services is used. As current source the *Global Ocean 1/12° Physical Analysis and Forecast model updated daily* is used. This model provides hourly surface current data and daily layered mean current data. For more information the reader is advised to visit the E.U. Copernicus Marine Service webpage ([EU Copernicus Marine 2006](#)).

10.2.2 Wind Dataset

As wind source, the *Global ocean wind L4 near real time 6 hourly observations* wind model from the E.U. Copernicus Marine Services is used. This model provides six-hourly surface wind data. For more information the reader is advised to visit the E.U. Copernicus Marine Service webpage ([EU Copernicus Marine 2006](#)).

10.2.3 Tidal Current Dataset

The tidal current information was received from the *Tidal Model Driver (TMD)* a MATLAB toolbox provided by the Oregon State University ([Egbert and Erofeeva 2002](#)). The tidal current is predicted. For Iceberg 4 the *Global Inverse Load Tide Model (TPX07.2)* and for Iceberg 3651 the *Arctic Ocean 5 km Inverse*

Model (AOTIM-5) is used. For more information the reader is advised to visit the Earth&Space Research webpage ([Earth&Space Research 1995](#)).

10.3 Detection of Tidal and Inertial Current Oscillation in the Iceberg Drift Velocity

This section provides examples of how the MEMD decomposes the iceberg velocity data. The velocity of the iceberg is calculated based on the hourly position updates. For reasons of clarity, only selected periods of the whole iceberg velocity signal available from the iceberg drift track is shown, to illustrate the usefulness of the decomposition.

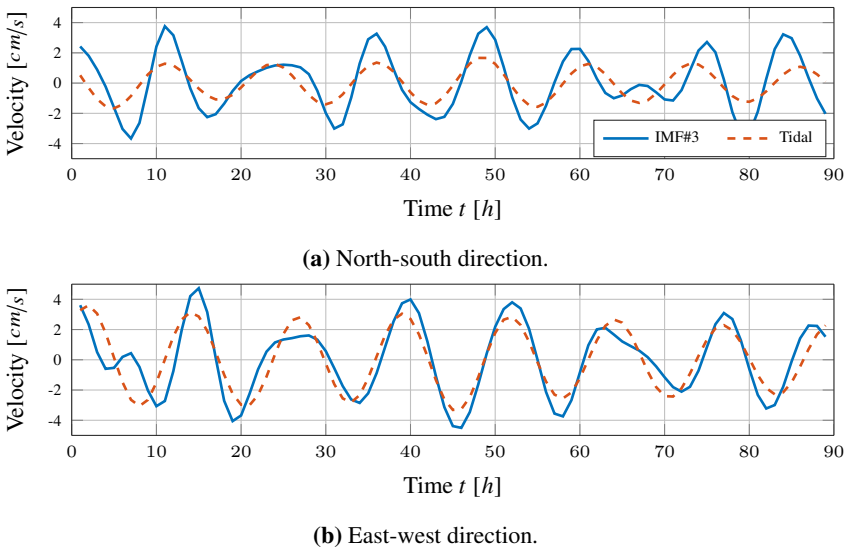


Figure 10.2: IMF#3 of the decomposed velocity signal of Iceberg 4 from May 8, 2015 3:30am to May 11, 2015 7:30pm. In comparison the tidal current using the tidal constituents M2, N2, S2 and K2 is shown.

10.3.1 Iceberg 4

Iceberg 4 was discovered close to Newfoundland at a latitude of about 51°N . The rotation rate of the Earth is about $\Omega = 7.2921 \times 10^{-5} \text{ rad s}^{-1}$. At the iceberg location, this results in an inertial oscillation period of about 15.5 h. The tidal currents at the iceberg location are relatively weak ([Padman and Erofeeva 2004](#)). The M2 tidal current constituent with a period of about 12.4 h dominates the tidal current. In north direction it has an amplitude of about 1.3 cm s^{-1} and in the east the direction about 3.2 cm s^{-1} . The other tidal current constituents have an amplitude of about 0.3 cm s^{-1} and 1 cm s^{-1} in north and east direction, respectively.

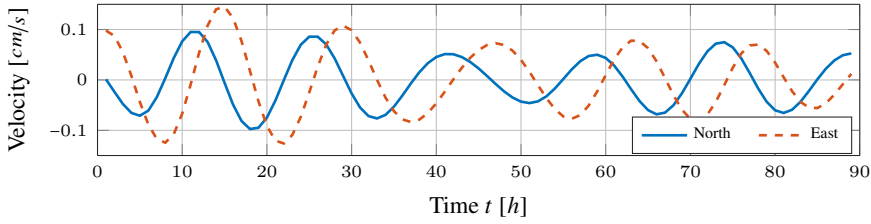


Figure 10.3: IMF#4 of the decomposed velocity signal of Iceberg 4 in the north and east direction from May 8, 2015 3:30am to May 11, 2015 7:30pm. This IMF has the same frequency as the inertial current oscillation.

The 37 days of iceberg velocity data is decomposed into ten IMFs. Of special interest are IMF#3 and IMF#4. These IMFs have an average period of 12.4 h and 16 h in the east direction and 11 h and 16 h in the north direction. Consequently, the tidal and inertial current components are detected and extracted in the iceberg velocity by the MEMD.

Fig. 10.2 shows IMF#3 and the sum of the tidal current constituents with a period of about 12 h. In east direction, the IMF#3 and the tidal current are very similar in phase and amplitude. In north direction, the phase is acceptably extracted but the amplitude is overestimated by the MEMD. Possible reasons are small errors in the tidal model, for example due to a coarse bathymetry map, the small amplitude of the tidal current that makes it difficult to extract the oscillation, and leakage between different numbered IMFs, for example IMF#3 and IMF#4. Leakage refers to a not perfect separation of two oscillations, which causes an oscillation that is present in two IMFs. The stronger amplitude in the north direction makes the tidal current less directional, such that the oscillation has a more *circular* behaviour.

It can be observed that the tidal current in the east direction is better extracted from the iceberg velocity than in the north direction. The frequencies of IMF#3 and IMF#4 are similar, which makes it difficult to separate both signals. The IMF#4, which represents the inertial current oscillation, is shown in Fig. 10.3.

The inertial current oscillation has a larger amplitude than the tidal current oscillation. In this period, the east direction of IMF#4 has a larger amplitude than the north direction. Consider a simplified inertial oscillation model

$$\frac{\partial u}{\partial t} - f v = \tau_u, \quad (10.1a)$$

$$\frac{\partial v}{\partial t} + f u = \tau_v, \quad (10.1b)$$

where u and v are the velocity in east and north direction, f is the Coriolis frequency and τ is a forcing term that depends on the wind (De Young and Tang

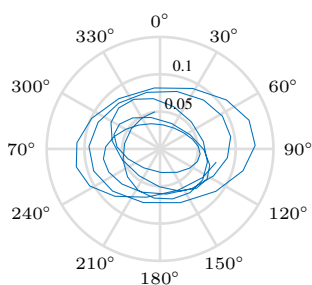


Figure 10.4: Polarplot of IMF#4 of Iceberg 4 from May 8, 2015 3:30am to May 11, 2015 7:30pm. The north direction is 0° and the east direction 90° .

1990). If the forcing is neglected the inertial oscillation should describe a circle. However, it is observed that the extracted inertial current is slightly elliptical (Fig. 10.4). Again, this may be due to a not perfect separation, but also due to the simplified model assumptions.

A new impulse to the inertial current oscillation can be observed at about 50 h. Here the phase changes and the ellipse is rotated and becomes more circular.

10.3.2 Iceberg 3651

For Iceberg 3651 the differentiation between tidal and inertial current is more challenging. The iceberg was tracked at a latitude of about 76.5°N . The period of the inertial oscillation is about 12.3 h. Consequently, it is almost the same as the period of the M2 and S2 tidal current constituents. Moreover, the tidal current is here stronger than at the location of Iceberg 4. The amplitude of the M2 tidal current constituent is in the north direction about 10 cm s^{-1} and in the east direction about 4 cm s^{-1} . The S2 tidal current constituent has an amplitude of about 4 cm s^{-1} in the north direction and 1.5 cm s^{-1} in the east direction. The tidal current describes an ellipse with the major axis directed to north-north-west.

The MEMD detects two oscillations with an average period of about 12.3 h and 12.5 h in the north and 12.2 h and 12.3 h in the east direction. Again, it is more challenging to detect correctly the oscillation in the direction with the smaller amplitude.

In general wind impulses, for example from a storm event, drive the inertial oscillation and cause the rotation of the surface in an entire region. These impulses may cause phase changes in the oscillation. In addition, both tidal and inertial oscillations have approximately the same frequency, which make a perfect separation between the two oscillations very challenging, and leakage can be observed in the results. Nevertheless, a combination of tidal and inertial current is detected in IMF#3 and IMF#4 (Fig. 10.5).

It can be seen that the amplitudes of the oscillation of the iceberg velocity is

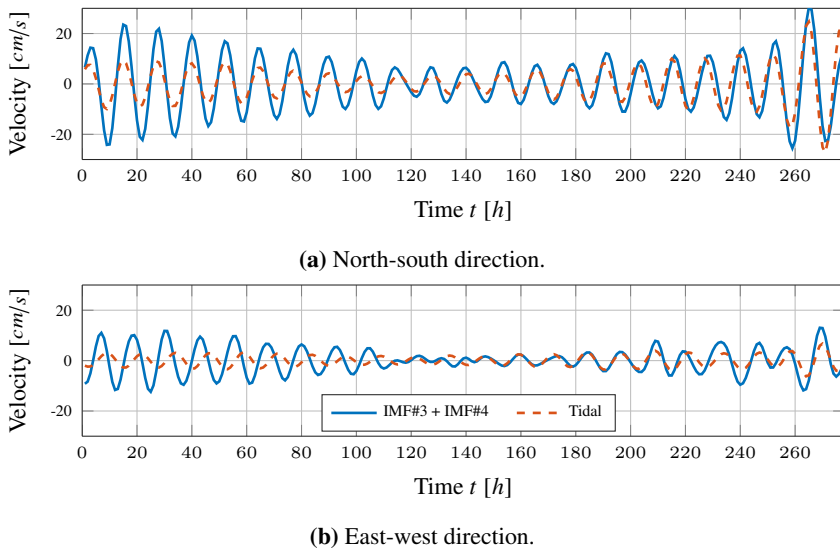


Figure 10.5: The sum of IMF#3 and IMF#4 of the decomposed velocity signal of Iceberg 3651 from August 8, 2016 2am to August 19, 2016 3pm. In comparison the tidal current using the tidal constituents M2, N2, S2 and K2 is shown.

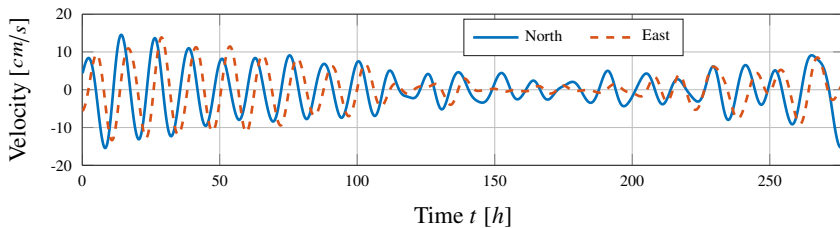


Figure 10.6: Tidal current subtracted from the sum of IMF#3 and IMF#4 of the velocity of Iceberg 3651 from August 8, 2016 2am to August 19, 2016 3pm.

larger than the tidal current amplitude at the beginning of the signal. Moreover, in the east direction the oscillations are out of phase for the first about 110 h. In the second part, the amplitude and phase of tidal current and iceberg velocity oscillation are similar.

Let us assume that the tidal current predicted by the Tidal Current Driver is approximately correct. In that case, we can subtract the tidal current from the iceberg velocity oscillation that contains tidal and inertial current. The resulting oscillation approximates the inertial current oscillation (Fig. 10.6).

For the first about 105 h we can detect an inertial current oscillation. New impulses are detected at the end of the observation period. However, it seems that several wind events are present during that time, which may initialize and change the inertial current. The polar-plot of the first part of the observation period is

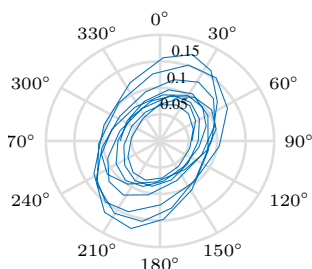


Figure 10.7: Polarplot of the subtraction of the tidal current from the sum of IMF#3 and IMF#4 of Iceberg 3651 from August 8, 2016 2am to August 12, 2016 11am (105 h). The north direction is 0° and the east direction is 90°.

shown in Fig. 10.7. The inertial current progression is slightly elliptical with the major axis directed to the northeast.

Let us assume that the amplitudes follow an exponential decay

$$A(t) = \exp(-rt), \tag{10.2}$$

where $1/r$ represents the dissipation time scale of the oscillation and t the time. A curve fitting results in an r of about 1.306×10^{-5} to $2.62 \times 10^{-5} \text{ s}^{-1}$. The detected dissipation time scale is, therefore, roughly 11 to 22 h. This is a shorter dissipation time than previously detected (De Young and Tang 1990). However, the dissipation time extracted here is roughly approximated, since only one event is analysed and an iceberg with unknown draft is used to estimate the inertial current oscillation. Nevertheless, it can be seen that by decomposing the signal and extracting the IMFs it is possible to receive significant information about local tidal and inertial current oscillations.

10.4 Further Analysis of the Iceberg Velocity using Current and Wind Data.

This section provides an outlook on how the MEMD can be used to analyse further current and wind models based on the iceberg velocity data.

10.4.1 Iceberg 3651

In the previous section, it was shown that the MEMD can help to identify the tidal and inertial current. Moreover, the measurement noise can easily be removed. Besides analysing the inertial and tidal frequencies, it is also possible to analyse IMFs with lower frequency components. This can be done separately or the IMFs with lower frequency components can be added up and the sum can be analysed. The biases may be analysed separately.

An example for Iceberg 3651 is given in Fig. 10.8. The sum of the IMFs

with lower frequency components and the bias for the iceberg velocity, surface and mean current and wind velocity is shown.

In north direction the iceberg velocity is well correlated with the surface current and wind velocity up to about 170 h (Fig. 10.8(a)). Thereafter, the velocities point in different directions. Moreover, the large peak at about 225 h is not present in the surface current and wind velocity. However, it is present in the mean current component. The mean current is calculated by taking the mean over the current layers up to a depth of 110 m. This decreases the peak at about 225 h. If only near-surface layers were considered the peak would be stronger, even though still not as strong as observed in the iceberg velocity. Nevertheless, it may be concluded that the iceberg is mostly driven by upper layer currents.

In the north direction, the bias of the iceberg velocity is well correlated with the bias of mean current (Fig. 10.8(b)). In the east direction, however, neither the currents nor the winds are positively correlated with the iceberg velocity. In fact, the correlation is negative. On the other hand, the oscillations of iceberg velocity and wind velocity are well correlated (Fig. 10.8(c)). If the wind and iceberg velocities are compared, it can be observed that the change of the iceberg velocity differs about 8 h to 20 h in comparison to the wind velocity changes (115 h, 200 h and 230 h). The surface and mean current are not well correlated. Especially the negative velocity change of the iceberg velocity at about 220 h lags about 24 h behind in the current velocities.

The latter illustrates the difficulty in the analysis of iceberg, wind and current data. In the east direction, the current velocity change lags behind the iceberg velocity while in the north direction the velocity change is simultaneous. Nevertheless, observing icebergs provides valuable information about the current and wind models and may help to improve them. The MEMD by decomposing the signal into different frequency modes eases the analysis and may reveal new features of the iceberg drift and its connection to current and winds and possibly the other driving forces.

However, these analyses have to be performed carefully, since the current, wind and tidal data may be inaccurate. Major uncertainties may corrupt their values in remote areas which have little direct data to drive or validate the models. Moreover, also in other areas the current, wind and tidal data may be inaccurate, which makes, for example, iceberg drift forecasting a very challenging problem (Anderson et al. 2016a).

10.5 Conclusion

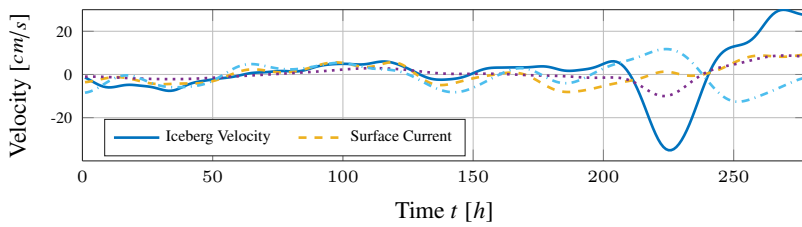
In this chapter, the MEMD was used to analyse iceberg velocity data. It was shown that the MEMD can help to detect and extract the tidal and inertial oscillation from the iceberg velocity data. The method was tested on two real iceberg trajectories.

Iceberg 4 was located close to Newfoundland where the period of the oscillations is about 12 h and 15.5 h. Hourly iceberg position updates are sufficient to detect these oscillations. Here the MEMD extracted without further post-processing the two oscillations. However, slight leakage was detected. This is not surprising since to separate two oscillations with such similar frequencies is an extremely challenging filtering problem.

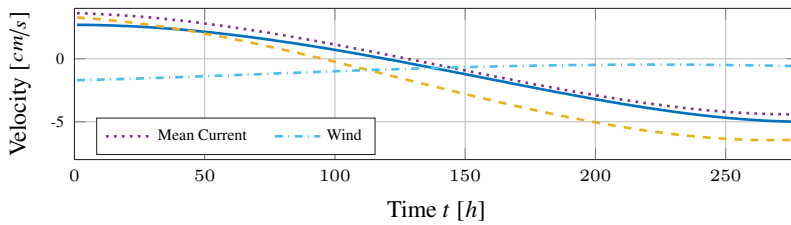
Iceberg 3651 was located in northern Baffin Bay. Here both oscillations have about the same frequency. Still two oscillations were detected by the MEMD but the inertial and tidal current were not well separated. Nevertheless, if information about the local tidal currents are available the inertial current oscillation could still be detected by subtracting in a second step the tidal oscillation from the extracted sum of tidal and inertial oscillation.

It was also shown that the MEMD may help to analyse correlations between current, wind and iceberg velocity. It is easily possible to remove fast frequency components or focus only on specific frequencies. This may help to improve the iceberg drift models but also the ocean current and meteorological models.

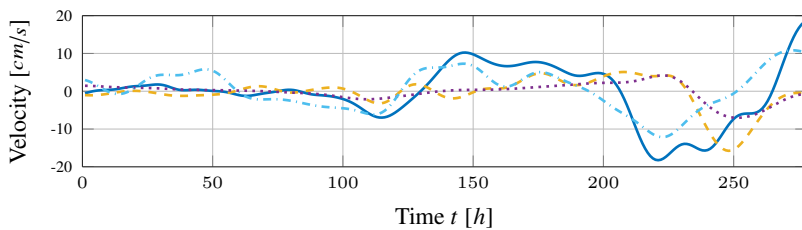
For future research to improve the separation of tidal and inertial oscillations one may consider implementing a two stage filtering process, in which the MEMD is on the first stage and a model based estimator on the second stage.



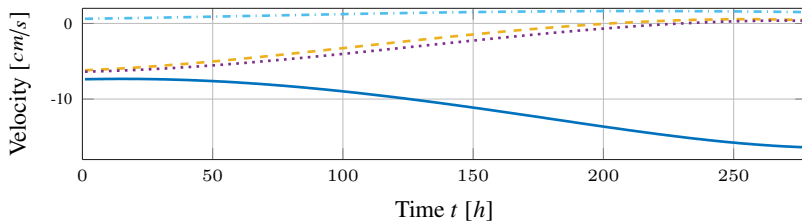
(a) Sum of IMFs in north direction.



(b) Bias is north direction.



(c) Sum of IMFs in east direction.



(d) Bias in east direction.

Figure 10.8: MEMD of iceberg, wind, surface current and mean current velocity of Iceberg 3651 from August 8, 2016 2am to August 19, 2016 3pm. The iceberg drifts at a latitude of about 76.5°N and a longitude of about $71.5^\circ\text{--}76.5^\circ\text{W}$. The lower numbered IMFs, which contain noise, tidal and inertial current oscillations, are removed and only higher numbered IMFs are considered. The wind velocity is scaled to 2% of its original velocity.

Chapter 11

Multivariate Empirical Mode Decomposition Forecast Scheme

This chapter is based on PAPER I. This chapter proposes an adaptive data-driven forecast algorithm using multivariate empirical mode decomposition (MEMD) to handle forecast problems. The algorithm identifies the common oscillatory modes and noise in the velocity of the floating object and its driving forces. After that, it decides which mode contributes to the movement and how the future movement of each mode can be predicted best with the available information. The efficacy of the proposed forecast algorithm is shown on a real iceberg drift dataset.

This MEMD forecast scheme is, in principle, a statistical forecast scheme as the one presented in Part III. The *training* set is based on the iceberg drift track and possible current and wind models. However, it is limited and the algorithm *forgets* everything that is not included in the multivariate empirical mode decomposition. Therefore, it is not able *learn*. Moreover, an error term is not identified. The forecast scheme has more similarities with a kinematic forecast model using components of the iceberg velocity to predict the future movement. Consequently, it was categorized in Part III.

11.1 Introduction

Oscillations are present in many applications from chemical engineering to medical applications to maritime processes (Miao and Seborg 1999, Taylor et al. 1998, De Young and Tang 1990). In the signal processing literature the topic received considerable attention to frequency tracking of stationary and non-stationary signals (Bittanti and Savaresi 2000) and oscillation characterisation (Srinivasan et al. 2007). In process control, the correct identification of oscillations can be vital to

the process and increases the performance of the considered application. For example, for process plants, oscillations due to nonlinearity, sub-optimal controller performance or disturbances may significantly affect the profitability and may be harmful to the plant equipment (Aftab et al. 2016). The correct identification and grouping of these oscillations improves the search for the root cause of the problem. Knowledge about oscillations also enables system prediction (Stone et al. 1996).

The empirical mode decomposition (EMD) is a data analysis method for non-linear and non-stationary time series that adaptively decomposes the series into a small number of independent intrinsic modes based on scale separation (Zhang et al. 2008). The multivariate EMD (MEMD) is an extension of the EMD, proposed by Huang et al. (1998), to n-variate signals (Ur Rehman and Mandic 2010b). In addition to the scale separation, the MEMD aligns modes of the n-variate signal. Consequently, common oscillatory modes of different signals can be grouped (Aftab et al. 2016).

The EMD is used in different forecast schemes to predict, for example, oil price changes (Zhang et al. 2008), the flow of passengers in a metro system (Wei and Chen 2012) or wind speed (Liu et al. 2012). Some of the forecast schemes connect the EMD with a learning algorithm based on neural networks (Wei and Chen 2012, Liu et al. 2012), and these schemes forecast a signal based on its past progression only.

In this chapter, a forecast scheme is proposed that uses the MEMD to decompose the observed and forecasted output signals together with all known input signals to detect common frequency modes. Moreover, it is assumed that forecasts of the input signals are available. However, these forecasts may be uncertain and error-prone, as is the case in iceberg drift predictions. Together with the MEMD, this can be used to forecast the output signals by first detecting which modes are highly correlated with the output signal and, second, checking if causality between the input and output signals for the separated modes exist.

11.2 Problem Description

The algorithm presented is designed to predict the output signals of a system. The discretisation of the set of ordinary differential equation of the system yields the following problem formulation:

$$\mathbf{x}_{k+1} = \mathbf{A}\mathbf{x}_k + \mathbf{B}_k\mathbf{u}_k + \mathbf{w}_k, \quad \mathbf{x}_0 = \mathbf{x}(t_0), \quad (11.1a)$$

$$\mathbf{y}_k = \mathbf{H}\mathbf{x}_k + \mathbf{v}_k, \quad (11.1b)$$

in which k denotes the samples taken at time t_k . The discretised states are represented by $\mathbf{x}_k \in \mathbb{R}^{n_x}$, the inputs by $\mathbf{u}_k \in \mathbb{R}^{n_u}$, and the measurements by $\mathbf{y}_k \in \mathbb{R}^{n_y}$. The vector $\mathbf{w}_k \in \mathbb{R}^{n_x}$ is state noise, which accounts for unknown disturbances

on the system states due to, for example, model uncertainty or uncertainty in the inputs \mathbf{u}_k . The system, input and output matrices are given by \mathbf{A} , \mathbf{B}_k , and \mathbf{H} , respectively. The measurement noise $\mathbf{v}_k \in \mathbb{R}^{n_y}$ is added to the measured outputs. At every time point t_k measurements $\mathbf{y}_{0:k}$, past and forecasted input signals $\mathbf{u}_{0:K}$ are available from the beginning of the observation to k or K , where $K > k$ (Fig. 6.7).

In addition, some input signals may be available from different sources m . These inputs $\mathbf{u}_{0:K}^{j,1:m}$ are all prone to errors and uncertainties, which makes the forecast of the system states extremely challenging.

Usually, several sources for wind and current forecasts are available providing, among others, a forecast for and at different frequencies. However, wind and especially, current forecasts are prone to errors and uncertainties. Moreover, the iceberg shape and drag coefficients are unknown, but required in the typically dynamic iceberg model, which introduces further uncertainties and sometimes poor forecast performance (Turnbull et al. 2015, Allison et al. 2014). If, however, the past iceberg trajectory is known, the forecast can be improved by estimating some of the iceberg shape parameters or correcting the current itself (Andersson et al. 2016a, Garrett 1985, Gaskill and Rochester 1984).

The data-driven algorithm proposed here avoids the necessary assumptions about iceberg parameters when using a dynamic model and forecasts the system only based on the past iceberg trajectory as well as all information available about the iceberg driving forces.

11.3 The Forecast Algorithm

In this section, a forecast algorithm is proposed that takes advantage of the alignment property of the MEMD (Sec. 3.2). The goal of this algorithm is to forecast the output

$$\mathbf{y}_{k+1} = \mathbf{H}(\mathbf{A}\mathbf{x}_k + \mathbf{B}_k\mathbf{u}_k + \mathbf{w}_k) + \mathbf{v}_{k+1}, \quad (11.2)$$

with the help of the observations $\mathbf{y}_{0:k}$ and all information of the input signals $\mathbf{u}_{0:K}^{1:m}$.

11.3.1 Basic Steps of Forecast Algorithm

1. Perform a 1st MEMD with the output signal $\mathbf{y}_{0:k}$ and all available input signals $\mathbf{u}_{0:k}^{1:m}$.
2. Perform the grouping algorithm and identify significant IMFs of the output signal \mathbf{y} .
3. Perform a 2nd MEMD with the input signals $\mathbf{u}_{0:K}^{1:m}$ (up to the forecast time t_K).

4. If the amount of IMFs differ in the 1st and 2nd MEMDs, then re-index the IMFs based on the correlation of the IMFs of the input signals $u^{1:m}$ in both MEMDs. The re-indexing has to be performed for the significant IMFs of the first MEMD only. The re-indexing guarantees that both MEMDs have the same amount of IMFs.
5. Perform the grouping algorithm for the 2nd MEMD and identify significant IMFs for the input signals $u^{1:m}$.
6. Connect both results of the grouping algorithm to know which IMFs of the input signal can be used to forecast the significant IMFs of the output signal.
 - (a) Forecast the output signal based on its past progression only (self-forecast).
 - (b) Use significant IMFs of the input signal to forecast the output signal (input-forecast).
7. For every significant IMF of the output signal, choose one of the two forecasts (forecast decision). Combine all IMF forecasts to the forecast of the output signal (forecast of the output signal).

11.3.2 Self-forecast

Before the self-forecast, the mean μ_i and standard deviation σ_i of the frequency of each significant IMF c_{ij} of the output signal \mathbf{y} are determined. IMFs with more than three maxima in the local signal (moving horizon) are fitted to a cosine signal, which gives the following nonlinear least-squares problem that, under mild conditions, can be reliably solved (Wright and Nocedal 1999)

$$\min_{\{\beta_i, \gamma_i, \phi_i\}} \sum_{n=k-l}^k \|c_{ij,n} - \mathbf{h}_n(\beta_i, \gamma_i, \phi_i)\|_{Q_n}^2 \quad (11.3a)$$

$$\begin{aligned} s.t. \quad & \mathbf{h}_n(\beta_i, \gamma_i, \phi_i) = \beta_i \cos(\gamma_i t_n + \phi_i) \quad \forall n = k-l, \dots, k, \\ & \mu_i - \sigma_i \leq \gamma_i \leq \mu_i + \sigma_i, \\ & -\pi \leq \phi_i \leq \pi, \\ & c_{ij,k} - \mathbf{h}_k(\beta_i, \gamma_i, \phi_i) = 0, \end{aligned} \quad (11.3b)$$

where $c_{ij,n}$ is the i^{th} IMF of the j^{th} output signal at time t_n and β_i , γ_i , and ϕ_i are the amplitude, frequency, and phase lag of the cosine function, respectively. An end-point constraint is introduced to avoid large deviation at the initial point of the

forecast. Moreover, Q_n can be used to weight recent times more strongly. Problems due to non-convexity were not experienced in the numerical experiments for this or the following optimisation problems.

The IMFs, which have less than three maxima in the local signal, and the residue are fitted with a third-order polynomial

$$\min_{\{\beta_{i,l_{0:3}}\}} \sum_{n=k-l}^k \left\| \mathbf{c}_{ij,n} - \sum_{l=0}^3 \beta_{i,l} t_n^l \right\|_{\mathbf{Q}_n}^2 \quad (11.4a)$$

$$s.t. \quad \mathbf{c}_{ij,k} - \sum_{l=0}^3 \beta_{i,l} t_k^l = 0, \quad (11.4b)$$

where $\beta_{i,l}$ are the parameters of the i^{th} IMF/residue and t_k is the time index. During the optimisation, the time horizon is scaled such that $t_k = 1$. The identity matrix was chosen as weighting matrix \mathbf{Q}_n in both optimisations.

11.3.3 Input-forecast

During the input-forecast, the significant IMFs of the output signal are forecasted with the significant IMFs of the input signal ($\delta_{ij} = 1$) that have the same index as

$$\min_{\{\beta_{ij}, \theta_i\}} \sum_{n=k-l}^k \left\| \mathbf{c}_{ij,n} - \sum_{\substack{p=1, \\ p \neq j}}^M \delta_{ip} \beta_{ip} \mathbf{c}_{ip,n} + \tilde{\delta}_{iN} \theta_i \right\|_{\mathbf{Q}_n}^2 \quad (11.5a)$$

$$s.t. \quad 0 \leq \beta_{ij} \leq \beta_{ij}^{max}, \quad (11.5b)$$

where the parameter β_{ij} are box constrained and δ_{iN} is the Kronecker delta

$$\tilde{\delta}_{iN} = 1, \quad \text{if } i = N \quad (11.6a)$$

$$\text{else } \tilde{\delta}_{iN} = 0. \quad (11.6b)$$

The algorithm can handle several forecast signals of the same system input $\mathbf{u}^{1:m}$. If the grouping algorithm identifies that n forecast signals of the same system input can be used to forecast the output signal, then they enter the optimisation (11.5) as a weighted sum

$$\mathbf{c}_{ij}^* = \sum_j^n \lambda_j \mathbf{c}_{ij}, \quad (11.7)$$

where λ_j are the weights with $\sum_j \lambda = 1$. The quantity of components M in (11.5) reduces the amount of different input signal groups P . The identity matrix was chosen as weighting matrix \mathbf{Q}_n in the optimisation.

All optimisation problems are solved with MATLAB using YALMIP (Lofberg 2004).

11.3.4 Forecast Decision

In this chapter, the self-forecast is used as the default and replaced if the value of the objective function of the input-forecast is smaller than the one of the self-forecast. Moreover, even if the residue is not identified as significant, then it is always considered and forecasted by the input-forecast.

11.3.5 Forecast of the Output Signal

Finally, the forecasted IMFs are combined to create the forecasted output signal

$$y_j(t) = \sum_{i=1}^N \delta_{ij} c_{ij}(t), \quad (11.8)$$

where it is assumed that the j^{th} component is an output.

11.4 Case Study

11.4.1 The Dataset

The studied iceberg in this chapter is Iceberg 4 (Sec. 4.1.3).

Hourly surface current, daily mean current and six-hourly wind data was received from the E.U. Copernicus Marine Service (Sec 9.5 (EU Copernicus Marine 2006)). Furthermore, a prediction of tidal current was calculated with the Tide Model Driver (TMD). In addition, measured wind data at a weather station close to the iceberg location was taken from the Environment Canada homepage. Consequently, the input data used in the case study does not represent a real forecast. Nevertheless, the case study shows the power of the proposed forecast algorithm.

11.4.2 Forecast Results

Three input groups are considered during the forecast: a tidal (one signal), a current (two signals), and a wind group (two signals). A five-days moving horizon is used in the grouping algorithm. At the beginning of the forecast, the moving horizon develops until day five of the iceberg drift observations.

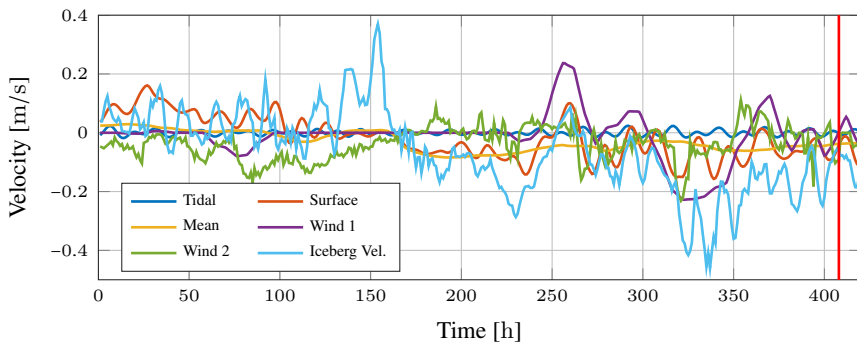


Figure 11.1: Input and output signals. The vertical red lines indicate the initial point of the forecast. The wind is scaled to 2% of its magnitude.

Forecast Example

To clarify how the forecast algorithm works the MEMD and the grouping algorithm is shown on one forecast example. To simplify the following presentation, the components of the north-south direction are shown only. One output signal and five input signals are considered in the forecast scheme (Fig. 11.1).

The result of the two MEMDs of the forecast algorithm is shown in Figure 11.2. The resulting IMFs in both decompositions are similar. Apparent differences in IMF#1-#3 are due to the small figure size and different line widths. Leakage effects between IMF#6 and #7 probably cause the difference in the Wind 1 signal.

Table 11.1 shows the results of the grouping algorithms. Significant IMFs of each signal are marked with \times . A circle around the IMF index indicates if the input-forecast is used. The zero, arrow up or downward mark shows if the input group is not considered, amplified or weakened in the input-forecast. The superscript gives the fraction with which each signal of the same input group is multiplied.

IMF#1 and IMF#2 represent measurement noise. IMF#3 and IMF#4 represent tidal (M2 and S2) and inertial current, respectively. The mean period of both oscillations is well detected. However, leakage between both IMFs occurs. Consequently, the separation between both modes is not perfect. In fact, this was expected, since the tidal current consists of several oscillations with periods around 12 h and 24 h. Moreover, the wind-driven inertial current is quite inconsistent as new wind impulses can cause phase shifts. The input-forecast amplifies the tidal current, weakens the surface current component, which also has tidal current information, and removes the wind component.

IMF#5 is forecasted by wind inputs only. The self-forecast scheme is used for IMF#6. This is not surprising since we detected leakage between IMF#6 and #7 of

Table 11.1 Signal composition of mode alignment in the iceberg forecast example.

	#1/#2	#3	#4	#5	#6	#7	#8	Res.
Ic.Vel.	-	×	×	×	×	-	×	×
Tidal	-	×↑	×↑	-	-	-	-	×↓
Su.Cur.	-	×↓	×↓	-	-	-	-	× ^{0.45} ↓
Me.Cur.	-	-	-	-	×↑	-	×0	× ^{0.55} ↓
Wi. 1	-	-	-	× ^{0.15} ↑	× ^{1.0} ↑	-	×↑	× ^{1.0} ↑
Wi. 2	-	×0	×0	× ^{0.85} ↑	× ^{0.0} ↑	-	-	× ^{0.0} ↑

the Wind 1 component. The self-forecast scheme also forecasts IMF#8, showing that mean current and Wind 1 cannot represent the oscillation accurately.

The input forecast scheme is used by default with all considered input signals for the residual. The Wind 1 is strongly amplified while other signals are weakened. A constant offset $\theta_i = -0.093$ m/s is used.

The forecast of the example is shown in Figure 11.3, and the dynamic iceberg model is used for comparison (Sec 2.3). The forecast of the dynamic iceberg model is initialised with the correct iceberg velocity providing the model the same information as the MEMD forecast scheme. The wave force \mathbf{f}_r is neglected. In addition, deterioration of the iceberg is not considered. Consequently, the forecast is performed with the estimated iceberg shape at the beginning of the observation. After 12 h, the position error for the presented MEMD forecast scheme is 2 km, while it is 9.6 km for the dynamic model.

The Overall Forecast Performance

The iceberg forecasts for the first 19 d of the iceberg drift are shown in Figure 11.4. A single 12 h forecast trajectory is displayed every 24 h. The proposed MEMD scheme can forecast the iceberg trajectory quite accurately.

The only instances when the dynamic model performs better than the MEMD forecast scheme is when the iceberg enters the sizeable right-hand bend. Nevertheless, the average end-position errors of the MEMD forecast and of the dynamic iceberg model are 3.9 km and 6.7 km, respectively. The maximum forecast error of the MEMD forecast scheme is 6.8 km while it is 16.4 km using the dynamic iceberg model. Hence, the uncertainty in the iceberg forecast is reduced considerably by the MEMD forecast.

11.5 Conclusion

A simple and completely adaptive forecast algorithm using MEMD is presented. The algorithm decomposes each input and output signal into several oscillatory modes. Based on the correlation of each mode with the original signal, it is then decided which mode should be forecasted. Moreover, by comparison between two different forecast strategies of each mode, it is decided if the input signals provide sufficient information to forecast the output signal. Otherwise, the default self-forecast is used.

The algorithm can handle information with different time scales and sources of the same input signal. It automatically chooses which information will most likely result in a useful forecast.

The algorithm was successfully evaluated on real iceberg drift data. It outperformed the forecast based on a dynamic model and reduced the uncertainty in the forecast considerably.

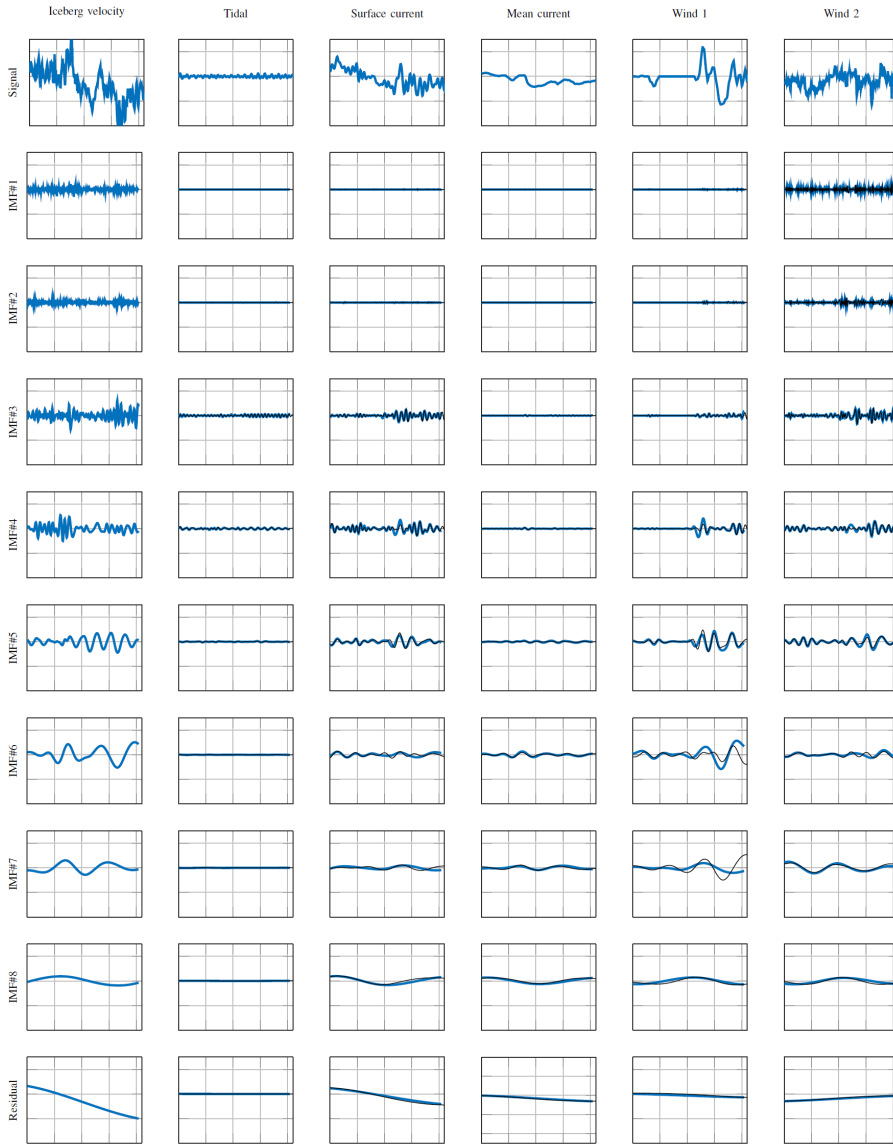


Figure 11.2: First (blue line) and second MEMD (black line) of the forecast algorithm input and output signals in the north-south direction. All y-axes have the same scaling. The wind is scaled to 2% of its magnitude.

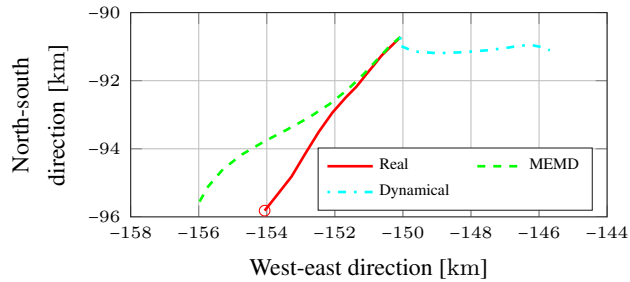


Figure 11.3: Forecast of the example considered. A forecast of the dynamic iceberg model is shown for comparison.

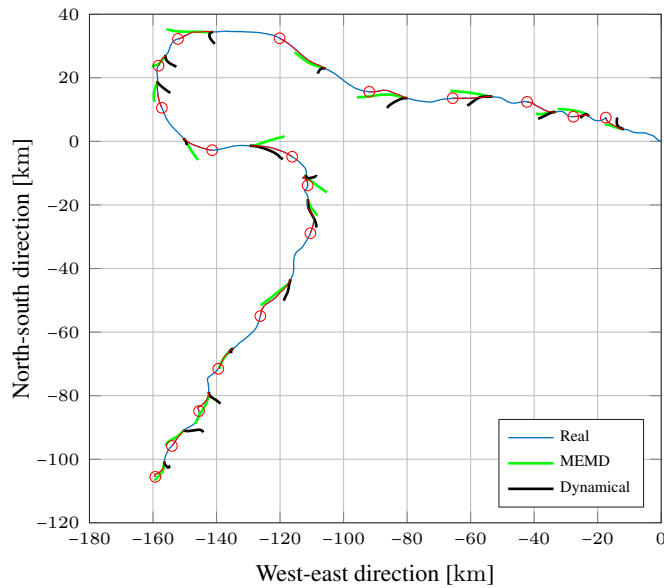


Figure 11.4: Forecast trajectories using the MEMD forecast scheme (green) and the dynamic model (black). Red represents the real 12 h trajectory shown, and the end point is marked. Every 24 h, a 12 h forecast trajectory is displayed.

Part V

Comparison of Forecast Algorithms

Chapter 12

Comparison of Statistical Iceberg Forecast Models

This chapter is based on PAPER C ([Andersson et al. 2018c](#)).

In this thesis, several iceberg forecast algorithms are proposed, which use iceberg position measurements to improve the short-term iceberg drift forecast. In this chapter, these statistical forecast methods and models are briefly reviewed. An extensive comparison between the statistical models, in addition to a dynamic iceberg forecast model, is performed on several iceberg drift trajectories. Based on this comparison a new statistical forecast scheme is proposed that combines some of the advantages of the other methods.

12.1 Introduction

Within this thesis several methods how to forecast an iceberg trajectory including past measurements are proposed (Sec. 7, Sec. 6, Sec. 9, Sec. 11). These sections are based on following articles [Andersson et al. \(2016d;a;b; 2017a\)](#). The proposals were tested and compared to the mechanistic dynamic model on different iceberg datasets. They all have in common that they are in average superior to the mechanistic dynamic model for short-term iceberg drift forecasts (up to 24 h). However, the methods themselves were not compared against each other. Moreover, it is difficult to conclude which one performs better based on the published articles.

Therefore, this chapter addresses this situation by giving a brief introduction to the methods and attempting to make a fair comparison between the forecast performances. The weaknesses and strengths of the methods are discussed and possible combinations to improve the forecast performance are suggested.

12.2 Theory and Methods

In this section the methods used in the forecast schemes are briefly presented.

When analyzing a temporal dataset of iceberg positions, the following discretization of a continuous time model can be used (3.2). In the context of this paper, the state \mathbf{x} is typically the two-dimensional iceberg position and velocity, \mathbf{u} the environmental driving forces, \mathbf{f} represents the momentum balance and \mathbf{w} the process noise. The position measurements \mathbf{y} is represented by the function \mathbf{h} and the measurement noise \mathbf{v} . The process noise \mathbf{w} accounts for unknown disturbances on the system states due to model uncertainty and uncertainty in the inputs \mathbf{u} .

Alternatively to the moment balance described in (3.2), this chapter uses a vector-autoregression model with the following structure

$$\mathbf{z}_k = \sum_{i=1}^p \mathbf{A}_i \mathbf{z}_{k-i} + \boldsymbol{\varepsilon}_k, \quad (12.1)$$

where $\mathbf{A}_i \in \mathbb{R}^{n_z \times n_z}$ is a real-values matrix containing the regression coefficients and $\boldsymbol{\varepsilon}_k \in \mathbb{R}^{n_z}$ is the residual, which are independently and identically distributed and serially uncorrelated (Barnett and Seth 2014). In context of this paper, $\mathbf{z} \in \mathbb{R}^{n_z}$ is either the two-dimensional iceberg velocity vector or a four-dimensional iceberg and wind velocity vector. The model (12.1) can be transformed into (3.2).

12.2.1 The Moving Horizon Estimator

The moving horizon estimator is used in several forecast schemes to estimate the states and parameters of the dynamic iceberg model. The MHE is introduced in Sec. 3.1.1.

12.2.2 The Extended Kalman Filter

In some of the forecast scheme the MHE can be replaced by the less complex extended Kalman filter (EKF). This may result in a loss of performance, but makes the implementation simpler. The EKF is introduced in Sec. 3.1.2.

12.2.3 Vector-Autoregression Model Fitting

The parameters of the Vector-Autoregression model (VAR) (12.1), the coefficients \mathbf{A}_i and the residual covariance matrix $\boldsymbol{\Sigma} = \text{cov}(\boldsymbol{\varepsilon}_k)$, are fitted to data by solving an optimization problem. The first represents the predictable structure of the data and the later the unpredictable. The VAR-model is introduced in Sec. 3.3.

12.2.4 The Multivariate Empirical Model Decomposition

The multivariate empirical mode decomposition (MEMD) is a fully data-driven adaptive signal processing method. The MEMD is an extension to multivariate

signals of the empirical model decomposition (EMD). The EMD decomposes a signal $\mathbf{z}(t)$ into amplitude- and/or frequency modulated components called intrinsic mode function (IMFs) $\mathbf{c}_l(t)$ and a bias term $\mathbf{r}(t)$. In the context of this thesis \mathbf{z} represents the iceberg velocity. The MEMD is introduced in Sec. 3.2.

12.3 Iceberg Drift Forecast Schemes

In this section the iceberg drift forecast schemes are briefly introduced. The forecast schemes are categorized in kinematic, statistical and hybrid forecast schemes similar to those in Marko et al. (1988), and help to connect the forecast schemes presented here to previously published ideas.

The *dynamic* forecast model uses the momentum equation, which calculates the acceleration based on the sum of forces acting on the iceberg. The *kinematic* forecast schemes predict the iceberg drift from superposition of past motions of the iceberg. The *statistical* forecast schemes use not only the observed iceberg motion, but also historical data at the iceberg location. A statistical iceberg model is fitted to the data that has a predictable and unpredictable part. The *hybrid* forecast schemes use a dynamic iceberg drift model but correct one or several parameters with help of the observed iceberg trajectory.

In the following sections it is explained how the forecasts are performed. In order to keep this review brief the particular methods that are used in a forecast scheme, like the moving horizon estimator or the empirical mode decomposition, are not explained in detail. Instead, a reference to the original paper and further references, directly explaining the particular methods used, are given in each section. Tab. 12.1 at the end of the section summarizes the performance of the methods.

12.3.1 Dynamic Forecast scheme

The dynamic forecast scheme (DYM) uses a dynamic iceberg drift model to predict the future iceberg trajectory (Sec. 2.3).

12.3.2 Statistical Forecast Scheme

The VAR Model Forecast Scheme

The Vector-Autoregression (VAR) model forecast scheme is presented in (Sec. 9). It uses the established kinematic relationship between iceberg, current and wind velocity

$$\boldsymbol{\nu} = \boldsymbol{\mu} + \alpha\boldsymbol{\omega}, \quad (12.2)$$

where $\boldsymbol{\nu}$, $\boldsymbol{\mu}$ and $\boldsymbol{\omega}$ are the iceberg, ocean current and wind velocity. The parameter α is about 0.017 to 0.02 (Smith 1993, Garrett et al. 1985, Bigg et al. 1997, Wagner et al. 2017). In addition, a current VAR model is identified based on historical

ocean current data in the region of interest. It is possible to identify a ocean current model for each grid cell for which current data is available, but it is also possible to choose one representative ocean current model for a certain region. The basic premise of the forecast scheme is that (12.2) holds and the current velocity (speed and direction) accounts for most of the uncertainty in the iceberg drift. The wind velocity, on the other hand, has a minor contribution to the uncertainty, since it is well forecasted by a weather forecast model. In this case the problem of forecasting the iceberg velocity can be transformed to a problem of forecasting the current velocity.

If wind information is received from a weather model, the following steps are performed in every forecast step for the VAR model:

1. Use a filter or estimator and the kinematic model (12.2) to obtain an estimate of the current velocity μ .
2. Forecast the current velocity μ using the identified VAR ocean current model.
3. Use (12.2) and the forecasted current velocity μ to calculate the corresponding iceberg velocity ν .
4. Integrate to the iceberg position.

In the VAR forecast scheme only a value for α has to be chosen. This reduces considerably the amount of parameters in comparison to the forecast schemes that use the mechanistic dynamic iceberg model. Moreover, information about the iceberg geometry are not necessary and the double integration from acceleration to position is avoided. On the other hand, the training set that is used to identify the VAR ocean current model influences the forecast performance.

The complexity of the forecast produced with the VAR model is moderate, since the VAR model is linear and a simple filter, for instance the moving average filter, can be used to smooth the iceberg position measurements.

12.3.3 Kinematic Forecast Schemes

The constant velocity forecast scheme

This is the simplest forecast model possible. It assumes that the iceberg velocity stays constant during the forecast periods and uses a simple integrator to calculate the iceberg position. Depending on the frequency in which iceberg position updates are available a filter is necessary to reduce the influence of measurement noise and fast frequency components. This forecast scheme is very simple and easy to implement, and provides a first estimate of the forecasted iceberg trajectory. Moreover, it is related to the theoretical current forecast scheme introduced

below. Both schemes assume either constant iceberg velocity or constant current velocity, which has a similar effect in the water drag force.

The MEMD Forecast Scheme

The multivariate empirical mode decomposition (MEMD) forecast scheme is presented in Sec. 11. It can detect oscillations, such as inertial or tidal oscillations, in the iceberg velocity signal. Several sources (ocean and weather models) that forecast current and wind velocities may be included to the scheme. These environmental models may forecast for a different time horizon and in different frequencies (daily, hourly etc.). Consequently, they may be more precise for different frequency bands.

The main idea is, therefore, to decompose the inputs (current and wind velocities) and the output (iceberg velocity) into frequency modulated components. Afterward, each frequency band is forecasted separately for each direction with the kinematic relationship

$$\nu^i = \sum_k \eta_k^i \mu_k^i + \sum_k \gamma_k^i \omega_k^i, \quad (12.3)$$

where η and γ are weighting parameters. The superscripts are related to the frequency bands and the subscript to possible multiple inputs from different wind and ocean current models.

The model (12.3) is similar to the kinematic model (12.2), but also uses a weighting factor for the current input. Smith (1993) used the same kinematic model, but he did not decompose the signal into different frequency bands. For each forecast step and frequency band the weighting parameters are recalculated based on the observed iceberg trajectory. Then it is evaluated for each frequency band whether the kinematic model 12.3 can forecast the iceberg velocity. Consequently, prior to each forecast it is assessed if causality between inputs and outputs exists, which is known as the Granger's causality principle (Granger 1969). If the assessment is negative the iceberg velocity of that frequency band is only forecasted with the past iceberg velocity.

The decomposition of the input and output signals into their frequency bands is performed by the MEMD. With the MEMD the data is filtered and oscillations, such as like tidal and inertial oscillations, are detected. Each frequency band is forecasted separately. Consequently, it is possible to include several wind and ocean current models, and choose for each frequency band which of them fit best to the observed iceberg velocity. On the other hand, this forecast scheme is the most complex and time consuming of all schemes presented in this article. In addition, it is necessary to observe the iceberg for some time. It is recommended to have at least two extrema of the oscillation that one would like to detect in the

data set. In case of the iceberg drift the inertial and tidal oscillations are the most important fast oscillations. Therefore, the MEMD needs iceberg drift data of about one day before it can detect these oscillations. The measurement frequency should exceed the Nyquist frequency (about 6 h). The MEMD becomes more precise as more data becomes available. As the MEMD forecast is purely data driven it can be difficult to pinpoint the cause of a good or bad forecast result (Andersson et al. 2017a).

An important adjustment from the original forecast algorithm presented in Sec. 11.3.1 is that if the 1st and 2nd MEMD result in a different amount of IMFs the *Self-forecast* (Sec. 11.3.2) is used without the *re-indexing* presented in Step 4. of the algorithm. The re-indexing is removed, since it is difficult and tends to introduce errors.

12.3.4 Hybrid Forecast Schemes

Ancillary current forecast scheme

The ancillary current forecast scheme (ACF) is proposed in Section 6. It was also used in a switching scheme in Sec. 8. The forecast scheme is a *hybrid* between mechanistic dynamic and statistical models, since it uses the mechanistic dynamic model but corrects some of its parameters based on the observed drift of the iceberg.

This forecast scheme was motivated by the idea of Smith (1993) who proposed to correct the drag coefficients (from air and water) of the dynamic iceberg model to improve the forecast. The correction of the drag coefficients based on past observation was also performed by Turnbull et al. (2015). In Section 6 it was shown if the drag coefficients are used as optimization variables the resulting variables lose their physical meaning and cannot be considered drag coefficients anymore. In addition, the estimated drag coefficient and chosen cross-sectional areas of the iceberg are codependent. If this correction scheme is used in a moving horizon window, strong changes and peaks of the drag coefficients were observed that degrade the forecast performance. The product of cross-sectional area and drag coefficients can only be estimated with a sufficiently long observation horizon (which guarantees that ocean current and wind inputs are unbiased). Alternatively to correcting the drag coefficients, the idea of an ancillary current was proposed (Sec. 6). The ancillary current is an artificial corrective current, which is added to the current input received from an ocean model

$$\tilde{\mu} = \mu + \mu^*, \quad (12.4)$$

where μ , $\tilde{\mu}$ and μ^* are the current from the ocean model, the corrected current and the ancillary current, respectively. The ancillary current is assumed to be

constant during the forecast and recalculated every time a new iceberg position measurement becomes available. This is done with a moving horizon estimator (Sec. 3.1.1). A simpler estimator, like the extended Kalman filter (Sec. 3.1.2), may also be used. The ancillary current has a smoother progression than the drag coefficients with less sudden changes and, therefore, improves the forecast performance considerably (Andersson et al. 2016a).

The underlying assumption of the ancillary current μ^* is that the current from an ocean model μ is biased, and that this bias changes only slowly over time. In fact, two other variables to correct the current input may also be used, e.g. absolute current velocity and direction. The desired property of the correction variables is that they only change slowly during the forecast.

In Andersson et al. (2016a) gives an example of how to predict the forecast performance based on the assumption that the ancillary current changes slowly over the forecast horizon.

Theoretical Current Forecast Scheme

The ancillary current forecast scheme uses currents from an ocean model (or other sources) at all times. With the ancillary current the deficiencies of the iceberg drift model and the data are captured and corrected. The approach corrects the current input, since this input is the source of the largest uncertainty (error). During the short-term forecast the ancillary current is assumed constant, since it is assumed that the bias in the current input varies slowly. Consequently, it is assumed that the first derivative of the current input $\dot{\mu}$ is approximately correct. If this is not the case and the ancillary current changes quickly, it may produce large forecast errors.

If the ancillary current changes quickly it may be beneficial to not use the current input μ at all, but estimate the total theoretical current instead (Andersson et al. 2016c)

$$\hat{\mu} = \mathbf{0}\mu + \mu^*, \quad (12.5)$$

where the $\mathbf{0}$ indicates that the ocean current input is not used.

The theoretical current $\hat{\mu}$ and it is assumed constant during the forecast. The theoretical current can be estimated in the same way as the ancillary current.

The theoretical current forecast scheme (TCF) is strongly related to the ancillary forecast scheme, but avoids error propagation from the ocean current model (or other current sources). On the other hand, a possibly valuable source of information is excluded from the forecast scheme. In this forecast scheme the main changes in the iceberg velocity after the transition period are caused by wind and wave inputs. Consequently, this forecast scheme has similarities with the constant iceberg velocity forecast scheme, which is a much simpler forecast scheme (Sec.

12.3.3).

Inertial Current Forecast Scheme

The inertial current forecast scheme (ICF) is presented in Sec. 7. It is also used in Sec. 8 to switch between the inertial and ancillary current forecast scheme.

The inertial current forecast scheme uses the mechanistic dynamic iceberg model in combination with a simple ocean current model. Instead of using a current input from ocean models or other sources as the ancillary current forecast scheme does, the inertial current forecast scheme estimates the complete ocean current. It assumes that the current consists of an oscillatory and slowly varying component

$$\tilde{\boldsymbol{\mu}} = \overline{\boldsymbol{\mu}} + \underline{\boldsymbol{\mu}}, \quad (12.6)$$

where $\overline{\boldsymbol{\mu}}$ and $\underline{\boldsymbol{\mu}}$ are the velocities of a inertial oscillation and slowly varying part, respectively.

The oscillatory part is the wind driven inertial oscillation, which can be approximated by

$$\dot{\overline{\boldsymbol{\mu}}} = \mathbf{B}(\boldsymbol{\omega}) + f\mathbf{k} \times \overline{\boldsymbol{\mu}} - c\overline{\boldsymbol{\mu}}, \quad (12.7)$$

where $\mathbf{B}(\boldsymbol{\omega})$ is the wind excitation, c is a decay factor, f is the Coriolis frequency and \mathbf{k} is the unit vector directed upwards parallel to the z -axis (De Young and Tang 1990). In the regions studied in this article the inertial oscillation has a period of about 12 h to 16 h.

The inertial current forecast scheme is more advanced than the theoretical current forecast scheme due to an explicit ocean current model. In this study the tidal currents were neglected in the inertial current forecast scheme. However, it is possible to extend (12.6) to explicitly consider the tidal currents, which should improve the method.

During the forecast the slowly varying part of the current is assumed constant while the oscillatory part is propagated with the model (12.7). Consequently, the inertial current forecast scheme is "located" between the ancillary and theoretical forecast schemes. Due to the explicit consideration of the inertial current it is expected that the slowly varying part is estimated more accurately. The estimation is challenging and performed with a moving horizon estimator (Andersson et al. 2016b). It is recommended to not use a simpler estimator, like the EKF, since it may have problems to separate the two current components.

12.4 Dataset

In this section the iceberg, current and wind datasets, which are used in the comparison of the methods are introduced.

Table 12.1: Brief summary of the forecast methods presented in Section 12.3. For each forecast method the name, abbreviation, classification, requirements and a short description is given. Except of the dynamic model every forecast scheme needs iceberg position measurements.

Name (-forecast scheme)	Abbr.	Class.	Requirement	Description
Dynamic model	DYM	dynamic	Current, wind, (waves) from meteorological and oceanographic models	Forecast of iceberg trajectory with momentum balance that calculates the acceleration based on sum of forces on the iceberg.
VAR model	VAR	statistical	Iceberg position meas.; Wind from meteorological model; Historical ocean current data	Offline identification of an statistical ocean current model. Estimation of iceberg and current velocity with kinematic iceberg model and a filter. The current velocity is forecasted with a statistical ocean current model, and the iceberg velocity is again calculated with kinematic iceberg model.
Constant velocity	CVF	kinematic	Iceberg position meas.	Estimation of iceberg velocity with filter. Constant iceberg velocity in forecast period.
MEMD model	MEMD	kinematic	Iceberg position meas.; Current, wind, (waves) from meteorological and oceanographic models (can be several)	Decomposition of inputs (current and wind vel.) and output (iceberg vel.) into frequency bands. Decision if causality exists between inputs and output for each frequency band. As a result iceberg vel. is forecasted in each band by linear combination of inputs or otherwise by autoregression.
Ancillary current	ACF	hybrid	Iceberg position meas.; Current, wind, (waves) from meteorological and oceanographic models	Correction of ocean current input of the dyn. model with estimated ancillary current, which is assumed constant during the forecast period.
Theoretical current	TCF	hybrid	Iceberg position meas.; Wind from meteorological model	Estimation of complete (theoretical) ocean current needed to explain observed iceberg drift. Does not use current input from ocean model. Estimated current is assumed constant in forecast period.
Inertial current	ICF	hybrid	Iceberg position meas.; Wind from meteorological model	Estimation of ocean current with simplified inertial and mean ocean current model. Mean current is assumed constant and oscillation of inertial current is propagated by a model in forecast period.

12.4.1 Iceberg Data

To assess the performance of the models described above, we compared their predictions with iceberg, current and wind datasets were recorded in 2015 and 2016. The characteristics of these datasets are described in detail in Sec. 4.

12.4.2 Current data

The current data set was received from the E.U. Copernicus Marine Service ([EU Copernicus Marine 2006](#)). The *Global Ocean 1/12° Physical Analysis and Forecast model updated daily* was used. The Operational Mercator global ocean analysis and forecast system at 1/12° provides 10 days of 3D global ocean forecasts updated daily. More specifically in this article the one hour surface current and daily layered mean current data is used. The depth of the layered current data is about 110 m. In fact, the current is already corrected by observation. Consequently, the case study presents hindcasts results. However, observation data in Northern Baffin Bay may be limited, reducing the possibility to correct the ocean current forecast.

The data assimilation into the model includes for instance drift data from SVP drifting buoys and sea surface height measurements from GLOSS, BODC and other sources. For more information the reader is advised to visit the E.U. Copernicus Marine Service webpage ([EU Copernicus Marine 2006](#)).

12.4.3 Wind Data

As wind source, the *Global ocean wind L4 near real time 6 hourly observations* wind model from the E.U. Copernicus Marine Services is used. The wind fields are estimated from scatterometer retrievals. They have a horizontal resolution of $0.25^\circ \times 0.25^\circ$ and are updated every 6 h. Possible empty data points were removed from the data set. In addition, the wind data points were linearly interpolated onto the current grid cells. For more information the reader is advised to visit the E.U. Copernicus Marine Service webpage ([EU Copernicus Marine 2006](#)). The wind data set does not represent forecasted wind. However, this will not influence the overall results and conclusions of the study. In fact, the dynamic iceberg drift model is likely the largest beneficiary.

12.5 Performance Indices

In order to quantify the forecast performance at a specific time, the mean $\hat{\zeta}$ over all end position forecast errors $\zeta = |\hat{\chi}_{k,end} - \chi_{k,end}|$ is calculated

$$\hat{\zeta}_N = 1/K \sum_{k=1}^K \zeta_k, \quad (12.8)$$

where $\hat{\chi}_{k,end}$ and $\chi_{k,end}$ are the end position of the forecast and measured drift trajectory at time t_k , K is the amount of forecasts and N the length of the forecast period.

An alternative, which considers the whole forecasted trajectory and not just the

end points, is the square root of the mean squared distance between the forecasted $\hat{\chi}$ and measured χ iceberg trajectory

$$\Xi_{N,k} = \sqrt{\frac{1}{N} \sum_{i=1}^N \|\hat{\chi}(t_k + ih) - \chi(t_k + ih)\|_2^2}, \quad (12.9)$$

where t_k is the initial time of the forecast and h is the time between measurements. The performance index (*PI*) for the whole observation horizon is the root mean square of ζ_N (12.9) with the same forecast horizon N

$$PI_N = \sqrt{\frac{1}{K} \sum_{k=1}^K \Xi_{N,k}^2}, \quad (12.10)$$

A relative performance index is the forecast error relative to the movement of the iceberg

$$|\chi_{k,end} - \hat{\chi}_{k,end}| < \kappa |\chi_{k,end} - \chi_{k,init}|, \quad (12.11)$$

where $\chi_{k,init}$ is the initial position of the measured iceberg trajectory at time t_k . The value κ is a performance index. For this chapter the following forecast categories are chosen (Fig. 9.1):

- Bad forecast: $\kappa > 1$,
- Acceptable forecast: $1 \geq \kappa > 0.75$,
- Good forecast: $0.75 \geq \kappa > 0.5$,
- Excellent forecast: $\kappa < 0.5$.

12.6 Comparison Iceberg Drift Forecast

In this section the performance of the iceberg drift forecast methods are discussed. Each forecast method predicts every hour the iceberg trajectory. These forecasts are compared to the actual observed iceberg trajectory and the error is calculated (Section 12.5).

In addition to the short-term forecast schemes presented in Section 12.3, the static forecast scheme (STAT) is included in the comparison. It is a "pseudo" forecast, which assumes that the iceberg does not move but remains at the initial location. It gives an indication of how fast the iceberg moves.

For each forecast method the same tuning was used for all iceberg trajectories

to show the robustness of the methods. The amount of forecasts of each iceberg varies due to the varying amount of available data for each iceberg.

Since a longer period is examined, a simple deterioration model is implemented assuming a daily 2% deterioration of the iceberg length, width, draft, and sail height. The results are relatively insensitive to different deterioration rates.

The discussion begins with Iceberg 2, since it is the iceberg with the shortest observation horizon, which helps to create clear figures. For the other icebergs it is often unpractical to show, for example, the forecast trajectories. A more detailed discussion of the forecast performance for the other icebergs is moved to the end of the chapter 12.A.

12.6.1 Iceberg 2

For Iceberg 2 66 forecasts are performed. The mean end-position error (12.8) and the standard deviation of every forecast method for different forecast horizons are given in Tab. 12.2.

The MEMD forecast scheme performs best up to a forecast horizons of 12 h. However, the MEMD scheme needs more data than the other methods before a forecast can be performed. Therefore, it begins later than the others. For forecasts of 12 h to 18 h the TCF scheme performs best. The VAR forecast scheme produces the smallest error for a forecast horizon of 24 h. Interestingly, the standard deviation of CVF and STAT forecast scheme are small indicating that the iceberg velocity experience similar changes over the whole observation horizon. The ancillary forecast scheme performs badly. One reason is that the ocean current input has to be corrected strongly. Moreover, this adaptation also changes constantly.

The end-position error of a 12 h forecast of every method is shown in Fig. 12.1(a). The corresponding iceberg trajectory and the forecast trajectories of the different methods are shown in Fig. 12.1(b). For reason of clarity the forecast trajectories are only shown for this iceberg and only every 12 h. Even though the forecast error is very similar for the statistical methods the end positions of the 12 h forecast trajectories differ considerably. Nevertheless, the forecast direction is often similar such that the trajectories are in the same sector.

The dynamic forecast model produces always a large forecast error, since the environmental forcing is not correctly represented for the iceberg. The ocean current direction is directed opposed to the drift direction over almost the entire observation period, which is the main reason for the large forecast error (mean absolute error about 140°). The wind direction correlates better with the iceberg drift in the observation horizon (mean absolute error about 60°), but at the beginning of the observation the iceberg drift and wind direction do not correlate well, which also contributes to the large forecast error in the first hours of the observation. Stronger

Table 12.2: Mean end-position-error (12.8) [km] for different forecast horizons of Iceberg 2. The standard deviation is given in brackets and the best forecast is marked bold. The best PI (12.10) is marked by a star. The static model gives an indication the iceberg drift distance within the forecast horizon.

	1 h	6 h	12 h	18 h	24 h
CVF	0.31 (0.18)	1.8 (1.0)	3.5 (1.7)	5.8* (2.5)	8.3* (3.4)
ACF	0.19 (0.10)	1.9 (1.3)	4.2 (3.5)	6.8 (4.1)	10.9 (5.8)
TCF	0.17 (0.08)	1.6 (1.0)	3.6 (2.6)	5.7 (3.5)	8.8 (5.1)
ICF	0.16 (0.07)	1.8 (0.9)	3.8 (2.6)	5.8 (3.7)	9.1 (5.1)
VAR	0.29 (0.16)	1.8 (0.9)	3.8 (2.3)	5.7 (3.7)	8.0 (4.8)
MEMD	0.10* (0.05)	1.6* (0.8)	3.6* (1.7)	6.2 (3.0)	10.0 (6.2)
DYM	0.52 (0.22)	4.4 (1.9)	9.0 (3.6)	12.9 (5.4)	16.5 (6.6)
STAT	0.46 (0.18)	2.7 (1.0)	5.6 (1.7)	7.8 (1.4)	10.7 (2.3)

winds and better directional correlation are the main reasons for the improvement of the dynamic iceberg forecast between 40 h to 65 h.

All statistical methods reduce the forecast error compared to the dynamic iceberg model considerably. The statistical models produce larger errors when the iceberg changes direction at 10 h and 45 h. The MEMD performs better than the other methods in the period 40 h to 50 h. Otherwise, it can be observed that the statistical methods behave similarly (Fig. 12.1(a)). Only the dynamic model has a completely different forecast behaviour, because the badly specified environmental forces are not corrected.

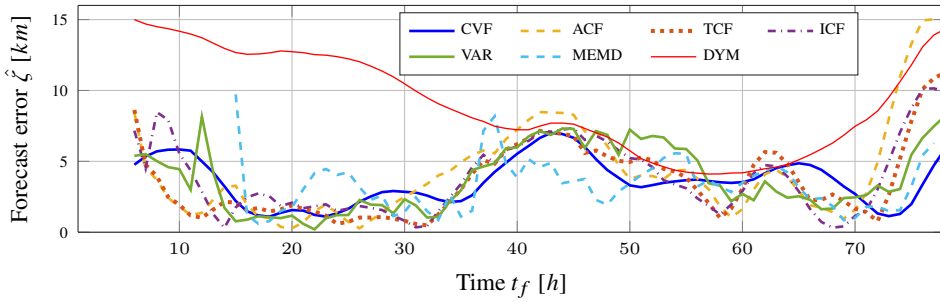
12.6.2 Iceberg 1

For Iceberg 1 160 forecasts are performed. The mean end-position error (12.8) and the standard deviation of all methods are shown in Tab. 12.3. The considerable larger forecast errors compared to Iceberg 2 are caused by several loops with a period of about 18 h to 24 h in the iceberg trajectory that are most likely caused by the current flows in and out of Conception Bay (between Grates Cove and Bonavista (Fig. 4.3)). A more detailed discussion can be found in 12.A.1.

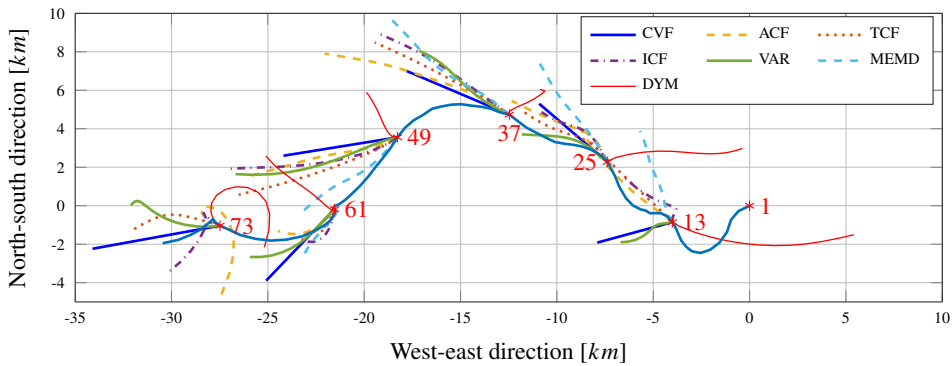
12.6.3 Iceberg 4

For Iceberg 4 674 forecasts are performed. It breaks apart after about 5.5 days. After evaluating the pictures of the iceberg, it is assumed that breakage happens at about 2/3 of the waterline length. Mass, width, draft, and sail are adjusted accordingly in the simulations. The two remaining icebergs (Iceberg 4 and Iceberg 4-3) are likely more dome-shaped than wedged. The shape factor is, therefore, adjusted after the breakage.

The performance of each forecast method is given in Tab. 12.4. The forecast



(a) Forecast error for different forecast schemes with a forecast horizon of 12h for Iceberg 2.



(b) Iceberg drift trajectory of Iceberg 2 and the 12 h forecast trajectories of the different forecast methods. The number marker corresponds to the time t_f in the upper figure.

Figure 12.1: Forecast results for Iceberg 2. The forecast error is shown in the upper figure, while the lower figure shows the corresponding iceberg drift trajectory.

of Iceberg 4 is much better than of Iceberg 1. The dynamic forecast model is outperformed by all statistical methods for the considered forecast horizons. Large errors in the statistical forecast (besides the MEMD and CVF) are not observed. More details can be found in 12.A.2.

12.6.4 Iceberg 4-3

For Iceberg 4-3 1161 forecasts are performed. The performance of each forecast method is given in Tab. 12.5. It is expected that the iceberg is small since it is a piece of Iceberg 4. The iceberg moves relative quick and the drift trajectory has several loops and direction changes. Therefore, the CVF and TCF that assume constant iceberg or current velocity perform not well. The introduction of the inertial current model in the ICF helps to detect the fast frequency components and improves the forecast considerably. Similarly the VAR model is able to forecast

Table 12.3: Mean end-position-error (12.8) [km] for different forecast horizons of Iceberg 1. The standard deviation is given in brackets and the best forecast is marked bold. The best PI (12.10) is marked by a star. The static model gives an indication the iceberg drift distance within the forecast horizon.

	1 h	6 h	12 h	18 h	24 h
CVF	0.81 (0.58)	5.2 (3.6)	9.6 (6.3)	15.0 (9.3)	20.6 (11.8)
ACF	0.34 (0.25)	3.4* (2.3)	7.3* (4.5)	11.8 (6.9)	17.5 (9.1)
TCF	0.38 (0.29)	4.0 (2.8)	8.6 (5.5)	13.0 (7.9)	18.6 (10.2)
ICF	0.33 (0.22)	3.6 (2.0)	7.8 (4.3)	12.0 (6.7)	17.1 (8.5)
VAR	0.72 (0.52)	3.9 (2.7)	6.6 (4.2)	9.6* (6.1)	12.8* (7.5)
MEMD	0.25* (0.21)	4.0 (2.7)	8.5 (5.2)	14.3 (10.4)	22.3 (24.1)
DYM	0.70 (0.46)	5.0 (2.3)	9.5 (4.5)	13.7 (6.2)	17.6 (7.2)
STAT	0.87 (0.58)	4.9 (3.0)	8.5 (5.0)	11.5 (7.1)	14.4 (9.0)

Table 12.4: Mean end-position-error (12.8) [km] for different forecast horizons of Iceberg 4. The standard deviation is given in brackets and the best forecast is marked bold. The best PI (12.10) is marked by a star. The static model gives an indication the iceberg drift distance within the forecast horizon.

	1 h	6 h	12 h	18 h	24 h
CVF	0.35 (0.19)	1.9 (1.2)	3.5 (2.8)	5.7 (4.5)	8.1 (6.5)
ACF	0.22 (0.13)	2.2 (1.2)	4.2 (2.4)	6.7 (3.8)	9.6 (5.6)
TCF	0.21 (0.12)	2.0 (1.1)	3.9 (2.2)	6.2 (3.7)	9.0 (5.7)
ICF	0.18 (0.11)	1.8* (1.0)	3.6 (2.1)	5.8 (3.6)	8.4 (5.4)
VAR	0.33 (0.18)	1.8 (1.0)	3.0* (2.2)	4.8* (3.6)	7.1* (5.2)
MEMD	0.14* (0.09)	2.1 (1.2)	4.1 (2.6)	6.7 (4.3)	9.7 (6.5)
DYM	0.38 (0.24)	3.4 (2.0)	7.2 (3.7)	11.1 (5.4)	14.7 (7.0)
STAT	0.68 (0.40)	4.0 (2.3)	7.7 (4.4)	11.5 (6.3)	15.2 (8.2)

some of the fast frequency components if they are present in the training data set. Hence, the detection of fast frequency components and the ability to forecast them, improves the forecast compared to methods, like CVF, that are unable to do it. More details about Iceberg 4-3 can be found in 12.A.3.

12.6.5 Iceberg 1040-1

For Iceberg 1040-1 865 forecasts are performed (Tab. 12.6). The ICF forecast scheme has the best forecast results since it is able to forecast fast frequency components. An additional advantage is that Iceberg 1040-1 is tracked in northern Baffin Bay where tidal and inertial frequencies are similar. The tidal current is not explicitly considered in the method, but it will correctly be detected and forecasted if it dominates the inertial current oscillation. More details about Iceberg 1040-1

Table 12.5: Mean end-position-error (12.8) [km] for different forecast horizons of Iceberg 4-3. The standard deviation is given in brackets and the best forecast is marked bold. The best PI (12.10) is marked by a star. The static model gives an indication the iceberg drift distance within the forecast horizon.

	1 h	6 h	12 h	18 h	24 h
CVF	0.74 (0.51)	4.6 (3.4)	8.2 (5.8)	12.9 (8.3)	17.9 (11.4)
ACF	0.31 (0.19)	3.3 (2.1)	6.5 (4.5)	9.3 (6.1)	13.3 (8.5)
TCF	0.33 (0.21)	3.6 (2.4)	7.2 (5.3)	10.0 (6.9)	14.4 (9.4)
ICF	0.26* (0.17)	2.7* (1.8)	5.7* (3.9)	8.2* (5.4)	11.5 (7.3)
VAR	0.66 (0.45)	3.6 (2.5)	5.7 (4.0)	8.0 (5.1)	10.5* (6.7)
MEMD	0.25* (0.18)	4.0 (2.7)	7.9 (5.2)	11.65 (7.2)	15.9 (9.7)
DYM	0.65 (0.44)	3.7 (2.4)	6.7 (4.2)	9.58 (5.9)	12.5 (7.5)
STAT	0.99 (0.55)	5.6 (3.0)	10.3 (5.3)	14.70 (7.4)	18.9 (9.6)

Table 12.6: Mean end-position-error (12.8) [km] for different forecast horizons of Iceberg 1040-1. The standard deviation is given in brackets and the best forecast is marked bold. The best PI (12.10) is marked by a star. The static model gives an indication the iceberg drift distance within the forecast horizon.

	1 h	6 h	12 h	18 h	24 h
CVF	0.53 (0.33)	2.85 (2.0)	5.8 (4.6)	9.9 (7.5)	14.0 (10.5)
ACF	0.31 (0.27)	2.9 (1.8)	5.3 (3.5)	9.2 (6.4)	12.5 (9.3)
TCF	0.31 (0.27)	2.9 (1.9)	5.2 (3.9)	9.1 (6.9)	12.5 (10.1)
ICF	0.25 (0.24)	2.3* (1.5)	4.7* (3.5)	8.2* (6.5)	11.7* (9.6)
VAR	0.51 (0.31)	2.6 (1.8)	5.3 (4.0)	8.8 (6.9)	12.4 (9.8)
MEMD	0.22* (0.13)	3.3 (2.0)	6.1 (4.1)	10.9 (7.1)	15.5 (10.5)
DYM	0.57 (0.29)	3.7 (2.0)	7.1 (4.2)	10.6 (6.1)	13.5 (7.8)
STAT	0.80 (0.49)	4.4 (2.8)	8.0 (5.3)	11.7 (7.6)	14.8 (9.8)

can be found in [12.A.4](#).

12.6.6 Iceberg 1040-2

For Iceberg 1040-2 865 forecasts are performed (Tab. [12.7](#)). The absolute error only increases slightly compared to the error of Iceberg 1040-1 even though the iceberg moves much faster as indicated by the static forecast error. The TCF performs best since the mean ocean current dominates the fast frequency components. Therefore, an explicit consideration of them in the ICF or VAR forecast scheme does not improve the forecast. More details about Iceberg 1040-2 can be found in Appendix [12.A.5](#).

Table 12.7: Mean end-position-error (12.8) [km] for different forecast horizons of Iceberg 1040-2. The standard deviation is given in brackets and the best forecast is marked bold. The best PI (12.10) is marked by a star. The static model gives an indication the iceberg drift distance within the forecast horizon.

	1 h	6 h	12 h	18 h	24 h
CVF	0.34 (0.28)	2.4 (1.7)	5.8 (3.8)	9.7 (6.0)	13.7 (8.1)
ACF	0.21 (0.25)	2.4 (1.8)	6.4 (4.7)	11.4 (8.1)	16.5 (11.4)
TCF	0.19 (0.24)	2.0* (1.4)	5.2* (3.2)	9.0* (5.5)	12.9* (7.7)
ICF	0.20 (0.24)	2.1 (1.4)	5.3 (3.2)	9.1 (5.4)	13.1 (7.5)
VAR	0.31 (0.27)	2.3 (1.7)	5.8 (3.9)	9.6 (6.2)	13.5 (8.6)
MEMD	0.14* (0.14)	2.8 (2.0)	6.9 (4.3)	11.7 (7.5)	17.1 (12.0)
DYM	0.61 (0.55)	5.2 (4.8)	10.7 (9.8)	15.8 (14.5)	20.3 (18.7)
STAT	1.08 (0.50)	6.4 (2.8)	12.8 (5.3)	19.2 (7.7)	25.6 (9.7)

Table 12.8: Mean end-position-error (12.8) [km] for different forecast horizons of Iceberg 5450. The standard deviation is given in brackets and the best forecast is marked bold. The best PI (12.10) is marked by a star. The static model gives an indication the iceberg drift distance within the forecast horizon.

	1 h	6 h	12 h	18 h	24 h
CVF	0.38 (0.20)	2.0 (1.1)	4.2 (1.8)	7.4 (3.4)	11.1 (4.8)
ACF	0.20 (0.11)	2.1 (1.2)	3.7 (2.2)	6.5 (3.9)	9.5 (5.5)
TCF	0.20 (0.12)	2.1 (1.2)	3.7 (2.1)	6.6 (3.8)	9.7 (5.4)
ICF	0.17 (0.10)	1.8* (1.1)	3.7 (2.1)	6.7 (3.7)	10.0 (5.3)
VAR	0.37 (0.20)	2.0 (1.1)	3.6* (1.7)	6.4* (3.3)	9.4* (4.4)
MEMD	0.15* (0.08)	2.1 (1.2)	4.6 (2.0)	8.2 (4.0)	12.2 (5.9)
DYM	0.45 (0.25)	3.9 (1.6)	8.6 (2.6)	13.4 (3.9)	18.1 (4.8)
STAT	0.79 (0.40)	4.6 (2.1)	9.1 (3.7)	13.5 (5.4)	17.8 (6.9)

12.6.7 Iceberg 5450

For Iceberg 5450 173 forecasts are performed (Tab. 12.8). The mean error and standard deviation are similar for the statistical methods. More details about Iceberg 5450 can be found in 12.A.6.

12.6.8 Iceberg 3534

For Iceberg 3534 334 forecasts are performed. The mean end-position error (12.8) for all forecasts is extremely small (Tab. 12.9). The VAR and ICF methods have a similar performance and outperform the other statistical methods. The iceberg moves relatively slowly, which explains the small absolute forecast error, which is the smallest of all icebergs discussed in this article. However, the standard deviation in comparison to drift forecast of the other icebergs is only superior for

Table 12.9: Mean end-position-error (12.8) [km] for different forecast horizons of Iceberg 3534. The standard deviation is given in brackets and the best forecast is marked bold. The best PI (12.10) is marked by a star. The static model gives an indication the iceberg drift distance within the forecast horizon.

	1 h	6 h	12 h	18 h	24 h
CVF	0.42 (0.30)	2.0 (1.5)	3.1 (2.1)	5.2 (3.8)	6.9 (5.2)
ACF	0.29 (0.24)	2.7 (2.0)	3.3 (2.6)	5.9 (4.5)	7.0 (5.5)
TCF	0.29 (0.23)	2.6 (2.0)	3.2 (2.6)	5.7 (4.6)	6.8 (5.7)
ICF	0.20* (0.15)	1.8* (1.2)	2.4* (1.7)	4.2* (3.0)	5.2 (4.0)
VAR	0.41 (0.29)	1.8 (1.3)	2.3* (1.7)	4.0 (3.0)	5.4* (4.1)
MEMD	0.22 (0.16)	2.4 (1.8)	3.2 (2.2)	5.3 (3.0)	6.7 (5.0)
DYM	0.42 (0.30)	2.2 (1.6)	3.6 (2.3)	5.6 (3.7)	7.2 (4.5)
STAT	0.54 (0.39)	2.8 (2.0)	4.7 (3.1)	7.1 (4.6)	9.2 (5.7)

Table 12.10: Mean end-position-error (12.8) [km] for different forecast horizons of Iceberg 3651. The standard deviation is given in brackets and the best forecast is marked bold. The best PI (12.10) is marked by a star. The static model gives an indication the iceberg drift distance within the forecast horizon.

	1 h	6 h	12 h	18 h	24 h
CVF	0.42 (0.27)	2.1 (1.7)	3.3 (4.0)	6.0 (6.4)	8.3 (9.4)
ACF	0.24 (0.15)	2.5 (1.6)	4.0 (3.4)	7.1 (6.1)	9.5 (9.0)
TCF	0.24 (0.15)	2.4 (1.6)	3.7 (3.4)	6.6 (6.1)	8.8 (9.0)
ICF	0.16* (0.12)	1.5* (1.4)	3.0 (3.5)	5.4 (6.3)	7.9 (9.4)
VAR	0.40 (0.25)	1.9 (1.4)	2.6* (3.1)	4.6* (5.1)	6.5* (7.0)
MEMD	0.18 (0.10)	2.3 (1.8)	4.2 (4.0)	7.8 (8.7)	11.9 (18.8)
DYM	0.46 (0.31)	2.9 (2.1)	5.2 (4.5)	8.4 (6.5)	11.1 (8.4)
STAT	0.63 (0.42)	3.3 (2.4)	5.9 (4.8)	9.1 (7.0)	11.9 (9.0)

longer forecast horizons. More details can be found in 12.A.7.

12.6.9 Iceberg 3651

For Iceberg 3651 250 forecasts are performed (Tab. 12.10). For shorter forecast horizons (1 h to 6 h) the ICF scheme performs best, while for longer forecast horizons (12 h to 24 h) the VAR scheme produces the best forecast. All statistical models outperform the dynamic model. However, the VAR model is by far the best for longer forecast horizons.

The forecast error for this iceberg is relatively small. Iceberg 3651 moves quicker than Iceberg 3534, which causes the larger absolute forecast error. The average velocity of Iceberg 3534 is 12 cm/s and of Iceberg 3651 it is 16 cm/s. More details can be found in 12.A.8.

12.6.10 Summary Iceberg Forecast

Fig. 12.2 displays the relative forecast performance of different methods of all icebergs. Even though the absolute error of Iceberg 3534 and Iceberg 3651 was smallest, Iceberg 1040-2 was forecasted the best relatively. Considering that the drift trajectory of Iceberg 1040-2 did not have loops or sudden direction changes, this is not surprising. The larger absolute error is caused by the considerable faster drift velocity.

Iceberg 1 was forecasted worse in relative and absolute values. The reason is the multiple loops in the observation period that are neither within the inertial nor tidal frequency.

Quantitatively, the difference between the performance indices (12.8) and (12.10) is relatively small and usually the same method performs best considering both indices. Therefore, the mean end position error (12.8) was usually used in this chapter, since the value is intuitive and easy to understand.

In comparison to the statistical methods it can be observed that in general the MEMD forecast scheme predicts the iceberg trajectory in the first hour very well. However, it degrades quickly for longer forecast horizons and produces a large absolute error. Considering the relative performance of the MEMD forecast scheme, which is only slightly worse than the VAR or ICF forecast schemes, one can see that the MEMD forecast scheme produces large forecasts error in cases when it produces a *bad* forecast. This is also indicated by a usually larger standard deviation of the MEMD forecast scheme.

The ICF or the VAR model usually produce the best statistical forecast. In fact, the ICF model is often better for shorter forecast horizons while the VAR model for longer. Therefore, a combination of both methods would be preferable.

For many of the iceberg trajectories it can be observed that the relative performance for the 12 h forecast is slightly better than the 6 h forecast. Most likely this is caused by the tidal current, which is either filtered or approximated. Its oscillation period correlates with the 12 h forecast. The largest offset is expected after 6 h. Moreover, it can be observed that the correct detection of the fast oscillations (inertial and tidal oscillations) improves the forecast, even though the oscillations themselves have only a minor influence on the forecast (especially 12 h and 24 h). However, a correct detection of the oscillations influences how well the non-oscillating part of the ocean current is estimated. Since the non-oscillating part is often assumed to be constant (or only changes slightly) in the statistical forecast schemes, its correct estimation at the beginning of the forecast is important.

An improvement with the statistical models in comparison to the dynamic model can be observed for all trajectories. However, the relative performance usually decreases for longer forecast horizons more strongly for the statistical methods than for the dynamic model. Consequently, for even longer forecast horizons it is

likely that the dynamic model at some point will produce a *less worse* forecast than the statistical methods. An interesting observation is that the standard deviation relative to the mean error is usually larger for the statistical methods than for the dynamic forecast method, even though both measures are smaller in absolute values for the statistical methods.

12.7 New Statistical Forecast Schemes

The comparison of the statistical methods in the previous section revealed that the ICF and VAR forecast schemes performed overall the best. Moreover, it was determined that the ICF forecast scheme usually performs better for shorter periods while the VAR forecast scheme is usually better longer forecast horizons.

Two different ways of how to combine the two methods can be thought of:

1. Replacing the moving average filter in the VAR forecast scheme with a Kalman filter using the identified VAR model as the observer model (VAR KF).
2. Instead of using a constant current input in the ICF and TCF forecast scheme, the current may be forecasted with the VAR model forecast (ICF VAR and TCF VAR).

For the first approach the VAR model is transformed into a state space model. Since this model is linear a Kalman filter and not a MHE is used. The estimated of iceberg and ocean current velocity at the beginning of the forecast becomes so model based. This decreases the time delay in the velocity estimates, which was introduced when a simple moving average filter was used. Moreover, a more precise detecting of measurement and process noise is possible. On the other hand, the filtering becomes more aggressive, meaning the velocity is less smooth compared to the moving average filter (this depends also on the tuning of the Kalman filter).

The forecast results for this approach for the data sets used in this study are shown in Tab. 12.11. The forecast of Iceberg 1, 2, 1040-2 and 5450 improves. Moreover, the 6 h forecast of Iceberg 4 and 4-3 improves. However, not all forecasts can be improved. The forecast performance of Iceberg 4-3, 3534 and 3651 decreases quite a bit for longer forecast horizons (12 h to 24 h). For Iceberg 4-3 the new approach increases the errors slightly for each of the peaks in the forecast performance (Fig. 12.5(a)). This may be reduced by a less aggressive filter with stronger smoothing. For Iceberg 3534 the overall performance for longer forecast horizons (12 h to 24 h) is better with the VAR model. Again, this may be due to a stronger smoothing. A similar observation can be done for Iceberg 3651. In

Table 12.11: Mean end-position-error (12.8) [km] for different forecast horizons of VAR forecast scheme with the Kalman filter. The standard deviation is given in brackets and bold numbers show an improvement of the forecast in comparison to the previous proposed forecast schemes.

	1 h	6 h	12 h	18 h	24 h
Iceberg 1	0.28 (0.24)	2.5 (1.9)	6.1 (3.7)	9.1 (5.5)	12.6 (6.8)
Iceberg 2	0.14 (0.08)	1.5 (0.7)	4.0 (2.0)	4.9 (2.5)	7.0 (3.4)
Iceberg 4	0.21 (0.12)	1.7 (1.0)	3.3 (2.3)	4.9 (3.6)	7.2 (5.4)
Iceberg 4-3	0.28 (0.19)	2.7 (1.8)	6.5 (4.4)	10.0 (6.6)	14.44 (9.2)
Iceberg 1040-1	0.40 (0.26)	2.4 (1.5)	4.9 (3.2)	8.3 (5.6)	12.0 (7.9)
Iceberg 1040-2	0.20 (0.24)	1.9 (1.5)	4.6 (3.1)	7.7 (4.9)	11.2 (6.8)
Iceberg 5450	0.27 (0.14)	1.9 (1.1)	3.3 (1.9)	5.9 (3.5)	9.1 (4.6)
Iceberg 3534	0.37 (0.24)	2.0 (1.3)	2.7 (2.0)	4.8 (3.4)	6.1 (4.3)
Iceberg 3651	0.29 (0.18)	1.7 (1.1)	2.9 (2.6)	5.4 (4.8)	7.8 (7.0)

fact, the new approach reduces the large error at the end of the observation horizon but increases it slightly during the other periods (Fig. 12.10(a)). In comparison to the VAR model forecast the 1 h and 6 h forecast of the new approach is clearly improved. It has to be kept in mind that the results depend on the tuning of the process and measurement covariances of the Kalman filter.

The inclusion of the VAR model forecast into the ICF forecast scheme is shown in Tab. 12.12. In general, it can be observed that the combination ICF and VAR is better than TCF and VAR. For some of the icebergs the 6 h forecast improves, however, a strong tendency to large outliers was observed. These have to be detected and removed from the forecast. A different tuning of the MHE may improve the situation. Nevertheless, it is not straight forward to improve the forecast performance by including the VAR forecast into the ICF forecast scheme.

12.8 Conclusion and Future Work

In this chapter different iceberg forecast schemes were compared over a forecast horizon of 1 h to 24 h. A summary of the average performance of every method on the presented iceberg tracks is given in Tab. 12.13. As expected the statistical forecast models generally outperformed the dynamic forecast model. However, it was also shown that the dynamic model sometimes performs better than the statistical methods. From the statistical forecast models the ICF and VAR model performed the best. On the other hand, each of the proposed statistical forecast models performed for specific icebergs and forecast horizons better than the others. The MEMD forecast scheme usually produced the best forecast for forecast horizons of about 1 h. The ICF forecast scheme performed well for forecast hori-

Table 12.12: Mean end-position-error (12.8) [km] for different forecast horizons of the ICF scheme forecasting the current with the VAR model. The standard deviation is given in brackets and bold numbers show an improvement of the forecast in comparison to the previous proposed forecast schemes.

	1 h	6 h	12 h	18 h	24 h
Iceberg 1	0.33 (0.22)	2.8 (1.8)	6.7 (4.8)	9.8 (6.6)	13.3 (8.3)
Iceberg 2	0.16 (0.07)	1.5 (0.9)	3.9 (2.2)	5.5 (3.3)	7.9 (4.3)
Iceberg 4	0.18 (0.11)	1.6 (0.9)	3.6 (2.3)	5.8 (3.7)	8.6 (5.5)
Iceberg 4-3	0.26 (0.17)	2.5 (1.9)	6.5 (5.4)	9.3 (7.3)	13.2 (10.5)
Iceberg 1040-1	0.27 (0.24)	2.7 (1.9)	6.7 (5.5)	10.9 (8.7)	15.3 (12.6)
Iceberg 1040-2	0.20 (0.24)	2.3 (3.5)	6.5 (10.4)	10.6 (15.1)	15.04 (21.6)
Iceberg 5450	0.17 (0.10)	1.7 (1.1)	3.7 (2.0)	6.5 (3.3)	9.8 (4.7)
Iceberg 3534	0.20 (0.15)	1.9 (1.4)	3.1 (2.8)	4.8 (4.3)	6.34 (5.8)
Iceberg 3651	0.16 (0.12)	1.5 (1.3)	3.1 (3.2)	5.3 (5.5)	7.8 (8.0)

zons up to 12 h, while the VAR forecast scheme usually performed best for longer forecast horizons (12 h to 24 h).

The MEMD and ACF forecast scheme generally do not perform well for longer forecast horizons (12 h to 24 h). In both cases the assumptions seemed to not hold. For the ACF it seems the assumption that the current model can be corrected with a constant term is not valid for longer forecast horizons. For the MEMD forecast scheme the assumption that all identified oscillations continue with a similar amplitude and frequency introduces a large error for longer forecast horizons (12 h to 24 h).

It has to be kept in mind, that the end-position errors (12.8) presented in this article can be influenced by tuning of the filters and estimators. We did not use an extensive amount of time on tuning. We also used the same tuning for all iceberg tracks. The results may be improved by improved tuning or individual tuning for each track. In general it can not be expected that a tuning that worked well on one track will also work well on another track, since the drift behavior of the icebergs is quite different. Sometimes a strong filtering of the iceberg velocity improves the forecast, even though it introduces a delay. In other cases the delay is the cause of a bad forecast. This two mechanism are the main difference between the VAR and VAR KF forecast method. It is difficult to tell a priori which tuning is better, but it was observed that strong filtering improves longer while aggressive filtering shorter forecasts.

A combination of the VAR and ICF forecast schemes is possible, but doing this did not combine the benefits from both schemes. Instead, it was better to use a Kalman filter with the identified model as an observer model in the VAR model forecast. This combination improved the short-term forecast of the VAR model

Table 12.13: Mean end-position-error (12.8) [km] for different forecast horizons of all iceberg for each method considered in the chapter. The standard deviation is given in brackets and the best forecast is marked bold. The static model gives an indication the iceberg drift distance within the forecast horizon. The VAR KF and ICF VAR are the two new forecast methods.

	1 h	6 h	12 h	18 h	24 h
CVF	0.53 (0.41)	3.1 (2.6)	5.8 (4.9)	9.4 (7.5)	13.2 (10.3)
ACF	0.27 (0.21)	2.8 (1.9)	5.3 (3.9)	8.5 (6.1)	12.0 (8.7)
TCF	0.28 (0.22)	2.8 (2.0)	5.3 (4.3)	8.4 (6.3)	11.9 (8.9)
ICF	0.23 (0.19)	2.3 (1.6)	4.6 (3.5)	7.4 (5.7)	10.5 (8.2)
VAR	0.49 (0.37)	2.6 (2.0)	4.6 (3.7)	7.2 (5.6)	9.9 (7.6)
MEMD	0.20 (0.15)	3.1 (2.2)	6.0 (4.5)	9.8 (7.2)	12.9 (11.5)
VAR KF	0.29 (0.22)	2.2 (1.5)	4.7 (3.6)	7.6 (5.7)	10.9 (8.0)
ICF VAR	0.25 (0.20)	2.4 (1.9)	5.2 (5.0)	8.2 (7.4)	11.4 (10.7)
DYM	0.54 (0.38)	3.7 (2.6)	7.1 (5.0)	10.5 (7.3)	13.7 (9.3)
STAT	0.82 (0.51)	4.6 (2.9)	8.6 (5.3)	12.7 (7.5)	16.4 (9.8)

considerably. Nonetheless, it did not perform equally well for all observed iceberg trajectories and sometimes it even degraded the forecast performance.

A comparison between the forecast performance of different icebergs should be performed with a relative performance index. This reveals how well the icebergs are forecasted relative to the velocity of the iceberg. About 70 % to 90 % of all forecasts performed by the statistical forecast models are classified as acceptable or better. This means the forecast error is at least in the same range as the drift distance of the iceberg in the period.

For future work a potential method to improve the iceberg drift forecast is by changing between different forecast methods, which are specialized for different forecast horizons. This change has to be performed by using the forecasted iceberg velocity from different models. For example, the ICF model is used up to a forecast horizon of 12 h, and for longer forecasts the position is used to initialize the VAR model.

Another possible improvement may be achieved by creating a more complex model for the ICF forecast scheme that not only considers the inertial current but also includes tidal currents explicitly in the observer model.

A further interesting research question is how well the relative forecast performance for longer forecast horizons can be predicted based on a 1 h, 3 h and 6 h forecast. Is it possible to classify a priori some forecasts as not trustworthy and how high is the success-rate of this classification?

12.A Extension to the Comparison of Iceberg Drift Forecasts

This appendix shows the iceberg drift trajectories of each iceberg, and the progression of the 12 h forecast error for some of the methods presented in the article.

12.A.1 Iceberg 1

In Tab. 12.3 the mean and standard deviation of the forecast methods are shown. The MEMD forecast scheme produces the best forecast within the first hour. For six hours the ancillary forecast scheme is the best. For longer forecast horizons the VAR forecast scheme produces the best results. If the PI (12.10) is considered the ancillary forecast scheme produces a better result than the VAR forecast scheme for a 12 h forecast.

Besides the CVF all methods are superior to the dynamic forecast model up to a forecast period of 12 h. For longer forecast horizons (18 h and 24 h) the TCF, MEMD and CVF schemes produce a larger average error than the dynamic model.

Interestingly, the standard deviation relative to the mean error is smaller for the dynamic forecast model compared to the statistical methods indicating that the statistical methods have a larger spread in the forecast errors.

The end-position error of a 12 h forecast of every method is shown in Fig. 12.3(a). The corresponding iceberg trajectory is shown in Fig. 12.3(b). The large standard deviation of the statistical methods (Tab. 12.3) are caused by the large error in the period 60 h to 85 h. This is the period where the iceberg enters the first large loop. The forecast error is also large when the iceberg exists the loops. These loops have a period of about 18 h to 24 h. The ocean eddies causing the looping are most likely provoked by the current flows in and out of Conception Bay (between Grates Cove and Bonavista (Fig. 4.3)).

The error progressions of the methods, besides the dynamic and static model, are similar. The static model serves as a reference to the iceberg drift velocity. The forecast performance is not good since the static model is often better than the other models (Fig. 12.3(a)). All methods rely on a similar principle, which makes it difficult to predict strong unexpected changes. Oscillations caused by tidal or inertial current can be forecasted by the ICF, VAR and MEMD forecast models.

The main advantage of the VAR model compared to the other methods is the reduction of the error between 70 h to 120 h. In this period the dynamic model also performs well, since it is able to forecast the second loop. On the other hand, the exit from the loop is forecasted by neither the dynamic nor statistical models.

12.A.2 Iceberg 4

In Tab. 12.4 the mean and standard deviation of the forecast methods are shown. The MEMD forecast scheme performs best in the first hour. Thereafter, the VAR forecast scheme is best.

The end-position error of a 12 h forecast of the VAR, ICF and dynamic forecast model is shown in Fig. 12.4(a). The corresponding iceberg trajectory is shown in Fig. 12.4(b). Larger errors in the statistical models are produced before the iceberg enters the curves at about 193 h and 289 h. These are not anticipated by the forecasts.

The statistical models behave similarly. The VAR model is superior to the ICF model especially in the second part of the observed iceberg trajectory. The forecast of the iceberg drift of Iceberg 4 with the statistical methods is good, and the error compared to the dynamic forecast model can be reduced considerably. For only a few short periods the dynamic model performs better than the statistical model forecast (Fig. 12.4(a)).

12.A.3 Iceberg 4-3

In Tab. 12.5 the mean and standard deviation of the forecast methods are shown. The MEMD forecast scheme performs best in the first hour. Thereafter, up to a forecast horizon of about 12 h the ICF scheme performs best. For longer forecast horizons up to 24 h the VAR model forecast is the best. The dynamic forecast model outperforms the CVF, TCF and MEMD scheme already after 12 h.

The end-position error of a 12 h forecast of the VAR, ICF and DYM model is shown in Fig. 12.5(a). The corresponding iceberg trajectory is shown in Fig. 12.5(b). The rapid changes in iceberg velocity and direction causes the strong oscillation in the forecast performance. This is also amplified by the squeezed x-axis.

The dynamic model has a similar performance as the statistical forecast methods. In the comparison of both approaches it can be observed that at the beginning (0 h to 250 h) the statistical models perform better, in the middle part (250 h to 500 h) the dynamic model performs better and in the end the statistical models perform again better.

Iceberg 4-3 is believed to be relatively small, which enables it to move relatively quickly. Consequently, the statistical models do not outperform the dynamic model by much. A similar observation was already made for the forecast of Iceberg 1, which had several unexpected loops in its trajectory.

12.A.4 Iceberg 1040-1

In Tab. 12.6 the mean and standard deviation of the forecast methods are shown. The MEMD forecast scheme is the best in the first hour, but for longer forecast

horizons (6 h to 24 h) the ICF scheme is the best. For longer forecast horizons the dynamic model outperforms the MEMD (18 h to 24 h) and the CVF (24 h) scheme. All other statistical forecast schemes are better than the dynamic model.

The end-position error of a 12 h forecast of the ACF, ICF and dynamic forecast model is shown in Fig. 12.6(a). The corresponding iceberg trajectory is shown in Fig. 12.6(b). The loops at the beginning of the observation and the left-turn at about 200 h are not well forecasted by the statistical model. The drift to the south (about 230 h to 370 h), on the other hand, is relatively well forecasted. In this period the fast frequencies (tidal and inertial current) are less important, since the overall iceberg velocity is relatively large.

The dynamic iceberg model does not forecast the iceberg track well at the beginning (1 h to 130 h), since both ocean current and wind do not correlate with the iceberg velocity. In the period 130 h to 180 h the iceberg is mainly wind driven, since the ocean current velocity is very small (close to zero). The loops observed in this period correlate with the current velocity, but the amplitude of the oscillation is damped in the current velocity to about 40 % relative to the amplitude observed in the iceberg velocity. In the period 300 h to 480 h wind and current velocity correlate well with the iceberg velocity. The left-turn at about 380 h is anticipated by the input data, but about 6 h time-displaced. In fact, also in the period 480 h to 650 h the wind velocity correlates well with the iceberg velocity. The error in the forecast is caused by the ocean current. Overall the wind input correlates well with the iceberg velocity in the period 350 h to 800 h.

Especially in the middle part of the track (200 h to 650 h) the statistical models perform better than the dynamic model. At the end the dynamic model is slightly better.

12.A.5 Iceberg 1040-2

In Tab. 12.7 the mean and standard deviation of the forecast methods are shown. For a one hour forecast the MEMD forecast scheme performs best. For longer forecast horizons the TCF scheme is the best, closely followed by the ICF scheme. The MEMD and ACF scheme have a considerably larger forecast errors. Every statistical forecast method outperforms the dynamic forecast scheme. Indeed, the dynamic forecast model performs badly for this iceberg trajectory. The reason is a strong over-prediction of the ocean current velocity in the first 100 h (Fig. 12.7(a)). Even though, the iceberg moves quickly in this period (average velocity 31 cm/s) the average velocity difference to the current velocity is about 45 cm/s.

The static model (STAT) indicates that the iceberg moves quickly in the entire observation period. Thus, the statistical models produce a larger error compared to some of the other icebergs, even though the iceberg trajectory is smooth without loops or sudden turns (Fig. 12.7(b)).

The statistical models behave similar (Fig. 12.7(a)). The dynamic model produces a very large error in the first 100 h, but in the period between 120 h to 200 h the dynamic model is slightly better than the statistical models. The two peaks (about 238 h and 276 h) in the forecast of the statistical models are caused by large measurement errors, which cause peaks in the iceberg velocity (to about 70 cm/s). It is due to transmission errors in the position data set of Iceberg 1040. In these two instances the error was not corrected since it would have needed post-processing, which was avoided in the comparison.

12.A.6 Iceberg 5450

In Tab. 12.8 the mean and standard deviation of the forecast methods are shown. For a one hour forecast the MEMD forecast scheme performs best. For a six hour forecast the ICF scheme is the best followed by the VAR forecast scheme. The latter also performs best for longer forecast horizons (12 h to 14 h). All statistical models outperform the dynamic model, which has a similar forecast error as the static model.

The end-position error of a 12 h forecast of the ICF, VAR and dynamic forecast model is shown in Fig. 12.8(a). The corresponding iceberg trajectory is shown in Fig. 12.8(b).

The statistical models predict the movement of Iceberg 5450 well, even though the iceberg moves relatively quickly (average velocity about 21 cm/s). The dynamic forecast model, on the other hand, is not able to forecast the iceberg drift as well. It is outperformed by the statistical models over almost the entire observation period.

12.A.7 Iceberg 3534

In Tab. 12.9 the mean and standard deviation of the forecast methods are shown. The statistical forecast models outperform the dynamic one. Exceptions are the ACF and MEMD forecast schemes. The VAR and ICF, which perform best for different forecast horizons, have a similar forecast performance. The other statistical models cannot compete with them.

The end-position error of a 12 h forecast of the ICF, VAR and dynamic forecast model is shown in Fig. 12.9(a). The corresponding iceberg trajectory is shown in Fig. 12.9(b).

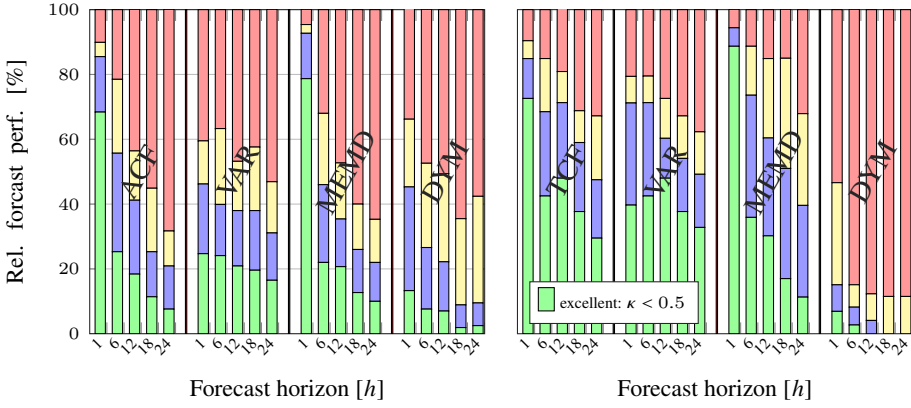
The statistical models perform for the most part of the observation period better than the dynamic model. This holds especially for the period 40 h to 130 h. Overall the forecast errors of the VAR and ICF model behave similarly, but it can be observed that the fast oscillations of the error are slightly different. Consequently, a combination of both forecast scheme would do even better. A similar behavior was also observed for the other icebergs.

12.A.8 Iceberg 3651

The end-position error of a 12 h forecast of the ICF, VAR and dynamic forecast model is shown in Fig. 12.10(a). The corresponding iceberg trajectory is shown in Fig. 12.10(b). The iceberg velocity increases strongly at the end of the observation period. This correlates with the forecast error. For this reason the standard deviation (Tab. 12.10) is also considerably larger than for Iceberg 3534 and Iceberg 5450.

The forecast performance of the statistical model is better than of the dynamic one. In fact, if only the first 200 h of the observation period are considered the 12 h mean forecast error is only about 1.36 km and the 24 h forecast error is about 3.95 km. This is a very small forecast error. The dynamic model also produces only a 3.3 km and 7.8 km error for a 12 h and 24 h forecast horizon, respectively. Again, the small absolute error is correlated with a small iceberg velocity during the period. Nonetheless, the strong oscillation in velocity causing small loops and a zigzag trajectory at the beginning of the observation does not influence the forecast negatively, since it is in the expected frequency of about 12 h. The loops at the beginning of the observation period are observed because of the small iceberg velocity. If the iceberg velocity is larger the inertial and tidal oscillations cannot be spotted so easily in the iceberg trajectory.

At about 210 h the velocity of the iceberg in both directions changes strongly. For this reason the forecast error increases strongly. The other large forecast error is due to the direction change at about 240 h. Obviously these changes are not explained by the wind and current data, which produces a large error in the dynamic model. In addition, the statistical models are not prepared for this sudden change, so they produce a large error.



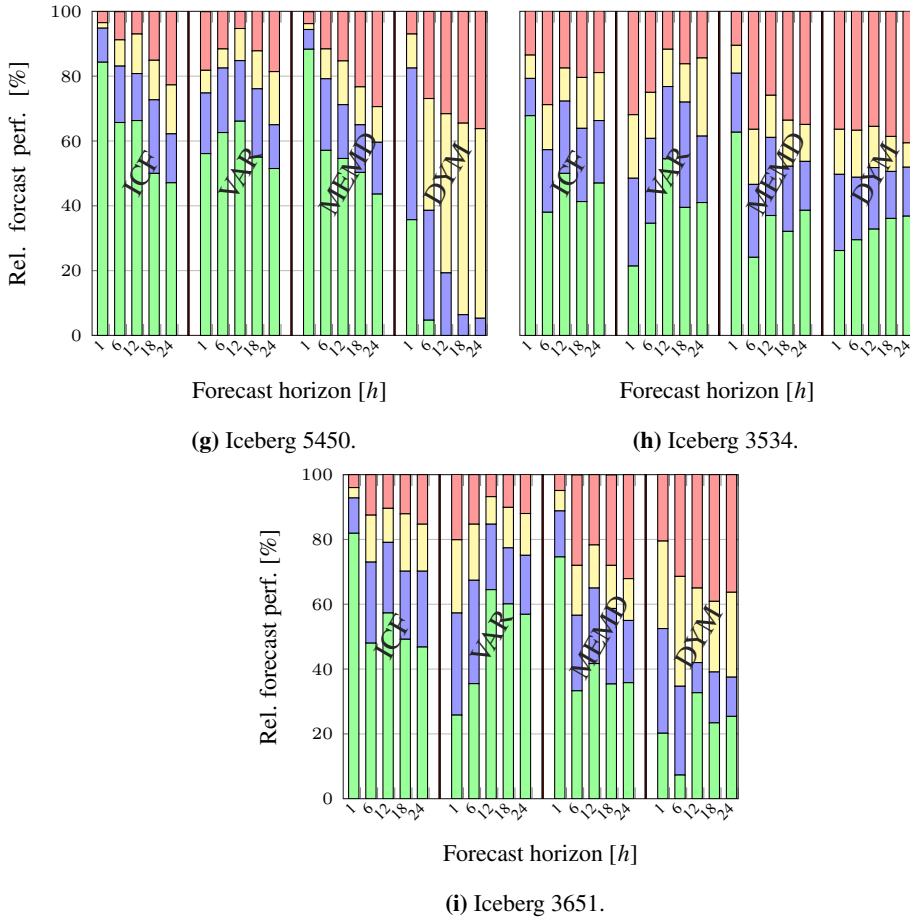
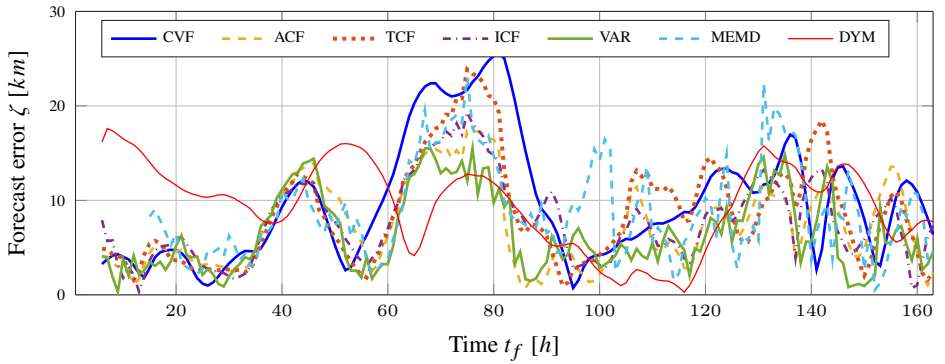
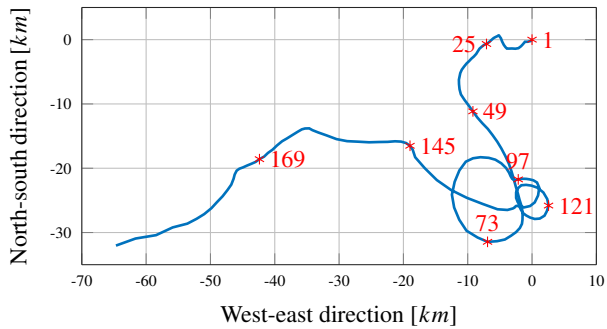


Figure 12.2: Relative forecast performance of the icebergs. The relative forecast performance is grouped in four categories (Sec. 12.5): bad (red), acceptable (yellow), good (blue), excellent (green). Each iceberg forecast performed is grouped in one of the categories. Each vertical bar shows the percentage of each category for a certain method and forecast horizon. The best of ACF, TCF or ICF is on the left hand side, followed by the VAR model and MEMD model. The dynamic model is on the right-hand side.

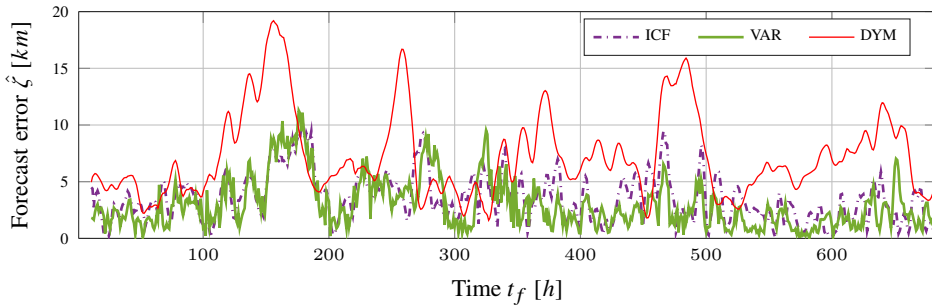


(a) Forecast error for different forecast schemes with a forecast horizon of 12 h for Iceberg 1.

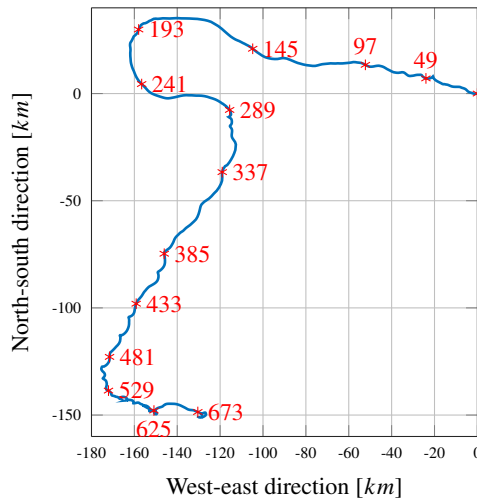


(b) Iceberg drift trajectory of Iceberg 1. The number marker corresponds to the time t_f in the upper figure.

Figure 12.3: Forecast results for Iceberg 1. The forecast error is shown in the upper figure, while the lower figure shows the corresponding iceberg drift trajectory.

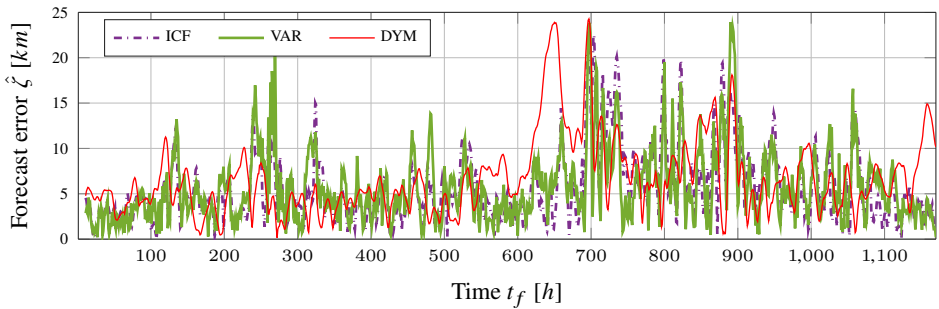


(a) Forecast error for different forecast schemes with a forecast horizon of 12 h for Iceberg 4.

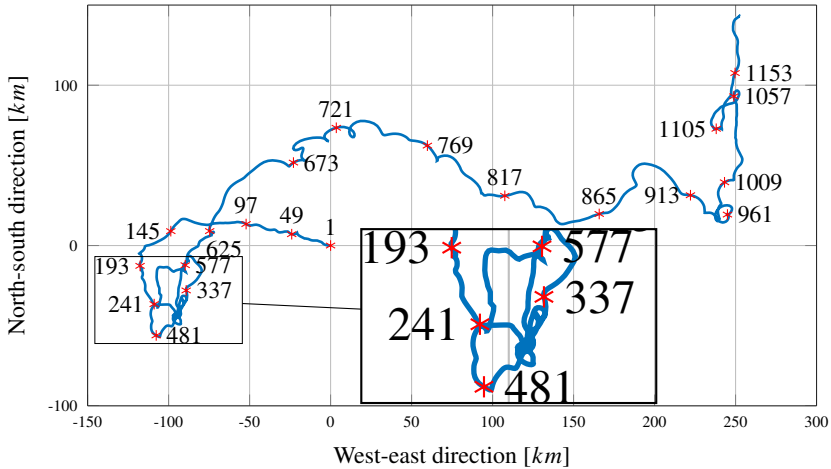


(b) Iceberg drift trajectory of Iceberg 4. The number marker corresponds to the time t_f in the upper figure.

Figure 12.4: Forecast results for Iceberg 4. The forecast error is shown in the upper figure, while the lower figure shows the corresponding iceberg drift trajectory.

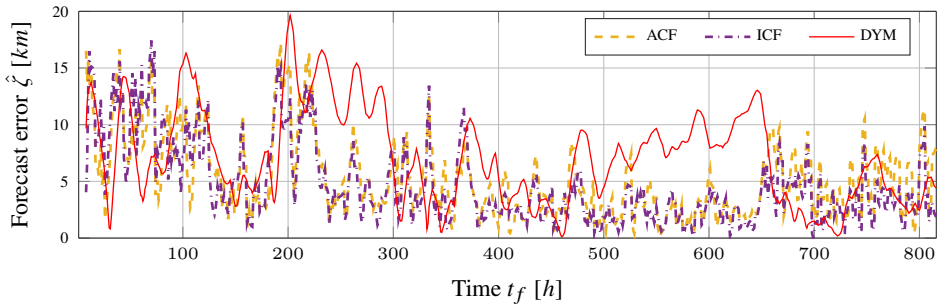


(a) Forecast error for different forecast schemes with a forecast horizon of 12 h for Iceberg 4-3.

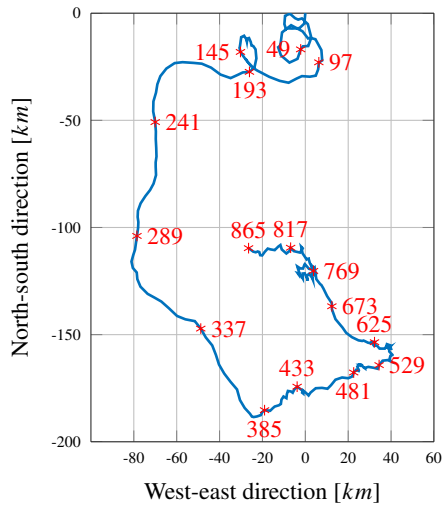


(b) Iceberg drift trajectory of Iceberg 4-3. The number marker corresponds to the time t_f in the upper figure.

Figure 12.5: Forecast results for Iceberg 4-3. The forecast error is shown in the upper figure, while the lower figure shows the corresponding iceberg drift trajectory. The inset magnifies the part of the track that contains many loops and direction changes.

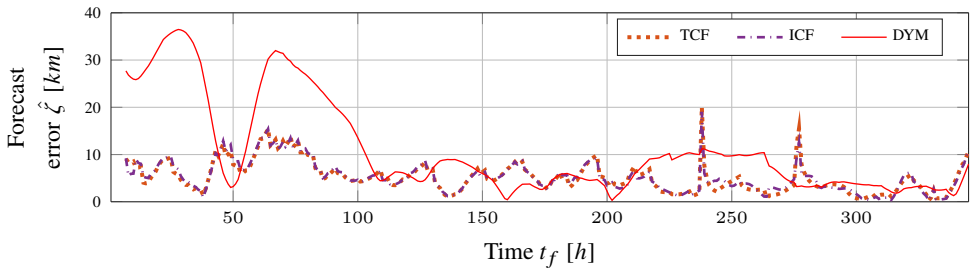


(a) Forecast error for different forecast schemes with a forecast horizon of 12 h for Iceberg 1040-1.

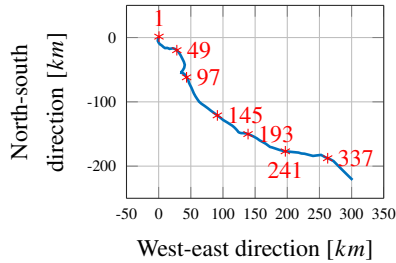


(b) Iceberg drift trajectory of Iceberg 1040-1. The number marker correspond to the time t_f in the upper figure.

Figure 12.6: Forecast results for Iceberg 1040-1. The forecast error is shown in the upper figure, while the lower figure shows the corresponding iceberg drift trajectory.

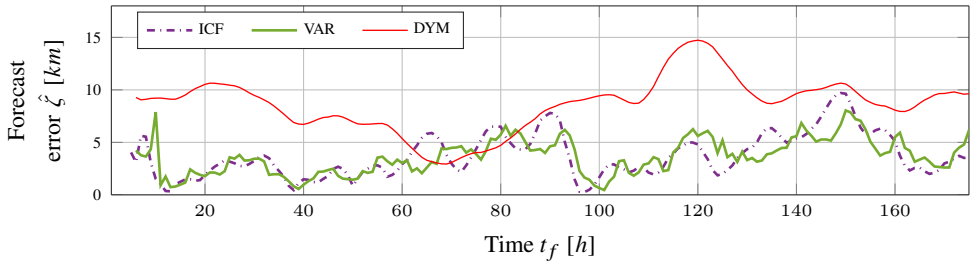


(a) Forecast error for different forecast schemes with a forecast horizon of 12 h for Iceberg 1040-2.

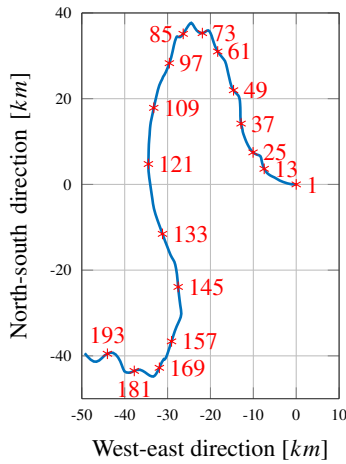


(b) Iceberg drift trajectory of Iceberg 1040-2. The number marker corresponds to the time t_f in the upper figure.

Figure 12.7: Forecast results for Iceberg 1040-2. The forecast error is shown in the upper figure, while the lower figure shows the corresponding iceberg drift trajectory.

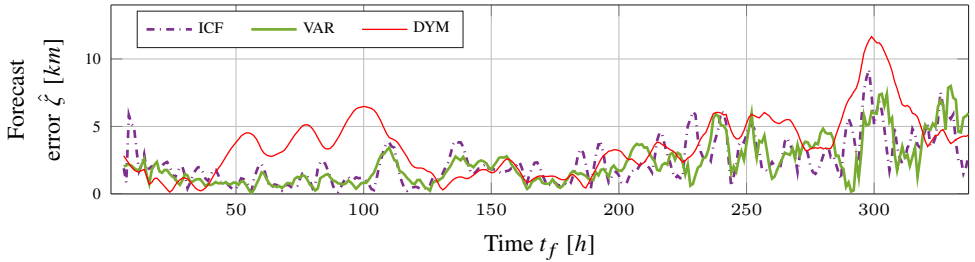


(a) Forecast error for different forecast schemes with a forecast horizon of 12 h for Iceberg 5450.

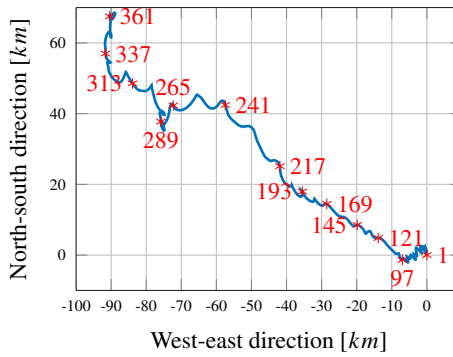


(b) Iceberg drift trajectory of Iceberg 5450. The number marker corresponds to the time t_f in the upper figure.

Figure 12.8: Forecast results for Iceberg 5450. The forecast error is shown in the upper figure, while the lower figure shows the corresponding iceberg drift trajectory.

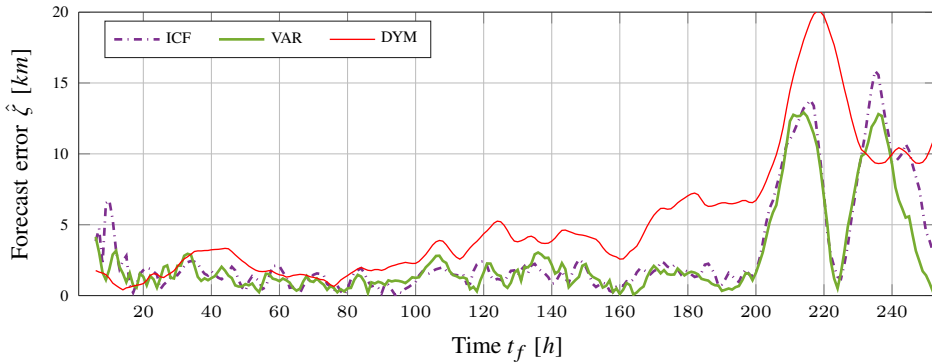


(a) Forecast error for different forecast schemes with a forecast horizon of 12 h of Iceberg 3534.

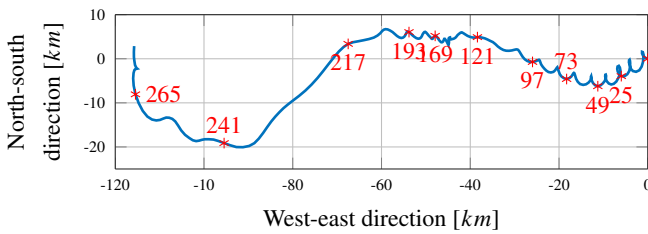


(b) Iceberg drift trajectory of Iceberg 3534. The number marker correspond to the time t_f in the upper figure.

Figure 12.9: Forecast results of Iceberg 3534. The forecast error is shown in the upper figure, while the lower figure shows the corresponding iceberg drift trajectory.



(a) Forecast error for different forecast schemes with a forecast horizon of 12 h of Iceberg 3651.



(b) Iceberg drift trajectory of Iceberg 3651. The number marker corresponds to the time t_f in the upper figure.

Figure 12.10: Forecast results for Iceberg 3651. The forecast error is shown in the upper figure, while the lower figure shows the corresponding iceberg drift trajectory.

Part VI

Parameter and State Estimation under Constraints

Chapter 13

Estimation of a Hydrodynamic Iceberg Geometry

This chapter is based on PAPER H ([Andersson et al. 2017c](#)). The sensitivity of the dynamic iceberg model to different parameters and inputs make the iceberg drift forecast challenging. Nevertheless, if the uncertainty of the current driving force on the iceberg is reduced by measuring the current at the iceberg location, it is possible under specific conditions to estimate the approximate iceberg shape. This iceberg shape geometry can be used directly in the dynamic iceberg model.

The chapter deals with a nonlinear parameter estimation problem with constraints on the parameters. A hydrodynamic iceberg geometry model enforces the constraints. The theoretical work on constrained estimation in Chapter 14 and 15 was motivated by the study presented here.

13.1 Introduction

In Spring 2015 ArticNet [ArcticNet \(2004-2018\)](#) and Statoil conducted an Off-shore Newfoundland Researcher Expedition. During this expedition a dataset of one iceberg track similar to the one collected by [Smith and Donaldson \(1987\)](#) was collected. This chapter discusses how current data collected close to the iceberg can be used to improve knowledge about the iceberg shape without profiling the iceberg keel.

13.2 Data Collection

In this section the first 6.5 h of the trajectory of Iceberg 4 are studied. In this period, the CCGS *Amundsen* was in close proximity to the iceberg and wind, wave and

current information were measured close to the iceberg. The dataset is described in detail in Sec. 5.2.

13.3 Estimation of the Iceberg Geometry

Even though Sec. 5.3 indicates that the dynamic iceberg drift model does not necessarily result in a good iceberg drift hindcast and is, therefore, outperformed by a simple kinematic model, it does describe the physics of the process more accurately than the kinematic model. If the current is measured close to the iceberg for some time, then it should be possible to estimate the scaled hydrodynamic iceberg shape. This scaling is introduced by the drag coefficient and is only possible if some confidence exist that the current input to the dynamic model is approximately correct. If this is not the case, then the current input is more strongly corrected than the shape and drag coefficients (Sec. 6.3). Such an iceberg shape estimation can reduce the uncertainty in the shape parameters and reduce forecast errors in the iceberg prediction.

13.3.1 The Iceberg Geometry Model

Additional information in the form of constraints in the estimation process usually improves the estimation results, since the parameter space is reduced. Therefore, an iceberg geometry model is developed that introduces several reasonable constraints to the estimation process.

The radii of the iceberg shape are constrained to positive numbers. Moreover, the change in the radii is constrained so that they must decrease from the middle of the iceberg height. From several 3D iceberg profiling projects (Younan et al. 2016), it was shown that icebergs often have a shoulder. Therefore, the first radius was constrained to be within 75 % to 120 % of the sail length. The radius can decrease, since the first layer, if Shipboard Acoustic Doppler Current Profiles (SADCP) are used, is quite deep such that a decrease must be possible. The shoulder, on the other hand, may cause an increase of the radius.

Based on Archimedes' law, the overall mass and keel volume V_{keel} can be calculated if the sail volume V_{sail} of the iceberg is known

$$V_{keel} = V_{sail} \frac{\rho_{ice}}{\rho_w - \rho_{ice}}, \quad (13.1a)$$

$$m = (V_{sail} + V_{keel})\rho_{ice} = \left(1 + \frac{\rho_w}{\rho_w - \rho_{ice}}\right) V_{sail}\rho_{ice}, \quad (13.1b)$$

where ρ_w and ρ_{ice} are the water and iceberg densities, respectively.

The sensitivity of (13.1b) to changes in the iceberg density ρ_{ice} is high such that a change of about 1 % in iceberg density causes an 8 % change in the estimated iceberg mass and keel volume. Nonetheless, the estimated keel volume can be

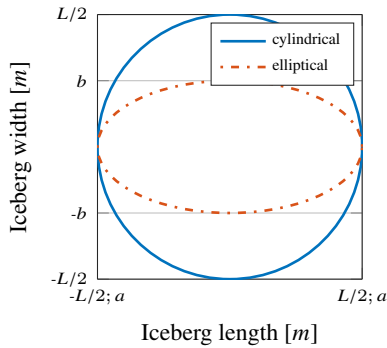


Figure 13.1: Cylindrical and elliptical iceberg geometries seen from above.

used with an idealised iceberg geometry assumption to constrain the overall keel volume. In this chapter, a cylindrical and elliptical iceberg geometry is considered (Fig. 13.1).

Cylindrical Iceberg Geometry.

The volume of each layer can be calculated with

$$V_i = \pi r_i^2 h_i, \quad (13.2)$$

where r_i is the radius of the layer and h_i is the layer height. The sum of the volumes must be the same as the estimated keel volume. The cross sections of each layer can be calculated with

$$A_i = 2r_i h_i. \quad (13.3)$$

Elliptical Iceberg Geometry.

The radius of the ellipse changes with the angle of attack by the forces. The radius can be calculated by

$$r(\theta) = \frac{ab}{\sqrt{(b \cos \theta)^2 + (a \sin \theta)^2}}, \quad (13.4)$$

where θ is the angle between the current direction and alignment of the minor axis b of the ellipse. Consequently, the alignment of the iceberg must be known. The volume of each elliptic layer can be calculated by

$$V_i = \pi a_i b_i h_i. \quad (13.5)$$

For simplicity it was assumed that the ratio between the major and minor axes is the same in each layer, such that

$$b_i = k a_i \quad (13.6)$$

holds, where k is the fixed ratio. The ratio k can either be estimated together with the layer radii or fixed based on the sail geometry. If the ratio k is estimated, then it is constrained to be within 0.3 to 1. Furthermore, it is assumed that the major and minor axes in each layer are aligned. As a result, the estimation problem for the elliptically shaped iceberg has the same amount of parameters or one parameter more compared to the estimation problem for the cylindrically shaped iceberg. The cross-section area in each layer of the elliptical iceberg geometry can be calculated by

$$A_i = 2r_i(\theta)h_i. \quad (13.7)$$

13.3.2 Estimation Algorithm

A constrained least-squares parameter estimation algorithm estimates the iceberg geometry. The discretisation of the continuous time model (2.1) yields

$$\mathbf{x}_{k+1} = \mathbf{f}(\mathbf{x}_k, \mathbf{u}_k, \mathbf{p}), \quad \mathbf{x}_0 = \mathbf{x}(t_0), \quad (13.8a)$$

$$\mathbf{y}_k = \mathbf{h}(\mathbf{x}_k) + \mathbf{v}_k, \quad (13.8b)$$

where $\mathbf{x} \in \mathbb{R}^{n_x}$ is the vector of differential states, $\mathbf{u} \in \mathbb{R}^{n_u}$ the vector of inputs, $\mathbf{y} \in \mathbb{R}^{n_y}$ the vector of outputs, and $\mathbf{p} \in \mathbb{R}^{n_p}$ vector of parameters. The measurement noise $\mathbf{v}_k \in \mathbb{R}^{n_y}$ is added to the measured outputs, and k denotes the samples taken at time t_k . The vector \mathbf{p} represents the shape parameters that are estimated.

The following optimisation problem is solved:

$$\min_{\{\mathbf{x}_i, \mathbf{v}_i, \mathbf{p}\}} \sum_{i=0}^N \|\mathbf{y}_i - \mathbf{h}(\mathbf{x}_i)\|_{\mathbf{R}^{-1}}^2 \quad (13.9a)$$

$$\begin{aligned} \text{s.t.} \quad & \mathbf{x}_{i+1} = \mathbf{f}(\mathbf{x}_i, \mathbf{u}_i, \mathbf{p}) \quad \forall i = 0, \dots, N-1 \\ & \mathbf{x}_i \in \mathbb{X}, \end{aligned} \quad (13.9b)$$

where $\mathbf{R} \in \mathbb{R}^{n_y \times n_y}$ is the measurement noise covariance matrix taken as the identity matrix. The set \mathbb{X} is closed and convex, and usually given by a finite dimensional polyhedral set

$$\mathbb{X} = \{\mathbf{x}_i \in \mathbb{R}^{n_x} \mid \mathbf{D}_x \mathbf{x}_i \leq \mathbf{d}_x\}, \quad (13.10)$$

where $\mathbf{D}_x \in \mathbb{R}^{n_x \times n_x}$ is a matrix. The optimization problem is a constrained least squares problem for which standard literature covering parameter estimation exists (Van Trees and Bell 2013).

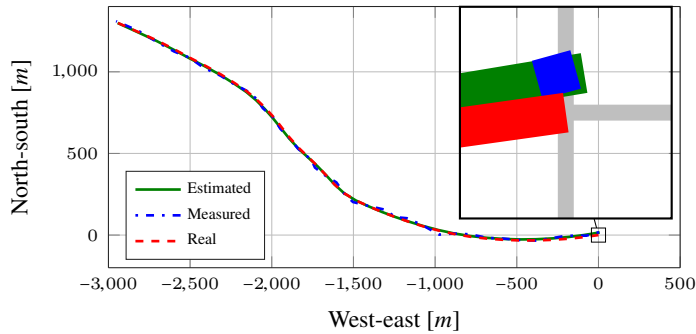


Figure 13.2: Iceberg drift: estimation of iceberg areas with measurement noise on iceberg position (Gaussian white noise $\mu = 0$, $\sigma = 10$).

13.3.3 Identifiability

Several simulation studies were performed to investigate if the parameters can be identified. The measured current, wind and wave forces were used to simulate the iceberg trajectory. If the simulated trajectory is used as position measurements without noise added, then the geometry parameters can be identified. Under these noise-free conditions, it is not necessary to include constraints to achieve identification. However, if measurement noise in the position measurements or current measurements is added, the correct geometry can only be approximated. Problematic is that the iceberg drift trajectories are relatively insensitive to changes in the iceberg geometry. An example of this is shown in Figure 13.2. Even though the estimated and measured drift trajectories of the iceberg are almost identical, the error in the estimate of the cross-section in comparison to the total cross-section area nearly 35%. Moreover, without constraints, the estimated iceberg geometry becomes, under noisy conditions, quickly non-physical, for example, with layers in the middle of the iceberg keel having a zero cross-sectional area.

Since the sensitivity of the iceberg geometry to the iceberg drift trajectory is small, it is difficult to estimate the iceberg geometry without additional information. Therefore, to reduce the parameter space and improve the estimation results, it is necessary to introduce a geometry model of the iceberg (Fig. 13.3). In addition, the parameter identification reaches an acceptable result more quickly, which is important because the timeframe of a ship or other device measuring the current regime close to the iceberg is limited.

The Cramér-Rao bound (Van Trees and Bell 2013), a lower bound on the identification error, depends on the current regime and the noise level. If the current is similar in every current layer and does not change much during observations, then the lower bound of the identification error is higher than in cases where the current regime changes actively. In the first case the information in the observations is low

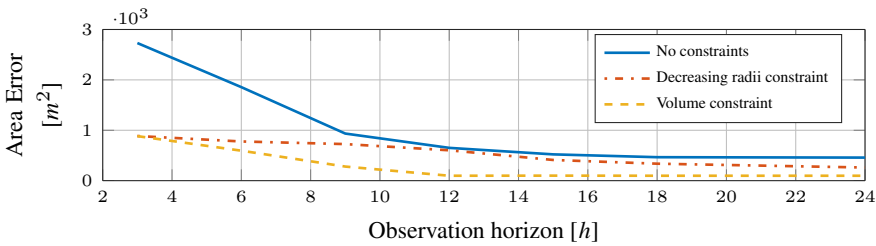


Figure 13.3: Error with different observation horizons and constraints for a nine layered iceberg keel.

while in the second case the information is higher which lowers the identification error.

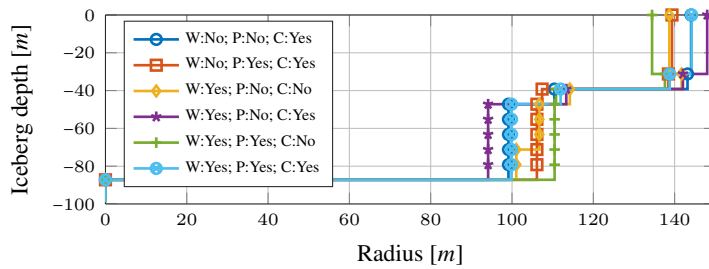
If the observation horizon is short, then it is usually only possible to estimate the axis that is perpendicular to the current drift direction, since the current regime does not change significantly and the iceberg only rotates slightly.

13.3.4 Geometry Estimation

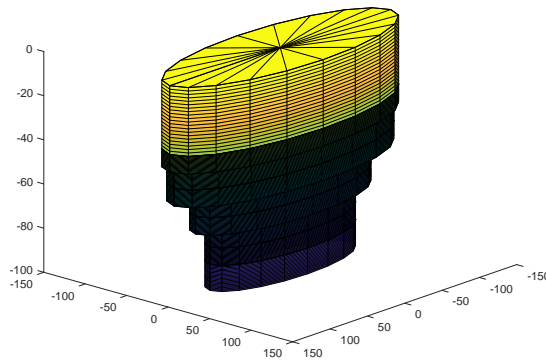
The iceberg keel geometry is estimated for different input signals. Based on the observation of the iceberg sail, the ratio k is set to be 0.35. Furthermore, it is tested how sensitive the shape estimation is whether the wave input, pressure gradient, and Coriolis forces are included. The manually observed wind input is used in all geometry estimations, and the different combinations result in eight geometry estimates. Six geometry estimates are shown in Figure 13.4(a) with an example of a 3D iceberg geometry in Figure 13.4(b). The overall iceberg geometry is similar even though different forces were included in the model. In almost every estimate, the iceberg layers from -40 m to -87 m do not show changing radii. This is caused by the volume constraint (13.1b) combined with too little excitation and a short observation horizon. Consequently, the estimation algorithm cannot distinguish between current layers. The deepest layer of all these iceberg geometries is estimated to be zero. Hence, the keel depth is estimated slightly smaller than what was measured with the SX90 sonar (Sec. 5.2).

The root mean square error is about 150 m to 200 m if either wave or Coriolis force is excluded from the model. If both forces are included, the root mean square error is about 580 m.

The two geometries where wave and Coriolis forces were excluded from the model are not shown. They resulted in a non-physical iceberg geometry. The radii of the second and third iceberg layers are in those cases estimated with zero length while the fourth layer has a large radius of about 250 m. Since the change of the radii is only constrained from the middle of the iceberg height to the deepest layer, this non-physical iceberg shape is possible during estimation. Further constraints may remove this problem.



(a) Iceberg geometry estimates for different input signals (W:wave force, P:pressure gradient force, C:Coriolis force).



(b) Example of a 3D hydrodynamic iceberg geometry.

Figure 13.4: Examples for estimates of the hydrodynamic iceberg geometry.

An increase of 10 % of the iceberg sail volume also increases the iceberg mass by 10 %. The radii in the iceberg geometry estimation increases as well, but the overall geometry stays similar to the original estimate. A similar effect has about a 1.5 % change of the ice density to which the iceberg mass is very sensitive.

13.4 Conclusion

Despite the problems with the dynamic model (Sec. 5), it is possible to approximate the hydrodynamic iceberg geometry with a simple parameter identification algorithm. Under the assumption that the dynamic iceberg model approximates the correct physical behaviour of the process, the hydrodynamic iceberg geometry can be estimated if the iceberg and current regime around the iceberg are observed for some time. This estimated hydrodynamic iceberg geometry is adjusted to the dynamic iceberg model and can afterwards be used efficiently for iceberg drift forecasts. The hydrodynamic iceberg geometry identification by the algorithm

presented in this chapter can be improved by collecting more knowledge about iceberg profiles, which can be transformed into further constraints to incorporate into the algorithm.

Chapter 14

Constrained Posterior Cramér-Rao Bound for Discrete-Time Systems

The chapter is based on PAPER I ([Andersson et al. 2017b](#)). It presents a Cramér-Rao lower bound for the discrete-time filtering problem under linear state constraints. A simple recursive algorithm is presented that extends the computation of the Cramér-Rao lower bound found in previous literature by one additional step in which the full-rank Fisher Information matrix is projected onto the tangent hyperplane of the constraint set. This makes it possible to compute the constrained Cramér-Rao lower bound for the discrete-time filtering problem without re-parametrisation of the original problem to remove redundancies in the state vector, which improves insight into the problem. It is shown that, in the case of a positive-definite Fisher Information Matrix, the presented constrained Cramér-Rao bound is lower than the unconstrained bound, and it is evaluated through an example.

The bound presented in this chapter holds for nonlinear systems with linear constraints. Even though it is likely that also nonlinear constraints will lower the bound, it is challenging to prove the projection results in a lower bound. Therefore, the presented lower bound was not used to analyse the estimation of the hydrodynamic iceberg geometry in Chapter 13.

14.1 Introduction

Discrete-time state estimation arises in adaptive control, identification, and in model-based control, where it is usually before the control prediction step. In general, it is

challenging to build an optimal estimator for such systems. Hence, it is necessary to turn to one of the many suboptimal filter techniques (Galdos 1980).

A common strategy to design such an estimator is to use the Bayesian approach. Closed form solutions exist only for a few cases, and often it is necessary to approximate the Bayesian solution numerically. However, filters based on such approximations lead to estimates that deviate from the ideal solution (Šimandl et al. 2001). Lower bounds on the mean-square error of an estimate can indicate performance limitations. Consequently, it can be used to determine whether imposed performance requirements are realistic or not (Galdos 1980, Šimandl et al. 2001, Tichavsky et al. 1998). The Cramér-Rao bound (CRB), given as the inverse of the Fisher information matrix (FIM), presents such a lower bound for dynamic models. However, in time-varying systems, the estimated parameter vector (the estimated state vector) must be considered random since it corresponds to an underlying nonlinear, randomly driven model (Tichavsky et al. 1998).

In Van Trees (1968), the CRB was extended for random parameter estimation and was successfully applied in state estimation for discrete-time nonlinear stochastic dynamic systems in Galdos (1980) and Bobrovsky and Zakai (1975). The fundamental principle for both bounds is to construct a suitable Gaussian system for which the mean square estimation error is a lower bound to that of the original system. Another approach computing the CRB for filtering problems was proposed by Tichavsky et al. (1998), which assumes the state history as a random parameter and obtains the CRB for the state as a lower right block of the CRB for the complete state history (Šimandl et al. 2001). They referred to the obtained bound as posterior CRB (PCRB).

In some applications, prior knowledge in the form of linear equality constraints is available. This information should result in improved estimates and a lower CRB (Marzetta 1993). One approach finding the CRB under constraints is to reparametrise the original problem and remove redundancies in the parameter vector. However, this may be difficult to implement hindering insights into the original unconstrained problem (Stoica and Ng 1998). Gorman and Hero (1990) proposed a convenient way to compute the constrained CRB for static problems where the bound equals the bound of the original unconstrained problem minus a correction matrix. The same result with a different proof was presented by Marzetta (1993). Another constrained CRB, which also holds for singular Fisher Information matrices, was presented by Stoica and Ng (1998). This theory was extended for complex parameters by Jagannatham and Rao (2004) and biased estimators by Ben-Haim and Eldar (2009).

This chapter connects the theory about constrained CRB with the PCRB for discrete-time systems presented by Tichavsky et al. (1998).

14.2 The CRB for the Nonlinear Filtering Problem

This section follows the posterior CRB presented in [Tichavsky et al. \(1998\)](#), which was also summarised in [Šimandl et al. \(2001\)](#). Consider the discrete-time nonlinear filtering problem

$$\mathbf{x}_{k+1} = \mathbf{f}_k(\mathbf{x}_k, \mathbf{w}_k) \quad (14.1a)$$

$$\mathbf{z}_k = \mathbf{h}_k(\mathbf{x}_k, \mathbf{v}_k), \quad (14.1b)$$

where k is the time index, and $\mathbf{x}_k \in \mathbb{R}^n$ and $\mathbf{z}_k \in \mathbb{R}^y$ represent the state and measurement vectors, respectively. The vectors $\mathbf{w}_k \in \mathbb{R}^n$ and $\mathbf{v}_k \in \mathbb{R}^y$ are mutually independent white noise processes, and \mathbf{f}_k and \mathbf{h}_k are nonlinear functions, which may depend on the time k . The white noise processes are described by known probability density functions (pdf) $p(\mathbf{w}_k)$ and $p(\mathbf{v}_k)$. Furthermore, it is assumed that the initial state \mathbf{x}_0 has a known pdf $p(\mathbf{x}_0)$.

Let the complete state and measurement histories up to the time instant k be denoted as $\mathbf{X}_k = [\mathbf{x}_0^T, \mathbf{x}_1^T, \dots, \mathbf{x}_k^T]^T$ and $\mathbf{Z}_k = [\mathbf{z}_0^T, \mathbf{z}_1^T, \dots, \mathbf{z}_k^T]^T$, respectively. The joint pdf of the state and measurement histories $p(\mathbf{X}_k, \mathbf{Z}_k)$ may be written as $p(\mathbf{X}_k, \mathbf{Z}_k) = p(\mathbf{Z}_k | \mathbf{X}_k) p(\mathbf{X}_k)$. Respecting this, the stochastic system (14.1) is a Markov process, so the logarithm of this pdf can be expressed as

$$\ln p(\mathbf{X}_k, \mathbf{Z}_k) = \ln p(\mathbf{x}_0) + \sum_{i=0}^k \ln p(\mathbf{z}_i | \mathbf{x}_i) + \sum_{i=1}^k \ln p(\mathbf{x}_i | \mathbf{x}_{i-1}). \quad (14.2)$$

If the expectation and derivatives exist, then the FIM for this system can be computed as

$$\mathbf{J}_{k|k}(\mathbf{X}_k) = -E \left(\nabla_{\mathbf{X}_k} [\nabla_{\mathbf{X}_k} \ln p(\mathbf{X}_k, \mathbf{Z}_k)]^T \right), \quad (14.3)$$

where we know that the inverse of the FIM bounds the mean square error matrix (MSEM)

$$\boldsymbol{\Sigma}_{k|k} = E \left\{ (\mathbf{X}_k - \hat{\mathbf{X}}_k)(\mathbf{X}_k - \hat{\mathbf{X}}_k)^T \right\} \geq \mathbf{J}_{k|k}^{-1}. \quad (14.4)$$

Following the notation used in [Šimandl et al. \(2001\)](#) and to simplify the derivation of the filtering estimate let us introduce the following $n \times n$ matrices

$$\mathbf{K}_{k+1}^k = E \{ -\nabla_{\mathbf{x}_k}^{\mathbf{x}_k} \ln p(\mathbf{x}_{k+1} | \mathbf{x}_k)^T \}, \quad (14.5a)$$

$$\mathbf{K}_{k+1}^{k,k+1} = E \{ -\nabla_{\mathbf{x}_k}^{\mathbf{x}_{k+1}} \ln p(\mathbf{x}_{k+1} | \mathbf{x}_k)^T \} = [\mathbf{K}_{k+1}^{k+1,k}]^T, \quad (14.5b)$$

$$\mathbf{K}_{k+1}^{k+1} = E \{ -\nabla_{\mathbf{x}_{k+1}}^{\mathbf{x}_{k+1}} \ln p(\mathbf{x}_{k+1} | \mathbf{x}_k)^T \}, \quad (14.5c)$$

$$\mathbf{L}_k^k = E \{ -\nabla_{\mathbf{x}_k}^{\mathbf{y}_k} \ln p(\mathbf{y}_k | \mathbf{x}_k) \}^T, \quad (14.5d)$$

where we define

$$\mathbf{D}_k = \mathbf{L}_k^k + \mathbf{K}_k^k + \mathbf{K}_{i+1}^k. \quad (14.6)$$

The lower index in (14.5) is the time instant of the state described by the transition pdf, while the upper index represents the states for which the derivatives of the transition pdf are performed.

Using (14.2) and the introduced notations (14.5), the FIM (14.4) decomposes into four blocks

$$\begin{aligned} \mathbf{J}_{k|k}(\mathbf{X}_k) &= \left[\begin{array}{ccc|c} \mathbf{D}_0 & \mathbf{K}_1^{0,1} & & \\ \mathbf{K}_1^{1,0} & \ddots & \ddots & \\ & \ddots & \mathbf{D}_{k-1} & \mathbf{K}_k^{k-1,k} \\ \hline & & \mathbf{K}_k^{k,k-1} & \mathbf{L}_k^k + \mathbf{K}_k^k \end{array} \right], \\ &= \left[\begin{array}{c|c} \mathbf{J}_{k|k}^{1,1} & \mathbf{J}_{k|k}^{1,2} \\ \hline \mathbf{J}_{k|k}^{2,1} & \mathbf{J}_{k|k}^{2,2} \end{array} \right] \end{aligned} \quad (14.7)$$

where the zero elements have been left empty and for $k = 0$ it holds $\mathbf{J}_{0|0}(\mathbf{x}_0) = \mathbf{L}_0^0 + \mathbf{K}_0^0$. The blocks of the FIM represent the state history decomposed as $\mathbf{X}_k = [\mathbf{X}_{k-1}^T, \mathbf{x}_k^T]^T$. Following this notation, we see that the time update can be expressed as (Šimandl et al. 2001)

$$\mathbf{J}_{k+1|k}(\mathbf{X}_{k+1}) = \left[\begin{array}{cc|c} \mathbf{J}_{k|k}^{1,1} & \mathbf{J}_{k|k}^{1,2} & 0 \\ \mathbf{J}_{k|k}^{2,1} & \mathbf{J}_{k|k}^{2,2} + \mathbf{K}_{k+1}^k & \mathbf{K}_{k+1}^{k,k+1} \\ \hline 0 & \mathbf{K}_{k+1}^{k+1,k} & \mathbf{K}_{k+1}^{k+1} \end{array} \right] \quad (14.8)$$

and the measurement update as

$$\mathbf{J}_{k|k}(\mathbf{X}_k) = \left[\begin{array}{c|c} \mathbf{J}_{k|k-1}^{1,1} & \mathbf{J}_{k|k-1}^{1,2} \\ \hline \mathbf{J}_{k|k-1}^{2,1} & \mathbf{J}_{k|k-1}^{2,2} + \mathbf{L}_k^k \end{array} \right]. \quad (14.9)$$

The dimension of the FIM (14.8) and (14.9) increase at each iteration. Furthermore, it can be seen that $\mathbf{J}_{k|k-1}(\mathbf{X}_k)$ and $\mathbf{J}_{k|k}(\mathbf{X}_k)$ are equal except for the lower-right corner block, which is \mathbf{K}_k^k compared to $\mathbf{K}_k^k + \mathbf{L}_k^k$.

Applying (14.4) to (14.9), a formulation for the inequality for the MSEM of a filtering estimate at time k can be obtained

$$E \left\{ (\mathbf{x}_k - \hat{\mathbf{x}}_k)(\mathbf{x}_k - \hat{\mathbf{x}}_k)^T \right\} \geq \mathbf{C}_{k|k} = [\mathbf{J}_{k|k}^{-1}(\mathbf{X}_k)]_{22}, \quad (14.10)$$

where $\mathbf{C}_{k|k}$ is the PCRFB of an estimate $\hat{\mathbf{x}}_{k|k}$. Using the matrix inversion lemma (A.1)-(A.2) and $\mathbf{J}_{k|k-1}^{2,2} = \mathbf{K}_k^k$, we obtain

$$\mathbf{C}_{k|k}^{-1} = \mathbf{L}_k^k + \mathbf{K}_k^k - \mathbf{J}_{k|k-1}^{2,1} [\mathbf{J}_{k|k-1}^{1,1}]^{-1} \mathbf{J}_{k|k-1}^{1,2} \quad (14.11)$$

for the measurement update. For the time-update with the same matrix inversion lemma, the following can be obtained

$$\begin{aligned} \mathbf{C}_{k+1|k}^{-1} &= \mathbf{K}_{k+1}^{k+1} - \begin{pmatrix} 0 & \mathbf{K}_{k+1}^{k+1,k} \end{pmatrix} \begin{pmatrix} \mathbf{J}_{k|k}^{1,1} & \mathbf{J}_{k|k}^{1,2} \\ \mathbf{J}_{k|k}^{2,1} & \mathbf{J}_{k|k}^{2,2} + \mathbf{K}_{k+1}^k \end{pmatrix}^{-1} \begin{pmatrix} 0 \\ \mathbf{K}_{k+1}^{k,k+1} \end{pmatrix} \\ &= \mathbf{K}_{k+1}^{k+1} - \\ &\quad \mathbf{K}_{k+1}^{k+1,k} \left(\mathbf{J}_{k|k}^{2,2} + \mathbf{K}_{k+1}^k - \mathbf{J}_{k|k}^{1,2} [\mathbf{J}_{k|k}^{1,1}]^{-1} \mathbf{J}_{k|k}^{2,1} \right)^{-1} \mathbf{K}_{k+1}^{k,k+1}. \end{aligned} \quad (14.12)$$

With (14.11) and $\mathbf{J}_{k|k-1}^{1,1} = \mathbf{J}_{k|k}^{1,1}$, $\mathbf{J}_{k|k-1}^{1,2} = \mathbf{J}_{k|k}^{1,2}$ and $\mathbf{J}_{k|k-1}^{2,2} = \mathbf{K}_k^k$ this can be reduced to

$$\mathbf{C}_{k+1|k}^{-1} = \mathbf{K}_{k+1}^{k+1} - \mathbf{K}_{k+1}^{k+1,k} \left(\mathbf{K}_{k+1}^k + \mathbf{C}_{k|k}^{-1} \right)^{-1} \mathbf{K}_{k+1}^{k,k+1}. \quad (14.13)$$

With (14.12), the measurement update can also be reduced to

$$\mathbf{C}_{k|k}^{-1} = \mathbf{C}_{k|k-1}^{-1} + \mathbf{L}_k^k, \quad (14.14)$$

which completes the recursion to compute the CRB for the time and measurement update.

14.3 Constrained CRB

In this section, the constrained CRB is introduced and will closely follow the derivation presented in [Stoica and Ng \(1998\)](#). However, the difference between this chapter is that they assumed a vector of non-random parameters is estimated. Here, a vector of random parameters \mathbf{X} based on a vector of observations \mathbf{Z} is estimated. It is required that the estimate $\hat{\mathbf{X}}$ satisfies l ($l < n$) continuously differentiable constraints,

$$\mathbf{f}(\hat{\mathbf{X}}) = 0. \quad (14.15)$$

It is further assumed that the set $\{\mathbf{X} | \mathbf{f}(\mathbf{X}) = 0\}$ is non-empty. The gradient matrix of the constraints can be defined as

$$\mathbf{F} = \frac{\partial \mathbf{f}(\mathbf{X})}{\partial \mathbf{X}^T}, \quad (14.16)$$

where it is assumed that (14.16) has a full rank for any \mathbf{X} satisfying (14.15). Thus, there exists an $n \times (n - l)$ matrix \mathbf{U} such that

$$\mathbf{F}\mathbf{U} = 0, \quad \mathbf{U}^T \mathbf{U} = \mathbf{I}, \quad (14.17)$$

where it is assumed that \mathbf{U} is independent of \mathbf{X} . While this is restrictive, it always holds for linear constraints. The likelihood function is given by (14.2) and lets us denote

$$\Delta = \nabla_{\mathbf{X}} \ln p(\mathbf{X}, \mathbf{Z}). \quad (14.18)$$

In this case, the FIM (14.3) is alternatively given as

$$\mathbf{J} = E(\Delta \Delta^T). \quad (14.19)$$

If the following conditions exist:

1. $\frac{\partial p(\mathbf{X}, \mathbf{Z})}{\partial x_i^j}$ is absolutely integrable with respect to \mathbf{X} and \mathbf{Z} for $i = 0, \dots, k$ and $j = 0, \dots, n$,
2. $\frac{\partial^2 p(\mathbf{X}, \mathbf{Z})}{\partial x_i^j}$ is absolutely integrable with respect to \mathbf{X} and \mathbf{Z} for $i = 0, \dots, k$ and $j = 0, \dots, n$, and
3. the conditional expectation of the error, given \mathbf{X} , is

$$\mathbf{B}(\mathbf{X}) = \int_{-\infty}^{\infty} [\hat{\mathbf{X}} - \mathbf{X}] p(\mathbf{Z}|\mathbf{X}) d\mathbf{Z}, \quad (14.20)$$

where $\mathbf{B}(\mathbf{X})$ denotes the bias of the estimate, then it is assumed that

$$\begin{aligned} \lim_{x_i^j \rightarrow \infty} \mathbf{B}(\mathbf{X}) p(\mathbf{X}) &= 0, & \text{for } i = 0, \dots, k \\ \lim_{x_i^j \rightarrow -\infty} \mathbf{B}(\mathbf{X}) p(\mathbf{X}) &= 0, & \text{and } j = 0, \dots, n \end{aligned} \quad (14.21)$$

With these conditions, it can be shown that the following holds (Van Trees and Bell 2013)

$$E((\hat{\mathbf{X}} - \mathbf{X}) \Delta^T) = \mathbf{I}, \quad (14.22)$$

which is the fact that is required such that

$$E((\hat{\mathbf{X}} - \mathbf{X}) \Delta^T) \mathbf{U} \mathbf{U}^T = \mathbf{U} \mathbf{U}^T. \quad (14.23)$$

Lemma 14.3.1. *If the condition holds, with \mathbf{U} defined in (14.17) and in case $\mathbf{U}^T \mathbf{J} \mathbf{U}$ is non-singular, then the constrained CRB is given as*

$$E \left\{ (\mathbf{X} - \hat{\mathbf{X}})(\mathbf{X} - \hat{\mathbf{X}})^T \right\} \geq \mathbf{U} (\mathbf{U}^T \mathbf{J} \mathbf{U})^{-1} \mathbf{U}^T. \quad (14.24)$$

Proof. Let \mathbf{W} be an arbitrary $n \times n$ matrix. Then

$$E \left\{ (\mathbf{X} - \hat{\mathbf{X}} - \mathbf{W}\mathbf{U}\mathbf{U}^T \Delta) (\mathbf{X} - \hat{\mathbf{X}} - \mathbf{W}\mathbf{U}\mathbf{U}^T \Delta)^T \right\} = E \left\{ (\mathbf{X} - \hat{\mathbf{X}}) (\mathbf{X} - \hat{\mathbf{X}})^T \right\} - \mathbf{W}\mathbf{U}\mathbf{U}^T - \mathbf{U}\mathbf{U}^T \mathbf{W}^T + \mathbf{W}\mathbf{U}\mathbf{U}^T \mathbf{J}\mathbf{U}\mathbf{U}^T \mathbf{W}^T \geq 0, \quad (14.25)$$

where the equality follows from (14.23) and the fact that \mathbf{U} is independent of \mathbf{X} . The inequality is a consequence of the positive semi-definiteness of the covariance matrix of $\mathbf{X} - \hat{\mathbf{X}} - \mathbf{W}\mathbf{U}\mathbf{U}^T \Delta$. For the rest of the proof the derivation in Stoica and Ng (1998) may be followed. ■

14.4 The Constrained CRB for the Nonlinear Filtering Problem

Theorem 14.4.1. *The constrained CRB for the nonlinear filtering problem can be computed by a time update*

$$\mathbf{C}_{k|k-1}^{-1} = \mathbf{K}_k^k - \mathbf{K}_k^{k,k-1} \left(\mathbf{K}_k^{k-1} + \tilde{\mathbf{C}}_{k-1|k-1}^{-1} \right)^{-1} \mathbf{K}_k^{k-1,k}, \quad (14.26)$$

a measurement update

$$\mathbf{C}_{k|k}^{-1} = \mathbf{C}_{k|k-1}^{-1} + \mathbf{L}_k^k, \quad (14.27)$$

and a constraint update

$$\tilde{\mathbf{C}}_{k|k} = \mathbf{U}_k (\mathbf{U}_k^T \mathbf{C}_{k|k}^{-1} \mathbf{U}_k)^{-1} \mathbf{U}_k^T. \quad (14.28)$$

Proof. It will be shown that the constrained CRB of the entire system (14.4) results in the same CRB as given by the recursion (14.26)-(14.28). This will be shown for the first time step, and afterwards it will be shown that this also holds for every following time step.

The following $2n \times 2n$ matrix gives the FIM for entire state and measurement history after the first time step

$$\mathbf{J}_{1|1}(\mathbf{X}_1) = \begin{pmatrix} \mathbf{K}_0^0 + \mathbf{L}_0^0 + \mathbf{K}_1^0 & \mathbf{K}_1^{0,1} \\ \mathbf{K}_1^{1,0} & \mathbf{L}_1^1 + \mathbf{K}_1^1 \end{pmatrix} \quad (14.29)$$

It is assumed that the constraints (14.15) depend only on the states at each time step. This gives a $2n \times 2(n-l)$ matrix

$$\mathbf{U}(\mathbf{X}_1) = \begin{pmatrix} \mathbf{U}(\mathbf{x}_0) & 0 \\ 0 & \mathbf{U}(\mathbf{x}_1) \end{pmatrix} = \begin{pmatrix} \mathbf{U}_0 & 0 \\ 0 & \mathbf{U}_1 \end{pmatrix} \quad (14.30)$$

where the matrix \mathbf{U}_i of each state is on the diagonal while all other entries are zero. Using (14.24), (14.30), and the matrix inversion lemma (A.1) on (14.29) to compute the constrained CRB for state \mathbf{x}_1 , we obtain

$$\tilde{\mathbf{C}}_{1|1} = \mathbf{U}_1 \left[\mathbf{U}_1^T (\mathbf{L}_1^1 + \mathbf{K}_1^1) \mathbf{U}_1 - \mathbf{U}_1^T \mathbf{K}_1^{1,0} \mathbf{U}_0 [\mathbf{U}_0^T (\mathbf{K}_0^0 + \mathbf{L}_0^0 + \mathbf{K}_1^0) \mathbf{U}_0]^{-1} \mathbf{U}_0^T \mathbf{K}_1^{0,1} \mathbf{U}_1 \right]^{-1} \mathbf{U}_1^T. \quad (14.31)$$

With the recursion (14.26)-(14.28) the constrained CRB for state \mathbf{x}_1 is

$$\tilde{\mathbf{C}}_{1|1} = \mathbf{U}_1 \cdot \left[\mathbf{U}_1^T \left(\mathbf{L}_1^1 + \mathbf{K}_1^1 - \mathbf{K}_1^{1,0} [\mathbf{J}_{0|0} + \mathbf{K}_1^0]^{-1} \mathbf{K}_1^{0,1} \right) \mathbf{U}_1 \right]^{-1} \mathbf{U}_1^T. \quad (14.32)$$

Comparing (14.31) and (14.32), the only thing left to prove is

$$\mathbf{U}_0 [\mathbf{U}_0^T (\mathbf{K}_0^0 + \mathbf{L}_0^0 + \mathbf{K}_1^0) \mathbf{U}_0]^{-1} \mathbf{U}_0^T \equiv [\mathbf{J}_{0|0} + \mathbf{K}_1^0]^{-1} \quad (14.33)$$

The left-hand side of (14.33) is rewritten slightly, and the binomial inverse theorem (A.4) applied

$$\begin{aligned} \mathbf{U}_0 \left[\mathbf{U}_0^T (\mathbf{K}_0^0 + \mathbf{L}_0^0) \mathbf{U}_0 + \mathbf{U}_0^T \mathbf{K}_1^0 \mathbf{U}_0 \right]^{-1} \mathbf{U}_0^T &= \mathbf{U}_0 \left[(\mathbf{U}_0^T (\mathbf{K}_0^0 + \mathbf{L}_0^0) \mathbf{U}_0)^{-1} - (\mathbf{U}_0^T (\mathbf{K}_0^0 + \mathbf{L}_0^0) \mathbf{U}_0)^{-1} \mathbf{U}_0^T \cdot \right. \\ &\quad \left. (\mathbf{I} + \mathbf{K}_1^0 \mathbf{U}_0 (\mathbf{U}_0^T (\mathbf{K}_0^0 + \mathbf{L}_0^0) \mathbf{U}_0)^{-1} \mathbf{U}_0^T)^{-1} \mathbf{K}_1^0 \mathbf{U}_0 \cdot (\mathbf{U}_0^T (\mathbf{K}_0^0 + \mathbf{L}_0^0) \mathbf{U}_0)^{-1} \right] \mathbf{U}_0^T. \end{aligned} \quad (14.34)$$

where $\mathbf{B} = \mathbf{U}_0^T$, $\mathbf{D} = \mathbf{K}_1^0$ and $\mathbf{C} = \mathbf{U}_0$. Given that

$$[\mathbf{J}_{0|0}]^{-1} = \mathbf{U}_0 (\mathbf{U}_0^T (\mathbf{K}_0^0 + \mathbf{L}_0^0) \mathbf{U}_0)^{-1} \mathbf{U}_0^T, \quad (14.35)$$

the binomial inverse theorem (A.4) is also applied to the right-hand side of (14.33)

$$\begin{aligned} [\mathbf{J}_{0|0} + \mathbf{K}_1^0]^{-1} &= \mathbf{U}_0 (\mathbf{U}_0^T (\mathbf{K}_0^0 + \mathbf{L}_0^0) \mathbf{U}_0)^{-1} \mathbf{U}_0^T - \mathbf{U}_0 (\mathbf{U}_0^T (\mathbf{K}_0^0 + \mathbf{L}_0^0) \mathbf{U}_0)^{-1} \mathbf{U}_0^T \cdot \\ &\quad \mathbf{B} (\mathbf{I} + \mathbf{D} \mathbf{C} \mathbf{U}_0 (\mathbf{U}_0^T (\mathbf{K}_0^0 + \mathbf{L}_0^0) \mathbf{U}_0) \mathbf{B})^{-1} \mathbf{D} \mathbf{C} \mathbf{U}_0 (\mathbf{U}_0^T (\mathbf{K}_0^0 + \mathbf{L}_0^0) \mathbf{U}_0)^{-1} \mathbf{U}_0^T, \end{aligned} \quad (14.36)$$

where $\mathbf{B} = \mathbf{I}$, $\mathbf{D} = \mathbf{K}_1^0$, and $\mathbf{C} = \mathbf{I}$. Comparing (14.34) and (14.36), we see that (14.33) holds.

For k time steps, it can be obtained similarly as before (14.29) - (14.32) that

$$\mathbf{U}_{k-1} \left[\mathbf{U}_{k-1|0}^T \mathbf{J}_{k|k-1}^{1,1} \mathbf{U}_{k-1|0} \right] \mathbf{U}_{k-1}^T \equiv [\mathbf{J}_{k-1|k-1} + \mathbf{K}_1^0]^{-1}. \quad (14.37)$$

Applying the matrix inversion lemma to the left-hand side plus the fact that the matrix \mathbf{U} is block-diagonal and setting in the recursive equations to the right-hand side, (14.37) can be reduced to (14.33). ■

14.5 Reduction of the Constrained CRB

In this section, it is established that the unconstrained CRB (14.4) is never smaller than the constrained CRB (14.24). Consequently, adding information about constraints reduces the CRB. This can be shown in the case where $\mathbf{J}_{k|k}$ is positive definite. Here, as shown in Stoica and Ng (1998) and Khatri (1966), the constrained CRB (14.24) can be written as

$$\mathbf{U}(\mathbf{U}^T \mathbf{J} \mathbf{U})^{-1} \mathbf{U}^T = (\mathbf{I} - \mathbf{J}^{-1} \mathbf{F}^T (\mathbf{F} \mathbf{J}^{-1} \mathbf{F}^T)^{-1} \mathbf{F}) \mathbf{J}^{-1} = \mathbf{Q} \mathbf{J}^{-1}, \quad (14.38)$$

where \mathbf{F} is given in (14.16) and indices and arguments were omitted for notational convenience. It can be shown that \mathbf{Q} is idempotent, which means

$$\mathbf{Q} = \mathbf{Q} \mathbf{Q}. \quad (14.39)$$

Furthermore, $\mathbf{I} - \mathbf{Q}$ is idempotent and \mathbf{J}^{-1} as well as $\mathbf{Q} \mathbf{J}^{-1}$ are symmetric. With these conditions, it can be proven that the constrained CRB reduces in the sense that the subtraction of the constraint from the unconstrained CRB is non-negative definite (Gorman and Hero 1990).

$$\begin{aligned} \mathbf{Q} \mathbf{J}^{-1} &= \mathbf{J}^{-1} - (\mathbf{I} - \mathbf{Q}) \mathbf{J}^{-1} \\ &= \mathbf{J}^{-1} - (\mathbf{I} - \mathbf{Q})(\mathbf{I} - \mathbf{Q}) \mathbf{J}^{-1} \\ &= \mathbf{J}^{-1} - (\mathbf{I} - \mathbf{Q}) \mathbf{J}^{-1} (\mathbf{I} - \mathbf{Q}) \\ &\leq \mathbf{J}^{-1} \end{aligned} \quad (14.40)$$

14.6 Computation of the Constrained CRB

The constrained CRB can be computed with the matrices (14.5) and the recursive equations (14.26) - (14.28). In the case of a positive definite FIM $\mathbf{J}_{k|k}$, (14.28) can be exchanged with (14.38), which may reduce the computational burden. Important to consider is that the constrained CRB is singular. Consequently, the constrained CRB is not invertible, which is not an issue in the recursion, but (14.26) can only be computed with the help of a matrix inversion lemma such as (A.3).

14.6.1 The Linear Gaussian Case

Let us consider the linear system with additive Gaussian state and measurement noise with linear equality constraints

$$\mathbf{x}_{k+1} = \mathbf{F}_k \mathbf{x}_k + \mathbf{w}_k \quad (14.41a)$$

$$\mathbf{z}_k = \mathbf{H}_k \mathbf{x}_k + \mathbf{v}_k, \quad (14.41b)$$

$$0 = \mathbf{A}_k \mathbf{x}_k, \quad (14.41c)$$

where \mathbf{A}_k is the gradient matrix of the constraints. The process covariance and measurement covariance is given by the positive definite matrices \mathbf{Q}_k and \mathbf{R}_k , respectively. For this special case, the matrices (14.5) have an analytical solution

$$\mathbf{K}_{k+1}^k = \mathbf{F}_k^T \mathbf{Q}_k^{-1} \mathbf{F}_k, \quad (14.42a)$$

$$\mathbf{K}_{k+1}^{k,k+1} = -\mathbf{F}_k^T \mathbf{Q}_k^{-1} = [\mathbf{K}_{k+1}^{k+1,k}]^T, \quad (14.42b)$$

$$\mathbf{K}_{k+1}^{k+1} = \mathbf{Q}_k^{-1}, \quad (14.42c)$$

$$\mathbf{L}_k^k = \mathbf{H}_k^T \mathbf{R}^{-1} \mathbf{H}. \quad (14.42d)$$

Using the matrix inversion lemma (A.3), the recursive equations (14.26) and (14.27) can be computed as

$$\mathbf{C}_{k|k-1} = \mathbf{Q}_k + \mathbf{F}_k \tilde{\mathbf{C}}_{k-1|k-1} \mathbf{F}_k^T, \quad (14.43a)$$

$$\mathbf{C}_{k|k} = \mathbf{C}_{k|k-1} - \mathbf{C}_{k|k-1} \mathbf{H}^T \left(\mathbf{R} + \mathbf{H} \mathbf{C}_{k|k-1} \mathbf{H}^T \right)^{-1} \mathbf{H} \mathbf{C}_{k|k-1}, \quad (14.43b)$$

which are the Kalman filter time and measurement update equations (Simon 2006). The constrained update step (14.28) should be computed using the right-hand side of (14.38)

$$\tilde{\mathbf{C}}_{k|k} = \mathbf{C}_{k|k} - \mathbf{C}_{k|k} \mathbf{A}_k^T \left(\mathbf{A}_k \mathbf{C}_{k|k} \mathbf{A}_k^T \right)^{-1} \mathbf{A}_k \mathbf{C}_{k|k}, \quad (14.44)$$

since it avoids the otherwise needed inversion of (14.43b).

14.7 Numerical Example

Simon (2010) presents a four-state navigation problem with equality constraints. The first two states present the positions and the last two states the velocities in the north and east directions, respectively. The velocity of the vehicle is in the direction of θ , which is an angle measured anti-clockwise from the east axis. A sensor provides a noisy measurement of the vehicle's north and east positions. The equations for this system can be written as

$$\mathbf{x}_{k+1} = \begin{pmatrix} 1 & 0 & T & 0 \\ 0 & 1 & 0 & T \\ 0 & 0 & 1 & 0 \\ 0 & 0 & 0 & 1 \end{pmatrix} \mathbf{x}_k + \begin{pmatrix} 0 \\ 0 \\ T \sin \theta \\ T \cos \theta \end{pmatrix} u_k + \mathbf{w}_k, \quad (14.45a)$$

$$\mathbf{y}_k = \begin{pmatrix} 1 & 0 & 0 & 0 \\ 0 & 1 & 0 & 0 \end{pmatrix} \mathbf{x}_k + \mathbf{v}_k, \quad (14.45b)$$

where T is the discretisation step size and u_k is the acceleration input. The covariance of process and measurement noise are

$$\mathbf{Q} = \text{diag}(4, 4, 1, 1), \quad \mathbf{R} = \text{diag}(900, 900) \quad (14.46)$$

and the initial estimation error covariance is

$$\mathbf{P}_0^+ = \text{diag}(900, 900, 4, 4), \quad (14.47)$$

where it holds

$$[\mathbf{P}_0^+]^{-1} = \mathbf{L}_0^0 + \mathbf{K}_0^0. \quad (14.48)$$

Since we know that the vehicle is on the road with a heading angle θ , the following holds

$$\tan \theta = \frac{x(1)}{x(2)} = \frac{x(3)}{x(4)}. \quad (14.49)$$

The constraints of the system can be expressed in the form $\mathbf{D}_i \mathbf{x}_k$ using either

$$\mathbf{D}_1 = \begin{pmatrix} 1 - \tan \theta & 0 & 0 & 0 \\ 0 & 0 & 1 & -\tan \theta \end{pmatrix} \quad (14.50)$$

or

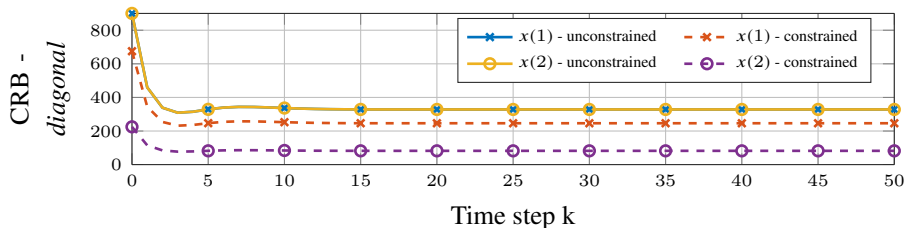
$$\mathbf{D}_2 = (0 \ 0 \ 1 \ -\tan \theta). \quad (14.51)$$

Consequently, the system has either one or two equality constraints.

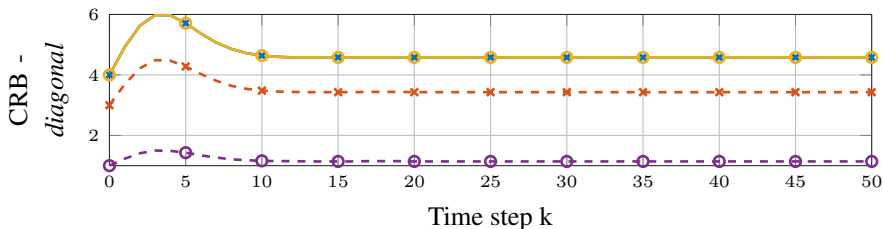
The recursive equations (14.43)-(14.44) are used to compute the constrained CRB for the system with \mathbf{D}_1 as the constrained gradient matrix of the system. The CRB for all states is shown in Figure 14.1. The CRB for the constrained system reduces since the constrained information is used to compute the bound. Similarly, the constrained CRB for the system using \mathbf{D}_2 as the gradient matrix of the constraints can be computed. Since \mathbf{D}_1 provides more information about the constraints on the position while the same information as \mathbf{D}_2 about the velocities, the constrained CRB using \mathbf{D}_1 is lower as the one using \mathbf{D}_2 for the position estimates (Fig. 14.2(a)) while the same for the velocity estimates (Fig. 14.2(b)).

The computed constrained CRB can be reached with equality if the constrained Kalman filter using the system projection method presented by Simon (2010) is used (Fig. 14.3). In this case, the initial estimation error covariance and the process noise covariance are projected onto the constrained surface such that they are consistent with the state constraints. Of all constrained linear estimators considered in Simon (2010), the Kalman filter using the system projection method reached the lowest error covariance for the presented problem.

Consider the problem where the sensor has a fault and is only able to provide a measurement of the vehicle's north position. It can be easily seen that the unconstrained problem becomes unobservable. This is not the case for the constrained problem using \mathbf{D}_1 . However, the problem is also unobservable if \mathbf{D}_2 is used since the constrained CRB of $x(2)$ grows without bounds (Fig. 14.4). The CRB of $x(2)$ of the unconstrained case grows quickly, while the CRB of $x(2)$ using \mathbf{D}_2 considerably evolves slower to infinity.



(a) Positions.

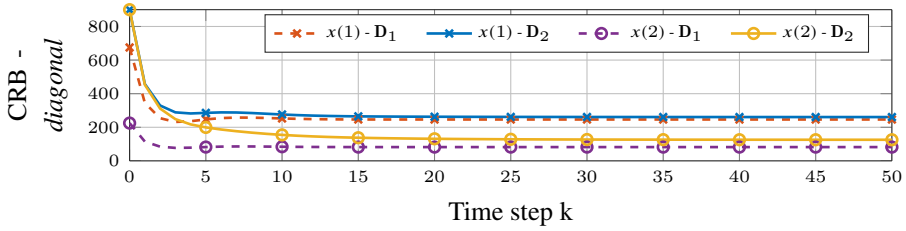


(b) Velocities.

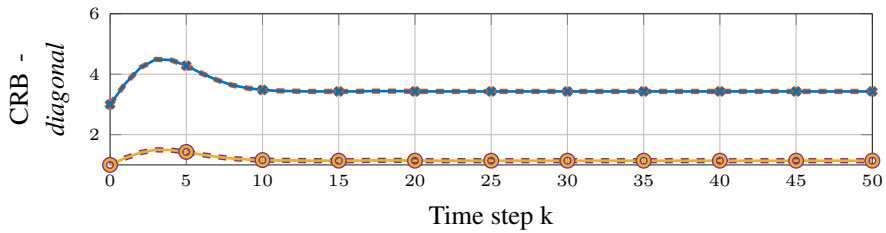
Figure 14.1: Constrained and unconstrained CRB for the state components of the navigation example.

14.8 Conclusion

A simple recursive algorithm to compute the CRB for the nonlinear filtering problem under linear state constraints is presented. The CRB version found in previous literature is extended by one step that projects the unconstrained CRB onto the tangent hyperplane of the constrained set. Two different equations are presented to perform the constraint update, and this update step reduces the CRB compared to the unconstrained CRB. The constrained CRB is illustrated on a navigation problem, where the constrained CRB reduces compared to the unconstrained one. Moreover, it is shown that a Kalman filter using a system projection method reaches the constrained CRB for the considered example. In addition, the constrained CRB can easily be used to investigate observability of a constrained problem.

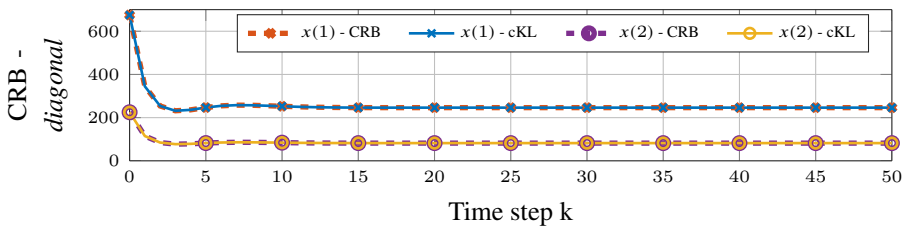


(a) Positions.

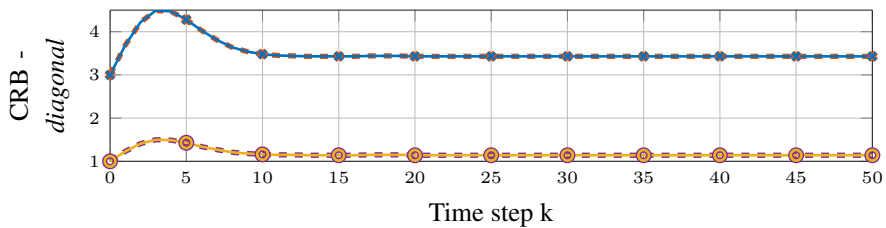


(b) Velocities.

Figure 14.2: Constrained CRB for the state components of the navigation example using either D_1 or D_2 .



(a) Positions.



(b) Velocities.

Figure 14.3: Constrained CRB and error covariance of the constrained Kalman filter (cKL) using the system projection method. The system is constrained using D_1 .

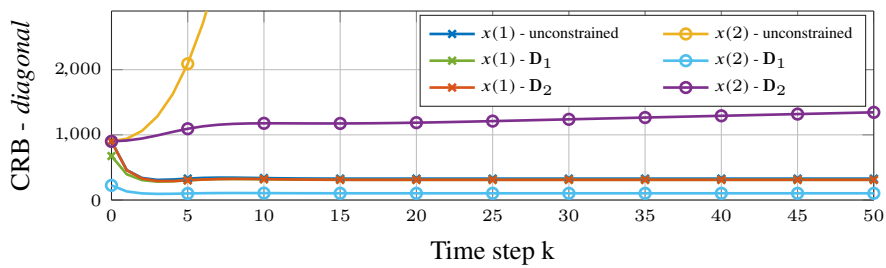


Figure 14.4: CRB for the state components of the position when only $x(1)$ is measured.

Chapter 15

On Kalman Filtering with Linear State Equality Constraints

The chapter is based on PAPER B ([Andersson et al. 2018a](#)). It is concerned with the state estimation problem for linear systems with linear state equality constraints. We re-examine the constrained Kalman filter variations and propose an alternative derivation to prove that using an oblique state projection gives a smaller error covariance. A simple example illustrates the performance of the different Kalman filters.

In this chapter, the constrained Cramér-Rao bound derived in Chapter 14 is used and, similarly, an error-covariance matrix for a Kalman filter with linear state equality constraints is derived.

15.1 Introduction

The discrete-time Kalman filter (KF) under linear equality constraints has been studied in [Simon and Chia \(2002\)](#), [Ko and Bitmead \(2007\)](#), and [Teixeira et al. \(2009\)](#). The inclusion of the constraint information should result in an improved estimate and a smaller error-covariance matrix ([Marzetta 1993](#)). One way to include the additional information is to reduce the system model and use the reduced state and the conventional KF ([Simon 2010](#)). However, this approach may be challenging to implement and may hinder insights into the original unconstrained problem ([Stoica and Ng 1998](#)).

For a conventional linear stochastic model with additive white process noise and linear equality constraints, the process noise must have a singular covariance matrix to be consistent with the linear constraints on the state ([Ko and Bitmead 2007](#)). This realisation leads to a modification of the initial estimation error co-

variance and the process noise covariance. After that, the conventional KF can be used. This approach is called the *system projection* approach (spKF) (Simon 2010)¹.

Another way to include equality constraints into the state estimate was presented by Simon and Chia (2002) by using the unconstrained KF to project the results onto the constraints subspace. This approach is called *estimate projection* KF (epKF) (Simon 2010).

A generalisation of the epKF was presented by Teixeira et al. (2009), where they used, in contrast to Simon and Chia (2002), the projected state and error covariance estimates in the recursion. They called this *equality constrained* KF (ecKF).

It was proven that the state error covariance of both projection approaches is smaller than that of the unconstrained estimate (Simon and Chia 2002, Ko and Bitmead 2007). Moreover, it was shown that the spKF has a smaller error covariance than the epKF (Ko and Bitmead 2007). Teixeira et al. (2009) compared all three constrained KF numerically, which all produced similar results in the examples concerning their performance measures. However, the epKF produces less accurate and informative forecasts. The main reason that the two others outperform the epKF is that the projected state and covariance matrix are not fed back into the recursion.

The contribution of this chapter is to show an alternative derivation of the ecKF coming from the Cramér-Rao lower bound. Moreover, it is analytically derived that using the ecKF results in a smaller error covariance compared to the epKF and spKF.

15.2 Four Kalman Filter Variants

Consider the discrete time invariant system given by

$$\mathbf{x}_{k+1} = \mathbf{A}\mathbf{x}_k + \mathbf{B}\mathbf{u}_k + \mathbf{w}_k, \quad (15.1a)$$

$$\mathbf{y}_k = \mathbf{C}\mathbf{x}_k + \mathbf{v}_k, \quad (15.1b)$$

where k is the time index, and $\mathbf{x}_k \in \mathbb{R}^n$ and $\mathbf{y}_k \in \mathbb{R}^y$ represent the state and measurement vectors, respectively. The state \mathbf{x}_k is known to be constrained such that

$$\mathbf{D}\mathbf{x}_k = \mathbf{0}. \quad (15.2)$$

The vectors $\mathbf{w}_k \in \mathbb{R}^n$ and $\mathbf{v}_k \in \mathbb{R}^p$ are mutually independent white noise processes with the covariances $\mathbf{Q}^c \in \mathbb{R}^{n \times n}$ and $\mathbf{R} \in \mathbb{R}^{p \times p}$. Furthermore, it is assumed that

¹In the original paper by Ko and Bitmead (2007) it is called *constrained Kalman filter*. We, however, will call it *system projection Kalman filter* as in Simon (2010) to avoid confusion with the *equality constrained Kalman filter* presented later.

the initial state \mathbf{x}_0 has a known pdf $p(\mathbf{x}_0)$.

The matrix $\mathbf{D} \in \mathbb{R}^{c \times n}$ (with $c < n$) is assumed to have full row rank. Moreover, it is assumed, without loss of generality, that the rows of \mathbf{D} are unit vectors. The constraint (15.2) implies that $\mathbf{x}_{k+1} = \mathbf{A}\mathbf{x}_k + \mathbf{B}\mathbf{u}_k + \mathbf{w}_k \in \mathcal{N}(\mathbf{D})$ (Ko and Bitmead 2007). Furthermore, it is assumed that the state stays within the constraint surface $\mathcal{N}(\mathbf{D})$ as this represents the physical constraints. In practice, this implies that each component of the state equation is constrained in $\mathcal{N}(\mathbf{D})$ (Ko and Bitmead 2007)

$$(\mathbf{A}\mathbf{x}_k, \mathbf{B}\mathbf{u}_k, \mathbf{w}_k) \in \mathcal{N}(\mathbf{D}). \quad (15.3)$$

15.2.1 The Unconstrained Kalman Filter

For completeness, the equations of the unconstrained Kalman predictor (KF), where $\mathbf{V}_k^{u,p,c,e} = (\mathbf{C}\Sigma_k^{u,p,c,e}\mathbf{C}^T + \mathbf{R})^{-1}$, are²

$$\begin{aligned} \mathbf{K}_k^u &= \Sigma_k^u \mathbf{C}^T \mathbf{V}_k^u, \\ \hat{\mathbf{x}}_{k+1}^u &= \mathbf{A}(\mathbf{I} - \mathbf{K}_k^u \mathbf{C})\hat{\mathbf{x}}_k^u + \mathbf{B}\mathbf{u}_k + \mathbf{A}\mathbf{K}_k^u \mathbf{y}_k \\ \Sigma_{k+1}^u &= \mathbf{A}\Sigma_k^u \mathbf{A}^T - \mathbf{A}\Sigma_k^u \mathbf{C}^T \mathbf{V}_k^u \mathbf{C}\Sigma_k^u \mathbf{A}^T + \mathbf{Q}^u, \end{aligned} \quad (15.4)$$

where \mathbf{Q}^u is the unconstrained process noise covariance matrix.

15.2.2 The Estimate Projection Kalman Filter

The epKF approach to the constrained filtering problem is to project the unconstrained estimate $\hat{\mathbf{x}}_k^u$ of the KF onto the constraint subspace (Simon and Chia 2002). The constrained estimate can be found by solving

$$\min_{\tilde{\mathbf{x}}_k^p} (\tilde{\mathbf{x}}_k^p - \hat{\mathbf{x}}_k^u) \mathbf{W} (\tilde{\mathbf{x}}_k^p - \hat{\mathbf{x}}_k^u)^T \quad \text{subject to } \mathbf{D}\tilde{\mathbf{x}}_k^p = \mathbf{0},$$

where $\tilde{\mathbf{x}}_k^p$ and \mathbf{W} are the constrained estimate and a positive-definite matrix, respectively. The solution to this problem is

$$\tilde{\mathbf{x}}_k^p = \mathbf{P}_{\mathcal{N}(\mathbf{D})}^{\mathbf{W}} \hat{\mathbf{x}}_k^u,$$

where $\mathbf{P}_{\mathcal{N}(\mathbf{D})}^{\mathbf{W}} \equiv \mathbf{I} - \mathbf{W}^{-1} \mathbf{D}^T (\mathbf{D}\mathbf{W}^{-1} \mathbf{D}^T)^{-1} \mathbf{D}$, which, in general, is an oblique projection. The smallest projected error covariance $\Sigma_k^p = \mathbf{P}_k^{\mathbf{W}} \Sigma_k^u (\mathbf{P}_k^{\mathbf{W}})^T = \mathbf{P}_k \Sigma_k^u$ is obtained if we set $\mathbf{W} = (\Sigma_k^u)^{-1}$ where Σ_k^u is the error covariance matrix of the unconstrained KF (Simon and Chia 2002, Simon 2010).

The complete epKF is, therefore, (15.4) combined with the projections

$$\begin{aligned} \tilde{\mathbf{x}}_{k+1}^p &= \mathbf{P}_{\mathcal{N}(\mathbf{D})}^{\mathbf{W}} \hat{\mathbf{x}}_k^u, \\ \Sigma_{k+1}^p &= \mathbf{P}_{\mathcal{N}(\mathbf{D})}^{\mathbf{W}} \Sigma_k^u. \end{aligned} \quad (15.5)$$

²The superscripts denote the unconstrained (u), estimate projection (p), system projection (c), and equality constrained Kalman filter (e).

Remark 15.2.1. *The epKF neither uses the projected error covariance nor the projected state in the recursion.*

15.2.3 The System Projection Kalman Filter

The spKF approach is based on the observation that the system can be projected onto the null space of \mathbf{D} . Let us denote the orthogonal basis of \mathbf{D} by \mathbf{U} , which satisfies

$$\mathbf{D}\mathbf{U} = 0, \quad \mathbf{U}^T\mathbf{U} = \mathbf{I}. \quad (15.6)$$

The projected system is (Ko and Bitmead 2007):

$$\mathbf{x}_{k+1} = \mathbf{P}_{\mathcal{N}(\mathbf{D})}(\mathbf{A}\mathbf{x}_k + \mathbf{B}\mathbf{u}_k + \mathbf{w}_k),$$

where $\mathbf{P}_{\mathcal{N}(\mathbf{D})} \equiv \mathbf{U}^T\mathbf{U}$ is the orthogonal projector onto the null space of \mathbf{D} . The difference between the oblique and orthogonal projection is that in the orthogonal projection onto the subspace \mathcal{M} along \mathcal{N} , the two subspaces \mathcal{M} and \mathcal{N} are orthogonal, while in the oblique projection this is not the case.

An important consequence from (15.3) is that the system matrix \mathbf{A} satisfies the following properties

$$\mathbf{A}\mathbf{x}_k = \mathbf{P}\mathbf{A}\mathbf{x}_k = \mathbf{A}\mathbf{P}\mathbf{x}_k,$$

where \mathbf{P} is any projection matrix onto the null space of \mathbf{D} . Moreover, by taking a conditional expectation for any given measurement $\mathbf{Y}_k = [\mathbf{y}_0^T, \mathbf{y}_1^T, \dots, \mathbf{y}_k^T]^T$, the following can be obtained (Ko and Bitmead 2007)

$$\mathbf{P}\mathbf{A} E\{\mathbf{x}_k|\mathbf{Y}_k\} = \mathbf{A}\mathbf{P} E\{\mathbf{x}_k|\mathbf{Y}_k\}.$$

It then follows that

$$\mathbf{A}\mathbf{P}\boldsymbol{\Sigma} = \mathbf{P}\mathbf{A}\boldsymbol{\Sigma} = \mathbf{A}\boldsymbol{\Sigma}, \quad (15.7a)$$

$$\mathbf{A}\mathbf{P}\boldsymbol{\Sigma}\mathbf{P}^T\mathbf{A}^T = \mathbf{P}\mathbf{A}\boldsymbol{\Sigma}\mathbf{A}^T\mathbf{P}^T = \mathbf{A}\boldsymbol{\Sigma}\mathbf{A}^T, \quad (15.7b)$$

where $\boldsymbol{\Sigma}$ is the error covariance matrix.

The spKF is given by (Ko and Bitmead 2007)

$$\mathbf{K}_k^c = \boldsymbol{\Sigma}_k^c \mathbf{C}^T \mathbf{V}_k^c, \quad (15.8a)$$

$$\begin{aligned} \bar{\mathbf{x}}_{k+1}^c &= \mathbf{P}_{\mathcal{N}(\mathbf{D})} \mathbf{A} (\mathbf{I} - \mathbf{K}_k^c \mathbf{C}) \bar{\mathbf{x}}_k^c + \mathbf{P}_{\mathcal{N}(\mathbf{D})} \mathbf{B} \mathbf{u}_k + \mathbf{P}_{\mathcal{N}(\mathbf{D})} \mathbf{A} \mathbf{K}_k^c \mathbf{y}_k \\ &= \mathbf{A} (\mathbf{I} - \mathbf{K}_k^c \mathbf{C}) \bar{\mathbf{x}}_k^c + \mathbf{B} \mathbf{u}_k + \mathbf{A} \mathbf{K}_k^c \mathbf{y}_k \end{aligned} \quad (15.8b)$$

$$\begin{aligned}
\Sigma_{k+1}^c &= \mathbf{P}_{N(\mathbf{D})} \mathbf{A} \Sigma_k^c \mathbf{A}^T \mathbf{P}_{N(\mathbf{D})} + \mathbf{P}_{N(\mathbf{D})} \mathbf{Q}^c \mathbf{P}_{N(\mathbf{D})} \\
&\quad - \mathbf{P}_{N(\mathbf{D})} \mathbf{A} \Sigma_k^c \mathbf{C}^T \mathbf{V}_k^c \mathbf{C} \Sigma_k^c \mathbf{A}^T \mathbf{P}_{N(\mathbf{D})} \\
&= \mathbf{A} \Sigma_k^c \mathbf{A}^T + \mathbf{Q}^c - \mathbf{A} \Sigma_k^c \mathbf{C}^T \mathbf{V}_k^c \mathbf{C} \Sigma_k^c \mathbf{A}^T,
\end{aligned} \tag{15.8c}$$

where $\mathbf{Q}^c = \mathbf{P}_{N(\mathbf{D})} \mathbf{Q}^u \mathbf{P}_{N(\mathbf{D})}$, which is singular. It is only necessary to modify the initial estimation error covariance and the process noise covariance. If \mathbf{Q}^c is the true process noise covariance, then it follows that this method gives the optimal state estimate (Simon 2010).

Remark 15.2.2. *It was shown in Ko and Bitmead (2007) that the error covariance matrix of the spKF is less than or equal to that obtained by the epKF. The main reason is that in the epKF, the projected covariance is not used in the recursion. Consequently, only information about the constraints in the most recent step of the epKF is used.*

15.2.4 The Equality Constrained Kalman Filter

A third option is to use the projected covariance matrix and state of the epKF in the recursion (Teixeira et al. 2009), which we will call ecKF. We will provide an alternative derivation of the covariance of this filter based on the constrained Cramér-Rao bound in Andersson et al. (2017b).

The proofs of the following Lemmas can be found in Andersson et al. (2017b), Stoica and Ng (1998), and Khatri (1966).

Lemma 15.2.3. *Consider the complete state history $\mathbf{X}_k = [\mathbf{x}_0^T, \mathbf{x}_1^T, \dots, \mathbf{x}_k^T]^T$ and the inverse of the error covariance matrix $\tilde{\Sigma}^{-1}$ of the state history with $\tilde{\mathbf{U}}$ defined in (15.6). If $\tilde{\mathbf{U}}^T \tilde{\Sigma}^{-1} \tilde{\mathbf{U}}$ is non-singular, then the constrained Cramér-Rao Bound is*

$$E \{ (\mathbf{X} - \hat{\mathbf{X}})(\mathbf{X} - \hat{\mathbf{X}})^T \} \geq \tilde{\mathbf{U}} (\tilde{\mathbf{U}}^T \tilde{\Sigma}^{-1} \tilde{\mathbf{U}})^{-1} \tilde{\mathbf{U}}^T. \tag{15.9}$$

Remark 15.2.4. *Lemma 15.2.3 was derived in Stoica and Ng (1998) for the estimation of non-random parameters. In Chapter 14, it was extended to the estimation of random parameters (Andersson et al. 2017b). The right-hand side of (15.9) is the greatest lower bound, which was obtained by solving a maximisation problem.*

Lemma 15.2.5. *If Σ is positive definite, then (15.9) becomes*

$$\mathbf{U} (\mathbf{U}^T \Sigma^{-1} \mathbf{U})^{-1} \mathbf{U}^T = \mathbf{P}_{N(\mathbf{D})}^{\Sigma^{-1}} \Sigma, \tag{15.10}$$

where $\mathbf{P}_{N(\mathbf{D})}^{\Sigma^{-1}} = \mathbf{I} - \Sigma \mathbf{D}^T (\mathbf{D} \Sigma \mathbf{D}^T)^{-1} \mathbf{D}$.

The projection of the unconstrained error covariance in (15.10) is the same as in the estimate projection approach using $\mathbf{W} = (\Sigma_k^u)^{-1}$.

The information matrix Σ^{-1} can be computed by (Simon 2010)

$$\Sigma_{k+1|k}^{-1} = \mathbf{Q}^{-1} - \mathbf{Q}^{-1} \mathbf{A} (\mathbf{F} + \mathbf{K} + \Sigma_{k|k}^{-1})^{-1} \mathbf{A}^T \mathbf{Q}^{-1}, \quad (15.11)$$

where $\mathbf{K} = \mathbf{C}^T \mathbf{R}^{-1} \mathbf{C}$ and $\mathbf{F} = \mathbf{A}^T \mathbf{Q}^{-1} \mathbf{A}$.

Theorem 15.2.6. *The error covariance of the ecKF can be computed by*

$$\Sigma_{k+1}^e = \mathbf{A} \Sigma_k^e \mathbf{A}^T - \mathbf{A} \Sigma_k^e \mathbf{C}^T \mathbf{V}_k^e \mathbf{C} \Sigma_k^e \mathbf{A}^T + \mathbf{Q}^e, \quad (15.12)$$

where $\mathbf{Q}^e = \mathbf{P}_{\mathcal{N}(\mathbf{D})}^{\Sigma^{-1}} \mathbf{Q} (\mathbf{P}_{\mathcal{N}(\mathbf{D})}^{\Sigma^{-1}})^T = \mathbf{P}_{\mathcal{N}(\mathbf{D})}^{\mathbf{Q}^{-1}} \mathbf{Q} (\mathbf{P}_{\mathcal{N}(\mathbf{D})}^{\mathbf{Q}^{-1}})^T = \mathbf{P}_{\mathcal{N}(\mathbf{D})}^{\mathbf{Q}^{-1}} \mathbf{Q}$.

Proof. Since the constraints \mathbf{D} are decoupled in time, the matrix $\tilde{\mathbf{U}} \in \mathbb{R}^{\text{kn} \times \text{k}(n-c)}$ is block-diagonal with \mathbf{U} repeated on the diagonal. The inverse of the unconstrained error covariance matrix of the entire state history (15.9) is given by (14.8), which is

$$\begin{aligned} \Sigma_{k+1|k}^{-1} &= \begin{bmatrix} \mathbf{J}_{k+1|k}^{1,1} & \mathbf{J}_{k+1|k}^{1,2} \\ \mathbf{J}_{k+1|k}^{2,1} & \mathbf{J}_{k+1|k}^{2,2} \end{bmatrix} \\ &= \left[\begin{array}{ccc|cc} \mathbf{K} + \mathbf{F} + \Sigma_{0|0}^{-1} & -\mathbf{A}^T \mathbf{Q}^{-1} & & & \\ -\mathbf{Q}^{-1} \mathbf{A} & \ddots & & \ddots & \\ & & \ddots & \mathbf{K} + \mathbf{F} + \mathbf{Q}^{-1} & -\mathbf{A}^T \mathbf{Q}^{-1} \\ \hline & & & -\mathbf{Q}^{-1} \mathbf{A} & \mathbf{Q}^{-1} \end{array} \right]. \end{aligned} \quad (15.13)$$

We proceed by showing equivalence between (15.12) and the right-hand side of (15.9) for \mathbf{x}_1 , which by the structure of $\Sigma_{k+1|k}^{-1}$ and $\tilde{\mathbf{U}}$ implies that it also hold for \mathbf{x}_k .

If we compute (15.9) for \mathbf{x}_1 using the matrix inversion lemma, then we obtain

$$\Sigma_1^e = \mathbf{U} \left[\mathbf{L} - \mathbf{G} \left\{ \mathbf{U} \left[\mathbf{U}^T \mathbf{J}_{1|0}^{1,1} \mathbf{U} \right]^{-1} \mathbf{U}^T \right\} \mathbf{G}^T \right]^{-1} \mathbf{U}^T \quad (15.14)$$

where $\mathbf{L} = \mathbf{U}^T \mathbf{Q}^{-1} \mathbf{U}$, $\mathbf{G} = \mathbf{U}^T \mathbf{Q}^{-1} \mathbf{A}$ and $\mathbf{J}_{1|0}^{1,1} = \mathbf{K} + \mathbf{F} + \Sigma_{0|0}^{-1}$. Using the binomial inverse theorem this expression can be transformed to

$$\Sigma_1^e = \mathbf{U} \left[\mathbf{L} - \mathbf{G} \left\{ \left(\left[\Sigma_0^e \right]^{-1} + \mathbf{F} \right)^{-1} \right\} \mathbf{G}^T \right]^{-1} \mathbf{U}^T, \quad (15.15)$$

where $\Sigma_0^e = \mathbf{U} \left(\mathbf{U}^T \left[\Sigma_{0|0}^{-1} + \mathbf{K} \right] \mathbf{U} \right)^{-1} \mathbf{U}^T$, which is the expression obtained using (15.12) on the left-hand side of (15.10) with the information matrix (15.11) as the projection. ■

The proof establishes a direct connection between the error-covariance matrix of the ecKF to the Fisher Information matrix and the Cramér-Rao lower bound. This also enables an analytical comparison between spKF and ecKF. Moreover, the necessity to guarantee numerically positive definiteness of (15.12) is avoided in the derivation.

Remark 15.2.7. Examining (15.12), only the process noise covariance matrix is projected. Consequently, the projection can be done a priori as in the system projection approach. Moreover, $\mathbf{P}_{\mathcal{N}(\mathbf{D})}^{\mathbf{Q}^{-1}}$ can be used instead of $\mathbf{P}_{\mathcal{N}(\mathbf{D})}^{\Sigma^{-1}}$.

The ecKF is given by

$$\begin{aligned}\mathbf{K}_k^e &= \Sigma_k^e \mathbf{C}^T \mathbf{V}_k^e \\ \tilde{\mathbf{x}}_{k+1}^e &= \mathbf{A}(\mathbf{I} - \mathbf{K}_k^e \mathbf{C}) \tilde{\mathbf{x}}_k^e + \mathbf{B} \mathbf{u}_k + \mathbf{A} \mathbf{K}_k^e \mathbf{y}_k \\ \Sigma_{k+1}^e &= \mathbf{A} \Sigma_k^e \mathbf{A}^T + \mathbf{Q}^e - \mathbf{A} \Sigma_k^e \mathbf{C}^T \mathbf{V}_k^e \mathbf{C} \Sigma_k^e \mathbf{A}^T,\end{aligned}\tag{15.16}$$

where $\mathbf{Q}^e = \mathbf{P}_{\mathcal{N}(\mathbf{D})}^{\Sigma^{-1}} \mathbf{Q}$. The difference from the spKF is the use of the oblique projection. In the next section, we show that this results in a smaller covariance.

15.3 Comparison of Constrained Kalman Filters

None of the constrained Kalman filters violates the constraints (Simon 2010, Ko and Bitmead 2007, Teixeira et al. 2009). Moreover, it was shown in Ko and Bitmead (2007) that the error covariance matrix Σ_k^c is less than or equal to Σ_k^p .

To prove that $\Sigma_k^c \geq \Sigma_k^e$, we need the following lemma about a monotonicity property of the Riccati difference equation (Bitmead and Gevers 1991).

Lemma 15.3.1. Consider two Riccati difference equations with the same \mathbf{A} , \mathbf{C} and \mathbf{R} matrices but possibly different \mathbf{Q}^1 and \mathbf{Q}^2 . Denote their solution matrices by Σ_k^1 and Σ_k^2 , respectively. Suppose that $\mathbf{Q}^1 \geq \mathbf{Q}^2$, and for some k we have $\Sigma_k^1 \geq \Sigma_k^2$, then for all $i > 0$, we have $\Sigma_{k+1}^1 \geq \Sigma_{k+1}^2$

A consequence of this lemma is that we only have to compare \mathbf{Q}^c and \mathbf{Q}^e to compare the error covariances of ecKF and spKF.

Lemma 15.3.2. The constrained error covariance Σ^e is less than or equal to the unconstrained one.

Proof. Σ and $\mathbf{P}_{\mathcal{N}(\mathbf{D})}^{\Sigma^{-1}} \Sigma$ are symmetric and $\mathbf{P}_{\mathcal{N}(\mathbf{D})}^{\Sigma^{-1}}$ and $\mathbf{I} - \mathbf{P}_{\mathcal{N}(\mathbf{D})}^{\Sigma^{-1}}$ are idempotent.

Therefore, the following holds (Gorman and Hero 1990):

$$\begin{aligned} \mathbf{P}_{\mathcal{N}(\mathbf{D})}^{\Sigma^{-1}} \Sigma &= \Sigma - (\mathbf{I} - \mathbf{P}_{\mathcal{N}(\mathbf{D})}^{\Sigma^{-1}}) \Sigma \\ &= \Sigma - (\mathbf{I} - \mathbf{P}_{\mathcal{N}(\mathbf{D})}^{\Sigma^{-1}}) (\mathbf{I} - \mathbf{P}_{\mathcal{N}(\mathbf{D})}^{\Sigma^{-1}}) \Sigma \\ &= \Sigma - (\mathbf{I} - \mathbf{P}_{\mathcal{N}(\mathbf{D})}^{\Sigma^{-1}}) \Sigma (\mathbf{I} - \mathbf{P}_{\mathcal{N}(\mathbf{D})}^{\Sigma^{-1}}) \leq \Sigma \end{aligned}$$

■

Theorem 15.3.3. For the constrained system (15.3), the error covariance sequence is

$$\Sigma_k^u \geq \Sigma_k^p \geq \Sigma_k^c \geq \Sigma_k^e.$$

Proof. The first inequality was shown in Simon and Chia (2002) and by Lemma 15.3.2. The second inequality was shown in Ko and Bitmead (2007). For the third inequality, consider

$$\begin{aligned} \mathbf{Q}^c - \mathbf{Q}^e &= \mathbf{U}\mathbf{U}^T \mathbf{Q}\mathbf{U}\mathbf{U}^T - (\mathbf{I} - \mathbf{Q}\mathbf{D}^T (\mathbf{D}\mathbf{Q}\mathbf{D}^T)^{-1} \mathbf{D}) \mathbf{Q} \\ &= \begin{pmatrix} \mathbf{D}\mathbf{Q} \\ -\mathbf{D} \end{pmatrix}^T \begin{pmatrix} (\mathbf{D}\mathbf{Q}\mathbf{D}^T)^{-1} & \mathbf{I} \\ \mathbf{I} & \mathbf{D}\mathbf{Q}\mathbf{D}^T \end{pmatrix} \begin{pmatrix} \mathbf{D}\mathbf{Q} \\ -\mathbf{D} \end{pmatrix} \geq 0, \end{aligned}$$

where we use $\mathbf{U}^T \mathbf{U} = \mathbf{I} - \mathbf{D}^T \mathbf{D}$ and omitted subscript k for notational simplicity. Positive semi-definiteness follows since any matrix $\begin{bmatrix} \Lambda^{-1} \mathbf{I} & \mathbf{I} \Lambda \\ \mathbf{I} \Lambda & \Lambda \end{bmatrix}$ is positive semi-definite (Bernstein 2005), and $\Sigma_k^c \geq \Sigma_k^e$ follows from Lemma 15.3.1. ■

15.4 Numerical Example

A simple numerical example is presented to illustrate the performance differences of the four estimators. The example is used as a benchmark (Simon and Chia 2002, Ko and Bitmead 2007, Simon 2010), and is a navigation problem with the following linear system and measurement equation

$$\begin{aligned} \mathbf{x}_{k+1} &= \begin{pmatrix} 1 & 0 & T & 0 \\ 0 & 1 & 0 & T \\ 0 & 0 & 1 & 0 \\ 0 & 0 & 0 & 1 \end{pmatrix} \mathbf{x}_k + \begin{pmatrix} 0 \\ 0 \\ T \sin \theta \\ T \cos \theta \end{pmatrix} u_k + \mathbf{w}_k, \\ \mathbf{y}_k &= \begin{pmatrix} 1 & 0 & 0 & 0 \\ 0 & 1 & 0 & 0 \end{pmatrix} \mathbf{x}_k + \mathbf{v}_k, \end{aligned}$$

where T is the discretization step size and u_k is the acceleration input. The states are the positions and velocities in north and east directions, respectively. The unconstrained covariance of process and measurement noise are

$$\mathbf{Q} = \text{diag}(4, 4, 2, 1), \quad \mathbf{R} = \text{diag}(900, 900)$$

and the initial estimation error covariance is

$$\mathbf{P}_0^+ = \text{diag}(900, 900, 4, 4).$$

It is known that the vehicle is on the road with a heading angle θ , which can be described by the constraint equation

$$\mathbf{D}\mathbf{x}_k = [1 + \tan^2 \theta]^{-1/2} (0 \ 0 \ 1 \ -\tan \theta) = 0$$

This results in the following projected noise covariances

$$\mathbf{Q}^c = \begin{pmatrix} 4 & 0 & 0 & 0 \\ 0 & 4 & 0 & 0 \\ 0 & 0 & 2.6250 & 1.5155 \\ 0 & 0 & 1.5155 & 0.8750 \end{pmatrix} \geq \begin{pmatrix} 4 & 0 & 0 & 0 \\ 0 & 4 & 0 & 0 \\ 0 & 0 & 2.4000 & 1.3856 \\ 0 & 0 & 1.3856 & 0.8000 \end{pmatrix} = \mathbf{Q}^e,$$

and initial error covariance

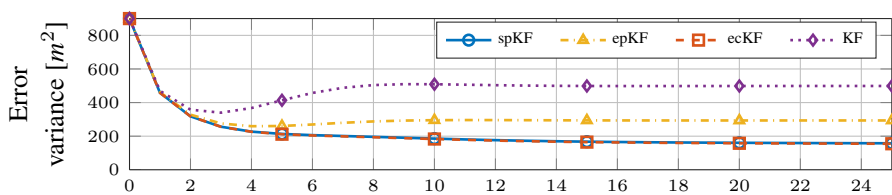
$$\Sigma_0^c = \Sigma_0^e = \begin{pmatrix} 900 & 0 & 0 & 0 \\ 0 & 900 & 0 & 0 \\ 0 & 0 & 3.0000 & 1.7321 \\ 0 & 0 & 1.7321 & 1.0000 \end{pmatrix}.$$

An initial state $\mathbf{x}_0^{u,p,c,e} = (0 \ 0 \ 10 \tan \theta \ 10)^T$, 2 s sampling period and 60° heading angle are used.

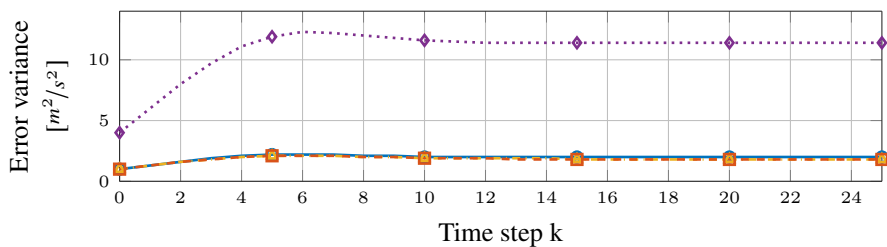
The variance of the north position and velocity estimate is shown in Figure 15.1. The eckf has the lowest variance for all states estimated. In the position estimate, the spkf performs only slightly worse while the position estimates of the epkf have a larger variance (Fig. 15.1(a)). This is different for the velocity estimates, which from the eckf still have the smallest variance while the variance of the velocity estimates for the epkf is smaller than the spkf. The latter may seem to contradict Theorem 15.3.3, but a plot of the two-norm of the error-covariance matrices reveals that this is not the case.

15.5 Conclusion

In this chapter, linear state estimation with linear equality constraints is revisited. A simple derivation of the covariance of the constrained Kalman filter is presented. This filter is compared to the system projection and estimate projection Kalman filter. It is proven that the oblique projection of the constrained Kalman filter results in the smallest error covariance.



(a) Position - $x_k(1)$.



(b) Velocity - $x_k(3)$.

Figure 15.1: Estimation error variance for the systems states.

Chapter 16

Concluding remarks

The thesis presented contributions within different areas of iceberg drift. The primary focus laid on improves short-term iceberg drift forecasts by including measurement updates about the iceberg trajectory into the forecast. In addition, a result in the field of estimation under constraints is presented. This chapter aims to briefly summarise the results and provide overall reflections looking at the complete results from the thesis. It also points out possible topics for future work. The reader is also referred to the detailed conclusion sections at the end of the chapters.

In Part I of the thesis, the iceberg dataset, which is an important part of the thesis and influenced it considerably, was presented. The Newfoundland dataset (Sec. 4.1) was collected in Spring 2015 during the Offshore Newfoundland Research Expedition conducted by Statoil and ArticNet. The author of this thesis joined this expedition, which was probably one of the most influential events throughout the work on this thesis. A unique dataset was collected, which helped validate many of the implemented ideas. During the expedition, the CCGS *Amundsen* stayed for a period of about 7 h near one iceberg and obtained measurements with several sensor platforms, including the environmental forces of winds, waves, and ocean currents. Even though an almost complete dataset was collected, it was not possible to hindcast the iceberg drift. Moreover, the variance of drift trajectories from the dynamic iceberg drift model was significant. The results were expected and agreed with previous literature and the results in the thesis. It is necessary to correct the parameter of the dynamic model with help of iceberg drift observations. It is expected that the observations are similar even if the 3D geometry of the iceberg is measured.

In practice, the information about the iceberg and the environmental forces is

more limited resulting in an even larger uncertainty of the future iceberg drift trajectory.

Part II discussed the *hybrid* forecast approaches, which combined the dynamic iceberg model with statistical methods. The ancillary and inertial current forecast schemes were proposed. The ancillary current forecast scheme was developed with the assumption that the ocean current input to the dynamic iceberg model is biased. The ancillary current corrects this bias, and it was assumed that the bias stays constant or, at least similar, during the forecast period. While the ancillary current forecast scheme was superior to the dynamic iceberg drift model, it inherited the disadvantage that it relied on erroneous current data. The bias that was assumed to be constant during forecast may change quickly over time such that the ancillary current forecast scheme produces an erroneous forecast. The disadvantage was overcome with the inertial current forecast scheme that estimated the complete ocean current with the help of a simplistic ocean model and the observed iceberg trajectory.

Part III formulated a statistical forecast approach. It was observed that in *hybrid* forecast schemes, the main objective was to forecast the ocean current correctly. Other uncertain parameters, for instance, the iceberg geometry or the drag coefficients, were not explicitly considered in the estimation process, but implicitly corrected by it. Moreover, the dynamic iceberg drift model reaches quasi-steady state quickly. This raised the question if the dynamic iceberg model is necessary for the short-term forecasts or if the empirical kinematic relationship between wind, ocean current, and iceberg velocity could be used for reducing the parameter space considerably. The explicit objective of the VAR model forecast was to forecast the ocean current using the iceberg as a drifter to improve the forecast. An improved forecast of the iceberg trajectory was mainly the result of an improved ocean current forecast. Moreover, the iceberg drift model was drastically reduced to its kinematic relationship between wind, ocean current, and iceberg velocity resulting in only one iceberg drift model parameter. Through several iceberg forecast examples, it was shown that this concept works well. In fact, this approach was one of the best iceberg drift forecast schemes in the overall comparison of all proposed schemes (Chapter V).

It is possible to identify one or several statistical ocean current models for every location where historical ocean current data is available (possibly for every grid cell of an ocean current model). This, in turn, can easily be used to identify unusual ocean currents or unusual iceberg behaviours to issue a warning to the operator.

Part IV showed how iceberg drift observations could be used to detect tidal and inertial ocean currents. Both oscillations have similar frequencies, and their separation imposes a challenging filtering problem. The multivariate empirical mode decomposition was used to solve the problem. In higher latitudinal locations, where both oscillations have the same frequency, a second filtering stage or more information about the oscillations was necessary, for instance, zero-crossing of the tidal oscillation. The analysis showed that a dynamic iceberg drift model is not strictly necessary for this filtering problem. In addition, the multivariate empirical mode decomposition can decompose simultaneously the iceberg velocity, ocean current, and wind inputs simultaneously into different frequency modulated components, since it behaves like a band-pass filter. The second chapter in Part IV suggested how this separation may be used for iceberg drift forecasts. At each forecast instance the inputs and outputs were decomposed into different frequency bands, and for each band, it was checked separately if the inputs forecast the iceberg velocity in the past. If they were, then the inputs were used to forecast the iceberg velocity in that frequency band. Otherwise, the iceberg velocity in the frequency band was forecasted by an auto-regression model. The MEMD forecast scheme showed very good forecast performance in the first hour showing it is a powerful filter. However, the performance decreased for longer forecast horizons indicating the forecast scheme needs improvement.

Part V offered a comparison between every short-term forecast scheme presented in this thesis. The comparison resulted in new ideas on how to combine the benefits of the forecast schemes. It was shown that it could not be guaranteed that one forecast scheme behaves better than the other approaches at all times. Moreover, all forecast schemes had at least short periods where they were superior. This held for the comparison between the newly-developed forecast approaches of this thesis, but also for the forecast using the conventional dynamic drift forecast model. However, the inertial current forecast scheme (Chap. 7) and the VAR forecast scheme (Chap. 9) produced, on average, the smallest forecast errors. It was observed that usually the *statistical* forecast approaches produced large or small forecast errors in the same period. Consequently, they have similar forecast properties.

Finally, Part VI investigated state and parameter estimation under constraints. The first chapter discussed an idea on how to estimate the hydrodynamic iceberg geometry if ocean currents, winds, and possibly, waves are measured close to the iceberg. The resulting geometry is weighted based on the drag coefficients chosen in the dynamic iceberg model. Since the iceberg drift is a slow process and parameter estimation requires input excitation, the iceberg has to be observed for

an extended time. To improve the estimation and converge quicker to a solution, constraints in the form of an iceberg geometry model were developed. This motivated the development of a Cramér-Rao bound for discrete-time systems under state constraints in the subsequent chapter. The bound holds for nonlinear systems under linear constraints. For a nonlinear system under nonlinear constraints, the projection of the unconstrained Cramér-Rao bound onto the constrained surface may also result in a reduction of the bound. However, with the approach that was taken in this thesis, it was not proven that this is a lower bound. In the final chapter, Kalman filtering with linear state constraints was discussed. In a similar fashion as in the derivation of the constrained Cramér-Rao bound, an error covariance for the Kalman filter with linear state constraints was derived. The results, in fact, in the smallest error covariance matrix, was analytically shown by comparison to other constrained Kalman filters.

Suggestions for Future Work

The thesis focused on developing short-term iceberg drift models that included iceberg position measurements. Each of the approaches can be improved (at least to some degree). In the ancillary current forecast scheme, it was not discussed as to how ocean current inputs from an ocean model can be combined with the ancillary current, which is estimated with the help of the iceberg track. The ancillary current will contain fast frequency modes (if the measurement frequency is sufficiently fast), which are not represented in the modelled ocean current. This can be implicitly handled by the estimator but an explicit consideration, for instance, by filtering with, e.g., an multivariate empirical mode decomposition, may improve the forecast. Similarly, the inertial current forecast scheme only considers the inertial current oscillation explicitly. The tidal current is not considered. Therefore, strong tidal current will most likely corrupt the inertial current estimation. Again, explicit handling either by extending the ocean current model or by a filtering step may improve the forecast.

In Part V, it was already shown that a combination of different forecast schemes could result in an even better drift forecast for specific forecast periods. Other combination may also be tested.

The forecast scheme presented in this thesis do not consider confidence regions or calculating the risk to a platform to collide with an iceberg. This may be incorporated into the forecast schemes. Monte Carlo simulations (in the context of the iceberg drift literature is often called *ensemble forecast*) may be implemented. An explicit representation of the error term is possible with the VAR forecast scheme. However, measured ocean current should be used in the identification of the ocean current model. How well this model will forecast the iceberg trajectory remains to be tested. It may be considered to use the measured ocean current only to identify

an error term.

In general, the forecast performance depends on a number of factors, for example, model error, input uncertainty, measurement errors, characteristics of unmeasured disturbances, forecast period and the forecast method. In terms of the iceberg forecast problem the forecast error of the dynamic iceberg model was often analysed by variation of its input and parameter values. However, how well the dynamic model represents the actual iceberg drift process was not evaluated. It was often concluded that the error is caused by deficiencies in the ocean current representation. An indication how important the unpredictable current structures (on spatial scales of a few to several kilometres) are given in the thesis. [Allison et al. \(2014\)](#) are the only ones that tried to quantify the parameter and input uncertainty in a more structured manner. Similar studies for different regions and base cases have to be performed. A few considered an explicit noise term ([Garrett 1985](#), [De Margerie et al. 1986](#), [Moore 1987](#)) which can be better analysed as more iceberg drift data becomes available due to, e.g. new satellite programs.

Measurements errors are usually neglected since in comparison to other source the position measurement of an iceberg tracked with a GPS beacon is rather good. Different forecast methods and model were compared in this thesis. Overall, a more structured approach to analyse the iceberg forecast problem is recommended. This can include, for example, also lab experience in an ocean basin to analyse the errors introduced to the drift due to the geometry simplifications in the dynamic iceberg model.

Another interesting approach may be to implement a switching scheme for all presented forecast algorithms similar to the one presented in Chapter 8. A possible performance measure may be the relative forecast performance. How well the classification for small forecast horizons is preserved into longer forecast horizons must be tested.

In general, it is recommended to establish a benchmark for iceberg drift forecast models. The benchmark should contain several iceberg drift trajectories possibly from different regions. These regions may be categorised into near coastal regions (continental shelf) and open ocean. Another category may be based on the diversity of ocean current regimes. For example, it can be expected that the iceberg drift forecast in a strait with consistent ocean current direction is superior to a forecast on a shelf with diverse ocean current directions.

The minimum length of the observation period must be discussed as it is recommended to be at least seven days. For shorter periods, it may be that the iceberg drift forecast results in either a good or bad forecast for the entire period. The position measurement frequency should be about one hour. The benchmark should permit a fair comparison and categorisation (which scheme in which situation) between different forecast schemes, which presently is challenging.

Part VII

Appendices

Appendix A

Linear Algebra

A.1 Matrix Inversion Lemma

The inverse of a 2×2 block matrix is given by

$$\begin{pmatrix} \mathbf{A} & \mathbf{B} \\ \mathbf{C} & \mathbf{D} \end{pmatrix}^{-1} = \begin{pmatrix} \mathbf{F}^{-1} & -\mathbf{A}^{-1}\mathbf{B}\mathbf{E}^{-1} \\ -\mathbf{D}^{-1}\mathbf{C}\mathbf{F} & \mathbf{E} \end{pmatrix}, \quad (\text{A.1})$$

where

$$\begin{aligned} \mathbf{E} &= \mathbf{D} - \mathbf{C}\mathbf{A}^{-1}\mathbf{B}, \\ \mathbf{F} &= \mathbf{A} - \mathbf{B}\mathbf{D}^{-1}\mathbf{C}. \end{aligned} \quad (\text{A.2})$$

Furthermore, the following holds

$$(\mathbf{A} + \mathbf{B}\mathbf{D}\mathbf{C})^{-1} = \mathbf{A}^{-1} - \mathbf{A}^{-1}\mathbf{B}(\mathbf{D}^{-1} + \mathbf{C}\mathbf{A}^{-1}\mathbf{B})^{-1}\mathbf{C}\mathbf{A}^{-1}, \quad (\text{A.3})$$

provided \mathbf{A}^{-1} exists.

A.2 Binomial inverse theorem

The binomial inverse theorem is a more general formula of (A.3), which also exist in cases of a singular matrix \mathbf{D} (Henderson and Searle 1981)

$$(\mathbf{A}^{-1} + \mathbf{B}\mathbf{D}\mathbf{C})^{-1} = \mathbf{A}^{-1} - \mathbf{A}^{-1}\mathbf{B}(\mathbf{I} + \mathbf{D}\mathbf{C}\mathbf{A}^{-1}\mathbf{B})^{-1}\mathbf{D}\mathbf{C}\mathbf{A}^{-1}. \quad (\text{A.4})$$

Appendix B

PAPER E: The Moving Horizon Estimator Used in Iceberg Drift Estimation and Forecast.

For completeness of the thesis PAPER E is included. The article presents a subset of PAPER A presented in Sec. 6.

Is not included due to copyright
available at [https://ieeexplore.ieee.org/
document/7810464/](https://ieeexplore.ieee.org/document/7810464/)
DOI: 10.1109/ECC.2016.7810464

References

- Aftab, M. F., Hovd, M., Huang, N. E., Sivalingam, S., 2016. An adaptive non-linearity detection algorithm for process control loops. *IFAC-PapersOnLine* 49 (7), 1020–1025.
- Allison, K., Crocker, G., Tran, H., Carrieres, T., 2014. An ensemble forecast model of iceberg drift. *Cold Regions Science and Technology* 108, 1 – 9.
- Andersson, J., Åkesson, J., Diehl, M., 2012. Casadi: a symbolic package for automatic differentiation and optimal control. In: *Recent Advances in Algorithmic Differentiation*. Springer, pp. 297–307.
- Andersson, L. E., Aftab, M. F., Scibilia, F., Imsland, L., 2017a. Forecasting using multivariate empirical mode decomposition – applied to iceberg drift forecast. In: *IEEE Conference on Control Technology and Applications (CCTA)*, Kohala Coast, Hawaii.
- Andersson, L. E., Brekke, E. F., Imsland, L., Scibilia, F., 2017b. Constrained posterior Cramér–Rao bound for discrete-time systems. *IFAC-PapersOnLine* 50 (1), 3768 – 3773, 20th IFAC World Congress.
- Andersson, L. E., Imsland, L., Brekke, E. F., Scibilia, F., 2018a. On Kalman filtering with linear state equality constraints. *Automatica* [submitted].
- Andersson, L. E., Scibilia, F., Copland, L., Aftab, M. F., Imsland, L., 2018b. Analysis of iceberg drift trajectories using the multivariate empirical mode decomposition. In: *The Twenty-eighth (2018) International Ocean and Polar Engineering Conference (ISOPE)*, Sapporo, Japan [accepted].
- Andersson, L. E., Scibilia, F., Copland, L., Imsland, L., 2018c. Comparison of statistical iceberg forecast models. *Cold Regions Science and Technology* [accepted].
- Andersson, L. E., Scibilia, F., Imsland, L., 2016a. An estimation-forecast set-up for iceberg drift prediction. *Cold Regions Science and Technology* 131, 88–107.

- Andersson, L. E., Scibilia, F., Imsland, L., 2016b. Estimation of systems with oscillating input - applied to iceberg drift forecast. In: IEEE Multi-conference on Systems and Control (MSC), International Conference on Control Applications (CCA), Buenos Aires. pp. 940–947.
- Andersson, L. E., Scibilia, F., Imsland, L., 2016c. An iceberg drift prediction study offshore Newfoundland. In: Arctic Technology Conference, St. John's, Newfoundland and Labrador, Canada. Offshore Technology Conference.
- Andersson, L. E., Scibilia, F., Imsland, L., 2016d. The moving horizon estimator used in iceberg drift estimation and forecast. In: European Control Conference (ECC), 2016. pp. 1271–1277.
- Andersson, L. E., Scibilia, F., Imsland, L., 2017c. A study on an iceberg drift trajectory. In: ASME 2017 36th International Conference on Ocean, Offshore and Arctic Engineering. Vol. 8. American Society of Mechanical Engineers, pp. V008T07A029–V008T07A029.
- Andersson, L. E., Scibilia, F., Imsland, L., 2018d. An iceberg forecast approach based on a statistical ocean current model. Cold Regions Science and Technology [submitted].
- ArcticNet, 2004-2018. [Online]. Available: www.arcticnet.ulaval.ca.
- Barash, R. M., 1966. Ice-breaking by explosives. Tech. rep., NAVAL ORDNANCE LAB WHITE OAK MD.
- Barker, A., Sayed, M., Carrieres, T., 2004. Determination of iceberg draft, mass and cross-sectional areas. In: Proc. International Offshore and Polar Engineering Conference'04. Vol. 2. pp. 899–904.
- Barnes, H. T., 1927. Some physical properties of icebergs and a method for their destruction. Proceedings of the Royal Society of London. Series A, Containing Papers of a Mathematical and Physical Character 114 (767), pp. 161–168.
- Barnett, L., Seth, A. K., 2014. The MVGC multivariate Granger causality toolbox: A new approach to Granger-causal inference. Journal of Neuroscience Methods 223, 50 – 68.
- Ben-Haim, Z., Eldar, Y. C., 2009. On the constrained Cramér–Rao bound with a singular fisher information matrix. IEEE Signal Processing Letters 16 (6), 453–456.
- Bernstein, D. S., 2005. Matrix mathematics: Theory, facts, and formulas with application to linear systems theory. Vol. 41. Princeton University Press Princeton.
- Bigg, G. R., Wadley, M. R., Stevens, D. P., Johnson, J. A., 1996. Prediction of iceberg trajectories for the North Atlantic and Arctic oceans. Geophysical Research Letters 23 (24), 3587–3590.
- Bigg, G. R., Wadley, M. R., Stevens, D. P., Johnson, J. A., 1997. Modelling the dynamics and thermodynamics of icebergs. Cold Regions Science and Technology 26 (2), 113–135.

- Bitmead, R. R., Gevers, M., 1991. Riccati difference and differential equations: Convergence, monotonicity and stability. *The Riccati Equation*, 263–291.
- Bittanti, S., Savaresi, S. M., 2000. On the parametrization and design of an extended Kalman filter frequency tracker. *Automatic Control, IEEE Transactions on* 45 (9), 1718–1724.
- Blanco-Velasco, M., Weng, B., Barner, K. E., 2008. ECG signal denoising and baseline wander correction based on the empirical mode decomposition. *Computers in biology and medicine* 38 (1), 1–13.
- Bobrovsky, B., Zakai, M., Dec 1975. A lower bound on the estimation error for Markov processes. *IEEE Transactions on Automatic Control* 20 (6), 785–788.
- Broström, G., Melsom, A., Sayed, M., Kubat, I., Dec. 2009. Iceberg modeling at met.no: Validation of iceberg model. Tech. Rep. 17, Norwegian Meteorological Institute.
- Bruce, J., Younan, A., MacNeill, A., et al., 2016. Applications of iceberg profiling data to improve iceberg management success. In: *Arctic Technology Conference*.
- Brun, R., Reichert, P., Künsch, H. R., 2001. Practical identifiability analysis of large environmental simulation models. *Water Resources Research* 37 (4), 1015–1030.
- C-CORE, 2002. Integrated ice management R&D initiative – year 2000. C-CORE Report R-00-C36 to Chevron, ExxonMobil, Husky, Norsk Hydro, PERD and Petro-Canada.
- C-CORE, 2007. Ice management for structures in sea ice with ridges and icebergs. Volume 1 - state of the art in iceberg management. C-CORE Report R-07-037-544.
- C-CORE, 2013. Needs analysis and project development for enhanced iceberg and sea ice drift forecasting - final report. C-CORE Report R-12-120-999, Revision 4.
- Chen, S.-h., Su, H., Zhang, R., Tian, J., 2008. Fusing remote sensing images using à trous wavelet transform and empirical mode decomposition. *Pattern Recognition Letters* 29 (3), 330–342.
- Coreless, M., Tu, J., 1998. State and input estimation for a class of uncertain systems. *Automatica* 34 (6), 757 – 764.
- Crepon, M., Houssais, M., Guily, B. S., 1988. The drift of icebergs under wind action. *Journal of Geophysical Research: Oceans* 93 (C4), 3608–3612.
- De Margerie, S., Middleton, J., Garrett, C., Marquis, S., Majaess, F., Lank, K., 1986. An operational iceberg trajectory forecasting model for the Grand Banks of Newfoundland. No. 52. *Environmental Studies Revolving Funds*.
- De Young, B., Tang, C., 1990. Storm-forced baroclinic near-inertial currents on the grand bank. *Journal of Physical Oceanography* 20 (11), 1725–1741.

- Earth&Space Research, 1995. [Online]. <https://www.esr.org/>. Available at: <https://www.esr.org/research/polar-tide-models/>.
- Egbert, G. D., Erofeeva, S. Y., 2002. Efficient inverse modeling of barotropic ocean tides. *Journal of Atmospheric and Oceanic Technology* 19 (2), 183–204.
- EI-Tahan, M., EI-Tahan, H., Venkatesh, S., et al., 1983. Forecast of iceberg ensemble drift. In: *Offshore Technology Conference*.
- Eik, K., 10 2008. Review of experiences within ice and iceberg management. *The Journal of Navigation* 61, 557–572.
- Eik, K., 2009. Iceberg drift modelling and validation of applied metocean hindcast data. *Cold Regions Science and Technology* 57, 67–90.
- EU Copernicus Marine, 2006. [Online]. <http://marine.copernicus.eu/>. Available at: <http://marine.copernicus.eu/services-portfolio/access-to-products/> [Accessed 23 Nov. 2017].
- Fuglem, M., Stuckey, P., Sept 2014. Definition for technical success of iceberg towing operations. In: *2014 Oceans - St. John's*. pp. 1–9.
- Fuglem, M., Younan, A., et al., 2016. A 3D time-domain model for iceberg impacts with offshore platforms and subsea equipment. In: *Arctic Technology Conference*.
- Galdos, J., 1980. A Cramér–Rao bound for multidimensional discrete-time dynamical systems. *IEEE Transactions on Automatic Control* 25 (1), 117–119.
- Garrett, C., 1985. Statistical prediction of iceberg trajectories. *Cold Regions Science and Technology* 11 (3), 255 – 266.
- Garrett, C., Middleton, J., Hazen, M., Majaess, F., 1985. Tidal currents and eddy statistics from iceberg trajectories off Labrador. *Science* 227 (4692), 1333–1335.
- Gaskill, H. S., Rochester, J., 1984. A new technique for iceberg drift prediction. *Cold Regions Science and Technology* 8 (3), 223 – 234.
- GEBCO, -. [Online]. Available at: <https://www.gebco.net/>.
- Goode, J., Teller, A., 1971. Ice breakage with explosives.
- Gorman, J. D., Hero, A. O., 1990. Lower bounds for parametric estimation with constraints. *IEEE Transactions on Information Theory* 36 (6), 1285–1301.
- Granger, C. W., 1969. Investigating causal relations by econometric models and cross-spectral methods. *Econometrica: Journal of the Econometric Society*, 424–438.
- Hajimolahoseini, H., Taban, M. R., Soltanian-Zadeh, H., 2012. Extended Kalman filter frequency tracker for nonstationary harmonic signals. *Measurement* 45 (1), 126–132.

- Hariharan, H., Gribok, A., Abidi, M. A., Koschan, A., 2006. Image fusion and enhancement via empirical mode decomposition. *Journal of Pattern Recognition Research* 1 (1), 16–32.
- Haseltine, E. L., Rawlings, J. B., 2005. Critical evaluation of extended Kalman filtering and moving-horizon estimation. *Industrial & engineering chemistry research* 44 (8), 2451–2460.
- Henderson, H. V., Searle, S. R., 1981. On deriving the inverse of a sum of matrices. *Siam Review* 23 (1), 53–60.
- Huang, N. E., Shen, Z., Long, S. R., Wu, M. C., Shih, H. H., Zheng, Q., Yen, N.-C., Tung, C. C., Liu, H. H., 1998. The empirical mode decomposition and the Hilbert spectrum for nonlinear and non-stationary time series analysis. In: *Proceedings of the Royal Society of London A: Mathematical, Physical and Engineering Sciences*. Vol. 454. The Royal Society, pp. 903–995.
- Jagannatham, A. K., Rao, B. D., 2004. Cramér–Rao lower bound for constrained complex parameters. *IEEE Signal Processing Letters* 11 (11), 875–878.
- Johannessen, K., Løset, S., Strass, P., 1999. Simulation of iceberg drift. In: *Proc. POAC*. pp. 97–105.
- Keghouche, I., Aug. 2010. Modeling the dynamics and drift of icebergs in the barents sea. Ph.D. thesis, University of Bergen.
- Keghouche, I., Bertino, L., Lisæter, K. A., 2009. Parameterization of an iceberg drift model in the Barents Sea. *Journal of Atmospheric and Oceanic Technology* 26 (10), 2216–2227.
- Khatri, C. G., 1966. A note on a MANOVA model applied to problems in growth curve. *Annals of the Institute of Statistical Mathematics* 18 (1), 75–86.
- King, T., Younan, A., Richard, M., Bruce, J., Fuglem, M., Phillips, R., et al., 2016. Subsea risk update using high resolution iceberg profiles. In: *Arctic Technology Conference*.
- Ko, S., Bitmead, R. R., 2007. State estimation for linear systems with state equality constraints. *Automatica* 43 (8), 1363 – 1368.
- Kubat, I., Sayed, M., Savage, S. B., Carrieres, T., 2005. An operational model of iceberg drift. *International Journal of Offshore and Polar Engineering* 15 (2), 125–131.
- Kühl, P., Diehl, M., Kraus, T., Schlöder, J. P., Bock, H. G., 2011. A real-time algorithm for moving horizon state and parameter estimation. *Computers & Chemical Engineering* 35 (1), 71–83.
- Kulakov, M. Y., Demchev, D. M., 2015. Simulation of iceberg drift as a component of ice monitoring in the West Arctic. *Russian Meteorology and Hydrology* 40 (12), 807–813.

- Landman, R., Kortela, J., Jämsä-Jounela, S.-L., 2014. Fault propagation analysis by combining data-driven causal analysis and plant connectivity. In: *Emerging Technology and Factory Automation (ETFA), 2014 IEEE*. IEEE, pp. 1–4.
- Large, W., Pond, S., 1981. Open ocean momentum flux measurements in moderate to strong winds. *Journal of physical oceanography* 11 (3), 324–336.
- Lichey, C., Hellmer, H. H., 2001. Modeling giant-iceberg drift under the influence of sea ice in the Weddell Sea, Antarctica. *Journal of Glaciology* 47 (158), 452–460.
- Liu, H., Chen, C., Tian, H.-q., Li, Y.-f., 2012. A hybrid model for wind speed prediction using empirical mode decomposition and artificial neural networks. *Renewable Energy* 48, 545–556.
- Lofberg, J., 2004. Yalmip: A toolbox for modeling and optimization in MATLAB. In: *Computer Aided Control Systems Design, 2004 IEEE International Symposium on*. IEEE, pp. 284–289.
- Mandic, D., Golz, M., Kuh, A., Obradovic, D., Tanaka, T., 2008. *Signal processing techniques for knowledge extraction and information fusion*. Springer.
- Marko, J., Fissel, D., Miller, J., 1988. Iceberg movement prediction off the Canadian east coast. In: *El-Sabh, M., Murty, T. (Eds.), Natural and Man-Made Hazards*. Springer Netherlands, pp. 435–462.
- Marzetta, T. L., 1993. A simple derivation of the constrained multiple parameter Cramér–Rao bound. *IEEE Transactions on Signal Processing* 41 (6), 2247–2249.
- McClintock, J., Bullock, T., McKenna, R., Ralph, F., Brown, R., 2002. Greenland iceberg management: Implications for grand banks management systems. PERD/CHC Report 20-65, AMEC Earth & Environmental and C-Core, St. John’s, NL.
- McGuire, P., Younan, A., Wang, Y., Bruce, J., Gandi, M., King, T., Keeping, K., Regular, K., et al., 2016. Smart iceberg management system—rapid iceberg profiling system. In: *Arctic Technology Conference*.
- Mellor, M., Kovacs, A., 1972. Destruction of ice islands by explosives. *Arctic Petroleum Operators’ Association*.
- Miao, T., Seborg, D. E., 1999. Automatic detection of excessively oscillatory feedback control loops. In: *Control Applications, 1999. Proceedings of the 1999 IEEE International Conference on*. Vol. 1. IEEE, pp. 359–364.
- Moore, M., 1987. Exponential smoothing to predict iceberg trajectories. *Cold Regions Science and Technology* 14 (3), 263 – 272.
- Mountain, D., 1980. On predicting iceberg drift. *Cold Regions Science and Technology* 1 (3-4), 273 – 282.

- Padman, L., Erofeeva, S., 2004. A barotropic inverse tidal model for the arctic ocean. *Geophysical Research Letters* 31 (2).
- Peng, Z., Peter, W. T., Chu, F., 2005. A comparison study of improved Hilbert–Huang transform and wavelet transform: application to fault diagnosis for rolling bearing. *Mechanical systems and signal processing* 19 (5), 974–988.
- Pollard, R., Jr., R. M., 1970. Comparison between observed and simulated wind-generated inertial oscillations. *Deep Sea Research and Oceanographic Abstracts* 17 (4), 813–821.
- Randell, C., Ralph, F., Power, D., Stuckey, P., et al., May 2009. Ss: Canadian: Atlantic development; technological advances to assess manage and reduce ice risk in northern developments. In: *Proc. Offshore Technology Conference*. Houston, TX.
- Rawlings, J. B., Bakshi, B. R., 2006. Particle filtering and moving horizon estimation. *Computers & Chemical Engineering* 30 (10-12), 1529–1541.
- Rilling, G., Flandrin, P., Gonçalves, P., Lilly, J. M., 2007. Bivariate empirical mode decomposition. *IEEE signal processing letters* 14 (12), 936–939.
- Rilling, G., Flandrin, P., Goncalves, P., et al., 2003. On empirical mode decomposition and its algorithms. In: *IEEE-EURASIP workshop on nonlinear signal and image processing*. Vol. 3. IEEE, pp. 8–11.
- Robertson, D. G., Lee, J. H., Rawlings, J. B., 1996. A moving horizon-based approach for least-squares estimation. *AIChE Journal* 42 (8), 2209–2224.
- Rudkin, P., Boldrick, C., Barron Jr, P., 2005. PERD iceberg management database. PERD/CHC Report, 20–72.
- Scibilia, F., Hovd, M., 2009. Multi-rate moving horizon estimation with erroneous infrequent measurements recovery. In: *Fault Detection, Supervision and Safety of Technical Processes*. pp. 1037–1042.
- Serrani, A., 2006. Rejection of harmonic disturbances at the controller input via hybrid adaptive external models. *Automatica* 42 (11), 1977–1985.
- Šimandl, M., Kráľovec, J., Tichavský, P., 2001. Filtering, predictive, and smoothing Cramér–Rao bounds for discrete-time nonlinear dynamic systems. *Automatica* 37 (11), 1703–1716.
- Simon, D., 2006. *Optimal State Estimation: Kalman, H Infinity, and Nonlinear Approaches*. Wiley.
- Simon, D., 2010. Kalman filtering with state constraints: a survey of linear and nonlinear algorithms. *Control Theory & Applications, IET* 4 (8), 1303–1318.
- Simon, D., Chia, T. L., 2002. Kalman filtering with state equality constraints. *IEEE transactions on Aerospace and Electronic Systems* 38 (1), 128–136.

- Smith, S. D., 1993. Hindcasting iceberg drift using current profiles and winds. *Cold Regions Science and Technology* 22 (1), 33–45.
- Smith, S. D., Banke, E., 1981. A numerical model of iceberg drift. In: *Proc. Port and Ocean Engineering under Arctic Conditions'81*.
- Smith, S. D., Banke, E., 1983. The influence of winds, currents and towing forces on the drift of icebergs. *Cold Regions Science and Technology* 6 (3), 241–255.
- Smith, S. D., Donaldson, N. R., 1987. Dynamic modelling of iceberg drift using current profiles. Fisheries and Oceans, Canada.
- Sodhi, D., El-Tahan, M., 1980. Prediction of an iceberg drift trajectory during a storm. *Ann. Glaciol* 1, 77–82.
- Srinivasan, R., Rengaswamy, R., Miller, R., 2007. A modified empirical mode decomposition (EMD) process for oscillation characterization in control loops. *Control Engineering Practice* 15 (9), 1135–1148.
- Stewart, R., 2005. Introduction to physical oceanography. Texas A & M University.
- Stoica, P., Ng, B. C., 1998. On the Cramér–Rao bound under parametric constraints. *IEEE Signal Processing Letters* 5 (7), 177–179.
- Stone, R. C., Hammer, G. L., Marcussen, T., 1996. Prediction of global rainfall probabilities using phases of the southern oscillation index. *Nature* 384 (6606), 252–255.
- Streit, R. L., Barrett, R. F., 1990. Frequency line tracking using hidden Markov models. *Acoustics, Speech and Signal Processing, IEEE Transactions on* 38 (4), 586–598.
- Stuckey, P., Younan, A., Burton, R., Alawneh, S., et al., 2016. Modelling iceberg-topsides impacts using high resolution iceberg profiles. In: *Arctic Technology Conference*.
- Taylor, J. A., Carr, D. L., Myers, C. W., Eckberg, D. L., 1998. Mechanisms underlying very-low-frequency RR-interval oscillations in humans. *Circulation* 98 (6), 547–555.
- Teixeira, B. O., Chandrasekar, J., Tôrres, L. A., Aguirre, L. A., Bernstein, D. S., 2009. State estimation for linear and non-linear equality-constrained systems. *International Journal of Control* 82 (5), 918–936.
- Tenny, M., Rawlings, J., May 8–10 2002. Efficient moving horizon estimation and non-linear model predictive control. In: *Proc. American Control Conference'02*. Vol. 6. pp. 4475–4480.
- Tichavsky, P., Muravchik, C. H., Nehorai, A., 1998. Posterior Cramér–Rao bounds for discrete-time nonlinear filtering. *IEEE Transactions on signal processing* 46 (5), 1386–1396.

- Turnbull, I. D., Fournier, N., Stolwijk, M., Fosnaes, T., McGonigal, D., 2015. Operational iceberg drift forecasting in northwest Greenland. *Cold Regions Science and Technology* 110, 1 – 18.
- Ur Rehman, N., Mandic, D. P., 2010a. Empirical mode decomposition for trivariate signals. *IEEE Transactions on signal processing* 58 (3), 1059–1068.
- Ur Rehman, N., Mandic, D. P., 2010b. Multivariate empirical mode decomposition. In: *Proceedings of The Royal Society of London A: Mathematical, Physical and Engineering Sciences*. Vol. 466. The Royal Society, pp. 1291–1302.
- Van Trees, H. L., 1968. *Detection, estimation, and modulation theory*. John Wiley & Sons.
- Van Trees, H. L., Bell, K. L., 2013. *Detection estimation and modulation theory*, pt. I. Wiley.
- Wächter, A., Biegler, L. T., 2006. On the implementation of an interior-point filter line-search algorithm for large-scale nonlinear programming. *Mathematical Programming* 106 (1), 25–57.
- Wagner, T. J., Dell, R. W., Eisenman, I., 2017. An analytical model of iceberg drift. *Journal of Physical Oceanography* 47 (7).
- Walter, E., Pronzato, L., 1997. Identification of parametric models. *Communications and Control Engineering* 8.
- Wang, Y., deYoung, B., Bachmayer, R., et al., 2015. A method of above-water iceberg 3d modelling using surface imaging. In: *The Twenty-fifth International Offshore and Polar Engineering Conference*. International Society of Offshore and Polar Engineers.
- Wei, Y., Chen, M.-C., 2012. Forecasting the short-term metro passenger flow with empirical mode decomposition and neural networks. *Transportation Research Part C: Emerging Technologies* 21 (1), 148–162.
- Wesche, C., Dierking, W., 2016. Estimating iceberg paths using a wind-driven drift model. *Cold Regions Science and Technology* 125, 31 – 39.
- WMO, 1970. *WMO sea-ice nomenclature, codes, and illustrated glossary*. World Meteorological Organization Rep. 259 (Tp.145), p. 147 Geneva.
- Wright, S., Nocedal, J., 1999. *Numerical optimization*. Springer Science 35, 67–68.
- Yang, F., Xiao, D., 2012. Progress in root cause and fault propagation analysis of large-scale industrial processes. *Journal of Control Science and Engineering* 2012.
- Yelland, M., Taylor, P. K., 1996. Wind stress measurements from the open ocean. *Journal of Physical Oceanography* 26 (4), 541–558.
- Younan, A., Ralph, T., Ralph, F., Bruce, J., 2016. Overview of the 2012 iceberg profiling program. In: *Arctic Technology Conference*.

- Yulmetov, R., Lubbad, R., Løset, S., 2016. Planar multi-body model of iceberg free drift and towing in broken ice. *Cold Regions Science and Technology* 121, 154 – 166.
- Zhang, X., Lai, K. K., Wang, S.-Y., 2008. A new approach for crude oil price analysis based on empirical mode decomposition. *Energy economics* 30 (3), 905–918.
- Zhou, M., Bachmayer, R., deYoung, B., et al., 2016. Adaptive heading controller on an underwater glider for underwater iceberg profiling. In: *Arctic Technology Conference*.